Near-field Imaging Using Self Mixing in Terahertz frequency Quantum Cascade Lasers

Pierluigi Rubino

Submitted in accordance with the requirements for the degree of Doctor of Philosophy

The University of Leeds

School of Electronic & Electrical Engineering

Pollard Institute

October 2019

The candidate confirms that the work submitted is his/her/their own, except where work which has formed part of jointly authored publications has been included. The contribution of the candidate and the other authors to this work has been explicitly indicated below. The candidate confirms that appropriate credit has been given within the thesis where reference has been made to the work of others.

Devices fabricated in Chapter 2 of this thesis appeared in publications as follows:

Rabi Chhantyal-Pun, Alexander Valavanis, James T. Keeley, Pierluigi Rubino, Iman Kundu, Yingjun Han, Paul Dean, Lianhe Li, A. Giles Davies, and Edmund H. Linfield, "Gas spectroscopy with integrated frequency monitoring through self-mixing in a terahertz quantum-cascade laser", *Optics Letters*, Vol. 43, Issue 10, pp. 2225-2228 (2018).

The THz QCL used for the measurements was fabricated and characterized by myself. Other authors were responsible for the measurements, analysis, QCL growth and supervision of the work.

J. Keeley, K. Bertling, P. L. Rubino, Y. L. Lim, T. Taimre, X. Qi, I. Kundu, L. H. Li, D. Indjin, A. D. Rakić, E. H. Linfield, A. G. Davies, J. Cunningham, and P. Dean, "Detection sensitivity of laser feedback interferometry using a terahertz quantum cascade laser", *Optics Letters*, Vol. 44, Issue 13, pp. 3314-3317 (2019).

The THz QCL used for the measurements was fabricated and characterized by myself. Other authors were responsible for the measurements, analysis, QCL growth and supervision of the work.

In loving memory of my aunt,

the late Anna Tarantino

Acknowledgements

First and foremost, it is a genuine pleasure to express my deep sense of gratitude to my supervisors, Dr. Paul Dean and Prof. John Cunningham for giving me the opportunity to do a PhD at University of Leeds. It was indeed a honour to be your PhD student during the last years under your guidance; I would like to thank you for all the help, advices and support throughout this journey. Thanks are due to Prof. Giles A. Davies and Prof. Edmund H. Linfield for all the valuable comments during the supervision meetings.

Special mention must go to Dr. James T. Keeley. Your help and your experience helped me on a daily basis; thanks for all the invaluable discussions and answers whenever I needed and for all the time you spent in the labs with me, sometime in vain. I must say you were incredibly helpful whenever I needed, even out of the working environment. You were a friend more than a colleague.

Another person who needs special attention is Dr. Iman Kundu. You trained me to fabricate the QCLs that I used for all the years of this PhD. I was always astonished looking at your passion to meticulously teach me every single step of fabrication. It's thanks to you I could fabricate so many good lasers. Special thanks go also to Dr. Mark C. Rosamond. You always had the right answer to solve any fabrication issue. I am also grateful to Dr. Alexander Valavanis, Dr. Andrew Burnett and Dr. Joshua Freeman for the countless help and for cheering the lab environment up whenever you were in.

I would like to make a special note to all my colleagues, not only the ones I shared the office with. Dr Reshma A. Mohandas, Dr. David Bacon, Dr. Chris Russell, Aleksandar Demic, Esam Zafar, Panayiotis Rodosthenous, Dr. Mustafa Bakr and Masoud Ghalaii.

Another special mention goes to the italian crowd at the university. Dr. Paolo Actis, Dr. Bruno Scaglioni, Francesco Colucci, Vanessa Mancini, Aleks Attanasio, Giovanni Pittiglio, Simone Calò, Nicola Fornarelli, Lavinia Barducci and Francesco Foglino. Thank you all to make me feel a bit closer to home.

Thanks to my housemate Simone Ambrogio. We shared not only a house, but also a bunch of experiences that I will never forget.

Special thanks to my beautiful girlfriend, Ayinalem, for the incredible support. I do not think I could finish my PhD without you.

I am thankful to my family for all the love and the support. From the decision to start a PhD despite being far from home. The courage and the strength they gave me was incredibly helpful.

Abstract

Self-mixing (SM) effect in terahertz (THz) quantum cascade lasers (QCLs) can be good a candidate to replace the standard detection systems, offering a compact and coherent detection. SM effect occurs when part of the radiation emitted from a laser and reflected from a target is re-injected into the laser cavity. The re-injected field interferes with the intra-cavity field creating perturbations that can be measured by recording the laser terminal voltage. Amplitude and phase of the re-injected field can be recorded.

In this work, SM detection in THz QCLs was used to acquire images of radically different samples; a human skin sample, a skin sample containing melanoma and silicon wafers. A noise equivalent power (NEP) of $\sim 1.4\text{pW}/\sqrt{Hz}$ is demonstrated, making SM techniques suitable for applications that requires detection of weak fields such as near-field (NF) systems.

NF imaging allows the investigation of micro- and nano-scale structures below the diffraction limit. In this work SM detection in a THz QCL was combined with a scattering-type near-field optical microscope (s-SNOM) to achieve a sub-wavelength resolution <100 nm. By exploiting the current-controlled frequency tuning of the THz QCL and the intrinsically coherent nature of the SM scheme, a stepped-frequency approach was developed to obtain interferometric data at each pixel of the image using an all-electrical approach. The possibility to retrieve complex permittivity information of materials is demonstrated by using two samples, Au/SiO_2 (gold on silicon dioxide) and Au/KBr (gold on potassium bromide).

The final part of this work is dedicated to the study and NF imaging of graphene with a particular focus on the possibility of imaging propagating plasmons using THz radiation. This thesis presents the relevant theory and describes the modelling of surface plasmons in graphene taking into account two possible substrates, SiO_2 and hexagonal boron nitride, h-BN.

Contents

List of publications

The following journal and conference papers were published by the author during the course of this work.

Journal papers

- J. Keeley, K. Bertling, P. L. Rubino, Y. L. Lim, T. Taimre, X. Qi, I. Kundu, L. H. Li, D. Indjin, A. D. Rakić, E. H. Linfield, A. G. Davies, J. Cunningham, and P. Dean, "Detection sensitivity of laser feedback interferometry using a terahertz quantum cascade laser", *Optics Letters*, Vol. 44, Issue 13, pp. 3314-3317 (2019).

- Rabi Chhantyal-Pun, Alexander Valavanis, James T. Keeley, Pierluigi Rubino, Iman Kundu, Yingjun Han, Paul Dean, Lianhe Li, A. Giles Davies, and Edmund H. Linfield, "Gas spectroscopy with integrated frequency monitoring through self-mixing in a terahertz quantum-cascade laser", *Optics Letters*, Vol. 43, Issue 10, pp. 2225-2228 (2018).

Conference papers

- A. Ottomaniello, J. Keeley, P. Rubino, L. Li, E. H. Linfield, A. G. Davies, P. Dean, A. Pitanti and A. Tredicucci1, "Self-mixing optomechanics with nanometer resolution in a Terahertz quantum cascade laser", *Infrared Terahertz Quantum Workshop (ITQW) 2019*, Ojai, California, USA, Sept. 2019.

- Pierluigi Rubino, James T. Keeley, Iman Kundu, L. Li, A. G. Davies, E. H. Linfield, J. Cunningham, Paul Dean, "Coherent THz apertureless near-field microscopy based on self-mixing in QCLs", *8^{th} International Quantum Cascade Laser School and Workshop IQCLSW 2018*, Cassis, France, Sept. 2018.

- Pierluigi Rubino, James T. Keeley, Iman Kundu, L. Li, A. G. Davies, E. H. Linfield, J. Cunningham, Paul Dean, "Coherent THz apertureless near-field microscopy based

on self-mixing in QCLs", *International Workshop frontiers of photonics, plasmonics and electronics with 2D nanosystems 2018*, Erice, Sicily, Italy, July 2018.

- Pierluigi Rubino, James T. Keeley, Iman Kundu, L. Li, A. G. Davies, E. H. Linfield, J. Cunningham, Paul Dean, "Coherent THz apertureless near-field microscopy based on self-mixing in QCLs", *Royal Microscope Society (RMS), Scanning probe microscopy (SPM) 2018*, Leeds, UK, June 2018.

- J. Keeley, P. Rubino, J. R. Freeman, K. Bertling, Y. L. Lim, R. A. Mohandas, I. Kundu, T. Taimre, L. H. Li, D. Indjin, A. D. Rakić, E. H. Linfield, A. G. Davies, and P. Dean, "Laser feedback interferometry using terahertz quantum cascade lasers", 8^{th} *International Quantum Cascade Laser School and Workshop IQCLSW 2018*, Cassis, France, Sept. 2018.

- Alexander Valavanis, Rabi Chhantyal Pun, James Keeley, Pierluigi Rubino, Iman Kundu, Lianhe Li, A. Giles Davies, E. H. Linfield and P. Dean, "Frequency-monitored gas spectroscopy through self-mixing interferometry in a terahertz quantum-cascade laser", *Infrared Terahertz Quantum Workshop (ITQW) 2017*, Singapore, Sept. 2017.

List of Figures

List of Tables

List of abbreviations

2D - Two-dimensional

3D - Three-dimensional

AFM - Atomic force microscope

AlGaAs - Aluminium-Gallium-Arsenide

AR - Active region

a-SNOM - Aperture-type scanning near-field optical microscopy

AuGeNi - Gold-Germanium-Nickel

BTC – Bound-to-continuum

CO_2 - Carbon dioxide

CSL – Chirped superlattice

CVD - Chemical vapour deposition

CW – Continuous wave

CWF - Coupling weight function

DAQ – Data acquisition (board)

DC – Direct current

DRI – Diffuse reflectance imaging

EO - Electro-optic (detection)

EM - Electromagnetic (waves)

EPE - Excess phase equation

ERF - Edge response function

eV - electron volt

FD - Finite-dipole (model)

FEL - Free electron laser

FET - Field-effect transistor

FFT – Fast Fourier transform

FIB - Focused ion beam

fs - Femto-second (laser)

FTIR – Fourier transform infrared (spectroscopy)

FWHM – Full-width half-maximum

GaAs – Gallium-Arsenide

h-BN - Hexagonal boron nitride

IMPATT - Impact avalanche transit time diodes

IR - Infrared

IV – Current-voltage

KBr - Potassium bromide

LFI - Laser feedback interferometry

L-He - Liquid helium

LI – Lasing power-current

LIA – Lock-in amplifier

LNP - Low noise preamplifier

LO - Longitudinal-optical (phonon)

MBE – Molecular beam epitaxy

MHz - Megahertz

Mid-IR – Mid-infrared

MM - Metal-metal (waveguide)

MTF - Modulation transfer function

NEP - Noise equivalent power

NF – Near-field

NW - Nanowire

OF – Optical feedback

PL - Photonic lattice

PMMA - Polymethil methacrylate

PP - Plasmon propagation

PSU - Power supply

QCL – Quantum cascade laser

QD - Quantum dot

QW - Quantum well

RF - Radio frequency

RMS – Root mean square

RP – Resonant-phonon

RPA - Random phase approximation

rpm - Revolutions per minute

RT - relaxation time

RTA - Rapid thermal annealer

SD – Standard deviation

SFI - Swept-frequency interferometry

SiO_2 - Silicon dioxide

SISP – Semi-insulating surface plasmon

SM – Self-mixing

SNR – Signal-to-noise ratio

SP - Surface plasmon

T_C – Time constant

TDS – Time domain spectroscopy

THz – Terahertz

Ti - Titanium

TM - Transverse magnetic (modes)

TPI – Terahertz pulsed imaging

TUNNETT - Tunnel injection transit time diodes

UV - Ultra-violet

1 Introduction

The terahertz (THz) frequency range lies in between the infrared (IR) and microwaves regions of the electromagnetic spectrum. It covers frequencies roughly spanning from 300 GHz to 10 THz (with associated wavelengths, λ from $\sim 1\,\text{mm}$ to $\sim 30\,\mu\text{m}$ and photon energies, from $\sim 1.2\,\text{meV}$ to $\sim 41\,\text{meV}$) and it is known as the connection point between electronic and photonic techniques (see figure 1.1 [1]). For decades it has been referred to as the "THz gap", because this region suffered from a lack of compact and efficient devices capable of generating and detecting THz radiation [31, 32]. However during the last 20 years intense interest from the scientific community boosted the development of technologies capable of addressing the THz region.

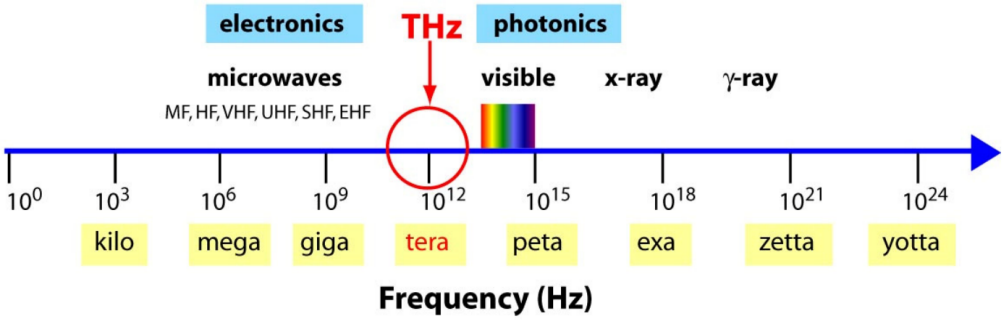

Figure 1.1: Schematic of the electromagnetic spectrum showing the THz region. Adapted from G. Williams [1].

1.1 Terahertz Radiation

The interest in THz radiation is related to the key applications that are being explored in this region of the electromagnetic spectrum, such as imaging [33], astronomy [34] and spectroscopy [35]. THz waves are excellent in security applications since they can detect explosives and concealed weapons thanks to their ability to penetrate clothing, plastics and many other non-metallic and non-polar materials [36, 37]. Furthermore THz radiation is non ionising and non destructive, due to the low photon energy, and it therefore has pontential to be a substitute for X-rays in airport security imaging [37]. THz biomedical

imaging is another appealing application because THz radiation is strongly absorbed by water making it ideal for the study and detection of cancerous tissues [38], both *ex vivo* and *in vivo* [39]. THz spectroscopy can be extremely effective since many molecules have their rotational and vibrational excitations in the THz region. For example, the identification of drugs [40] and explosives materials [41] are applications based on the THz spectroscopy; astronomers exploit THz detectors to probe the spectra of thermal emissions from stellar dust clouds [42] in order to understand star formation and the abundance of elements into the cosmos. THz spectroscopy is also used to monitor atmospheric composition and pollution [43, 44]. Other applications have also been demonstrated including THz wireless telecommunications [45] and darki-field imaging of biomedical tissues [46].

Industrial applications have been so far limited due to the lack of high power, room temperature and efficient source of THz radiation. Of remarkable interest is the work of the company TeraView, that manufacture systems based on THz pulsed imaging capable of analysing the thickness of car paint layers and of pharmaceutical tablet coatings [47, 48]. Today most of the high power THz sources operate at cryogenic temperature [49, 50] or through the need of expensive pump lasers [51]. Since the THz region is the connection point between electronics and photonics, the generation of coherent THz waves has usually required the conversion of electrical signals to higher frequencies or from down-conversion of optical frequencies. Frequency multipliers generate THz frequencies in a non-linear circuit by inefficiently distorting the input signal into higher harmonics with low optical powers [52]. For example, electric devices such as Schottky diode multipliers have been able to generate powers of $\sim 15\,\mu$W at 1.7 THz [53]. Resonant tunnelling diodes (RTDs) based on GaInAs/AlAs have been used to generate and amplify THz radiation to power level of $\sim 23\,\mu$W at 342 GHz and $\sim 0.6\,\mu$W at 1.02 THz [54]. Other solid-state devices such as impact avalanche transit time diodes (IMPATT), tunnel injection transit time diodes (TUNNETT) and Gunn devices are restricted to operating at frequencies of few hundreds of GHz due to frequency roll-off [54, 55]. On the other hand, the conversion of optical signal to lower frequencies has been achieved by using femtosecond sources, lasing in the visible or IR region, to excite electron-hole pairs in a crystal. For example,

excitation of a GaSe crystal has produced THz radiation in the range 0.18 - 5.27 THz with an average power of ~ 1 mW [56]. Early methods include using subpicosecond laser pulses to generate a broadband THz radiation from a photoconductive antenna [57] or a photoconductive Hertianz dipole [58] with no need for cryogenic temperatures. THz wave parametric oscillator have been employed for THz generation by using a non-linear crystal in a Fabry-Perot cavity, excited by an ultrafast laser [59]. Also gas lasers have been used for generating THz radiation where the lasing frequency depends on the gas in the laser cavity; methanol is a commonly used gas for this since it has a lasing transition at 2522.78 GHz. Despite the optical power levels being of the order of 20 mW, they require kilowatt energy consumption, effectively limiting the applications [54, 60]. Another method to generate THz radiation is the use of free electron lasers (FEL); in this system an alternating magnetic field accelerates the electrons, producing high power and tunable THz radiation [61], but it has the disadvantage of being large and very expensive as well as requiring strong magnetic fields.

The invention of the quantum cascade lasers (QCLs) in the 1994 [62] is considered as major breakthrough in this context. After their inception as mid-IR sources, in 2002 the first QCL lasing in THz region was reported [63]. THz QCLs will be discussed in detail in Chapter 2.

1.2 Terahertz imaging

THz imaging is considered as one of the most important application of THz radiation. The first reported THz imaging system dates back to 1976 [64], where a simple apparatus was used to acquire images of a metallic key enclosed within a vinyl case and a cardboard box filled with rubber, in transmission and reflection by using a GaAs detector cooled to 4.2K. Two years later a second THz imaging system was demonstrated for detection of defects in polyethilene-insulated power cables [65]. Thanks to the properties of the THz radiation, THz imaging systems have shown a remarkable growth in different application areas, including for biomedical imaging, pharmaceutical inspection, and the non-destructive analysis and identification of materials [36, 37, 66]. THz waves are able

to penetrate materials that are opaque to visible and IR frequencies like plastic, papers, ceramics and woods. Also fabrics have shown transmission for frequencies lower than 1 THz [67]. The resolution, limited by the diffraction of the beam waist, is sub-millimetre, making the THz radiation optimal for quality control like coating of tablets [68, 69] or to monitor the thickness of paint [70]. The ability to excite vibrational and rotational states of molecules makes it ideal for chemical identifications [35, 66, 71]. THz is also strongly absorbed by polar molecules like water making THz imaging a perfect tool for biomedical applications in that it can differentiate tissue types, so permitting cancerous tissues to be diagnosed, for example [39]. The light sources for the aforementioned imaging applications usually exploit bulky and expensive systems based on ultrafast lasers for the THz generation. Furthermore, some imaging applications demand a continuous wave (CW) source which have been demonstrated by using a multiplied Gunn emitter combined with a femto-second laser [72] or a CW photomixer [73].

THz QCLs, on the other hand, are compact, high power, tunable and CW sources which do not require the use of an ultra fast laser [9, 74, 75]. All these characteristics make the THz QCLs an ideal light source for coherent imaging systems [13]. Incoherent and coherent image acquisitions are both possible, depending of whether the recorded image is based only on the THz power or its phase information is extracted.

1.2.1 Incoherent imaging with THz QCLs

Examples of incoherent detection are those based on thermal detectors such as cryogenically cooled bolometers [76, 77] or pyroelectric sensors [3]. These kind of detectors have demonstrated high sensitivity and high dynamic range, allowing detection of samples with high attenuation. An image is usually reconstructed by raster-scanning the sample, placed at focus point of the THz beam, and recording the THz power at each pixel. The time for acquisition is dictated by the pixel size, integration time and the speed of the detector. Thermal detectors are generally and necessarily slow, requiring sample translation for acquisition, resulting in typical dwell times of seconds per pixel. Recently, however, a fast acquisition was demonstrated by using THz QCL lasing at ~ 2.5 THz [2], figure 1.2. The

THz beam is collimated by means of a 50 mm diameter poly-4-methylpentene-1 (TPX) lens onto a flat rotating mirror. The mirror deflects the beam onto a sample, which can also be tilted; the beam is focused through a HDPE lens. By steering the mirror the beam waist is scanned across the sample. The beam transmitted through the sample is then recorded on a Ge:Ga photo-conductive detector. The system is capable of reconstructing a 2D image of 4550 pixels in 1.1 second. By rotating also the sample even a 3D image can be recorded.

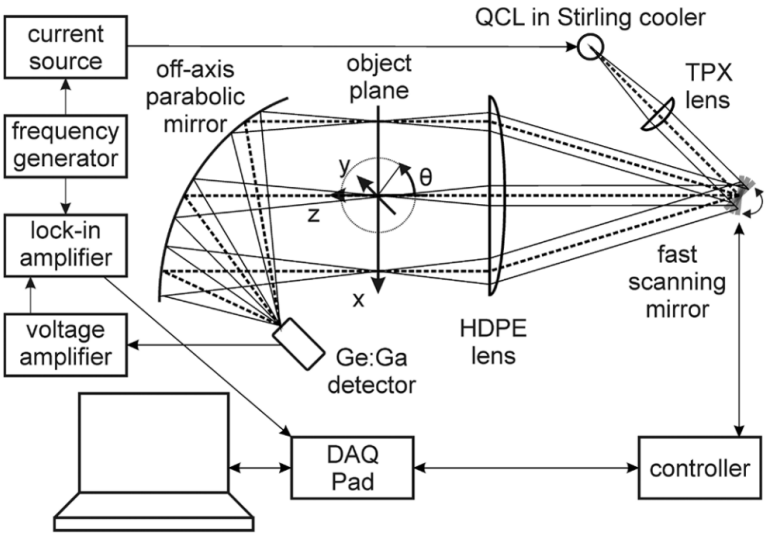

Figure 1.2: Experimental setup used for fast incoherent acquisition. Adapted from N. Rothbart [2].

QCLs have shown also the possibility of real-time imaging at ~ 20 fps (frames per second), by exploiting micro-bolometer array detectors and high power THz QCLs, recording frames in transmission and reflection [78, 79].

Diffuse THz imaging has also shown interesting benefits. Samples which are highly attenuating or too thick cannot be imaged in a transmission system since the beam can be easily absorbed. Diffuse reflectance imaging (DRI) overcome this problem by collecting the radiation diffuse or specularly reflected from a sample surface. THz DRI was demonstrated by imaging admixtures of polymethyl methacrylate (PMMA) and polystyrene powders (PMMA is highly absorbing while polystyrene is weakly absorbing) in different concentrations [3]. The system consists of a QCL lasing at 2.8 THz and cooled to ~ 5 K; the radiation

focused on the sample is collected by two different detectors. A pyroelectric sensor was used to detect the specularly reflected beam, and a helium-cooled silicon bolometer used to collect the diffused beam, as shown in figure 1.3(a). Different mixtures, ranging from 0 % to 100 % of PMMA, were placed in a polystyrene sample holder made of 10mm-deep compartments, as shown in figure 1.3(b).

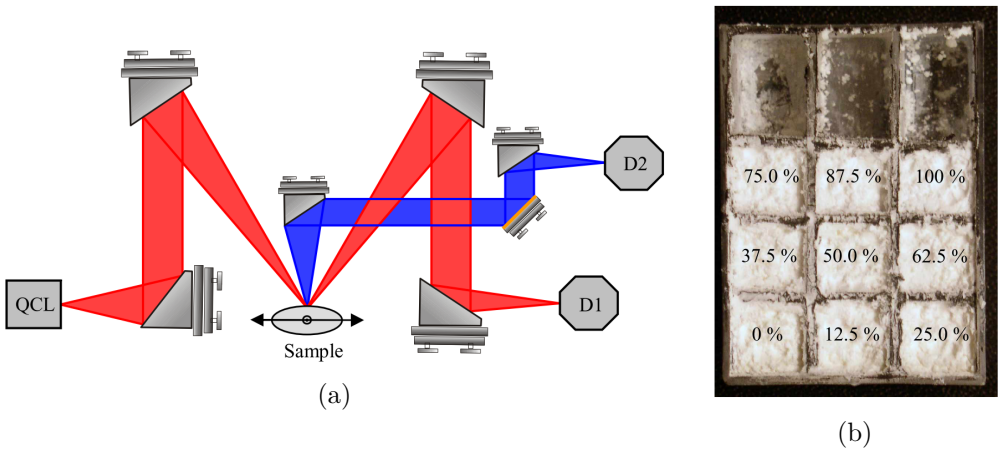

(a) (b)

Figure 1.3: A diffuse THz reflectance imaging system. (a) Schematic of the setup. (b) Photograph of the sample holder containing different mixtures of PMMA and polystyrene in PMMA concentration. Adapted from P. Dean [3]

Despite the specular reflectance image, figure 1.4(a), shows the beam reflected from the lid of the sample holder, the diffuse image, figure 1.4(b), clearly identify the differences of absorption due to the amount of PMMA in the mixture. Different beam scattering of the particles is excluded due to similar particle size and refractive indices for PMMA and polystyrene.

All the schemes adopted for these imaging applications measure only the THz magnitude. In some cases, better information on the sample can be extracted if the phase of the THz field is also recorded. For example 3D reconstruction of the object or the complex refractive index (or complex permittivity) of the material can be retrieved by adopting a coherent imaging scheme.

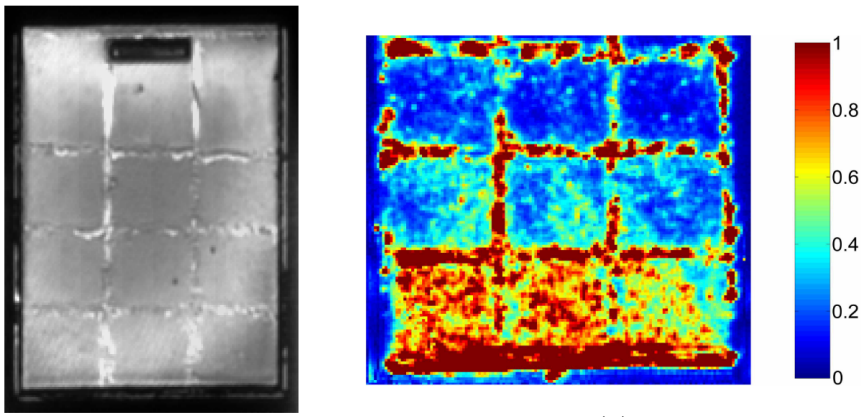

(a) (b)

Figure 1.4: (a) Specular and (b) diffuse reflection images of the sample holder containing different mixtures of PMMA and polystyrene. Adapted from P. Dean [3]

1.2.2 Coherent imaging with THz QCLs

A different method for coherent detection of the THz field in a QCL is known as heterodyne detection. This approach considers the use of a mixer to mix the original THz field with a reference signal from a local oscillator so creating an intermediate frequency which is then detected through a spectrometer [80, 81]. QCLs are usually affected by electrical and thermal noise, which affect the QCL spectral stability. This creates a downside to the heterodyne approach which needs high frequency stability, making the need of a feedback loop to control the emitted frequency essential [82].

Another coherent approach is called inverse-synthetic aperture radar (ISAR) [4]. The authors employed the beam of a THz QCL lasing at 2.408 THz running in CW and mixed with the radiation of a very stable CO_2 laser-pumped molecular laser as a local oscillator, operating on the 2409.293 GHz line of CH_2DOH, through 2 Schottky diode mixers, used as reference and as receiver.

Figure 1.5(a) shows the setup used for the ISAR imaging. The system used an intermediate frequency of 1.048 GHz for both reference and receiver, which was also used to stabilise the THz QCL frequency to the CO_2 laser, achieving a QCL linewidth of 20-30 kHz. A Fourier transform analysis of the data through lock-in detection allowed magnitude and phase to be recorded with a sub-millimetre resolution of 0.4 and 0.6 mm respectively in

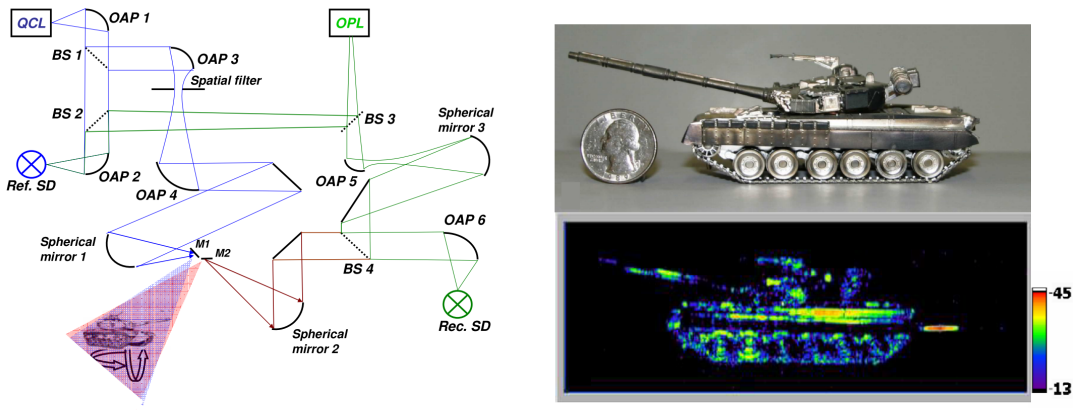

(a) (b)

Figure 1.5: (a) Schematic of the setup for the ISAR imaging system.(b) Top, a photograph of a plastic tank covered by aluminium; bottom, the obtained THz picture. Adapted from A. Danylov [4]

azimuth and elevation of the sample. Figure 1.5(b) shows a photograph on the top and the THz image obtained, of a plastic tank covered by aluminium.

A different system for coherent imaging employed a single mode QCL lasing at 2.5 THz which was stabilised to a near-IR fs-laser comb [5]. Two electro-optic (EO) detection units were used; EO1, to lock the QCL frequency to high harmonic of the fs-laser repetition frequency of $\sim$250 MHz and EO2 and to detect the beam reflected from the sample, figure 1.6(a). The beams of the two lasers were first split and then focused on the EO units generating beat-notes at 10 MHz for EO1 and 10.07 MHz for EO2, which are mixed to the signals created by two RF generators allowing lock-in detection of the THz field at 70 kHz. Figure 1.6(b) shows the THz power image and the unwrapped phase image of a 10 cent Euro coin obtained with this system.

Despite these systems allowing coherent imaging recording magnitude and phase of the THz field, their complexity makes them less than ideal since they require separate laser sources and detectors. A more compact coherent detection system is based on the self-mixing phenomenon, which has been exploited with several different kind of lasers.

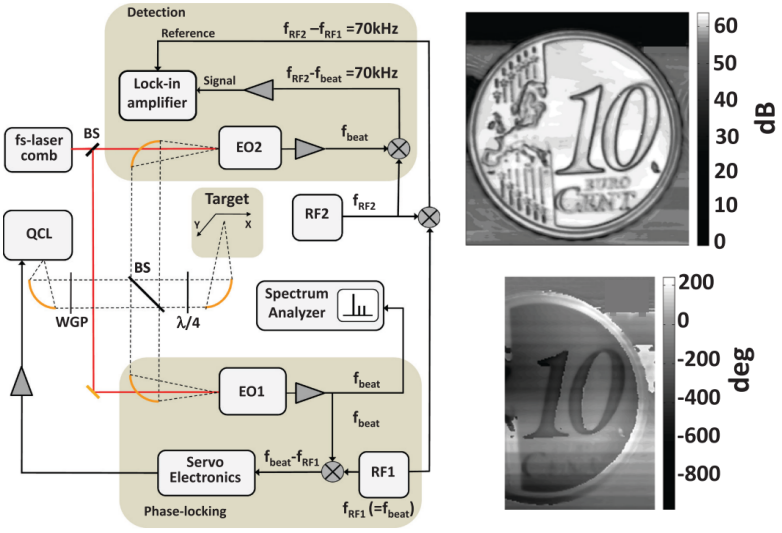

(a) (b)

Figure 1.6: (a) Schematic of the setup for THz QCL imaging using electro-optic sampling.(b) Top, a THz power image and bottom, the unwrapped phase of a 10 cent Euro coin. Adapted from M. Ravaro [5]

1.3 Self-Mixing

The self-mixing (SM) phenomenon occurs when part of the emitted radiation of a laser is reflected back into the laser cavity. The interference creates perturbation to the laser parameters as threshold gain, emission frequency, optical power and laser voltage, which sense the interference in term of magnitude and phase. The absence of an external detector makes the self-mixing system very compact and intrinsically coherent. The first evidence of the self-mixing effect date back to 1962 and was used with a Helium-Neon (He-Ne) laser to discriminate and suppress against the unwanted lasing orders from the reflection of an external mirror [83, 84]. Initially, the change in output power due to variation of external cavity length, with periodicity of half-wavelength, was measured from the rear laser facet by using a photodetector [85]. In the 1972 the measurement of the output power through a photodetector was modified to the measurement of the laser voltage [86]. After the invention of the solid-state lasers [87–89] similar experiments were conducted for lasing mode suppression [90]. Despite early observations of change in the threshold carrier density of semiconductor lasers depending on the phase of the reflected beam [91],

the first theoretical model of a laser under feedback was proposed by Lang and Kobayashi in 1980 [92]. The model describes that the change in carrier density caused by the optical feedback creates changes in medium refractive index, altering the laser emission frequency. In Chapter 3 of this thesis the equations resulting from this model are explained in detail. The first real applications used a CO_2 laser for Doppler velocity measurements [93] and 2 years later same application was demonstrated with a solid-state laser diode [94]. A large number of self-mixing applications have been demonstrated since then, including liquid flow velocity [95–99], displacement sensing [100–106], distance measurements [106–108] and analysis of laser parameters such as the linewdith [109] and linewidth enhancement factor [110–112]. Thanks to the peculiarity of being sensitive to the sample reflectivity and morphology, SM has also been used for coherent imaging systems such as surface profiling [113–115] and 3D imaging [108, 116–119]. Recently the SM effect has also been exploited with THz QCLs making use of their compact size and strong stability under optical feedback. In Chapter 3 a section is dedicated to a range of applications of systems based on SM in a THz QCL.

The resolution of an imaging system is limited to the wavelength of the light source. For example, the wavelength dependent resolution of an imaging system based on THz QCLs has been calculated to be $\sim 64\,\mu m$ at 3 THz [66], but experimentally a resolution of $\sim 200\,\mu m$ is common due to the irregularity of the beam spot [120]. In the chapter 4 of this thesis the spatial resolution will be calculated by adopting the square wave modulation transfer function (MTF).

In the last decades near-field techniques have opened up the possibility of achieving sub-wavelength resolutions (less than $\lambda\,/\,1000$) for imaging and spectroscopy [6, 121–123].

1.4 Near-field optics

The near-field (NF) interaction is that which occurs between light and an object whose size is smaller than the light wavelength [123, 124]. The idea of near-field interaction dates back to 1928 when E. Synge, in a letter to A. Einstein, suggested the possibility to overcome the diffraction-limit imposed by the light wavelength by passing the light

through a pinhole smaller than the wavelength, or using a tiny particle in close proximity of the specimen to scatter the light to image the surface of a sample [125, 126]. Despite the experimental difficulties of that period to create such a system, he suggested to use a pinhole in a metal plate or a quartz cone coated with metal except of the tip. Similar difficulties were experienced also by J. A. O'Keefe, when in 1956 he proposed a similar idea, underlining also the difficulties to scan the sample with micrometre resolution and to control the distance between sample and aperture [127]. In 1972 E.A. Ash and G. Nichols demonstrated for the first time the possibility to overcome the resolution of the light by employing microwaves with wavelength $\lambda = 3\,\mathrm{cm}$ so achieving a resolution of $500\,\mu\mathrm{m}$ ($\lambda/60$) through an aperture with diameter $\mathrm{d} = 1.5\,\mathrm{mm}$. 12 years later the first scanning optical near-field microscope was proposed by two groups [128, 129], both showing the possibility of achieving nanometre resolution by using visible light. In 1989 Fischer and Pohl carried out an experiment using a gold coated polystyrene particle irradiated by a visible laser radiation to image a thin metal film with 320 nm holes with a spatial resolution of 50 nm [130], basing the explanation of the results on the antenna theory. Their experiments detected oscillation of the plasma on a thin metal film which was already predicted by other experiments in 1968 by two groups [131, 132], but never actually imaged then. These early observation of surface plasmons (SPs) opened up one of the today major application of near-field microscopy, the *nanoplasmonic*.

From that moment two different types of near-field microscopy have co-existed: these are aperture-less or scattering-type scanning near-field optical microscopy (s-SNOM) and aperture based scanning near-field optical microscopy (a-SNOM). Near-field microscopy is today a major technique for applications like spectroscopy [123, 133–135], detection and imaging of propagating surface plasmons in metals [122, 136–139] and graphene [25–28, 140–146], single-molecules detection [134, 147–150], retrieval of complex constants of materials [151–153] and imaging mobile carriers in semiconductor devices [6]. s-SNOM systems are commercially available, and usually implemented in conjunction with atomic-force microscopes (AFM), where the radiation is scattered on tips having sizes in the nanometre range. Many of these systems exploit heterodyne detection to record magnitude

and phase data from objects. The detection is based on the standard thermal detection like cryogenically cooled bolometers [6], as shown in figure 1.7(a) or through the use of a DAC board [135] for s-SNOM, and dipole antennas for the a-SNOM [154], figure 1.7(b). On the other hand, the self-mixing scheme offers compactness, owing to the absence of an

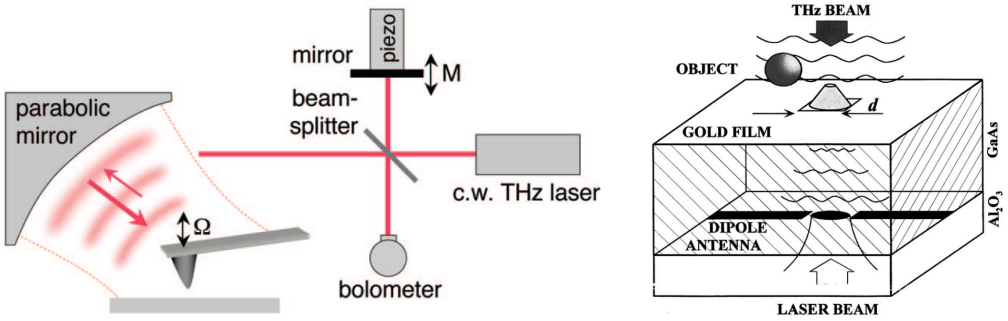

(a) (b)

Figure 1.7: (a) Schematic of s-SNOM system using a cryogenically cooled bolometer, adapted from A. Huber [6].(b) Schematic of a-SNOM system using a dipole antenna, adapted from O. Mitrofanov [7].

external detector, and the possibility to retrieve phase information by simply changing the external cavity length [155]. Up to date self-mixing scheme adapted to near-field imaging are few [122, 155]; in this thesis the near-field imaging using self mixing in terahertz QCLs will be demonstrated in two applications: in Chapter 5, an all-electrical approach will be used to retrieve information (magnitude and phase) of complex permittivity of two different crystals and, in Chapter 6 THz NF imaging will be exploited to image possible THz plasmon propagations on graphene.

1.5 Structure of this thesis

Chapter 2 presents a general theory of the functioning of THz QCLs, with explanation of the different active region designs, waveguides and how to achieve a single mode emission by FIB milling a photonic lattice of the top contacts. In this chapter fabrication methods will be also explained followed by the results obtained from the characterisation of the QCLs in terms of optical power and spectral characteristic for pulsed and continuous wave operation.

Chapter 3 is dedicated to self-mixing theory, presenting the two-, and three-mirror models and explaining the excess phase equation from the Lang and Kobayashi. This is followed by simulation of the self-mixing voltage and the explanation of experiments conducted in order to measure the detection sensitivity of a system based on the self-mixing effect in a THz QCL.

In Chapter 4 key parameters such as spatial resolution, signal-to-noise (SNR) ratio for imaging silicon wafers will be discussed and demonstrated. This chapter continues with a demonstration of self-mixing images in a THz QCL in the far-field by acquiring imaging of silicon wafers for photovoltaic applications. The possibility of imaging impurities embedded in the silicon wafer surface will be also demonstrated, followed by the opportunity to show the application of the self-mixing imaging also in transmission. The chapter concludes with the acquisition of the THz images from healthy human skin samples and cancerous human skin, showing the different absorption of the cancerous layers.

Chapter 5 presents the setup of a bespoken THz s-SNOM system to use a self-mixing scheme and its limitations. The chapter continues with the setup of the commercial s-SNOM system based on an AFM platform (a neaSNOM made by the company Neaspec GmbH). The system is characterised in order to understand its spatial resolution and how it changes as a function of the tip tapping amplitude. Approach curves are presented. The SNR of the system is then demonstrated for a sample of Si on Au defined by electron-beam lithography. The chapter will then focus on an all-electrical approach proposed in order to record phase and magnitude information from different samples, and this approach demonstrated by using two different crystal, a silicon dioxide, SiO_2, and a potassium bromide, KBr , crystal. It is shown how the results are related to the sample complex permittivities.

Finally, Chapter 6 presents the theory and modelling of THz surface plasmons (SPs) in graphene. A detailed theory from application of Maxwell equations is followed by a model constructed from the Fresnel equation for p polarized light, in order to understand the THz near-field interaction with graphene supported by two different substrates, SiO_2 and hexagonal boron nitride, *h*-BN. The fabrication of the samples will also be explained. THz NF images of the graphene samples defined in different structures will be shown along the

Raman spectra acquired for each sample. Discussion of the results will be focused on a comparison of the THz images and the Raman spectra and how defects affect them.
At the end of every chapter a conclusion section summarizes all the results and proposes future work that could be usefully carried out.

2 Terahertz Quantum Cascade Lasers (THz QCLs)

The term laser refers to *Light Amplification by Stimulated Emission of Radiation.* The first demonstration of this phenomena is attributed to T. Maimam, who stimulated optically coherent radiation in a ruby crystal emitting light at $\lambda \sim 694$nm [156, 157]. Two years later, R. N. Hall *et al* demonstrated the first diode laser, by electrically stimulating a p-n junction of GaAs which was able to emit coherent radiation at $\lambda \sim 840$nm [89]. In a laser diode the lasing wavelength depends mainly on the energy difference between valence and conduction band (Energy Gap, E_g = E_c - E_v) of the material used. The energy gap is an intrinsic property of materials and so this peculiarity restricts the possible lasing wavelengths in a solid-state semiconductor laser. Long wavelength lasers, like THz lasers in particular, are quite difficult to fabricate, because the energies associated with THz radiations are in the order of the optical phonon energies (a few tens meV), instead of hundreds of meV for the usual semiconductor energy band gap. For this reason, the scientific community has spent much effort to engineer new designs of semiconductor materials in order to create new band structures and so lasing frequencies. New nano-structures such as quantum dots (QDs, 0D), nanowires (NWs, 1D), and quantum wells (QWs, 2D) have emerged in which the strong quantum confinement leads to lasing frequencies which are not imposed by the energy band gap, but by confinement within the conduction or valence bands. Quantum confinements leads to an increase in the density of states at band edges, so effectively creating more available states for optical transitions [158] (see figure 2.1).

The first QW laser was invented 13 years later than the diode-laser, by Van der Ziel *et al* [159]. This consisted of a GaAs-$Al_{0.2}Ga_{0.8}As$ multilayer grown on a GaAs substrate in which they reported lasing at wavelength $\lambda \sim 822$nm by optically stimulating the medium. The radiation energy of 1.509eV was slightly greater than the GaAs energy band gap owing to the quantum confinement. The demonstration of the first quantum cascade laser (QCL) was in the 1994 by J. Faist *et al* [62]. They created a superlattice of $Al_{0.48}In_{0.52}As/Ga_{0.47}In_{0.53}As$ grown on a InP substrate able to lase at $\lambda \sim 4.2\mu$m ($\nu \sim$71THz) at cryogenic temperature when electrically stimulated. In the last two decades

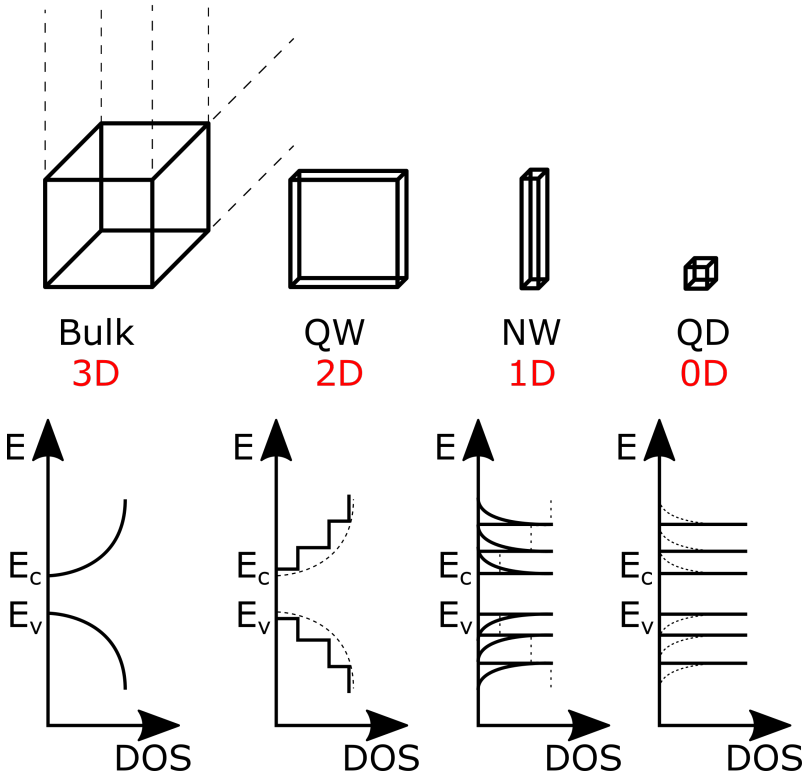

Figure 2.1: Quantum confinement effect explained schematically. QW, quantum wells; NW, nanowire; QD, quantum dot.

since this first demonstration, many steps forward have been achieved in the band engineering of the QCLs, leading to different lasing frequencies and emitted optical powers and covering the so called THz gap in the electromagnetic spectrum [8, 36, 160].

In this chapter a brief review of the theory of functioning THz QCLs will be given, along with experimental results and fabrication processes for lasing of different multimode QCLs operating around $\sim 3.4THz$. Moreover the experimental results from some of the fabricated QCLs in which a photonic lattice has been created by ion milling in order to establish a single mode emission will be shown and discussed.

2.1 Introduction to QCLs

As mentioned above, in diode lasers, the photon emission wavelength is imposed by the material energy gap, i.e. lasers emit photons when an electronic transition between two energy levels (the conduction and valence band) occurs. In order to emit photons, the

number of electrons populating the upper lasing level needs to be greater than the lower lasing level to create a so-called population inversion. In case of quantum wells, the quantum confinement creates different discrete energy bands (called subbands) in the conduction band, opening the possibility of so-called inter-subband transitions. Population inversion is an essential feature required for net amplification of light not only in this case, but is valid for any type of laser.

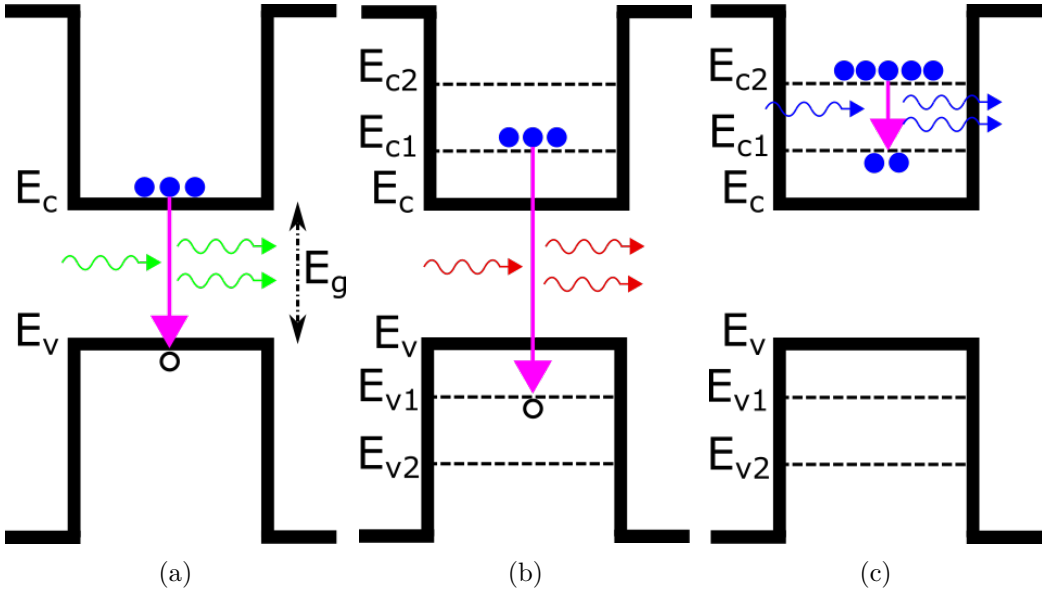

Figure 2.2: Optically pumped lasers; population inversion is an essential feature for net light amplification. Electronic transitions: (a) between CB and VB for a laser diode, (b) between CB and VB for a QW, (c) between subbands in CB for a QW.

In optically stimulated lasers, population inversion occurs thanks to an incoming photon (with energy $\hbar\nu$ equal to the difference of energy bands linked to the transition) which is absorbed by carrier in the lower level. The carrier is then promoted to the upper level and subsequently decays emitting a photon. The emitting photon will have energy $\hbar\nu$ greater or equal to the difference of energy bands associated to the transition. In the case of a laser diode $\hbar\nu \geq E_c$ - E_v (see figure 2.2(a)); in a QW transitions can occur between conduction band (CB) and valence band (VB) as well as only in CB, hence $\hbar\nu \geq E_{c1}$ - E_{v1} (see figure 2.2(b)) or $\hbar\nu \geq E_{c2}$ - E_{c1} (see figure 2.2(c)), where the latter one is the inter-subband transition. In a single QW with infinite width the energy difference between

two levels is given by equation 2.1 [161].

$$E_n = \frac{(\hbar\pi n)^2}{2m^* L}, \tag{2.1}$$

where $\hbar$, m^* and L are respectively the Planck constant, electron effective mass inside the well and the well thickness. Equation 2.1 explains that the energy difference between levels can be tuned by changing the thickness of the QW.

QCLs are unipolar lasers with heterostructures of coupled quantum well and potential barrier units stacked together which are able to emit photons when electrically stimulated. The bands of the quantum wells bend when a bias is applied along all the QCL structure. When the energy levels of the quantum wells are aligned the electron is allowed to tunnel from one QW to the next. A miniband in the thicker QW extracts the electron and tunnels it through to the next module. In this thicker QW the electron decays to the lower state thanks to a phonon (or by an electron-electron) scattering process which is faster than the radiative transition, effectively creating a population inversion and the avalanche effect which gives the name to the laser, a quantum cascade. The active region of the laser is identified as the whole lasing region made of the repetition of the same module. In this case the radiative transitions occur within the conduction band, as shown in figure 2.3.

Following equation 2.1 the lasing frequency of a QCL can be modified by modifying the thickness of the QWs in the structure. Although their first use was for the generation of IR radiation [62], in 2001 Kohler *et al* [63] were able to engineer a QCL (with a GaAs/AlGaAs heterostructure) lasing in pulsed mode at $\nu \sim 4.4$THz ($\lambda = 67\mu$m), handling few milliwatts of optical power and working up to 50K. By a few years later the QCLs were able to handle 250mW up to 169K in pulsed mode and 130mW up to 117K in continuous wave mode [8]. At the present, 25 years later their invention, THz QCLs can handle up to 2.4W at 10K and up to 1.8W at 77K, lasing at $\nu \sim$4.4THz [49]. Moreover through a cryogenic free system, it has recently been demonstrated a QCL operation at 206K with peak power of 1.2mW in pulsed mode [162]. Different performances (lasing frequency and optical power) are obtained by different active region structures, waveguides, physical dimensions and

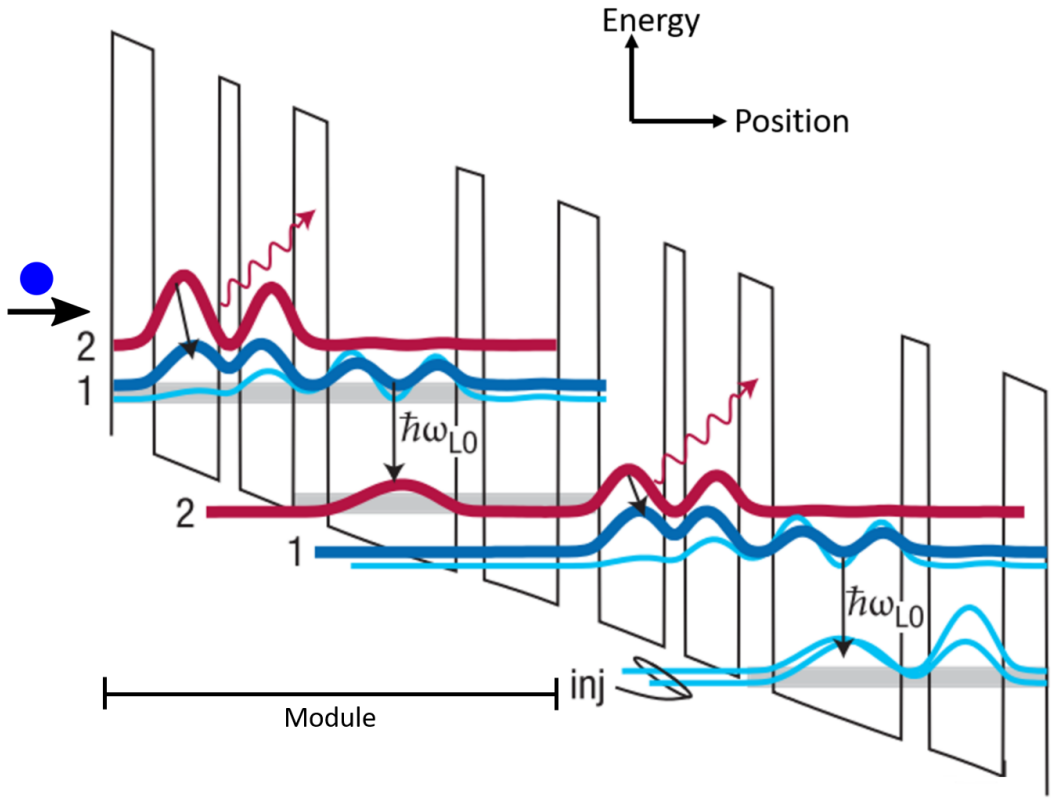

Figure 2.3: Basic functioning of a QCL. Adapted from Williams B. [8].

temperature.

Increase of temperature affects lasing threshold and optical power which tends to decrease because of population inversion degradation. Factors causing this degradation at high temperatures are the thermal backfilling and the thermally excited LO-phonon scattering [8]. In figure 2.4 a schematic of the population inversion degradation due to thermal effect is shown. By increasing temperature, the thermal backfilling occurs because the injector miniband tends to excite electrons with a Boltzmann distribution, promoting them to the lower lasing level, E_1. Also thermally activated LO-phonons scattering can occur because electrons in the upper lasing level, E_2, can absorb enough kinetic-energy to emit a LO-phonon and to relax to the lower lasing level without emitting photons.

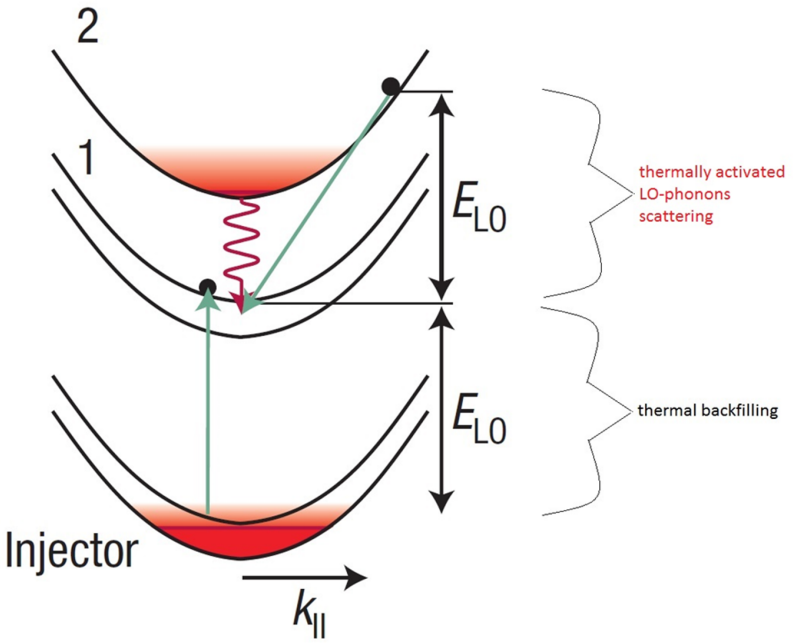

Figure 2.4: Thermal backfilling and thermally excited LO-phonon scattering are the major processes causing population inversion degradation. Adapted from Williams B. [8].

2.2 Design of active regions for THz QCLs

Epitaxially grown GaAs/$Al_xGa_{1-x}As$ is the most frequently used material for the structure of the THz QCL active regions (AR). The population inversion mechanism changes depending on the structure and might not only mediated by electron scattering with crystal phonons but also by electron-electron scattering. The scheme shown in figure 2.3, for example, is referred to the resonant-phonon structure (RP), but there are in total 4 main active region designs able to lase in the THz region of the electro-magnetic spectrum [8]. In order to compare different structures and waveguides a intersubband transistions peak gain is given by:

$$g(\omega_0) \propto \frac{\Delta N f_{21}}{\Delta \omega} \tag{2.2}$$

Where ΔN is the is the three-dimensional intersubband population inversion and $\Delta\omega$ is the transition linewidth. The oscillator strength f_{21} is proportional to the stimulated-emission cross-section and depends heavily on the overlap and symmetry of the wavefunctions

responsible for lasing. The main AR designs are listed below:

- Chirped Superlattice (CSL)
- Bound-To-Continuum (BTC)
- Resonant-Phonon (RP)
- Hybrid / Interlaced

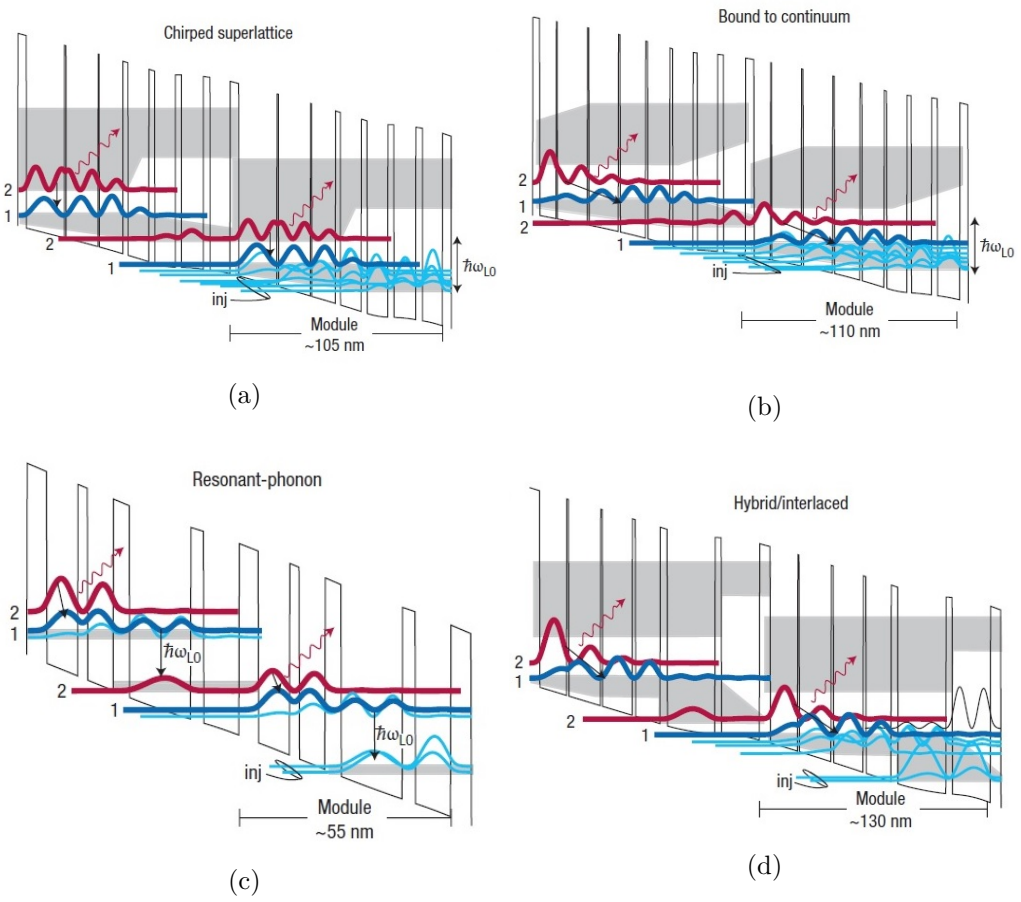

Figure 2.5: THz QCL active region designs: (a) Chirped Superlattice (CSL)(b) Bound-To-Continuum (BTC), (c) Resonant-Phonon (RP) (d) Hybrid / Interlaced. Red wavefunction indicates the upper lasing level; blue wavefunction is the lower lasing level; grey band is the so called miniband. Adapted from Williams B. [8].

2.2.1 Chirped Superlattice (CSL)

The CSL was the first design to be used for THz generation from a QCL. In the CSL design 2 states are responsible for the lasing transition, and population inversion is achieved by a combination of well tunneling and intersubband scattering [63]. The wavefunctions of the quantum wells in the active region are coupled to form minibands and thus photons are generated when the electrons decay from the lowest state of the upper miniband (2) to the highest state of the lower miniband (1), as shown in figure 2.5(a). A population inversion occurs because the electron-electron scattering within the miniband (intra-miniband scattering) is favoured over inter-miniband transition. This scattering allows electrons to relax to the bottom of the miniband, spontaneously emitting LO-phonons and leaving state 1 empty. A population inversion is also favoured by a density of states argument that brings to emit photons on $2 \rightarrow 1$ band-edge transition ($f_{21} \approx 2.5 - 3$), and not on another higher state of upper miniband. Despite this, this design has the advantage of low threshold current density, though thermal backfilling can limit its operation at high temperatures.

2.2.2 Bound-to-continuum (BTC)

In the BTC active region, as shown in figure 2.5(b), the inversion population mechanism is equivalent to the CSL one but a bound state is imposed to act as the upper lasing level. The design is based on a superlattice, but the bound state is created by a doping of the first quantum well [163, 164]. The radiative transition is less coupled than the CSL one ($f_{21} \approx 1.5$ - 2) and occurs diagonally in real space with an increased lifetime. BTC active regions are less subject to thermal backfilling and as a result exhibit improved temperature and power performance [163, 165].

2.2.3 Resonant-Phonon (RP)

The RP design is baed on a 3-wells structure where (see figure 2.5(c)) the collector and injector states are engineered to be separated by $E_{LO} = 36meV$, in $GaAs$, from the lower

lasing level [164]. The electron in the lower lasing level tunnels to the next well and decay to the collector by emitting a LO phonon through very fast sub-picosecond LO-phonon scattering, consequently enhancing the population inversion. The radiative transition is more vertical than BTC and the wavefunction of the lower lasing state (1) has a better overlap with injector state than the upper lasing state (2). In this way a longer lifetime of the state 2 compared to state 1 is ensured. The oscillator strength is small, f_{21} ≈0.5 - 1, and the current threshold high because the state alignment is more complicated to achieve, though the module length is one-half compared to the BTC or CSL design, so a good optical power is obtained by repeating more modules in the same amount of space [166].

2.2.4 Hybrid/Interlaced

The Hybrid design is in between that of BTC and RP (see figure 2.5(d)). Like the BTC design, the upper lasing state is a bound state while the lower lasing state is at an energy difference from the injector equal to a LO-phonon energy. The depopulation of the lower lasing state is achieved by both electron-electron and phonon scattering processes, which are both very fast. While the RP design requires high threshold current, the BTC design starts lasing at a low threshold current. Although both designs are combined to produce this hybrid design [167], the impact of the hybrid design has been limited mainly to situations where a relatively long wavelength is required [8].

2.3 Waveguides for THz QCLs

There are 2 major THz QCL waveguides: Semi insulating-surface plasmon (SI-SP) and Metal-metal (MM) waveguides. Three parameters can well describe the waveguide performance: α_w, α_m, and Γ are respectively called the waveguide loss coefficient, mirror loss coefficient and waveguide confinement factor. α_w takes account of scattering and absorption within the waveguide; α_m takes account of the optical coupling losses principally caused by facet reflections; Γ accounts the overlap of the mode with active region. Along with these factors, the gain, g_{th}, required to reach lasing threshold is another important

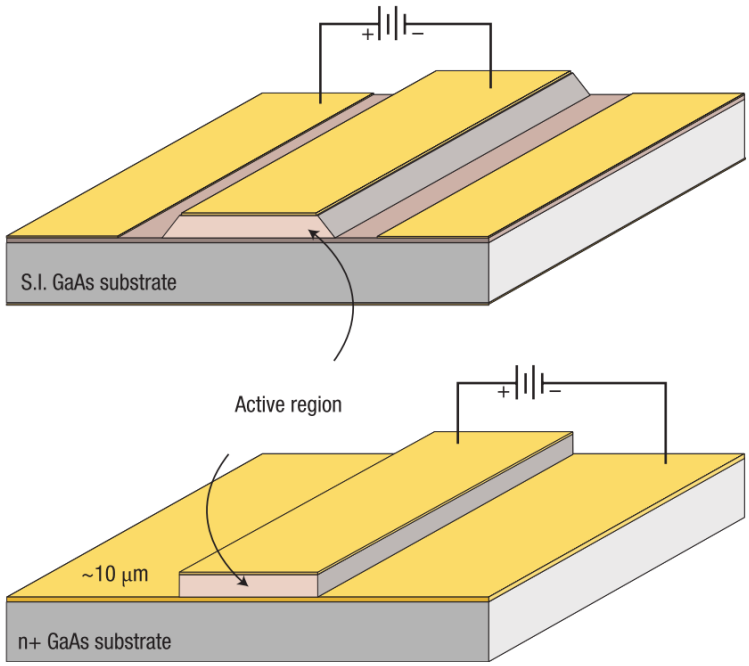

Figure 2.6: Waveguides used for THz QCLs. The top image shows the semi insulating-surface plasmon (SI-SP) waveguied. The bottom image shows the metal-metal (MM) waveguide. Adapted from Williams B. [8].

parameter since they are all linked each other by equation 2.3.

$$\Gamma g_{th} = \alpha_w + \alpha_m. \tag{2.3}$$

In the SI-SP waveguide, the active region is buried between a top metal layer and a bottom heavily doped (n+) thin layer of GaAs (acting as a plasmonic layer). It is all grown on a semi-insulating GaAs substrate. Usually if the ridge is wider than 100μm, the confinement factor will be in the range $\Gamma \approx$0.1-0.5 and the modes tend to extend into the substrate. For ridges narrower than 100μm, the modes will be squeezed into the substrate [8, 63, 168]. For the MM waveguide the active region is buried between two metal layers. As result the modes are almost totally confined within the active region, i.e. $\Gamma \approx$1. This strong MM waveguide confinement allows to have physical dimensions (vertical and lateral) smaller than the wavelength. Although they both have similar lasing threshold, MM tends to have better temperature performance, instead SI-SPs have higher

optical power and better beam patterns [8, 63, 168].

2.4 Single mode emission of THz QCL through a Phase-Adjusted Finite-Defect Site Photonic Lattice

In some applications such as for self-mixing imaging [12] and spectroscopy [169] a single-mode emission from the THz QCL is highly desirable. Some applications in addition also require a continuous wave frequency-tunability with current [116, 170]. Recently an interesting study conducted within our group by Kundu *et al* [9] achieved great frequency tunability and spectral control by exploiting a phase-adjusted finite-defect site Photonic Lattice (PL) created by focus ion beam (FIB) milling on the top metal layer and penetrating into the active region of the QCLs fabricated in SI-SP waveguide. This creates a so called photonic stopband because of the strong refractive index contrast (Δn_{eff}=$n_{eff,m}$-$n_{eff,e}$) between the metallized ($n_{eff,m}$) and the etched ($n_{eff,e}$) part of the waveguide. Moreover the PL does not extend the entire width of the ridge which is 150μm, but only for 130μm; the PL also does not extend through the entire length of the ridge but only through a part, roughly in the middle of it as shown in figure 2.7. One of the devices in

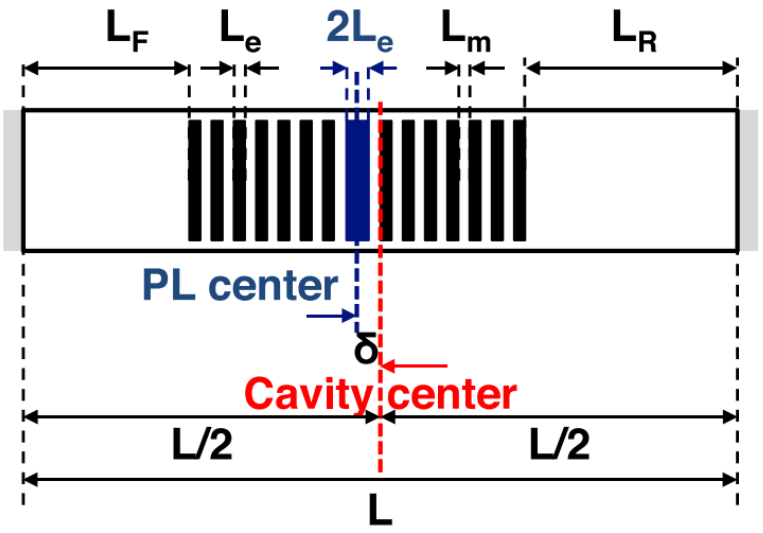

Figure 2.7: Schematic of a THZ QCL with a central π-phase-adjusted PL. L is the length of the QCL, L_e is the length of the etched part, L_m the length of the metallized part, L_F and L_R are the distances from the front and rear facet of the QCL. The center of the PL has a δ offset from the center of the QCL. Adapted from Kundu I. [9].

the study was engineered to have a discrete tuning following its multimode and blueshift emission, increasing the driving current, I_{QCL}, before the creation of the PL. Despite the predicted emission frequencies are ∼23GHz lower than the simulation, their experimental results have shown a good agreement to the discrete frequency tuning of ∼43GHz. Moreover the device has shown a continuous wave frequency tuning of ∼-3.8GHz across the range I_{QCL}=0.5-1.2A (see figure 2.8).

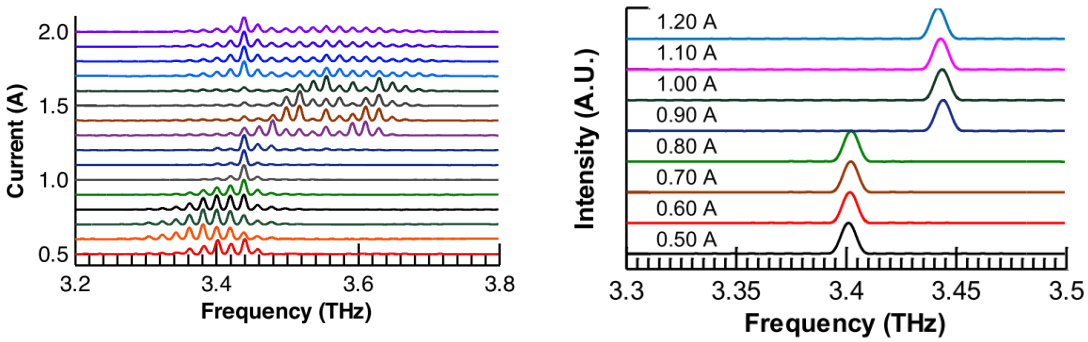

(a) (b)

Figure 2.8: Spectrum of a THz QCL (a), recorded at $T = 6K$ before the creation of the PL and (b) at $T = 30K$ after the PL. Adapted from Kundu I. [9].

A THz QCL with a PL as shown in [9] is a perfect candidate to be used for the study of this thesis; self-mixing imaging requires a stable single mode emission and a continuous frequency tuning which follows the increase of I_{QCL} exactly as shown in figure 2.8(b). For this reason, by using a FIB, a similar π-phase-adjusted PL will be created on the THz QCL exploited throughout the study of this thesis. In the next section fabrication of the QCL and the relative PL will be shown followed by optical power-current and voltage-current (LIV), and spectral characterization.

2.5 Fabrication of THz QCLs

The QCL used in this thesis is based on the active region (AR) design described in [171]. The wafer, L1180, was grown on a semi insulating GaAs substrate using molecular beam epitaxy by Dr. Lihane Li at University of Leeds. An initial 250 nm thick GaAs buffer was followed by a 300 nm thick $Al_{0.5}Ga_{0.5}As$ etch-stop layer and a 700 nm thick n-GaAs

contact layer, which was Si-doped to a density of ρ=2×10^{18}cm^{-3}. 115 repeats of the AR were then grown to a total thickness of ∼14.25μm, followed by a second 50 nm thick n-GaAs (ρ=5×10^{18}cm^{-3}) top-contact layer. A piece measuring roughly 8mm×6mm was cut from the wafer. and processed into 3 QCL ridges of width = 150μm and length = 6mm with a SI-SP waveguide following the procedure explained in [172]. A detailed list of the processing steps is explained in the next sections.

2.5.1 Edge Bead Removal

The sample of MBE wafer to be processed was first rinsed in acetone and isopropyl alcohol (IPA) to remove any dust or particles from the surface. For each solvent the sample was placed in a ultrasonic bath (Bandelin Sonorex Digital 10P), at 20% of its maximum power, for 5 minutes with the subsequent N_2 blow dry. Complete cleaning was ensured by ashing the sample in a plasma asher, an Emitech K1050X, at 50W power for 5 mins. Shipley S-1813 photoresist was then spun onto the sample surface a rate of 5000 rpm for 30 seconds, to a thickness of ∼1.2μm, followed by a soft-bake on a hotplate at 115°C for 1 min to remove any excess solvent. Edge-bead removal consisted of a photo-lithographic step to remove the thicker resist at the corner edge of the sample. This step was essential to ensure correct adhesion of the photo-lithographic mask during exposure. Exposure was carried out in a UV mask aligner with a lamp of wavelength of 310nm at 10mW/cm^{-2} for 30 s, followed by a developing in Microposit MF-319 developer for 75 s.

2.5.2 QCL ridge definition

Once the photoresist edge beads were removed the sample was exposed through a ridge mask in the same UV mask aligner with same exposure power for 4-5 seconds. This step defined a QCL ridge 150μm wide; a developing in MF-319 developer for 75 s removed the unwanted resist. The sample surface covered by the photoresist would ho on to be that part which was not attacked by subsequent wet etching.

In figure 2.9(b) it is possible to note the resist crosses on the sides of the image; these were used as alignment mark for the next photo-lithographic steps. The sample was then

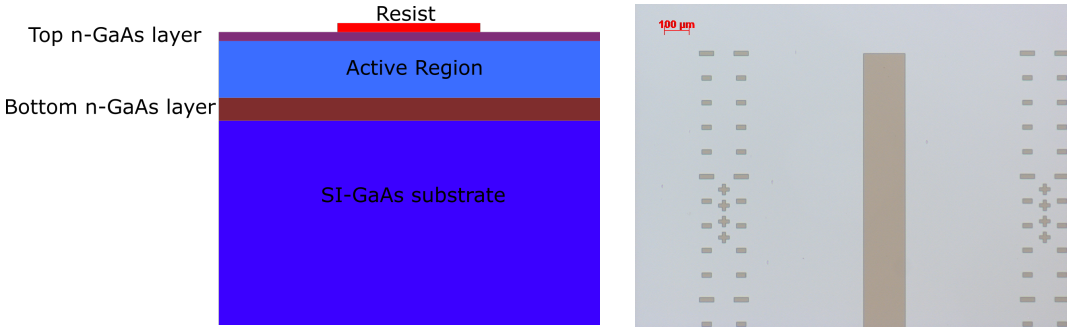

(a) (b)

Figure 2.9: Ridge definition photolithography. (a) schematic; (b) real image taken from an optical microscope a 5× magnification. The scale bar on the top left of the image is $100\mu m$.

attached on a sample glass by few drops of photoresist between the bottom face of the sample and glass surface, with a subsequent soft-bake at 115°C for 1 minute. The ridge was etched using a wet chemical etch in an acid solution comprised of H_2SO_4:H_2O_2:H_2 with ratio respectively of 1:8:40. This produced a uniform etching rate of $\approx 1\mu$m/min when left resting for roughly 15 minutes at 25°C. The etching process was carefully checked every 1-2 minutes at the start, and every 30 seconds when approaching the desired end, using an Alpha step D-500 surface profiler, in order to examine the depth of etching. Considering that the AR was $\sim 14\mu$m deep, the process was stopped when the ridge reached a thickness of $\sim 13.8\mu$m to make sure not to etch beyond the bottom n-GaAs layer. Wet etching can be slightly anisotropic if the sample is left dormant in the solution, and for this reason it was constantly agitated in an "8" shaped pattern to ensure uniformity. Finally, the resist was removed by soaking the sample in acetone. Figure 2.10 shows a schematic and an optical micrograph image of a typical sample after the wet etching step.

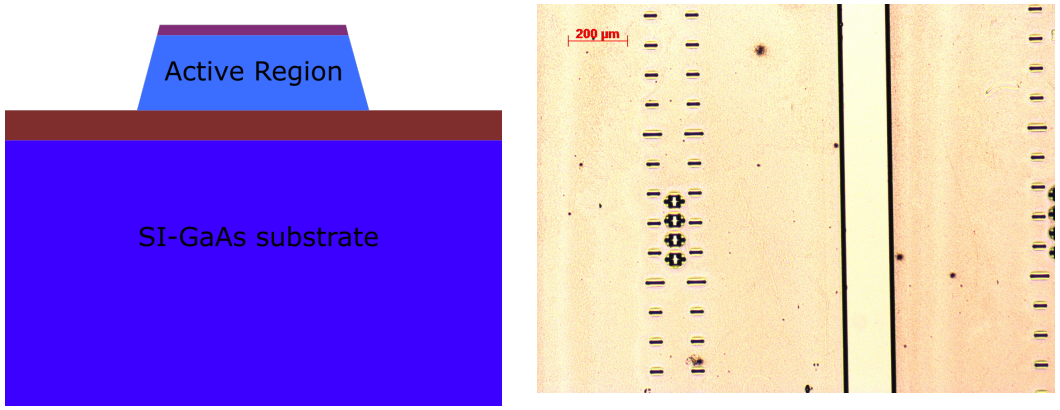

(a) (b)

Figure 2.10: Ridge wet etching. (a) schematic; (b) optical image taken from an optical microscope a 5× magnification. The scale bar on the top left of the image is 200μm.

2.5.3 Bottom contacts definition

In this part of the processing the bottom n-GaAs layer was covered by an alloy of AuGeNi, in order to create a bottom ohmic contact. S1813 was again deposited by spinning and soft baked at 90°C for 1 minute. After the exposure in the UV mask aligner, the sample was soaked in chlorobenzene for 2 min. The chlorobenzene has the ability to harden the resist by changing its solubility [173]. This was done with purpose of creating an undercut profile which improves the metal's ability to break and facilitating the lift-off process after metal evaporation. The sample was developed in MF 319 for 90 seconds and then rinsed in DI water.

Once the area of the bottom contacts 200μm wide was defined by photolithography, metallization was carried out in a Leybold thermal evaporator at vacuum pressure P<2×10^{-6}mBarr. A layer of AuGeNi 250 nm thick was evaporated; the subsequent lift-off process was done by leaving the sample in an acetone beaker for 3-4 hours. The lift-off was carefully checked through an optical microscope and in some cases the use of a soft brush was needed to remove the unwanted metal, paying attention not to ruin the QCL ridge. The sample was then cleaned by rinsing it in IPA and then blow dried by N_2.

The sample was then placed in a Rapid Thermal Annealer (RTA) from AnnealSys. The annealing process was carried out at 430°C for 1 min, in order to make the Ge atoms of

the AuGeNi diffuse into the n-GaAs bottom layer. This established an ohmic contacts between the two, effectively reducing the contact resistivity [174] while also reducing the metal stress. The diffusion of the *Ge* atoms was also visible through optical microscope images where the evaporated metal became darker due to the diffusion sites. A schematic of the bottom contacts processing along with images taken from an optical microscope at 5× magnification is shown in the figures 2.11, 2.12, 2.13.

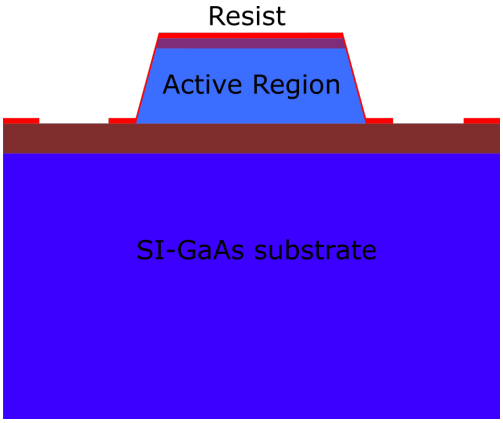

(a)

(b)

Figure 2.11: Bottom Contacts Photolithography. (a) schematic; (b) optical image taken using an optical microscope a 5× magnification. The scale bar on the top left of the image is 100μm.

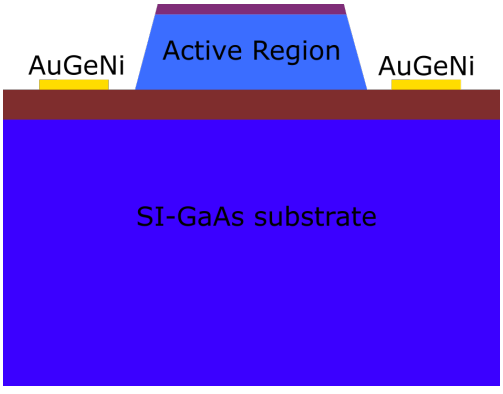

(a)

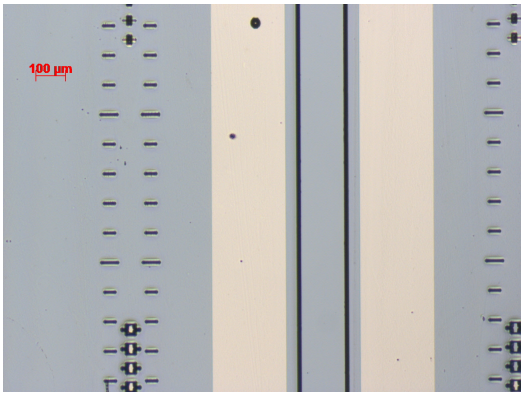

(b)

Figure 2.12: Bottom Contacts Evaporation. (a) schematic; (b) optical image taken using an optical microscope a 5× magnification. The scale bar on the top left of the image is 100μm.

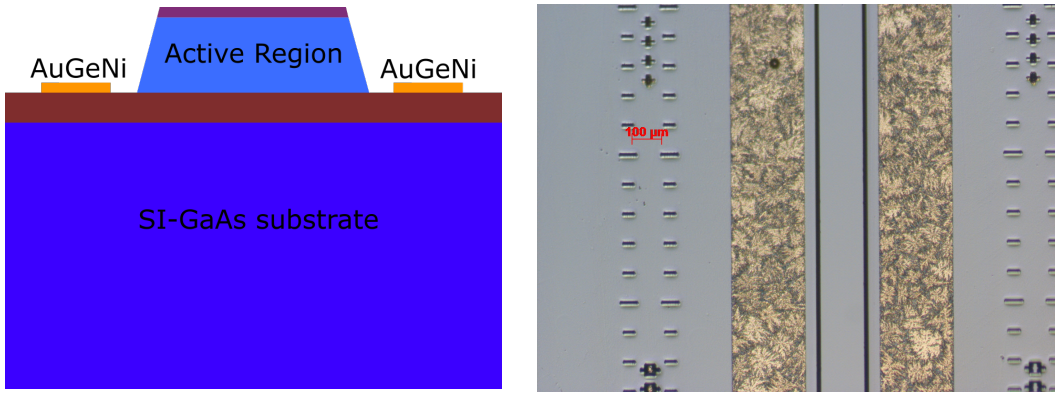

(a) (b)

Figure 2.13: Bottom Contacts Annealing. (a) schematic; (b) optical image taken using an optical microscope a 5× magnification. The scale bar on the top left of the image is 100μm.

2.5.4 Top contacts definition

An alloy of AuGeNi was also used for the top contacts of the QCL. The steps to define them were similar to what has been done for the bottom contacts: spinning S1813 photoresist, baking and photolithography followed chlorobenzene soaking and developing in MF319. The difference in this case was that the top contacts were defined to be two strips of alloy 20μm wide on top of the ridge. 100nm thick AuGeNi was evaporated in in the Leybold thermal evaporator at vacuum pressure P<2×10^{-6}mBarr. Lift-off was carried out in a beaker acetone for few hours, and by helping the process using a soft-brush where needed, but in this case no annealing was used in order to prevent diffusion of Ge into the active region which may alter waveguiding. A sequence of images in figure 2.14 and 2.15 explain schematically and with the real images the processing of the top contacts.

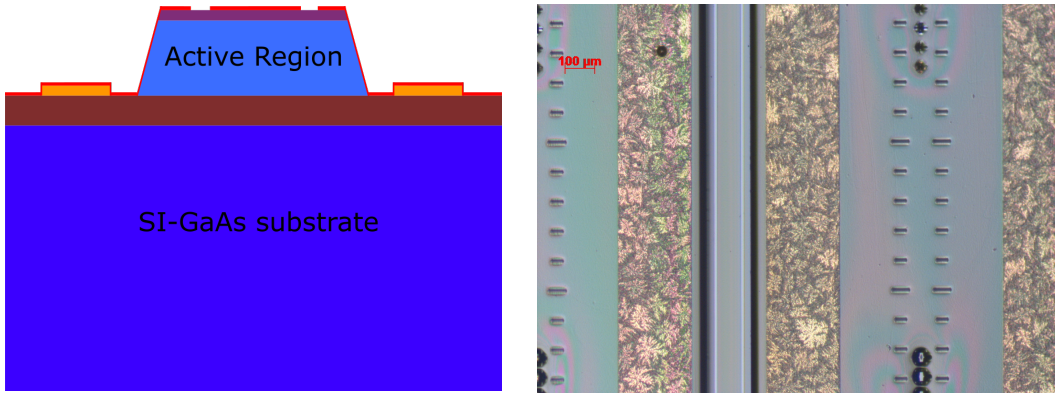

(a) (b)

Figure 2.14: Top Contacts Photolithography. (a) schematic; (b) optical image using from an optical microscope a 5× magnification. The scale bar on the top left of the image is 100μm.

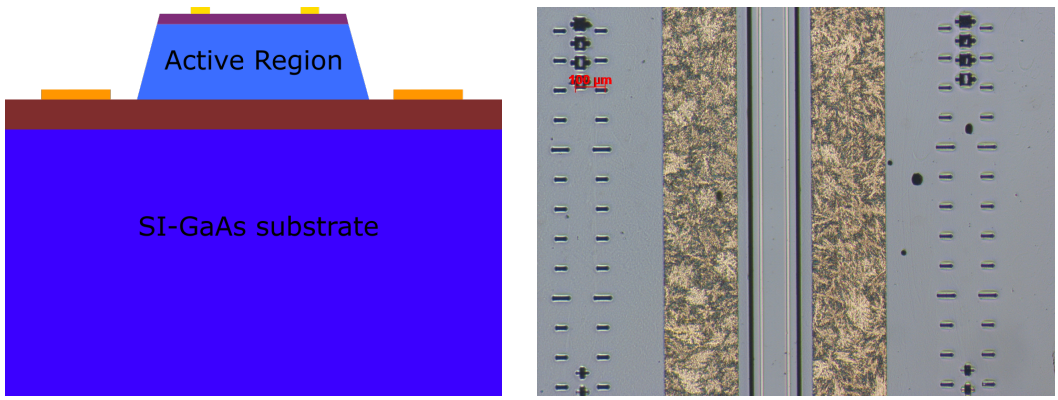

(a) (b)

Figure 2.15: Top Contacts Evaporation. (a) schematic; (b) optical image using from an optical microscope a 5× magnification. The scale bar on the top left of the image is 100μm.

2.5.5 Over-layer Metallisation

As previously mentioned the procedure shown in this chapter is referred to THz QCL processed in a SI-SP waveguide. In order to confine the THz radiation within the active region a Ti/Au overlayer was used to cover top and bottom contacts. This over-layer is useful also to facilitate the wire bonding of the device. Following the same steps adopted for the bottom contacts definition comprising S1813 photoresist spinning, photolithography, chlorobenzene soaking and developing in MF319, the sample was placed in a Edwards Turbo thermal Evaporator at vacuum pressure P<2×10^{-6}mBarr. 20 nm of Ti followed by 120nm of Au were evaporated on the sample surface. Lift-off in acetone dish for few hours, helped by a pipette blowing and soft-brush, was carried out later on. Finally the sample was cleaned by IPA rinsing and plasma ashing at 50W for 5 minutes. Figures 2.16 and 2.17 show this section of the processing.

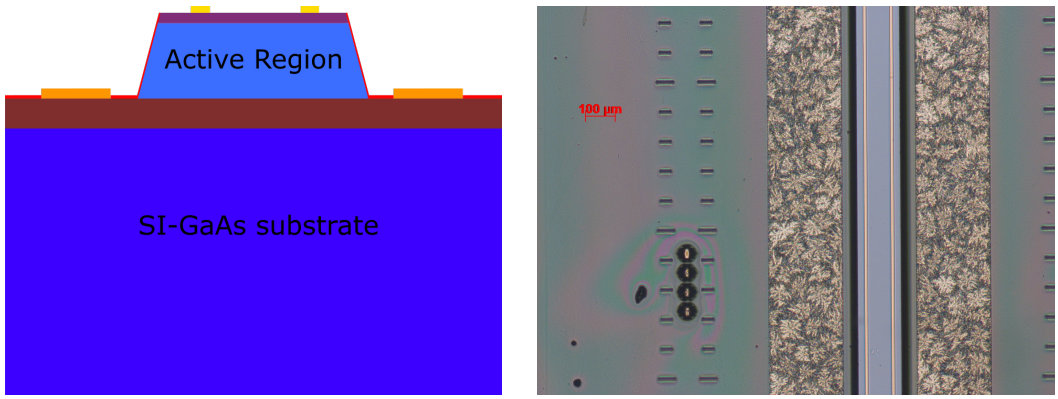

(a) (b)

Figure 2.16: Over-layer Photolithography. (a) schematic; (b) optical image using from an optical microscope a 5× magnification. The scale bar on the top left of the image is 100μm.

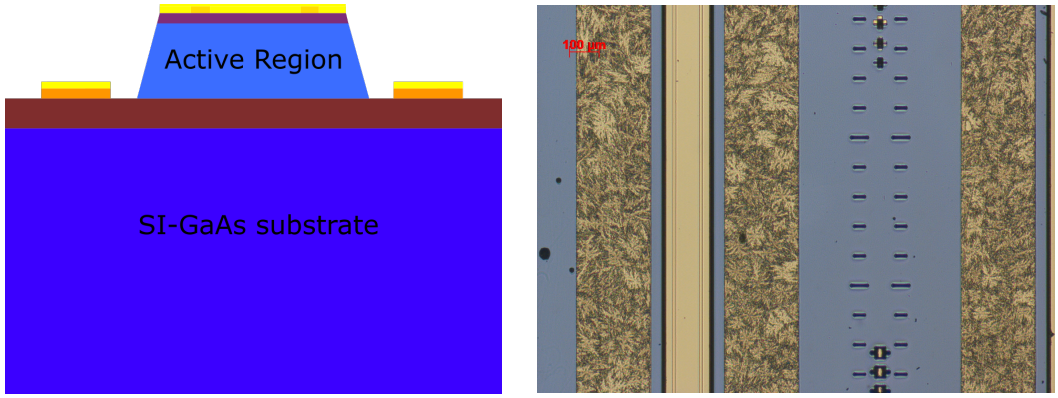

(a) (b)

Figure 2.17: Over-layer Evaporation. (a) schematic; (b) optical image using from an optical microscope a 5× magnification. The scale bar on the top left of the image is 100μm.

2.5.6 Substrate thinning and metal sintering

The MBE layers of wafer, L1180, were grown on a ∼700μm-thick SI-GaAs substrate. Since THz QCLs work at cryogenic temperatures, in order to reduce thermal resistance the substrate needed to be thinned to ∼150 - 200 μm. Substrate thinning was therefore carried out using the same etching solution used for the ridge definition but with different concentrations. This time H_2SO_4:H_2O_2:H_2 with concentrations respectively 1:8:1 ensured an etching rate ≈15μm /min faster than the rate used for the QCL ridge etching. S1813 was firstly spun on the top face of the sample and baked at 90°C for 1 min. The sample was then stuck on a sample glass with the laser ridge facing down using wax. Two small pieces of wax were melted on to one side of the glass placing it on a hot plate at 75°C. The sample was gently placed on the wax, taking care to cover the ridge face and part of the side wall of the sample. This was done with purpose of protecting the ridge from the etching solution which could be translated in a permanent damage of the sample. At this stage, the glass was placed on a cold metal finger to make solidify the wax. The glass with the sample on it was immersed in the acid solution and kept agitating to ensure etching uniformity; the thickness was monitored using a Testronic micrometer roughly every ten minutes until the thickness reached the desired level. Once finished, the glass was placed

again on a hot plate at 75°C in order to melt the wax and remove the sample. Excess wax on the sample was then dissolved in 3 bathing rounds of trichloroethylene (TCE), being very careful not to break the ridge considering that the sample now was particularly thin, and finally by cleaning the photoresist in a beaker of acetone. A final step of metallisation was performed by evaporating in an Edwards Turbo thermal Evaporator a layer of Ti/Au to a thickness respectively of 20nm/200nm. This was done in order to improve thermal dissipation when the sample was mounted on a copper block through a layer of melted Indium (as explained in the next section). Finally the metal over-layer of the sample was sintered in an RTA at 270°C for 4 minutes. This part of the process was carried out in order to make the over-layer and the alloy AuGeNi of the bottom and top contacts to adhere each other by agglomerating all the metal particles. At this stage some bubbles due to gasification of a component of the alloy appeared on the top metal contacts, and these are also visible in the optical image, as shown in figure 2.18(b).

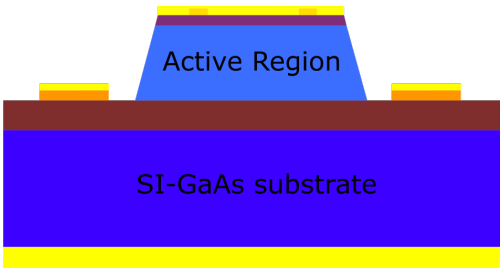

(a)

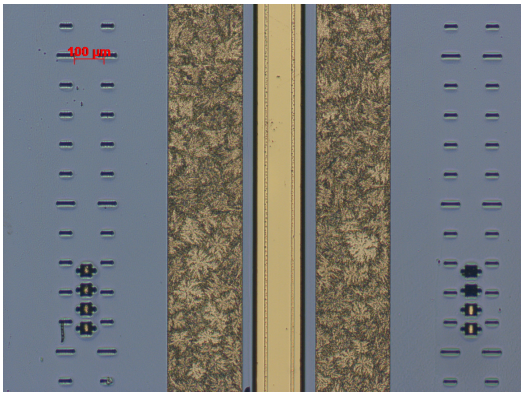

(b)

Figure 2.18: (a) Schematic of substrate thinning and metallisation; (b) real image taken from an optical microscope a 5× magnification after sintering the metal at 270°C for 4 minutes. The black dots on the top contacts are due to gasification of a component of the alloy. The scale bar on the top left of the image is 100μm.

2.5.7 Ridge cleaving and bonding

The samples so processed typically incorporated 3 ridges, each 6mm long and 150μm wide and spaced roughly 1mm each other. In order to separate each ridge a JFP S-100 scriber

was used. Two scribing marks in the middle space ,along the ridge length were made and then each ridge was manually separated. The desired length of every ridge was then scribed away from the ridge in order not to damage it and manually separated with the same previous procedure. Scribing mark made well away from the ridge ensured a QCL mirror-like facet, as shown in figure 2.19, which was important to ensure good performance with low losses.

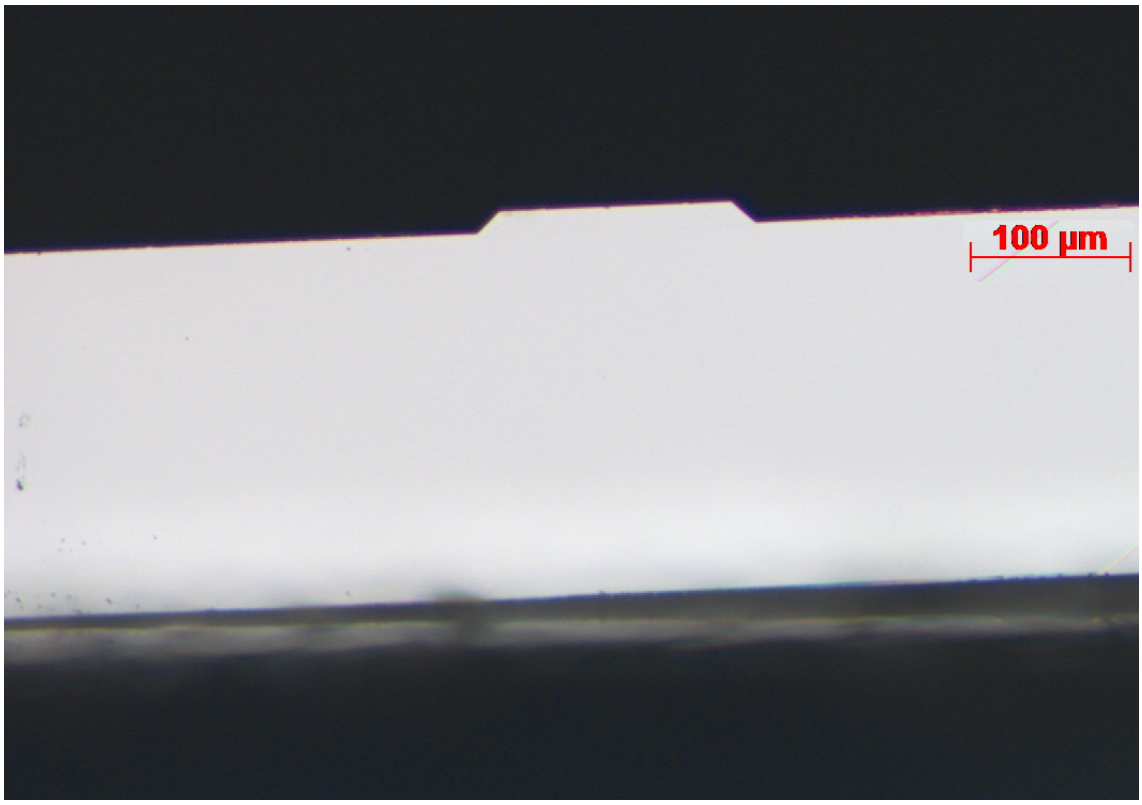

Figure 2.19: A 10× magnification image of a QCL facet taken with an optical microscope.

A polished copper block 20mm×7mm×2mm, covered by Ti/Au was used as mounting base for the QCL. Two Au coated ceramic pads were glued using GE vanish at the ends of the block and were used as contact pads. The GE vanish was cured at 100°C for 10 minutes to ensure a good solidification. In order to solder the QCL a small piece of Indium was placed on the Cu block. On a hot plate the copper block was heated up to 150°C, which is above the In melting point. The melted indium was then spread into a uniform layer using a flat head screwdriver. After the QCL was gently placed on the In molten layer,

two metal needles were then used to slightly press the QCL in order to make it adhere well. At this stage, the hot plate temperature was reduced to make the In solid while the QCL was being pressed by the needles. The QCL soldered to the copper block was then moved to a Kulicke & Soffa 4524 ball bonder machine in order to create electrical contacts. Au bond wires were used to bond the top contact to one of the contact pads and the bottom contact was directly bonded to the copper block which was used a ground.

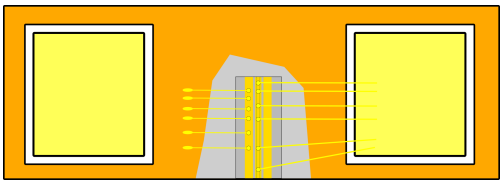

(a)

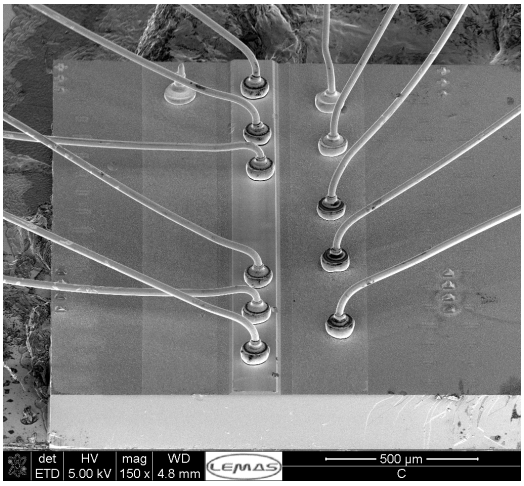

(b)

Figure 2.20: (a) Schematic of the QCL mounted and bonded; (b) a SEM image of the device, special thanks to Dr. I. Kundu for the SEM image.

2.6 THz QCL Characterization

Characterization of the QCL, in both pulsed and CW mode, was carried out by mounting the device onto the cold finger of a continuous flow liquid helium Janis ST-100 cryostat. Electrical connections were made by two copper pins inside the cryostat. Thermal insulation was established by creating vacuum at a pressure P<4×10^{-6}mBarr and the cryostat was then cooled down to ~4K.

2.6.1 Pulsed mode

Figure 2.21 shows the experimental set-up used to acquire Light-Current-Voltage (LIV) characteristic of the THz QCL in pulsed mode. An Agilent 8114A pulse generator (APG)

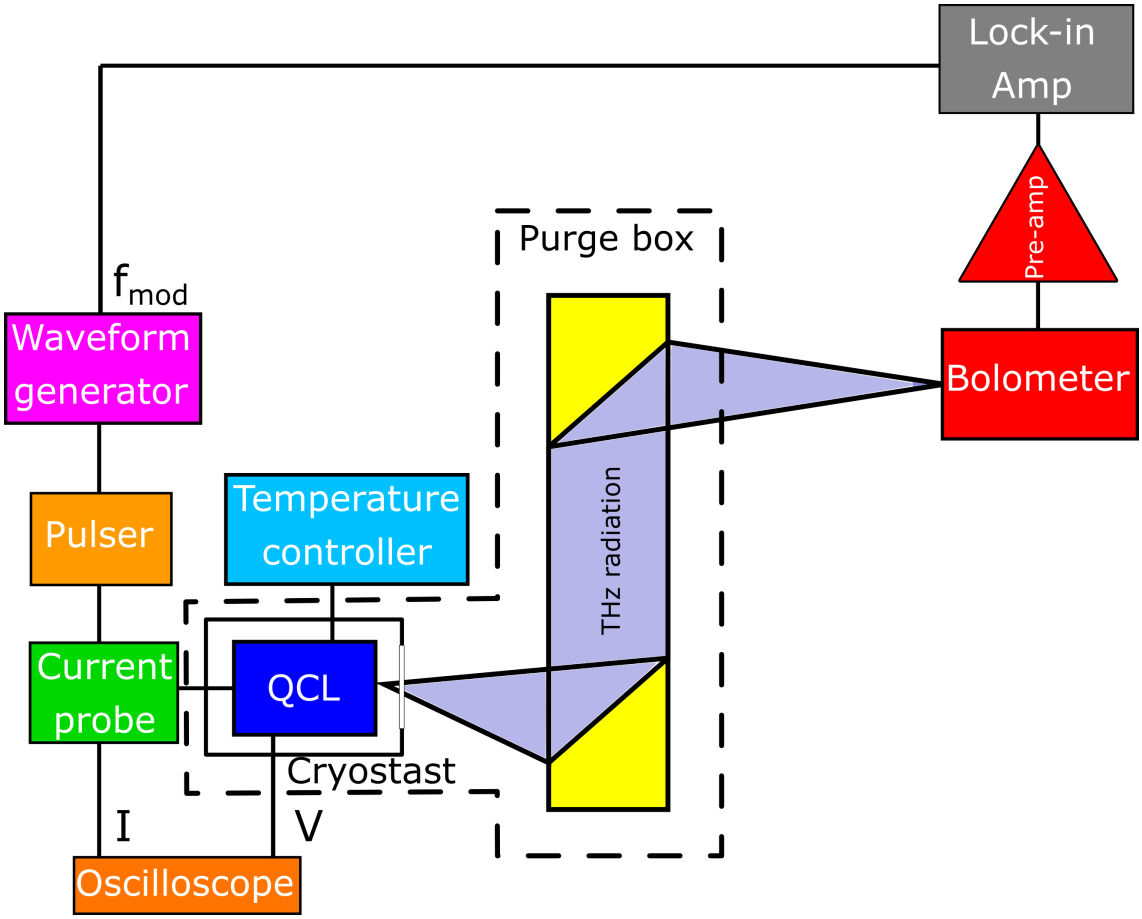

Figure 2.21: Schematic of the experimental set-up used for pulsed LIV characterisation of the QCL.

was used to power the QCL with 10 KHz pulses at 2% of duty cycle which were electrically gated at ∼167 Hz by an Agilent arbitrary waveform generator (AWG). Voltage and Current were measured through a digital Oscilloscope Keysight 2002A connected to the PC; a temperature controller was used to monitor and keep constant the heat sink temperature of the QCL. The cryostat was mounted on a XYZ micro-translation stage, and two f/3 parabolic mirrors were used to collimate and focus the THz beam onto the cooled bolometer. The cryostat and the two parabolic mirrors were placed in a N_2-purged box in order to reduce the air absorption effect of the THz beam. The signal from the bolometer was referenced at 167 Hz to the waveform generator, matching the best response time of the bolometer, trough a pre-amplifier and acquired with a lock-in amplifier. A LabView

program on a PC managed and acquired the data. The optical power (in mW) was acquired using a Thomas Keating (TK) power meter, by reducing the reference frequency at its best response time, ∼30Hz.

A Bruker Optics IFS66/V FTIR spectrometer based on a Michelson Interferometer was used for the spectral characterisation of the QCL. The cryostast was moved to a different setup and the THz radiation was focused onto the aperture of the spectrometer through two f/3 parabolic mirrors, as shown in figure 2.22.

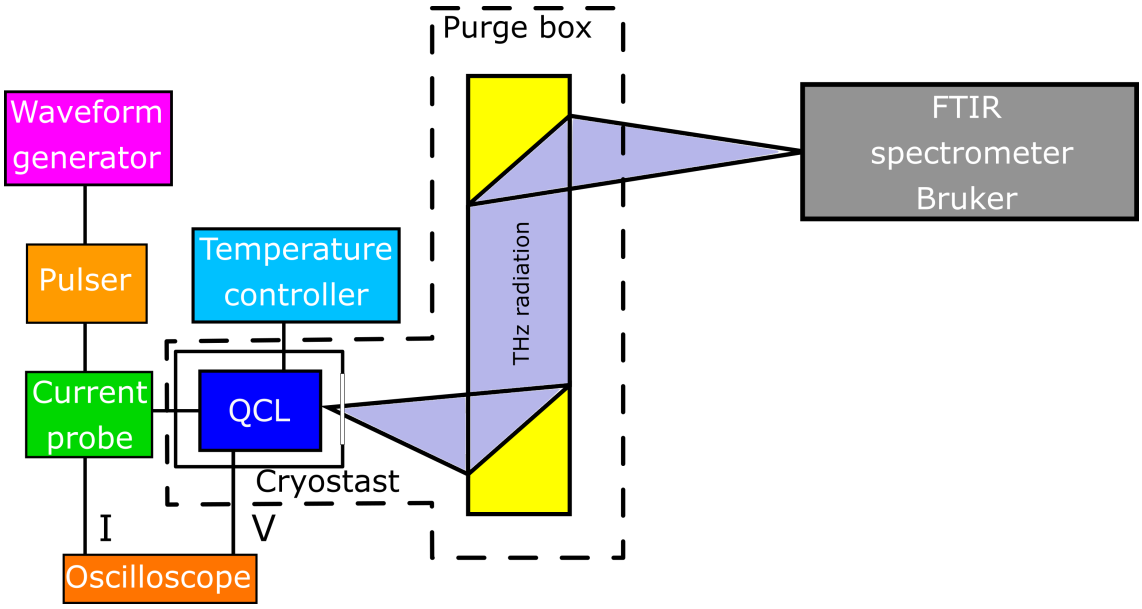

Figure 2.22: Schematic of the experimental set-up used for the spectral characterisation of the QCL.

2.6.2 CW mode

In order to measure the CW characteristics of the QCL the experimental set-up was slightly modified and waveform generator and pulser replaced with a standard Tektronix DC power supply (PSU) to power the QCL. Optical modulation at ∼167 Hz of the THz beam was made by using a mechanical chopper referenced to the lock-in amplifier, figure 2.23. Power measurements with the same TK power meter were carried out at a modulation frequency ∼30Hz. Spectra were acquired with the same set-up shown in figure 2.22, and the QCL was powered by a standard PSU.

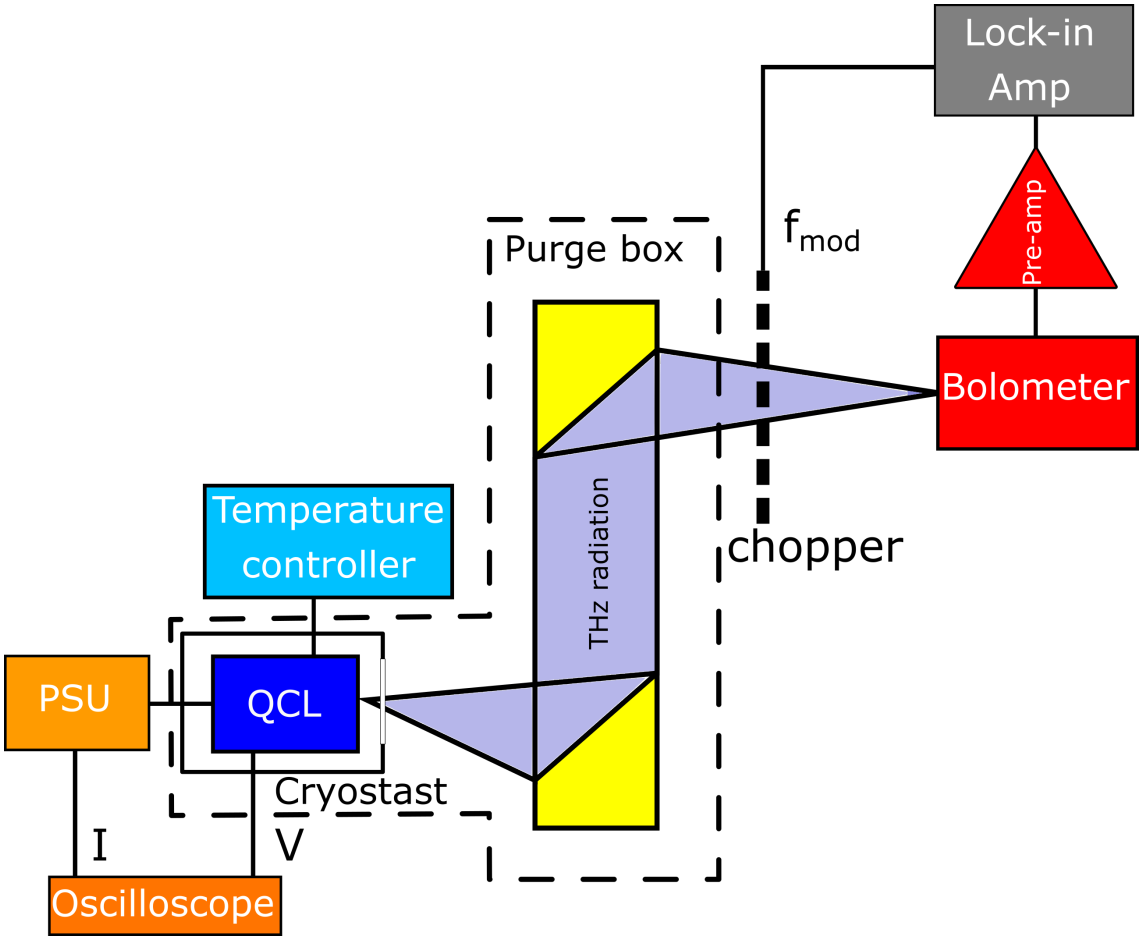

Figure 2.23: Schematic of the experimental set-up used for Cw mode characterisation of the QCL.

2.7 Results

Different QCLs were fabricated and characterised, but one of them has been used predominantly throughout this thesis, and hence only its results will be shown in this section. As mentioned in the fabrication section, the wafer L1180 was grown by Dr Liahne Li in the University of Leeds MBE system. The wafer, based on a hybrid design, was slightly modified with respect to the original structure proposed by Wienold [171] in order to lase in the range $\sim 3.3 - 3.6THz$ and processed into a SI-SP waveguide. A ~1.8mm long and 150μm wide ridge was cleaved and mounted on a copper block. The device was then mounted in the cryostat by applying thermal grease between the block and cold finger to ensure good thermal contact. The LIV and spectral characteristic of the device are

presented in the following section, in both pulsed and CW mode.

2.7.1 Pulsed mode

The light emission (LIV) of L1180 THz QCL was recorded at different heat-sink temperatures every 10K step up to 100K and then every 5K until lasing stopped.

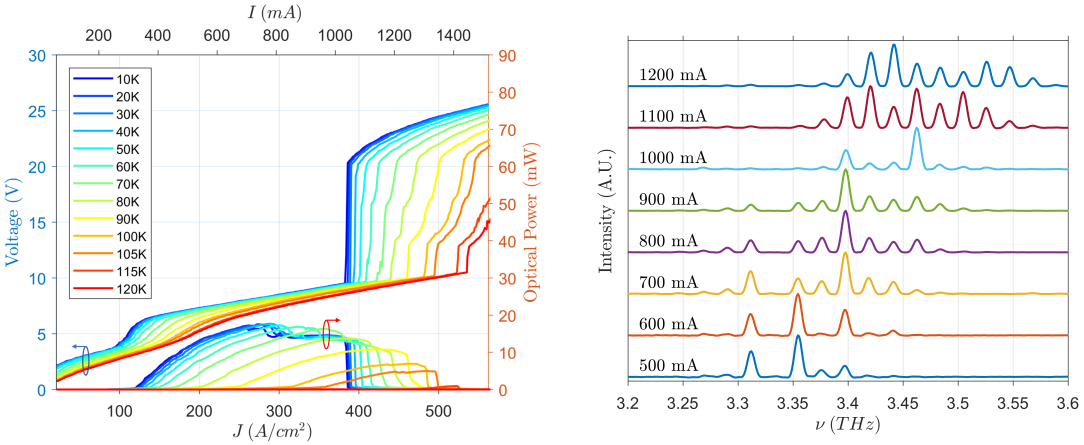

(a) (b)

Figure 2.24: (a) Pulsed LIV characteristics and (b) spectrum at 10K of L1180.

Figure 2.24(a) shows the LIV plot as function of current density, J (and current, I, on the top) of the device acquired in pulsed mode. A peak power of ∼20mW at 10K, a maximum operating temperature of 120K and a low current density threshold at 10K, ∼120A/cm^2, are in good agreement with the predicted structure performance [9, 171]. The shape of the V-I graph similar in every QCL and can be explained as follow: before the threshold current the lasing levels between the QWs are misaligned and no optical output power is visible because no tunneling occurs. When the states start to align the population inversion is just enough for the device to lase. Optical power increases as more electrons are tunneling to the upper lasing level. The optical peak power is achieved when the alignment is optimal. Any further increase in electric field misaligns the bands, resulting in the resistance increasing and a dramatic decrease in lasing power occurs, until it completely dies out. The spectral measurements, shown in figure 2.24(b), were performed at 10K and show multi-mode frequency lasing with main peaks ranging from ∼3.35THz to ∼3.45THz

depending on the driving current. Between 600mA and 700mA and between 900mA and 1000mA the main frequency changes occur because of the alignment of different states and are referred to as mode-hopping. The multi-mode nature at each driving current of the device is dictated by the Fabry-Perot mode spacing, which follows equation 2.4.

$$\Delta\nu = \frac{c}{2nL}, \tag{2.4}$$

where $\Delta\nu$ is the frequency difference between the modes, c is the speed of light, n is the refractive index of the gain medium and L is the cavity length of the ridge. In this case L≈1.8mm and n∼3.5 for GaAs yielding $\Delta\nu$ ∼23GHz, which is in good agreement with the experimental mode spacing of $\Delta\nu$ ∼21GHz. The differences can be attributable with small differences of n or L given by the finite accuracy of the cavity dimensions.

2.7.2 CW mode

The LIV characteristic of L1180 in CW mode was measured between 30K and 60K heat-sink temperature with step of 5K.

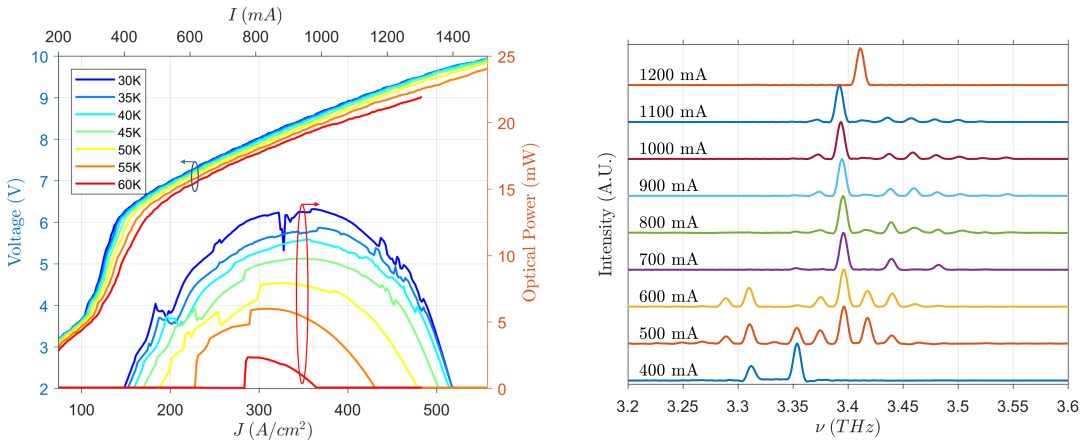

(a) (b)

Figure 2.25: (a) CW LIV characteristics and (b) spectrum at 30K of L1180.

Figure 2.25(a) and 2.25(b) show respectively the CW LIV curve and the CW spectra , measured at 30K, of L1180. A peak power of ∼13mW at 30K, a maximum heat-sink temperature of 60K and a threshold current density of ∼150A/cm^2 at 30K are in good

agreement with the expected performance of the QCL [9, 171]. The spectrum shows main frequency peaks ranging from ∼3.35THz to ∼3.41THz by increasing driving current, plus some Fabry-Perot modes spaced at $\Delta\nu$ ∼21GHz. These results are in good agreement with the pulsed measurements and the wafer structure.

2.7.3 Single mode emission

As previously mentioned in this chapter, single mode emission is important for application like self-mixing imaging, or for near-field imaging based on self-mixing in a THz QCL. In the chapters 4, 5 and chapter 6 these two applications will be demonstrated through the use of the QCL shown in this chapter. Single mode emission has been achieved thanks to the support of Dr. I. Kundu who is also the author of the study *"Frequency Tunability and Spectral Control in Terahertz Quantum Cascade Lasers with Phase-Adjusted Finite-Defect-Site Photonic Lattices"* [9]. A PL 166μm long, using a 13.2 μm grating period with a 70 % duty cycle and a central 8μm wide phase defect was created using FIB milling by Dr. I. Kundu, on L1180 through the top contact layers as in [9], as shown in figure 2.26(b). In figure 2.26(a), the CW spectrum at 30K of L1180 is shown. Each peak has been

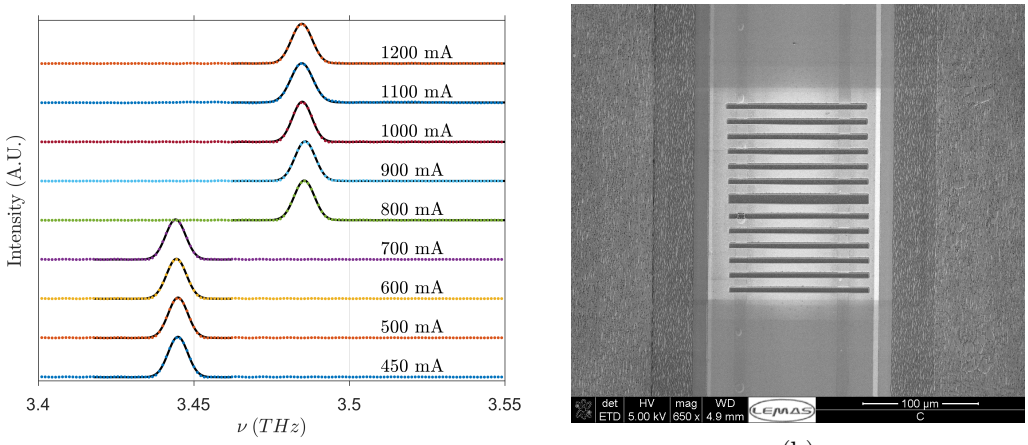

(a) (b)

Figure 2.26: (a) CW spectrum at 30K after FIB milling, every peak has been fit with a Gaussian fit. (b) SEM picture of the PL on L1180.

fit with a Gaussian curve in order to extract the peak frequency. Single mode emission of ν ∼3.445THz was observed at I_{QCL}=450mA. At I_{QCL}=800mA the lasing frequency

has shifted to ν ~3.485THz, giving a discrete shift of ~40GHz in good agreement with [9]. Furthermore the single mode of the two discrete frequencies, has shown a continuous frequency tuning of ~-1GHz, as shown in figure 2.27.

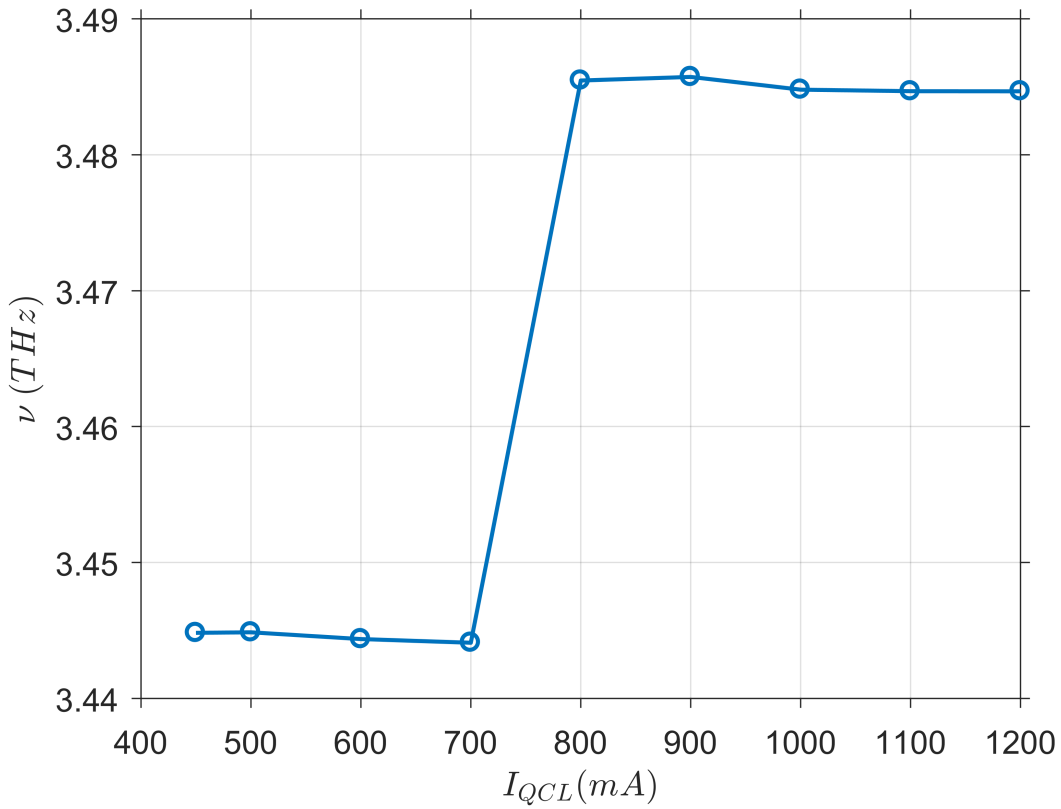

Figure 2.27: QCL frequency as function of I_{QCL} after FIB milling a PL through the top-contact layers of L1180.

2.8 Conclusions

In this chapter the general functioning of a THz QCL was explained. The processing of a wafer into THz QCL based on the structure adapted from the proposed one by [171] and fabricated in a SISP waveguide has been shown. Characterisation of the THz QCL through its LIV curve and spectrum are in agreement with the literature in terms of optical power (~20mW at 10K in pulsed and ~13mW at 30K in CW) and lasing frequency (~3.3-3.5THz). Furthermore single mode emission of ~3.445THz in CW mode thanks to a

photonic lattice with a π-phase adjusted incorporated in it was achieved as in [9], making this QCL the perfect candidate for self-mixing imaging or near-field imaging based on self-mixing. In the next chapters the single mode emission and the continuous frequency tuning of the aforementioned QCL will be exploited to take images and demonstrate the possibility to retrieve information about permittivity of materials.

3 Self-mixing in THz QCLs

The foundations of a theoretical model for the self-mixing (SM) effect in lasers were set by Lang and Kobayashi [92] who have described a laser diode under optical feedback by employing coupled rate equations for the electric field and current density. While a laser cavity can be considered as a Fabry-Perot (FP) resonator where the laser facets act as two internal reflecting mirrors, a laser under external feedback can be described by a three mirror model [175]. In this chapter two and three mirror models, based on those derived by Tucker [176] and generalized by Keeley [14], will be described and also some preliminary SM results will be shown. Furthermore a set of experiments to quantify the detection sensitivity of the SM will be shown. A noise equivalent power (NEP) of $\sim$1.4pW/$\sqrt{Hz}$ will be demonstrated. The subsequent chapters will be dedicated to the experimental demonstration of far-field and near-field imaging using the SM effect in a THz QCL, allowing fundamental information of materials, such as the complex permittivity, to be mapped spatially.

3.1 Two-mirror model for a laser without external optical feedback

A Fabry-Perot cavity laser of length L can be seen as consisting of two mirrors, M_1 and M_2, with amplitude reflection coefficients, r_1 and r_2, respectively, and a gain medium with refractive index n_e. The assumption is that a uniform plane wave is injected from M_1 and travels to M_2 in the positive direction z, as shown in figure 3.1.
The electric field as a function of space and time is defined as,

$$E(z,t) = E_0 \cos(\omega t - \beta z), \tag{3.1}$$

where z is the longitudinal distance along the cavity, t the time, E_0 is the amplitude of the electric field, $\omega = 2\pi\nu_0$ is the angular frequency of the travelling wave and $\beta = 2\pi n_e/\lambda$ is the wavenumber in the cavity. This field can alternatively be expressed as a complex

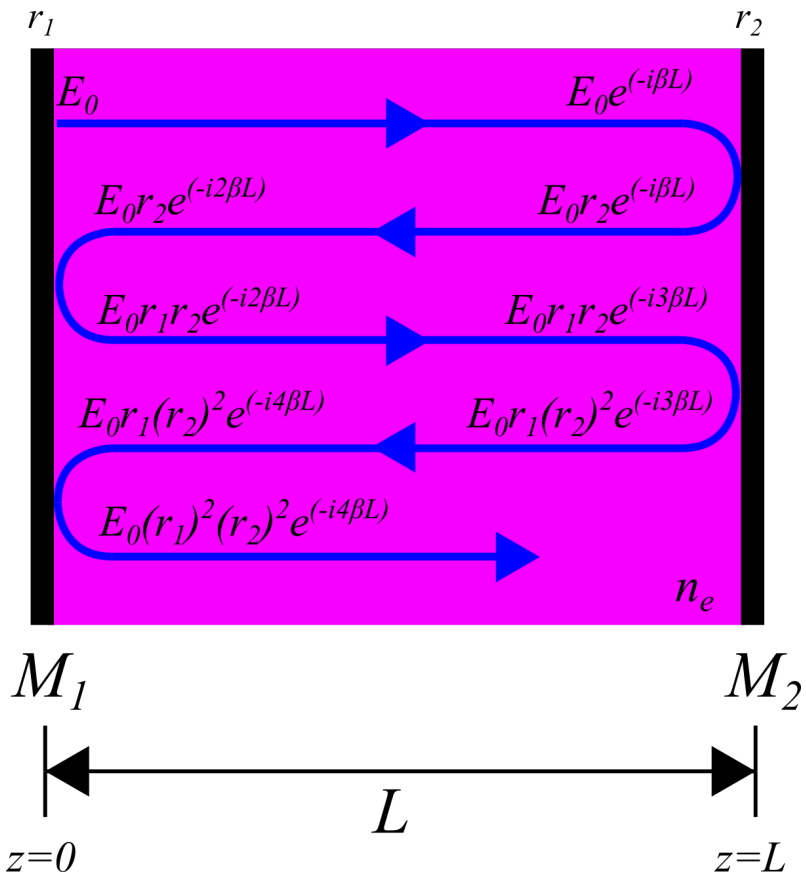

Figure 3.1: Schematic of a Fabry-Perot cavity.

electric field with real and imaginary components following the relation,

$$E(z,t) = Re[E_0 e^{i(\omega t - \beta z)}] = Re[\tilde{E} e^{i\omega t}], \tag{3.2}$$

where,

$$\tilde{E} = E_0 e^{-i\beta z}, \tag{3.3}$$

is the time-independent component of the electric field which contains the amplitude and the phase information of the wave. This notation is often used in order to simplify the arithmetic and to avoid the use of sinusoidal functions.

Referring to figure 3.1, an electromagnetic wave propagating from M_1 to M_2 inside the medium experiences a phase shift, βL, following which part of it is internally reflected by

the facet mirror M_2. The rest of the wave is emitted through the facet. The internally reflected component is subjected to an amplitude change affected by the reflection coefficient, r_2. In turn, this reflected wave returns to M_1 where it undergoes another phase and amplitude change of βL and r_1 respectively; after one round-trip the electric field has the form, $E_0 r_1 r_2 e^{-i2\beta L}$. In this way the wave will experience both a phase and amplitude change at every internal reflection. At the same time a second wave will travel from the initial point on the same path as the first wave. As a consequence, interference between the two can occur and if they have the same phase the waves will interfere constructively. Mathematically, the laser will have an optical output when the round-trip phase shift,

$$2\beta L = m2\pi, \tag{3.4}$$

where m is an integer. Re-writing the phase constants, this will occur when,

$$\frac{m\lambda}{2} = n_e L. \tag{3.5}$$

Given a fixed cavity length, equation 3.5 is only satisfied for discrete wavelengths λ at which the cavity will resonate. In a practical laser device each wave will also experience gain and absorption as it propagates through the cavity. This can be described using the power gain per unit length, g, and the power loss per unit length, α_s, which are both functions of the wavelength. The cavity will resonate for specific wavelengths (or frequencies ν) if the power gain is greater than the power loss. The laser power is proportional to the electric field squared, hence equation 3.3 can be re-written as,

$$\tilde{E} = E_0 e^{\left(-i\beta + \frac{1}{2}(g(h\nu) - \alpha_s(h\nu))\right)z}. \tag{3.6}$$

After one round-trip the electric field will become,

$$E_0 r_1 r_2 e^{\left(-i\beta + \frac{1}{2}(g(h\nu) - \alpha_s(h\nu))\right)2L}. \tag{3.7}$$

Assuming a resonant wavelength, we arrive at the amplitude condition for lasing,

$$r_1 r_2 e^{(g(h\nu)-\alpha_s(h\nu))L} = 1, \tag{3.8}$$

which can be rearranged to give the threshold gain condition,

$$g_{th} = \alpha_s + \frac{1}{L}\ln(\frac{1}{r_1 r_2}). \tag{3.9}$$

This condition can be satisfied by multiple resonant cavity modes simultaneously, but as already shown in the previous chapter (see Section 2.7.3) a cavity can be perfectly engineered to achieve a single mode emission, which is particularly desirable for laser self-mixing scheme. As such, all subsequent theory will consider a laser emitting on a single cavity mode.

3.2 Three mirror model for a laser with external optical feedback

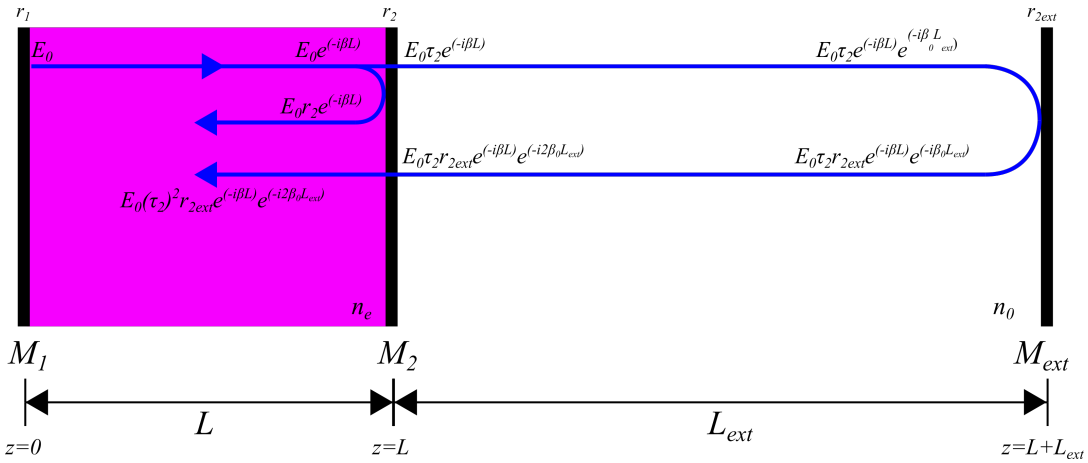

Figure 3.2: Three mirror model schematic of a Fabry-Perot cavity under external optical feedback.

The self-mixing effect occurs when part of the laser radiation is reflected from an external object and re-injected back into the laser cavity. The two-mirror model shown in the previous section can be extended by introducing a third-mirror, M_{ext}, as an external reflector with reflection coefficient r_{2ext} at distance L_{ext} from the laser facet (see figure 3.2).

The external medium has refractive index n_0, hence the light wavenumber can be defined as $\beta_0 = 2\pi n_0/\lambda$. In this case, the internal round-trip of the radiation is different from the external one, but the analysis of the internal electric field is sufficient to understand the device behaviour [14, 96, 175, 177] (see figure 3.2). A complex effective reflection coefficient, r_{eff}, can be used in order to simplify the model to a two-mirror model (see figure 3.3). r_{eff} combines the reflection coefficients of the external mirror, r_{2ext} and the laser facet, r_2 according to the relation,

$$r_{eff}(\nu) = r_2 + (1 - |r_2|^2) r_{2ext} e^{-i2\pi\nu\tau_{ext}}, \tag{3.10}$$

where ν is the lasing frequency with external feedback, $\tau_{ext} = 2L_{ext}n_0/c$ is the external cavity round-trip propagation time with constant refractive index, n_0 and c is the speed of light in vacuum. The first term of the equation 3.10 represents the reflection from M_2 and the second term describes the part of the light that is re-injected and transmitted through M_2 after being reflected from M_{ext}. It's worth mentioning that equation 3.10 is valid only for a single round-trip of the external cavity, which implies a laser under weak feedback, i.e. $r_2 \gg r_{2ext}$. Stronger feedback is taken into account by adding more terms, containing a summation of the multiple reflected electric fields, to the second term of equation 3.10 [178–180]. However the self-mixing experiments are usually conducted in a regime of weak feedback, and so this theoretical analysis will assume a laser under weak feedback.
Equation 3.10 can be re-written as,

$$r_{eff}(\nu) = |r_{eff}(\nu)| e^{-i\phi_r}, \tag{3.11}$$

where $|r_{eff}(\nu)|$ and ϕ_r are respectively the amplitude and phase of the effective reflection coefficient. Under weak feedback it is possible to assume $Re[r_{eff}(\nu)] \gg Im[r_{eff}(\nu)]$ [95] since $r_2 \gg r_{2ext}$, and so amplitude and phase are given by,

$$|r_{eff}(\nu)| \approx Re[r_{eff}(\nu)] \approx r_2[1 + k_{ext}\cos(2\pi\nu\tau_{ext})], \tag{3.12}$$

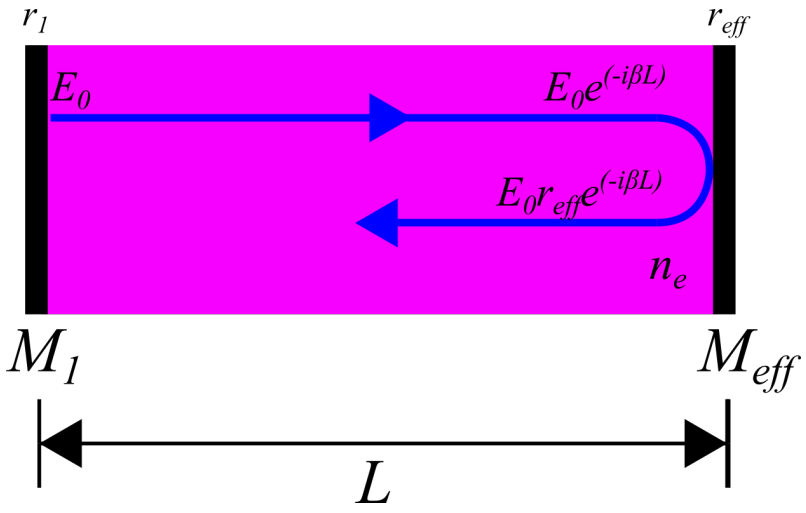

Figure 3.3: Effective two mirror model schematic of laser under external optical feedback.

$$\phi_r \approx \frac{Im[r_{eff}(\nu)]}{r_2} \approx k_{ext} \sin(2\pi\nu\tau_{ext}), \tag{3.13}$$

where,

$$k_{ext} = \frac{r_{2ext}}{r_2}\left(1 - |r_2|^2\right). \tag{3.14}$$

k_{ext} is known as the feedback coupling coefficient and represents the portion of light coupled back into the laser cavity. This parameter is represented experimentally as,

$$k_{ext} = \epsilon\sqrt{\frac{R_{2ext}}{R_2}}(1 - R_2) \tag{3.15}$$

where ϵ is the coupling-efficiency factor which takes account of external losses, misalignment and mismatch between the reflected radiation and the cavity mode; R_2 and R_{2ext} are the power reflection coefficients of M_2 and M_{ext} respectively.

The optical feedback into the laser cavity affects the laser properties including the output frequency, linewidth, and threshold gain resulting in a change to the output power. By taking into account the effective reflection coefficient and assuming a single lasing frequency with gain and loss independent of the frequency, equation 3.8 can be re-written to

give the round-trip amplitude condition for a laser under feedback,

$$r_1|r_{eff}|e^{(g(h\nu)-\alpha_s(h\nu))L} = 1. \tag{3.16}$$

Also by analogy with equation 3.4, the round-trip phase condition becomes,

$$\frac{4\pi n_e \nu L}{c} + \phi_r = m2\pi, \tag{3.17}$$

where n_e is the effective refractive index. Following this perspective also the threshold gain (see equation 3.9) can be re-written accounting for the effective reflection coefficient given by equation 3.12,

$$g_{th} = \alpha_s + \frac{1}{L}\ln(\frac{1}{r_1 r_2[1 + k_{ext}\cos(2\pi\nu\tau_{ext})]}). \tag{3.18}$$

As a consequence the difference in threshold gain because of the feedback can be calculated as,

$$\Delta g = g_c - g_{th} = \frac{1}{L}\ln\left(\frac{1}{1 + k_{ext}\cos(2\pi\nu\tau_{ext})}\right) = \frac{-\ln(1 + k_{ext}\cos(2\pi\nu\tau_{ext}))}{L}. \tag{3.19}$$

Considering that in the weak feedback regime $k_{ext} \ll 1$, the log can be expanded as a Taylor series, giving

$$\Delta g = -\frac{k_{ext}}{L}\cos(2\pi\nu\tau_{ext}). \tag{3.20}$$

Equation 3.20 explains that the threshold gain is periodic with L_{ext}. Also, the gain difference will have its minimum ($\Delta g = 0$) for specific external phase, $\phi_{ext} = (1+2m)\pi/2$, where m is an integer.

From an experimental point of view, the self-mixing signal is typically measured as a change in the laser power or laser voltage V, which are both assumed to be proportional

to the change in gain. This leads to the formulation of the self-mixing voltage as follow,

$$\Delta V_{SM} \propto \epsilon\sqrt{R_{2ext}}\cos\left(\frac{4\pi L_{ext}\nu}{c}+\theta\right). \tag{3.21}$$

The term in the cosine is the external phase, ϕ_L, and θ in equation 3.21 is the phase change that can arise due to a change in sample depth or due to a phase change on reflection. Equation 3.21 describing the voltage perturbation caused by optical feedback in a THz QCL is a crucial relationship which will be used throughout this thesis. The dependence of $\Delta \mathrm{V}_{SM}$ on the external target reflectance and round-trip phase will be exploited to acquire images of different samples in the far-field and near-field, and also to retrieve fundamental information of material properties including complex permittivity.

3.3 Excess phase equation

The evaluation of the relationship between self-mixing voltage and phase, equation 3.21, needs the lasing frequency under optical feedback to be calculated, because the round-trip phase condition, equation 3.17, indicates a change in frequency (and also cavity refractive index, n_e) in the presence of feedback. The theory has been adapted from laser diodes under feedback and applied also to QCLs [102, 181, 182].

A rigorous explanation starts by taking into account variation in $n_e\nu$ under feedback,

$$\Delta(n_e\nu) = \nu_0\Delta n_e + n_e\Delta\nu. \tag{3.22}$$

The variation in the effective refractive index Δn_e can in turn be expressed as a function of the changes in carrier concentration and also lasing frequency $\Delta\nu$,

$$\Delta n_e = \frac{\delta n_e}{\delta N}\Delta N + \frac{\delta n_e}{\delta \nu}\Delta\nu. \tag{3.23}$$

Here n_e is a function of the carrier concentration and its variation with N is related to the variation in gain by the linewidth enhancement factor, α, by [177],

$$\frac{\delta n_e}{\delta N}\Delta N = -\frac{\alpha c}{4\pi\nu_0}\Delta g. \tag{3.24}$$

Equation 3.23 can be combined with equations 3.17, 3.22 and 3.24 to give the excess phase (the change in round-trip phase $\Delta\phi_L$) equation due to optical feedback,

$$\Delta\phi_L = \frac{4\pi L}{c}\left(-\frac{\alpha c}{4\pi}\Delta g + \nu_0\frac{\delta n_e}{\delta\nu}\Delta\nu + n_e\Delta\nu\right) + \phi_r. \tag{3.25}$$

The last two terms in the brackets contain a common $\Delta\nu$ that can be reduced by introducing the effective group refractive index, n_g, which considers the change of the cavity refractive index, n_e as a function of the change in frequency, $\delta\nu$, due to feedback[177],

$$n_g = n_e + \nu\frac{\delta n_e}{\delta\nu}. \tag{3.26}$$

Substituting and reordering, equation 3.25 can be written as,

$$\Delta\phi_L = \frac{4\pi n_g L}{c}\Delta\nu - \alpha\Delta g L + \phi_r. \tag{3.27}$$

This last equation can be further simplified by exploiting equation 3.20 for the gain variation and equation 3.13 for the phase shift to give,

$$\Delta\phi_L = \frac{4\pi n_g L}{c}\Delta\nu + k_{ext}[\sin(2\pi\nu\tau_{ext}) + \alpha\cos(2\pi\nu\tau_{ext})]. \tag{3.28}$$

Furthermore the round-trip delay of the laser cavity can be given by [177]

$$\tau_L = 2n_g\frac{L}{c}. \tag{3.29}$$

By substituting this into equation 3.28 and rearranging the second term, the excess phase can be written as,

$$\Delta\phi_L = 2\pi\tau_{ext}(\nu - \nu_0) + C\sin(2\pi\nu\tau_{ext} + \arctan\alpha). \tag{3.30}$$

At the resonant frequency of the compound cavity $\Delta\phi_L = 0$, and this equation can be solved to extract the parameters related to the self-mixing effect. Here C is called the *feedback parameter* and is equal to,

$$C = \frac{\tau_{ext}}{\tau_L} k_{ext}\sqrt{1+\alpha^2}. \tag{3.31}$$

C is a quantity which explains how optical feedback affects the behaviour of the laser, and depending on the value of C, different operating regimes can be quantified [10, 183]:

- $C \ll 1$, is the *very weak feedback regime*. The self-mixing voltage V_{SM} has sinusoidal behaviour as function of the external phase, ϕ_L.
- $0.1 < C < 1$, is the *weak feedback regime*. V_{SM} starts to distort and loses the sinusoidal behaviour.
- $1 < C < 4.6$, is the *moderate feedback regime*. V_{SM} is three-valued for certain values of ϕ_L, showing a sawtooth like shape with possible hysteresis due to jumps in phase.
- $C > 4.6$, is the *strong feedback regime*. V_{SM} is very unstable and can be even five-valued. The laser can enter a chaotic regime.

Stronger feedback causes a large change in the device refractive index, which affects the external phase, ϕ_L, causing in turn the distortion in the function periodicity shown in figure 3.4(b). On the other hand it has been demonstrated that THz QCLs are intrinsically stable under optical feedback [181], hence a stable self-mixing regime is expected for all the experimental work presented in this thesis. Moreover the assumptions of functioning in a weak feedback regime automatically excludes moderate and strong feedback regime

for the self-mixing applied to THz QCL used in this work, but for clarity these two levels of C are still shown. The combination of equations 3.21 and 3.30 (when $\Delta\phi_L = 0$) fully

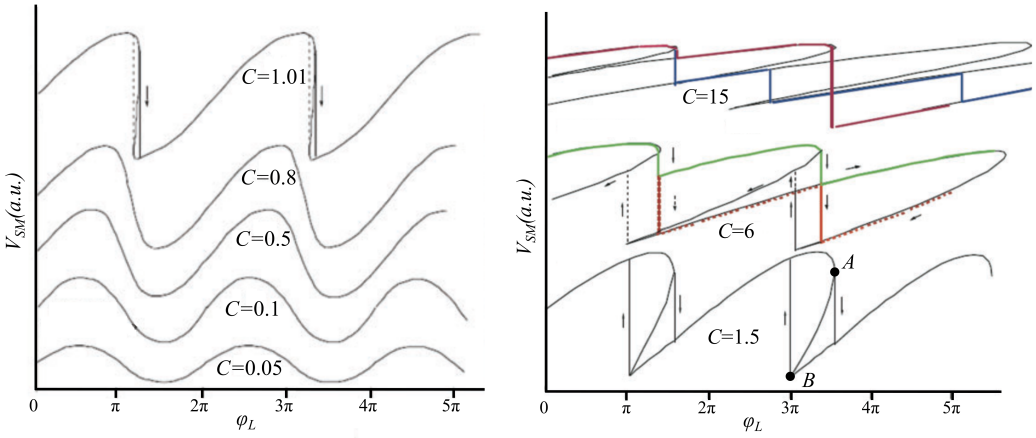

Figure 3.4: (a) V_{SM} waveforms calculated for different C ranging from 0.05 to 1.01 and (b) for C ranging from 1.5 to 15. The instability of V_{SM} is already noticeable for $C = 1.5$ shown in the region between points A and B. V_{SM} jumps down due to an increase of ϕ_L from point A. When V_{SM} is at point B, a decrease of ϕ_L causes V_{SM} to jump up. Adapted from S.Donati [10].

describe the change in the QCL voltage under feedback and its dependence on different experimental parameters including the QCL lasing frequency, external cavity length, feedback parameter and complex reflectivity of the external target. These equations will be exploited throughout this thesis to extract information, such as the complex permittivity, from samples under analysis.

3.4 Simulation of self-mixing voltage signal

Examples of V_{SM} waveforms can be simulated through the use of equations 3.30 and 3.21 for different feedback parameters and linewidth enhancement factors. The interferometric fringes are obtained by extending the external cavity length or by changing the lasing frequency because they both affect the external phase, equation 3.21. In this section these simulations were performed in MATLAB using the code given by Kliese *et al* [19]. The first example is obtained by extending the external cavity length by $\Delta L_{ext} = 200\mu$m for different C, using $\nu = 3.45$ THz, $L_{ext} = 0.75$ m and $\alpha = 0$.

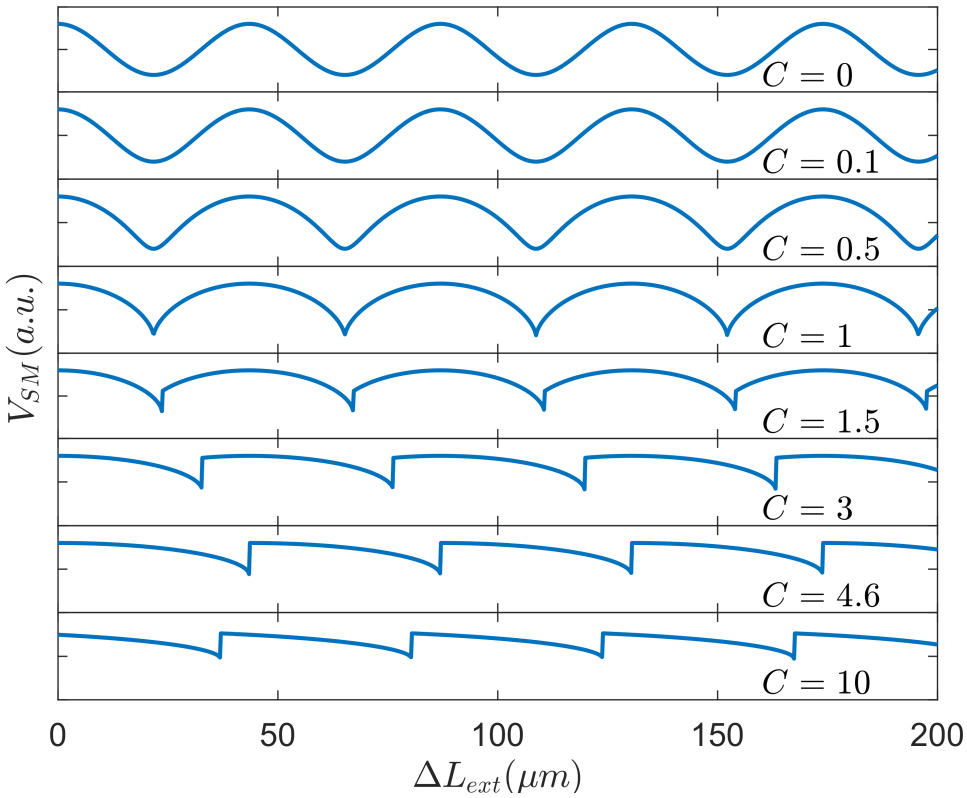

Figure 3.5: Simulation of V_{SM} waveform by extending the cavity length for different levels of C.

The different feedback regimes can be identified by the shape of the waveforms (see figure 3.5). For C=0 the fringes show a sinusoidal behaviour which starts to distort for 0.1<C<1. For C>1 the jumps shown in figure 3.4(b) become visible and for further increase of the level of C the sinusoidal behaviour is fully lost in favour of a sawtooth-like. Here the strong feedbacks change the device refractive index affecting, in turn, the periodicity of the fringes.

Also the linewidth enhancement factor affects the shape of the SM interferometric fringes. The linewidth enhancement factor is a dimensionless parameter which relates the refractive index to the gain in semiconductor lasers (see equation 3.24). Finite values of α around 0.5 have been demonstrated using self-mixing measurements with THz QCLs [184], despite $\alpha \sim 0$ was expected. This non-zero value has been attributed to parasitic absorption in

states not directly involved with lasing phenomena, due to the optical feedback inside the laser cavity. Understanding how to morphology of the self-mixing fringes are affected by different linewidth enhancement factors is important in order to extract information from the waveforms. By analogy with the previous simulation of V_{SM}, here the waveforms are obtained by extending the external cavity length by $\Delta L_{ext} = 200\mu$m for different α, using $\nu = 3.45$ THz, $L_{ext} = 0.75$ m and C=1.

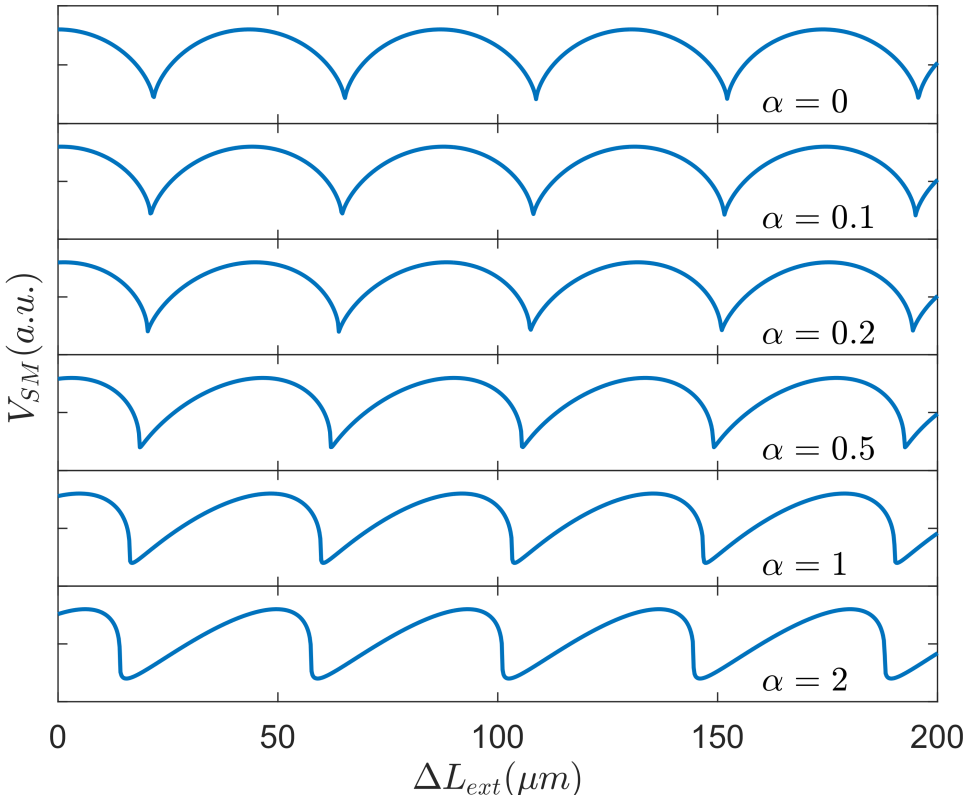

Figure 3.6: Simulation of V_{SM} waveform by extending the cavity length for different levels of α.

The symmetry of the fringes is affected by α (see figure 3.6). A value of α greater than 0 creates asymmetric fringes that are skewed on one side. This was also experimentally confirmed by Green *et al* [184] where they reported skewed self-mixing interferometric signals with $\alpha \sim 0.5$ and C<1 obtained with a THz QCL lasing at 2.55 THz. The choice of simulating SM fringes up to such values of $\alpha \sim 2$ is dictated by the fact that despite lower

values of α are expected from the experiments, a $\alpha \approx 1.9$ has been previously reported [155], using a similar experimental set-up and laser as the one used in this thesis. Such value of α was considered appropriate for a THz QCL operating close to current threshold in a self-mixing scheme. Also another group using real-time THz imaging through self-mixing in a QCL has reported values of $\alpha \approx$-0.9$\pm$ 0.3, substantially deviating from $\alpha \approx$0.5 and this was attributed to the QCL design which exploited a phonon-assisted electron injection [16].

Simulations of self-mixing signal can also be gained by changing the lasing frequency (see equation 3.21). Similarly to the previous simulation interferometric fringes are obtained by ranging ν between 3.45 THz and 3.4505 THz for different C, using $L_{ext} = 0.75$ m and α=0. Equally to V_{SM} simulated by extending L_{ext}, figure 3.7 shows fringes with sinusoidal

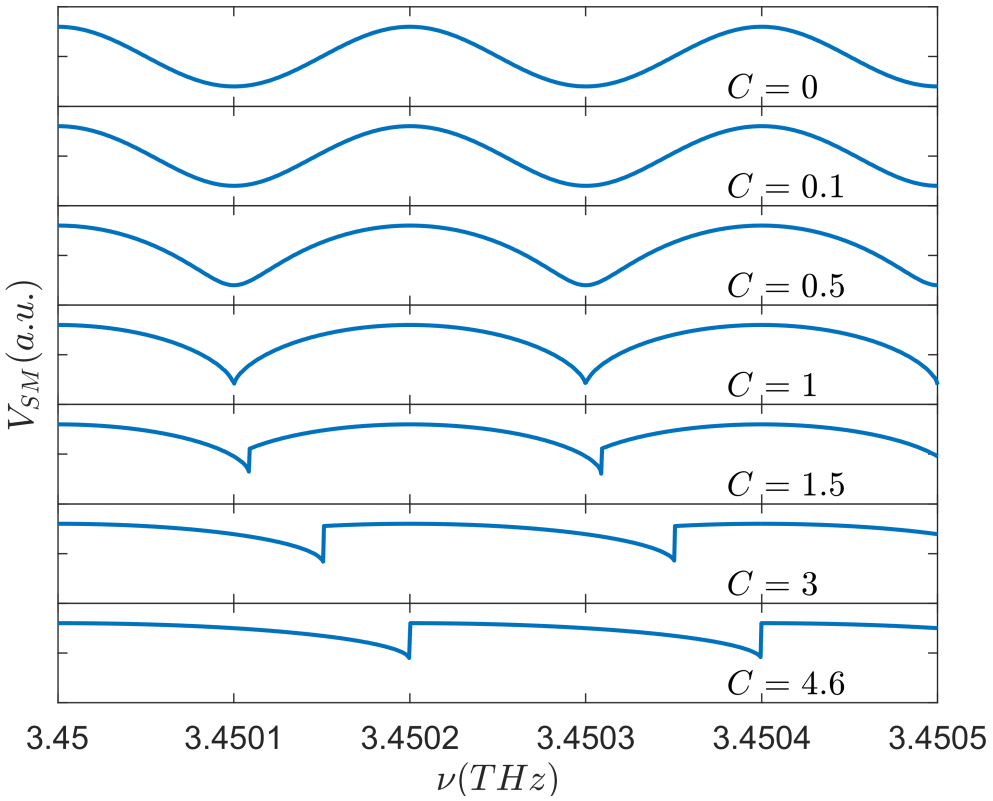

Figure 3.7: Simulation of V_{SM} waveform by changing the lasing frequency for different levels of C.

behaviour for C=0. For 0.1<C<1 the waveforms start to distort and for C>1 they fully lose the sinusoidal shape with the jumps (see figure 3.4(b)) becoming more prominent. From the experimental point of view, the waveforms can be acquired by both extending the cavity length and by changing the lasing frequency. In the next chapters the second method will be shown that is faster and does not require a translational stage to move the sample in order to extend L_{ext}. Moreover thanks to a single-mode THz QCL, this method known as swept-frequency, will be used in the chapter 4 to measure the resolution limit of an imaging system based on the self-mixing in a THz QCL and to acquire images of silicon wafers for photovoltaic applications and skin tissues; in the chapter 5 will be also used to extract information such as complex permittivity of crystals under analysis.

3.5 Detection sensitivity of SM

There are many QCL applications that need high detection sensitivities. Among these, s-SNOM (scattering-type scanning near-field optical microscopy) has shown the capability to overcome the diffraction limit imposed by the beam waist by focusing the beam on a nano-meter scaled metallic tip and collecting the scattered beam on a detector (see section 1.4 of chapter 1). However this technique will be demonstrated in more details in chapter 5 and chapter 6. These systems have achieved remarkable optical resolutions up to $\lambda/1000$ although require a high sensitivity detection due to the small scattering cross section of the nano-metric tip (typically $r_{tip} \sim 20$ nm) [122, 155, 185]. The cross section scales with r_{tip}^3 and so the detection sensitivity can ultimately limit the highest resolution attainable. Specifically, the cross section is particularly small at THz wavelengths. Similarly, for gas spectroscopy and sensing applications exploiting SM in THz QCLs [169, 186], the detection sensitivity influences the maximum extinction coefficient that can be measured. In order to understand and quantify the detection sensitivity achievable using the SM effect in a THz QCL a set of experiments has been conducted. The experiments were conducted by using a QCL consisting of a 14 μm-thick GaAs/AlGaAs 9-well active region lasing at ~3.4 THz, processed into a semi-insulating surface-plasmon (SISP) ridge waveguide with dimensions of 2.9 mm $\times$ 150 μm. The active region of this laser is based on the same

structure described in the section 2.5 of chapter 2 with a design proposed by Wienold *et al* [171]. The QCL was mounted on the cold finger of a continuous L-He flow Janis ST-100 cryostat (see figure 3.8(a)) equipped with Polyethylene (PE) windows used for the transmission of the THz beam. The QCL was cooled and kept at a constant temperature of 25K±0.01K throughout all the experiments.

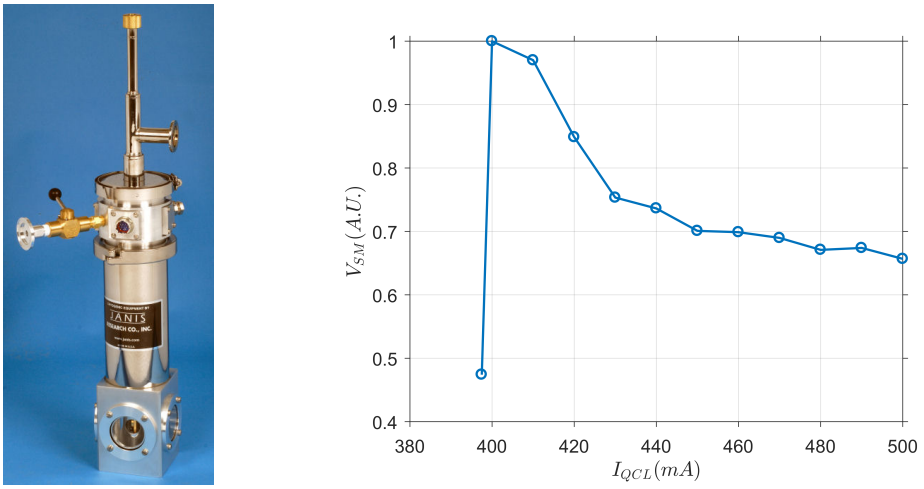

(a) (b)

Figure 3.8: (a) The Janis ST-100 cryostat used to cool and keep the QCL at a temperature of 25K±0.01K. (b) SM voltage signal V_{SM} as a function of driving current I_{QCL} with no additional external cavity attenuation.

Two 2-inch-diameter parabolic f/2 gold coated mirrors were used to focus the THz beam onto the surface of a planar gold mirror, which was mounted on a translational mechanical stage capable of movements along the direction, Z, of propagation of the THz beam with μm resolution. The external cavity length was L_{ext} ≈0.48m through an unpurged atmosphere. A laser driver was used to power the QCL through a continuous driving current of 400 mA, just above the lasing threshold of 380 mA, where the SM voltage signal was measured to be the greatest (see figure 3.8(b)). At this driving current, the emitted power, measured at the external planar mirror using a calibrated THz power meter, was found to be ∼22.4μW.

The perturbation created by the optical feedback in the laser cavity was measured through V_{SM}, which was recorded through to the laser terminal voltage by a lock-in amplifier

(LIA) referenced to an optical power modulation imposed by a mechanical chopper at f_{Mod} ~200Hz, using an integration times, T_C=10s. The lock-in detection considers the modulation of the optical signal at a specific frequency (f_{Mod}) in order to maximise the sensitivity of the detection. The f_{Mod} is used as a reference to the LIA in order to distinguish and to measure the optical signal respect to the background signal, therefore reducing the measurement noise. The idea behind these experiments is to measure the V_{SM} waveform by extending the external cavity length by ΔL_{ext}=200μm, with 4μm step, for increased THz beam attenuation. The attenuation was accomplished by introducing calibrated THz power attenuators in the external cavity path. A scheme of the set-up used for these experiments is shown in figure 3.9.

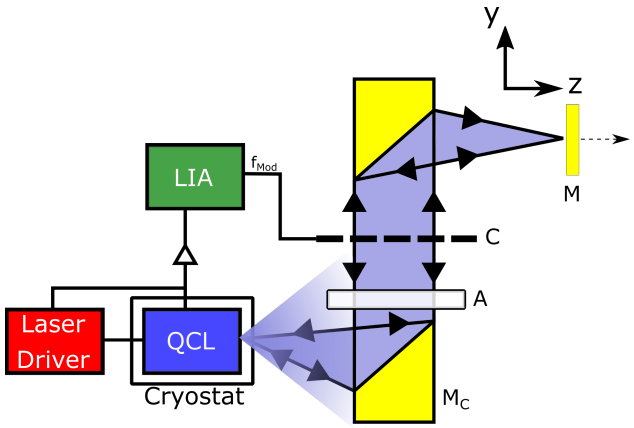

Figure 3.9: Experimental system for measuring the detection sensitivity of self-mixing based on a THz QCL. LIA, lock-in amplifier; C, mechanical chopper; A, THz attenuators; M, moveable planar mirror; M_C, collection mirror.

In order to take account of the attenuation for these experiments, equation 3.21 has to be re-written following the relation,

$$V_{SM} \propto \sqrt{\varepsilon_a \varepsilon_c \varepsilon_r} \sqrt{R_{2ext}} \cos\left(\frac{2\pi L_{ext}\nu}{c} + \theta\right). \tag{3.32}$$

Here the coupling-efficiency factor, ϵ has been broken down into three attenuation factors. The power attenuation factor ε_c is a coupling constant inherent to the optical system that accounts for loss due to imperfect collection of the radiation emitted from the laser by the f/2 parabolic collection mirror, including loss due to imperfect transmission through the

cryostat window. The power attenuation factor ε_r represents the reinjection loss between the external planar mirror and the laser cavity, including the loss due to transmission through the cryostat window, and spatial mode mismatch between the reflected and cavity modes. The power attenuation factor ε_a is a coupling constant accounting for additional attenuation introduced to the external cavity. The linewidth enhancement factor and the feedback parameter (see equation 3.31) obtained by the excess phase equation will dictate the behaviour of V_{SM} as function of the extension of the external cavity length (see figure 3.5 and 3.6). Here also the feedback coupling coefficient (see equation 3.15), which is directly related to the coupling-efficiency factor, has to be written taking account of the three attenuation factors described above, as shown in equation 3.33.

$$k_{ext} = \sqrt{\varepsilon_a \varepsilon_c \varepsilon_r} \sqrt{\frac{R_{2ext}}{R_2}} (1 - R_2). \tag{3.33}$$

A concise algorithm which solves self-mixing equations for arbitrary feedback levels [19] was used to fit the recorded V_{SM} waveforms and to extract the values of the parameters and attenuation factors used for the analysis. Moreover, It is interesting to evaluate the intrinsic limit for the maximum tolerable power attenuation for the QCL used for these experiments, and to compare this figure with the measured value. It can be expected that OF induces a non-negligible effect on the operating parameters of a laser when the rate of the photon reinjection to the cavity exceeds the rate of spontaneous emission in the cavity [187]. Using a recently reported reduced rate equation model of a THz QCL under optical feedback, this condition can be expressed as [29],

$$\frac{2k_{ext}}{\tau_L} S > \frac{M \beta_{sp} N_3}{\tau_{sp}}, \tag{3.34}$$

where S is the photon number, M is the number of periods in the QCL active region, β_{sp} is the spontaneous emission factor, N_3 is the upper lasing level carrier number, and τ_{sp} is the spontaneous emission lifetime.

From measurements of the power at both the cryostat window and at the external planar

mirror, the collection losses in the system is determined to be $\varepsilon_c \sim$-10 dB. In this experiment ε_a was controlled by introducing calibrated THz power attenuators in the external cavity, which provided a double-pass (power) attenuation in the range 0–90 dB. This allowed the maximum tolerable additional cavity attenuation to be determined, as the level of attenuation where interferometric variations on the laser terminal voltage were reduced to the voltage noise level.

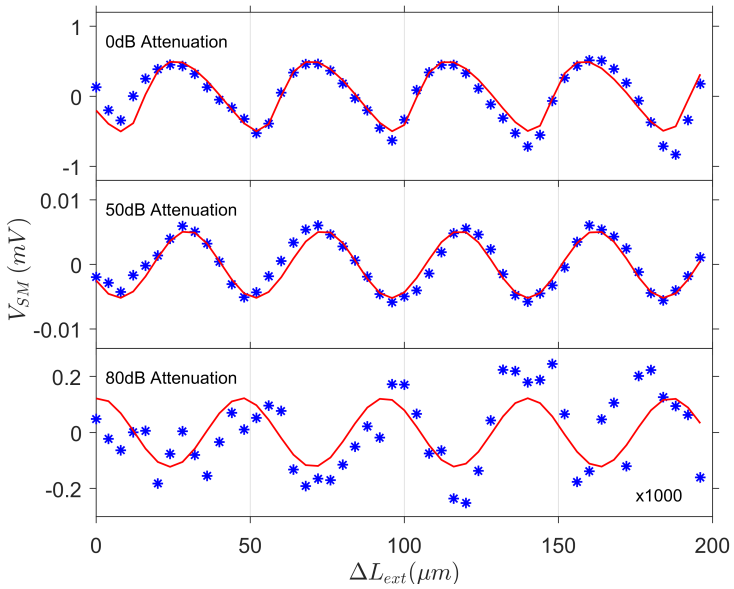

Figure 3.10: Interferometric waveforms measured for an external cavity extension of 200 μm under various levels of double-pass power attenuation ε_a^2. Also shown (red lines) are fits to eq. 3.32. The data shown in the bottom panel has been scaled by a factor 1000

Figure 3.10 shows the SM voltage waveforms recorded for varying degrees of additional cavity attenuation. The non-sinusoidal form of these interferograms is a result of ν in equation 3.32 being dependent on the external cavity length, as described by the excess phase equation (see equation 3.30) [19, 92]. The magnitude of this perturbation to the lasing frequency under optical feedback is also dependent on the feedback parameter C (see equation 3.31). Also shown in figure 3.10 are fits of the data to equation 3.32. In the case of ε_a=1 (i.e. with no additional attenuation in the external cavity) it is possible to determine values C=0.4 and α =-1.9 from the fit to our data. Although values of α in the range $\sim$-0.1 to $\sim$0.5 are typically obtained from THz QCLs based on a bound-to-

continuum active region design [102], it's worth noting that values significantly deviating from this range have been reported elsewhere [16] for active regions with phonon-assisted electron injection such as that employed in this experiment.

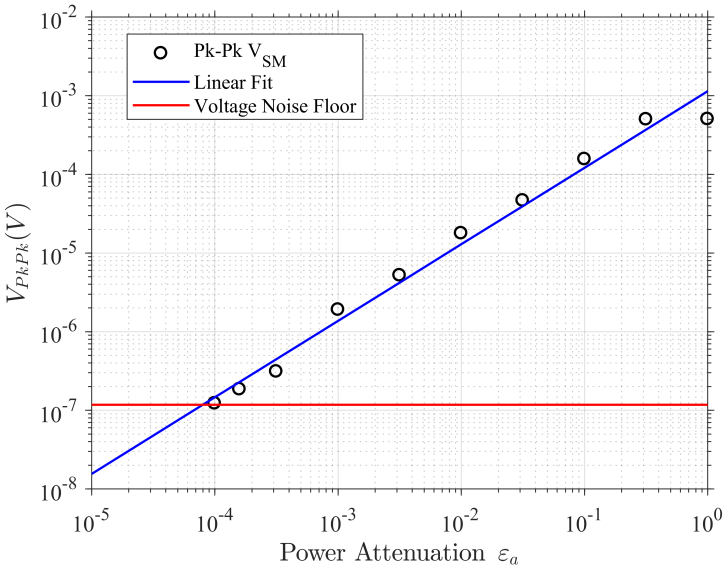

Figure 3.11: Peak-to-peak values of the SM voltage interferograms, V_{PkPk}, as a function of additional power attenuation introduced in the external cavity, ε_a. The horizontal line indicates the voltage noise floor in our system, at a level $\sim$1.5 $\mu V/\sqrt{Hz}$.

Figure 3.11 shows the peak-to-peak values of the SM voltage interferograms, V_{PkPk}, determined from the fits to the data shown in figure 3.10, plotted as a function of additional field attenuation in the cavity; a linear relationship between $\sqrt{\varepsilon_a}$ and V_{PkPk} can be established, as expected from equation 3.32. Also shown in figure 3.11 is the voltage noise floor in the system, which is dominated by current noise in the laser driver. Other sources of noise in our system, such as the input noise of the lock-in amplifier are on the order of $\sim nV/\sqrt{Hz}$, far below the laser driver noise.

As can be seen, variations on the laser voltage can be resolved with up to $\sim$-80 dB of additional attenuation introduced in the external cavity. Based on the power measured in the external cavity, and without accounting for reinjection losses, this measurement corresponds to a detection noise equivalent power (NEP) of $\sim$1.4 $pW/\sqrt{Hz}$.

By estimating the reinjection losses in the system it is possible to estimate the correspond-

ing minimum detectable power coupled coherently to the laser active region. Using the fitted values for C and α in equation 3.31 and assuming R_{2ext}=1 for the gold mirror and R_2=0.32 for the laser facet we can estimate the attenuation factor $\varepsilon_c\varepsilon_r$=0.0034, for our optical system via equation 3.33. By accounting for the measured value ε_c ∼-10 dB, it is possible therefore to obtain ε_r.

ε_a (dB)	C	$\sqrt{\varepsilon_c\varepsilon_r}$	ε_r (dB)	Reinjected Power (fW/$\sqrt{Hz}$)
0	0.39	0.0033	-39.5	0.16
-10	0.24	0.0063	-34	0.56
-20	0.13	0.0112	-28.9	1.81
-30	0.03	0.0086	-31.3	1.04

Table 3.1: Fitting parameters and estimated values of the minimum detectable reinjected power obtained from measurements with different external attenuations ε_a

Table 3.1 summarizes the results of this analysis for each of the four measurements up to -30 dB of additional cavity attenuation; we note that the small values of C ($\ll$0.1) resulting from greater attenuation (ε_a < -30 dB) cannot be obtained reliably from the fitting procedure. These reinjection losses shown in table 3.1 arise primarily from coherent coupling of the returning field to the laser cavity. Indeed, the spot size of the returning beam focused on the laser facet is expected to be on the order ∼250 μm [12], far larger than the 14 μm x 150 μm facet of the laser active region. It's worth also noting that the variation in ε_r between measurements can be explained by the fact that the insertion of attenuators in the external cavity can change the divergence angle of the propagating field. As such, the attenuation ε_r cannot be assumed to act independently to ε_a. Nevertheless, from our measured NEP of ∼1.4 pW/$\sqrt{Hz}$, we can obtain the reinjected power for each of these four measurements. Based on these results (see Table 3.1) we can estimate that our NEP corresponds to only ∼1 fW/$\sqrt{Hz}$ coupled coherently to the laser active region. As such, improvements in the coupling to the active region could in principle lead to further improvement in the NEP. Finally, by evaluating equations 3.33 and 3.34 using typical values for our QCL device [29] (see Table 3.2), we predict an intrinsic limit for the maximum tolerable total power attenuation equal to ∼150 dB, which is in reasonable

agreement with the experimentally determined value of $\varepsilon_a\varepsilon_c\varepsilon_r$ ∼-(80+10+35)=-125 dB. The discrepancy between these values can be attributed to voltage noise in our system, which is dominated by the laser driver and could be reduced through the use of a more stable current source, for example, a dc battery.

R_{2ext}	1
R_2	0.324
M	117
β_{sp}	1.63×10^{-4}
N_3	1.07×10^{-7}
τ_{sp}	5.1×10^{-6} s
τ_L	7.04×10^{-11} s
S	3.69×10^{7}

Table 3.2: QCL device parameters used to predict the maximum tolerable total power attenuation in LFI[29]

3.6 Conclusions

In this chapter the theory describing the self-mixing effect in lasers has been explained. The three-mirror model allowed the derivation of two fundamental equations (3.21 and 3.30) useful to describe the behaviour of a QCL under optical feedback. In particular, the aim of this chapter was to provide insight of how it is possible to exploit the self-mixing effect in a THz QCL to extract both the amplitude and phase of the field reflected from a remote target, which can be related to sample properties such as the complex permittivity. Furthermore, the detection sensitivity of an LFI scheme based on a THz-frequency QCL has been quantified. The measurements demonstrated that variations on the laser voltage induced by OF to the laser can be resolved with the reinjection of powers as low as ∼-125 dB of the emitted power, which corresponds to a NEP for the used scheme of ∼1.4 pW/$\sqrt{Hz}$. By estimating the reinjection losses this value corresponds to NEP ∼1 fW/$\sqrt{Hz}$, demonstrating the high suitability of the SM effect to applications that require the detection of weakly scattered THz radiation, such as THz-s-SNOM.

4 THz imaging (far field) based on Self-Mixing in a QCL

Over the past years THz imaging techniques have shown an immense growth as imaging is considered one of the most promising applications for THz radiation. Interest is focused on various fields and applications such as biomedical imaging[38, 170, 188–197], pharmaceutical inspection [68, 70, 198] and non-contact and non-destructive analysis, as well as spectroscopic identification of materials for security applications [36, 199]. Indeed, THz radiation has many properties that make it attractive for imaging applications. For example, many dry non-polar (non-metallic) materials like plastics, fabrics [67], wood and papers are transparent to THz. Combining these features with the resolution imposed by the diffraction limit of its sub-millimeter wavelength makes the THz radiation a good candidate for non destructive inspection, quality control and security scanning functions [37, 200]. At the same time, the low energy of THz photons (on the order of few meV) allows the ability to excite vibrational (and rotational) states of organic and inorganic molecules that cannot be accessed through other frequency ranges. For example, numerous explosives and drug-of-abuse exhibit spectral absorption features in the THz range [35, 41, 71, 201–203]. In a similar way, THz diffuse imaging has been applied to discriminate between different powder mixtures of polymers such as Perspex and Polystyrene in different concentrations [3]. On the other hand, THz is strongly absorbed by water and merging this peculiarity with its non-ionizing property (due to the low photon energy) makes THz imaging an important tool for biomedical applications [191, 192]. It opens the possibility of new interesting studies on different healthy tissue types, as well as cancerous tissues due to their higher water content [38, 170, 189–191, 193, 194, 197].

It's worth mentioning that other THz imaging techniques which do not rely on QCLs as a light source are usually restricted to low THz powers, in the order of μW. Most common sources are broadband THz sources based on photoconductive emission, which requires femtosecond laser excitation [68, 190, 193]. On the other hand, THz QCLs are compact sources of THz radiation offering high power, coherent continuous-wave (CW) operation, narrow intrinsic linewidth and good tunability [62, 63]. These properties make THz QCLs

well suited for imaging applications, and over the past decade significant effort has been devoted to the development of imaging systems using these sources [8, 11–13, 116, 122, 155, 204]. The majority of these systems acquire images by raster-scanning a sample through the focused THz beam and recording pixel-by-pixel the response of an external detector, most commonly an incoherent thermal detector such as a Golay cell, cryogenically cooled bolometers or pyroelectric sensors [8, 11], with the inconvenience of having a low speed, and in case of the pyroelectric detector, low sensitivity. In contrast, acquiring images through the SM technique in a THz QCL offers a coherent imaging approach that does not need an external detector; instead the emitted THz radiation is reflected from the sample and coupled into the laser cavity, which causes a measurable perturbation to the laser voltage that depends on the phase and amplitude of the reflected THz wave [11–14, 116].

4.1 Applications of self-mixing in THz QCLs

Self-mixing in a THz QCL has been exploited for different applications including far-field and near-field coherent imaging (in 2D and 3D) [12, 13, 15, 116, 122, 155, 170, 185, 204, 205], gas-spectroscopy [169], velocimetry and displacement sensing [102, 206], and material analysis [182]. The experimental systems are usually compact because there is no need of an external detector since the QCL is able at the same time to generate and detect the radiation. All of these applications use the three-mirror model and equations 3.21 and 3.30 to extract fundamental information about the samples. In the case of 2D imaging, the QCL is kept at stable temperature and driven with a constant current while the sample is placed on a movable stage. The sample is raster-scanned in two dimensions parallel to the direction of beam propagation and a 2D image can be acquired by mechanically (or electrically) modulating the THz beam in order to allow lock-in detection of the self-mixing voltage signal (see figure 4.1).

The equations of the three-mirror model also allow the reconstruction of a three-dimensional image when the target is placed on a moveable stage capable of longitudinal (z) translation [13]. This technique exploits the fact it is possible to extract the magnitude and phase from a SM interferometric waveform recorded through lock-in detection of V_{SM} when the

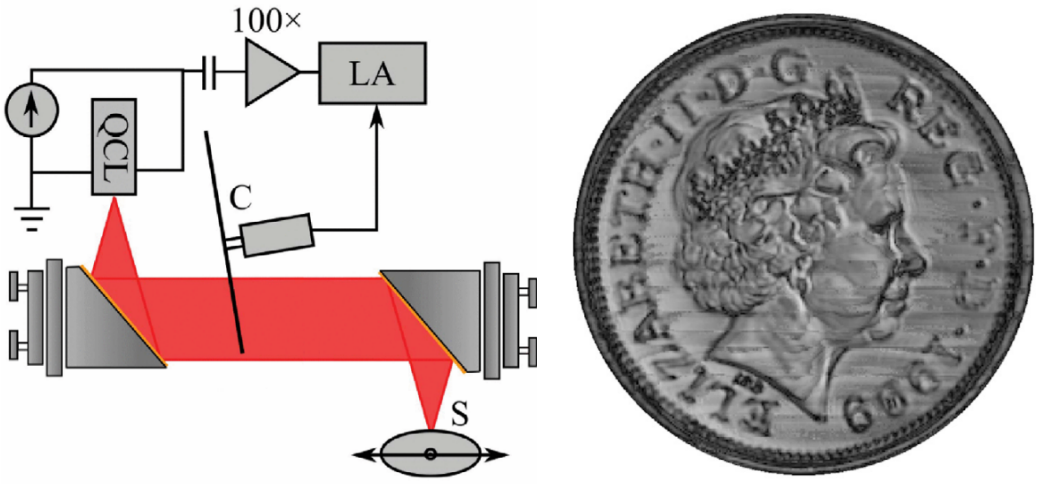

(a) (b)

Figure 4.1: (a) Schematic of the experimental set-up used for 2D imaging through SM in a THz QCL by mechanically modulating the beam; adapted from P. Dean [11]. (b) A high resolution image of a UK two-pence coin; adapted from P.Dean [12].

sample is moved along the z direction. In accordance with equations 3.21 and 3.30 the magnitude is related to sample reflectance and the phase to the sample height.

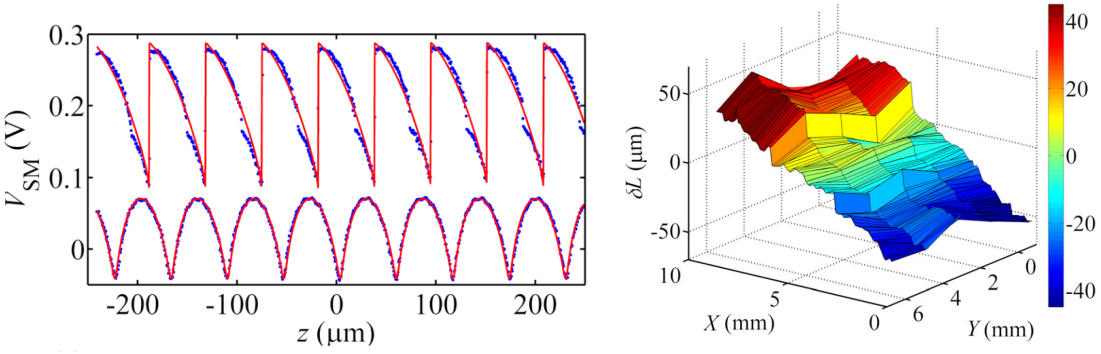

(a) (b)

Figure 4.2: (a) SM waveform obtained by translating a wet etched $GaAs$ sample along z direction. The top waveform correspond to the part of the sample coated with Au. (b) 3D reconstruction of the sample. Adapted from P.Dean [13].

Figure 4.2(a) shows a SM voltage interferometric waveform obtained from a $GaAs$ sample consisting of 3 steps, each of $10\mu m$ height, formed by wet chemical etching. Half of the sample was coated with a layer of gold in order to provide a high reflectance region (top trace). All the data was acquired by keeping I_{QCL} and T_{QCL} constant while the

external cavity length was changed. The sample was scanned in two dimensions and a V_{SM} waveform recorded at each pixel. The V_{SM} waveforms were each fitted with equations 3.21 and 3.30 using $\epsilon\sqrt{R_{2ext}}$, C, α, L_{ext} as free parameters. Figure 4.2(b) shows the 3D reconstruction of the sample, in which the change in the external cavity length due to sample height, δL, has been extracted from the values of L_{ext}. In this scheme the depth resolution has been estimated to be $\sim 2\mu m$. Although the technique works well, the main limitation is the slow image acquisition speed ($\sim 0.05 pixels/s$).

A faster technique to obtain interferometric waveforms avoids the need of extending the external cavity length. This technique, known as swept-frequency interferometry (SFI), exploits the possibility to change the QCL lasing frequency to obtain waveforms in time domain. A complex fast fourier transform of the waveform allows to retrieve magnitude and phase data for each pixel. A more detailed discussion of this technique will be provided in the section 4.2. Nevertheless, the depth resolution of this technique has been reported to be $\sim 0.1\mu m$ with a rate up to $\sim 40\, pixels/s$ [14]. The 3D profile of a sample can then

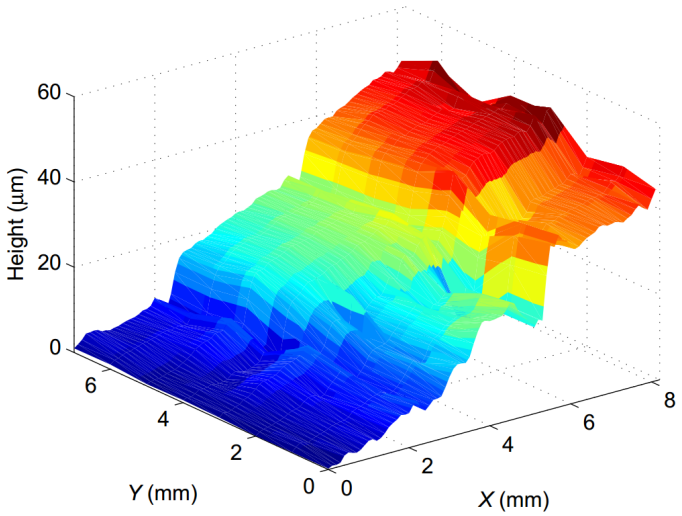

Figure 4.3: Image of the same sample shown in 4.2(b) obtained through swept-frequency measurements. Adapted from J. Keeley [14].

be created by converting the phase into a height map by accounting for the laser emission

wavelength and for the double pass of the beam in the SM system,

$$dL = \frac{\phi\lambda}{4\pi}, \tag{4.1}$$

assuming that there are no phase changes due to changes in permittivity of the sample. The results of the analysis are shown in figure 4.3 for the same sample shown in figure 4.2(b).

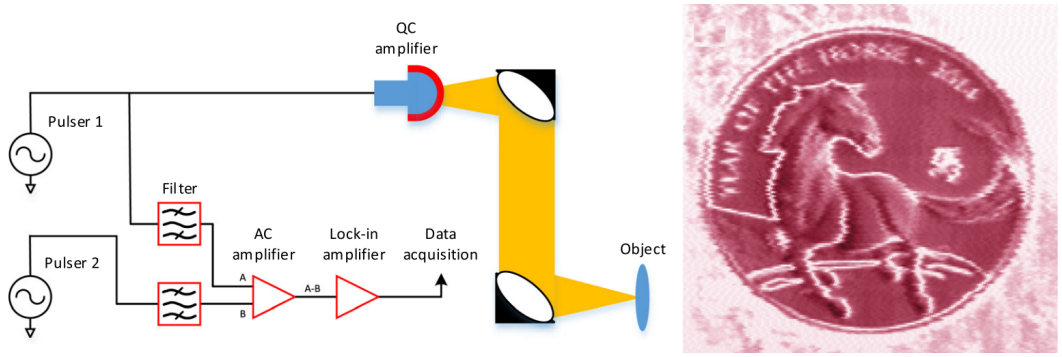

(a) (b)

Figure 4.4: (a) Schematic diagram of the imaging set-up employing the self-mixing effect in a quantum cascade amplifier. (b) Image of a Lunar Year of the Horse 2014 Gold Coin with a diameter of 16.5 mm, acquired at 2.9 THz with a rate of 20000 $pixels/s$. Adapted from Y. Ren [15].

The self-mixing effect in a laser has been also exploited through the use of a quantum cascade amplifier providing gain at ∼2.9 THz [15]. The amplifier consisted of an anti-reflective (AR) lens coupled to the facet of a QCL. The AR lens has the effect of enhancing the mirror losses, hence suppressing the lasing action. The optical feedback to the amplifier, created by introduction of an external reflector, initiates the lasing action and the emission enhances the photon-assisted transport and, in turn, reduces the laser voltage. The QC amplifier is biased by fast pulses (10-20 kHz repetition rate with 6 % duty cycle) and a second pulse generator with same input levels is used as a constant calibration system. The pulses are filtered by band pass filters and coupled into a low noise differential amplifier providing a gain of 46dB. Finally the output of the differential amplifier is fed into a lock-in amplifier locked to the pulse generator biasing the QC amplifier. The sample is raster-scanned into the direction perpendicular to the beam path (see figure 4.4(a)).

The image acquisition rate up to 20000 $pixels/s$ has been demonstrated with 10 μs lock-in integration time, 1 μm step size and the total acquisition time of 3 min by recording an image of Lunar Year of the Horse Gold coin (see figure 4.4(b)).

Another example of different set-up using the self-mixing effect in a THz QCL is the scheme suggested by Wienold *et al* [16]. In this case the group used a fast-scanning mirror to steer the THz beam, rather than raster-scanning the sample. A fast scanning rate up to 2 Hz (2200 $pixels/s$) has been demonstrated, eventually limited by the mechanical inertia of the scanning mirror. The schematic of the set-up is shown in figure 4.5(a). An image of a German 50-cent coin obtained at 3.3 THz using a spiral scan is shown in figure 4.5(b).

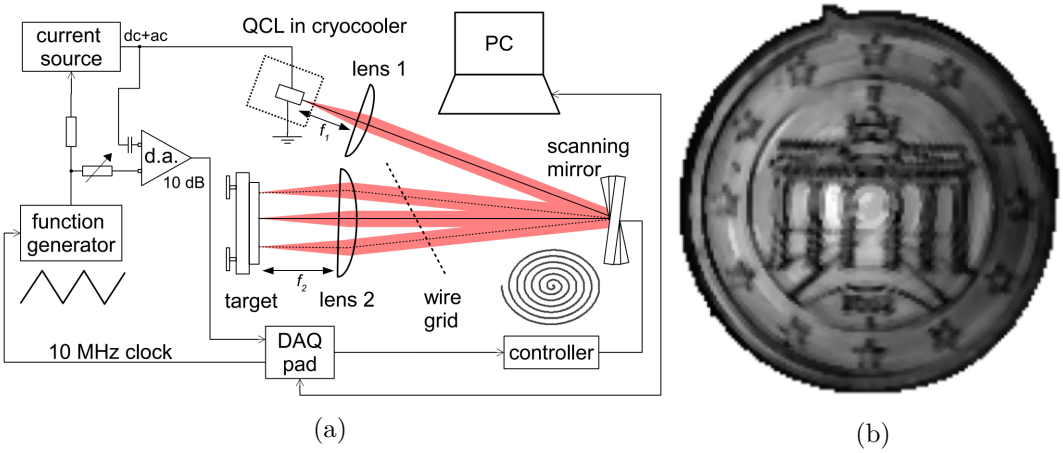

Figure 4.5: (a) Schematic diagram of the imaging set-up employing self-mixing effect where the THz beam is deflected by a fast scanning mirror. (b) Image of a German 50-cent coin acquired at 3.3 THz with a frame rate of 1 Hz. Adapted from M. Wienold [16].

In this chapter far-field THz imaging based on the SM effect in a THz QCL is demonstrated. The suitability of this approach for acquiring images of various radically different samples is demonstrated for the first time; specifically, a human skin sample, a skin sample containing melanoma and silicon wafers. In the latter case, the possibility to implement this technique for the detection of cracks and impurities in silicon wafers, crucial for the fabrication a solar grade wafers, is demonstrated. In the case of human skin samples, contrast between different tissue types, including healthy skin tissue and skin cancer, is shown both in magnitude and phase images. Also the possibility of using the SM technique in double-pass transmission mode is demonstrated. Important parameters of our

imaging system including the imaging resolution limit in the far-field and signal-to-noise ratio (SNR) will also be characterised.

4.2 Experimental set-up for imaging using the SM effect in QCLs

Imaging through SM effect does not require an external detector, since the laser is the source and the detector of the optical signal. The experiments in this chapter were conducted by using a QCL consisting of a 14 μm-thick GaAs/AlGaAs 9-well active region lasing at ∼3.4 THz, processed into a semi-insulating surface-plasmon (SISP) ridge waveguide with dimensions of 1.8 mm × 150 μm. The QCL was first fully characterized in pulsed and CW mode as shown in chapter 2 (see figure 2.24 and 2.25); then a photonic lattice 166 μm long with a 13.2 μm grating period with a 70% duty cycle and a central 8 μm wide phase defect was created by FIB milling in order to achieve single mode emission (see figure 2.26(a)). The laser was mounted on the cold finger of a continuous flow cryostat and maintained at a constant temperature of 25K±0.01K. A laser driver was used to drive the QCL just above the threshold current at 470mA. Two 2-inch-diameter parabolic f/2 mirrors were used to focus the THz beam onto the sample surface. The external cavity length was ∼0.4m through an unpurged atmosphere. The results of the 2D imaging shown in this chapter were achieved by mechanically modulating the THz beam through a chopper at the frequency f_{Mod} ∼220Hz. The sample, placed on the focal point of the beam, was raster-scanned in both X and Y directions with different step sizes using two computer controlled translation stages with μm resolution. V_{SM} pixel by pixel was measured across the laser terminals through the lock-in amplifier (LIA) referenced to f_{Mod} using different integration times (T_C). The lock-in detection considers the modulation of the optical signal at a certain frequency (f_{Mod}) in order to maximise the sensitivity of the detector. The f_{Mod} is used as a reference to the LIA in order to distinguish and to measure the optical signal respect to the background signal, therefore reducing the measurement noise. A schematic representation of this set-up is shown in figure 4.6(a).

In some cases acquiring interferometric waveforms was necessary. A method to do this through the just described 2D imaging system was to extend the external cavity length

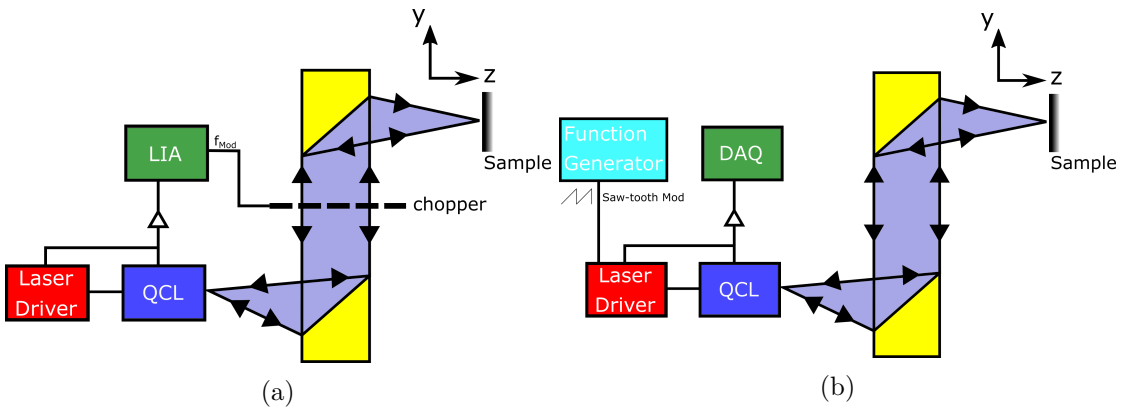

Figure 4.6: The two experimental set-ups for SM imaging through a THz QCL. LIA, lock-in amplifier. QCL, Quantum Cascade Laser. DAQ, data acquisition board. The beam from the QCL is projected and focused, using two f/2 parabolic mirrors, onto the sample. (a) Through mechanical modulation; (b) swept-frequency, with a saw-tooth modulation superimposed on the QCL.

in order to acquire the waveform pixel by pixel as function of L_{ext} (see equation 3.21), making the image acquisition slow.

By exploiting the dependence of the QCL emission frequency on driving current (as shown, for example, in figure 2.27) a different approach to obtain an interferometric waveform can be used that avoids the need to scan the sample along the z direction, making the data acquisition faster. In this technique, known as swept-frequency feedback interferometry [116, 204], an electric saw-tooth modulation is superimposed on the driving current of the QCL, which chirps the lasing frequency. The SM waveforms are then obtained by subtracting the QCL terminal voltage under feedback (V_{QCL}) from the QCL terminal voltage without feedback (V_{QCL0}) (see figure 4.7).

The same QCL used for the 2D imaging system (see figure 4.6(a)) was also used to acquire images through SFI. The laser was mounted on the cold finger of a continuous flow cryostat and maintained at a constant temperature of 25K±0.01K. A laser driver was used to drive the QCL at 430 mA and a 2000 mV, 90% duty cycle, 1 kHz frequency saw-tooth modulation was superimposed by a function generator. This modulation created a lasing frequency change of $\Delta\nu \sim$-1 GHz (see figure 2.27) every cycle. The LIA was replaced by a National Instruments data acquisition (DAQ) board (NI-DAQmx USB-6251 BNC) able to directly

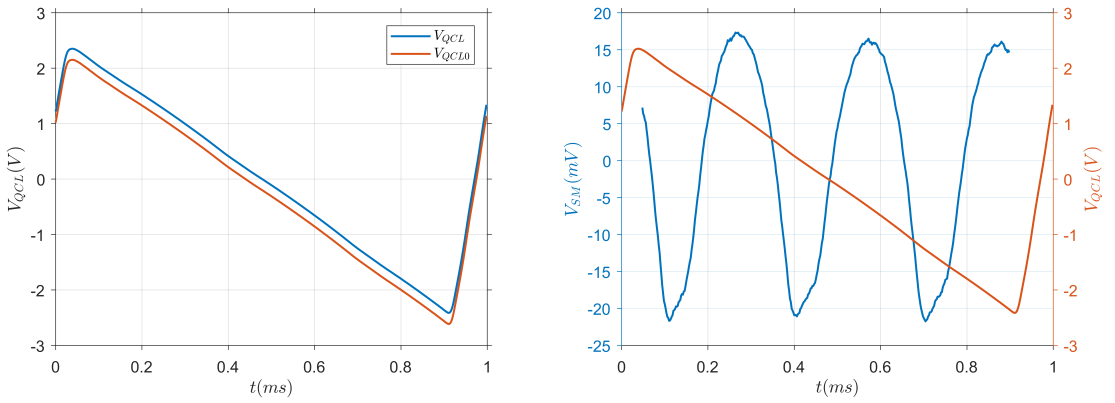

(a) (b)

Figure 4.7: (a) Terminal voltage, with saw-tooth modulation, of QCL with (V_{QCL}, blue) and without (V_{QCL0}, red) feedback, with offset for clarity. (b) Interferometric waveform (V_{SM}) resolved by subtracting V_{QCL} to V_{QCL0}.

measure the voltage across the QCL with 16 bit resolution at $500{\times}10^3 samples/s$. The signal from the function generator that imposed the saw-tooth modulation was used as a trigger for the DAQ board, which was connected to the computer. Two 2-inch-diameter parabolic f/2 mirrors were used to focus the THz beam onto the sample surface. The external cavity length was ∼0.4m through an unpurged atmosphere. The sample was raster scanned in X and Y direction by two translational stages with μm resolution and the laser terminal voltage was measured at each pixel. A schematic of the SFI set-up is shown in figure 4.6(b). In order to acquire the swept-frequency waveforms the laser voltage under optical feedback needed to be subtracted to the laser voltage without feedback. This was achieved by blocking the THz beam, while the saw-tooth modulation was imposed to the laser. Exemplar SFI fringes are shown in figure 4.7(b).

This approach generates SM fringes for each pixel in the time domain, and in order to resolve the phase and magnitude of the fringes a complex Fast Fourier transform (FFT) can be performed. The interferometric phase of the SM waveform during a swept-frequency scan is given by,

$$\Phi(t) = \frac{4\pi L_{ext}\gamma t}{c} + \frac{4\pi L_{ext}\nu_0}{c} = 2\pi f_c t + \phi, \tag{4.2}$$

where ν_0 is the laser frequency without feedback at t=0 and $\phi = \arctan\left(\frac{Im(\hat{I})}{Re(\hat{I})}\right)$ is the

initial phase of the SM fringe, which can be calculated from the real and imaginary parts of the FFT $\hat{I}(f_c)$. The carrier frequency of the fringes f_c is given by $f_c = 2\gamma L_{ext}/c$ [14], in which the modulation rate of the laser, $\gamma\,[Hz/s]$, can be calculated from the tuning coefficient of the laser $k\,[Hz/A]$ and the applied current modulation $[A/s]$.

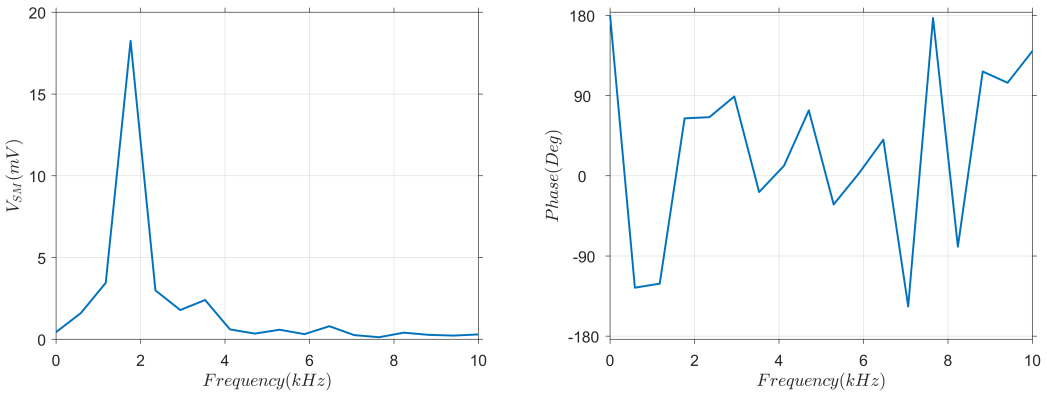

(a) (b)

Figure 4.8: Swept-frequency SM. (a) Resolved magnitude and (b) phase by performing a complex FFT analysis on swept-frequency interferometric fringes as shown in figure 4.7(b).

Figure 4.8 shows the magnitude and phase spectra obtained from the SM waveform shown in figure 4.7(b). In this case the spectra show the maximum magnitude at 1.7 kHz frequency. The broad peak shown in the magnitude spectrum can be associated with the low resolution of the FFT; in order to obtain a narrower peak (a higher resolution of the FFT) the same waveform can be repeated more times. In fact, the waveform shown in figure 4.7(b) is obtained from only 1 iteration of the waveform recorded over a time period ($\sim$ 1ms); by concatenating multiple waveforms the resolution of the FFT can be improved, as shown in figure 4.9. The phase is obtained from the phase spectrum, evaluated at the same frequency as the peak in the magnitude spectrum ($\sim$ 1.7 kHz). It's worth mentioning that the swept-frequency technique cannot directly differentiate between positive and negative shifts of phase over a period of 2π. This translates to discontinuities in the phase signal when an extreme value, $+\pi$ or $-\pi$, is reached; when the optical phase is decreasing or increasing, although it is physically continuous, it can jump to the other end of the interval. In order to reconstruct a physical phase, the phase jumps can be

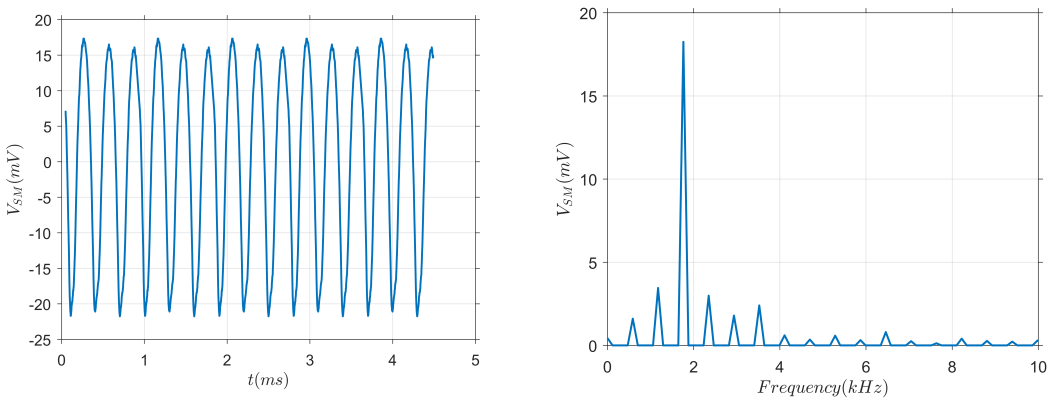

(a) (b)

Figure 4.9: Swept-frequency SM. (a) Interferometric waveform and (b) the magnitude after the FFT, obtained by concatenating 5 iterations performed on the same pixel.

removed by adding or subtracting multiples of 2π to the original phase map [14].

4.3 Characterisation of imaging systems

In order to understand the performance characteristics of the imaging systems based on self-mixing, a series of experiments have been conducted to quantify the important parameters of spatial resolution and SNR. A comparison of the SNR between mechanical modulation approach and SFI, in particular, is undertaken within the context of imaging silicon wafers relevant to the manufacture of photovoltaic cells, which will be analysed in depth in the section 4.4, showing the possibility to exploit the imaging system based on SM in a THz QCL as tool for crack and impurity detection.

4.3.1 Imaging spatial Resolution

The spatial resolution of the system does not depend on the modulation scheme employed, because it depends on the wavelength and the optics used for the measurements. The SFI offers the advantage to split between amplitude and phase of the waveform. From the experimental point of view this facilitates the acquisition of the image of the resolution target used for this experiment because it avoids the need of adjusting the tilt of the sample with respect to the THz beam direction, when only the amplitude is needed. In

fact, the tilt affects the phase of the waveform but it does not affect its amplitude, which will always be resolved. The spatial resolution of the system has been evaluated using a gold-on-glass resolution target. The resolution target is made of 10 groups of 5 equally spaced gold bars, defined by standard optical lithography with a metal thickness of $\sim$ 300 nm. The gold groups have different widths, from the widest, 2 mm gold bars spaced 2 mm apart, to the narrowest, 200 μm gold bars spaced 200 μm apart. Figure 4.10 shows a visible camera picture of the resolution target in question.

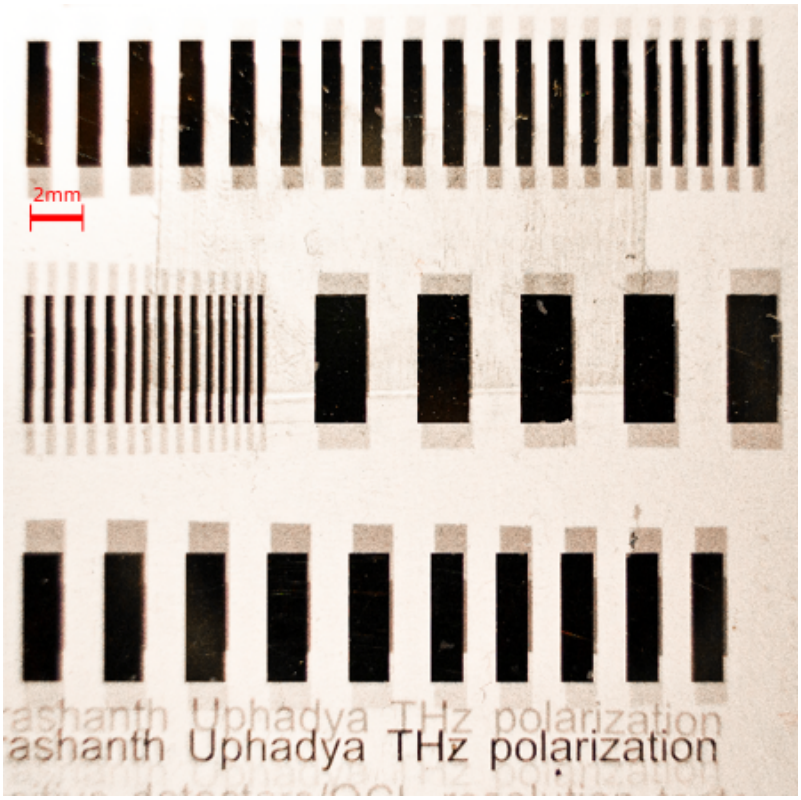

Figure 4.10: Photo taken from a visible camera of the resolution target used to evaluate the system spatial resolution. Gold bars appear black due to high reflectivity. Also shadows are visible on the back.

In figure 4.11, the THz magnitude image of the resolution target obtained through SFI of is shown. This image consists of 881 $\times$ 17 pixels with pixel size of 25 μm along the horizontal (X) direction and 2 mm along the vertical (Y) direction. The spatial resolution has been evaluated along the horizontal direction because it is expected to be equal in both the directions, therefore the choice of the different pixel size. The big disparity of

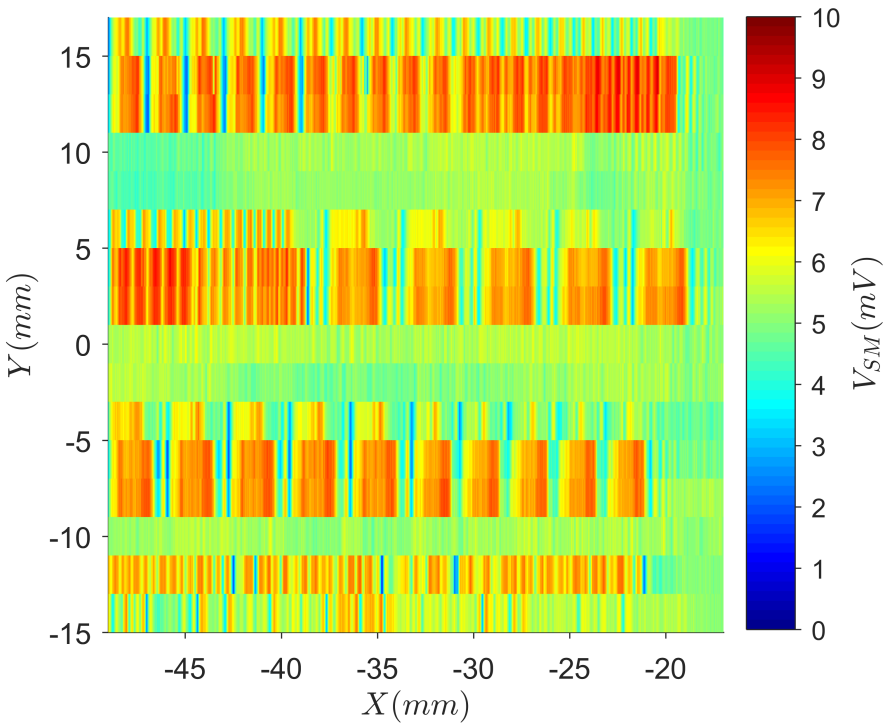

Figure 4.11: THz magnitude image from SFI of the resolution target shown in 4.10. 881×17 pixels ($X \times Y$)

pixel size along X and Y directions is reflected in the THz image, creating a shadow effect of the signal along Y, as can be seen from figure 4.11. Using this image the modulation transfer function (MTF) [120] has been measured in order to estimate the resolution limit of our far-field imaging system. The MTF evaluation considers how an original square wave (in this case the gold bars) is transferred to an image through an imaging system. By one definition the resolution limit is when the MTF falls below 20 %. Equation 4.3 defines the square wave MTF [120].

$$MTF = \frac{V_{Max} - V_{Min}}{V_{Max} + V_{Min}}, \tag{4.3}$$

where V_{Max} and V_{Min} are respectively the maximum and minimum V_{SM} extracted from figure 4.11 for each single bar. All the MTF values were averaged for the group of bars and normalized to the MTF obtained by the absolute max and min of V_{SM} extracted

from all the gold bars, following equation 4.4.

$$MTF_{absolute} = \frac{V_{absolute,max} - V_{absolute,min}}{V_{absolute,max} + V_{absolute,min}}. \tag{4.4}$$

The voltage signal used for the calculation of the MTF was extracted from the line profile at fixed Y positions through the centre of the gold bars; Y = 13mm, 3mm, -7mm respectively.

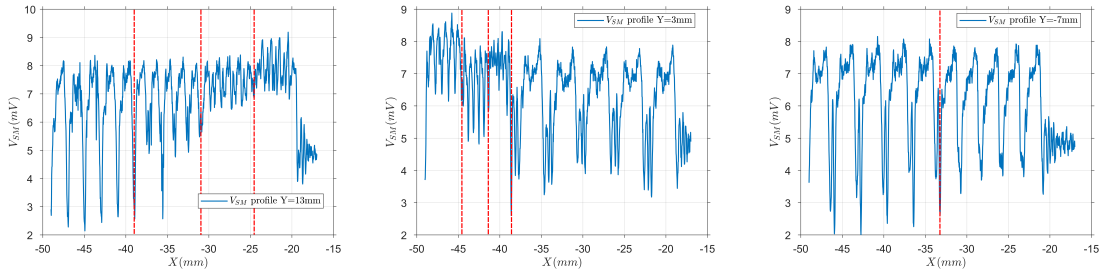

(a) (b) (c)

Figure 4.12: Profile of swept-frequency SM signal magnitude of (a) Top Y = 13mm, (b) Middle Y = 3mm and (c) Bottom Y = -7mm of the gold bars extracted from figure 4.11

Figure 4.12 shows the signal profiles extracted from the gold bars in figure 4.11. As an example, figure 4.12(c) shows data from two group of bars separated by a dashed red line; the bars on the left of the red line have size of 1.5 mm and give a signal size V_{Max}-V_{Min} ∼ 6 mV, while the bars on the right have size of 1.3 mm and give a signal size of V_{Max}-V_{Min} ∼ 4.5 mV. From these profiles, the MTF was calculated using equation 4.3 normalized to equation 4.4 for each group of gold bars and plotted against the spatial frequency expressed in mm^{-1}, which corresponds, for a single group, to the number of gold bars divided by their occupied space [3, 120].

Figure 4.13 shows the measured square wave MTF for our imaging system. The error bars correspond to the propagation of the standard deviation of the averaged MTF after normalization, for each group of 5 gold bars. Taking account of this experimental error, the spatial frequency at which the MTF falls totally below 20 % is ∼2.5 mm^{-1}. This value is equivalent to 200 μm wide gold bars spaced 200 μm from each other. For the far-field imaging approach used here, in which the sample is scanned through the beam focus, the resolution is limited by the beam spot size, which is a function of the lasing frequency and

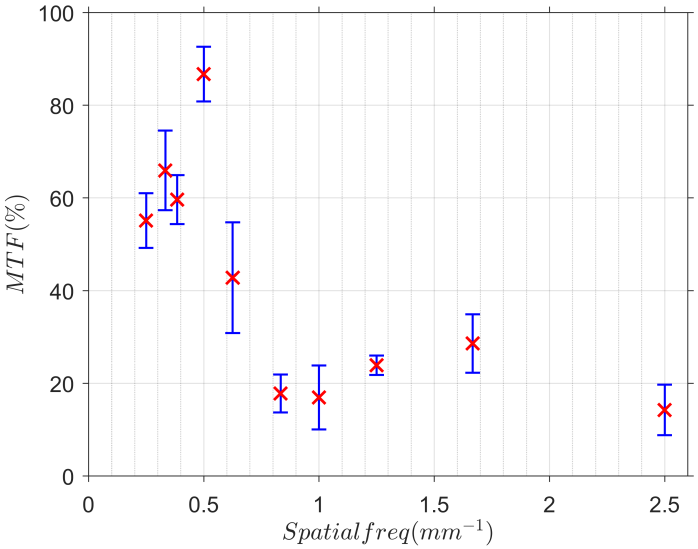

Figure 4.13: Measurements of the modulation transfer function (MTF) of our imaging setup, with error bars.

the diffraction limit of the optical system [205]. The lasing frequency used for this work is f$\sim$3.4 THz, which corresponds to a wavelength $\lambda \sim 88\,\mu$m. For a perfect Gaussian beam profile focused by a lens with f-number $f/1$, at a wavelength $\lambda = 88\ \mu$m (f$\sim$3.4 THz), the diffraction-limited beam waist has been calculated to be 56 μm [11]. This discrepancy can be explained by noting that the beam profile emitted from THz QCL devices is typically irregular [207, 208]. Indeed the measured resolution limit of 200 μm of resolution limit is a valid value and consistent with that reported elsewhere [3, 11, 13, 116, 120, 204, 205].

4.3.2 Signal-to-noise ratio SNR for imaging silicon wafers

Another important parameter to take account of in an imaging system is the signal-to-noise ratio. The general definition of the imaging SNR is the ratio between mean and standard deviation of a SM signal, recorded over a flat part of a specific image, at the maximum of a fringe [11, 14, 206]:

$$SNR = \frac{\overline{V_{SM}}}{\sigma_{V_{SM}}} \tag{4.5}$$

In this work SNR has been evaluated for the 2 different approaches used for imaging silicon wafer containing surface inclusions. The values of SNR shown in this section are intended only to represent and compare the SNR achievable when imaging silicon wafers with THz radiation. Indeed, considering that part of the radiation is transmitted through the silicon wafers and only a small fraction of it is reflected, the values yielded by the SNR calculation cannot be compared with the SNR calculated by imaging a metallic sample as in [14], where the metal is reflecting back into the laser cavity a higher fraction of radiation. A much lower level of SNR is expected for the silicon wafers because of the lower SM signal. In this study the SNR has been evaluated as follows. For the mechanical modulation scheme, the SNR has been measured for different integration times, T_C, of the lock-in amplifier by recording 1000 times the V_{SM} measured for a single pixel with the chopper kept at a fixed modulation frequency f_{Mod} = 120 Hz. For the swept-frequency approach, keeping the modulation frequency at f_{Mod} = 1 kHz the SNR has been measured for different amounts of waveform averaging, repeating this measurements 100 times (the $N_{measurements}$) on a single pixel.

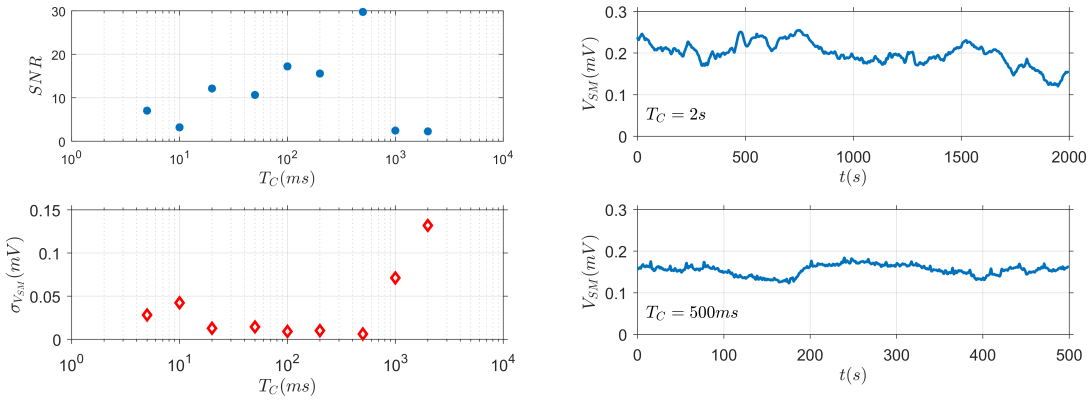

(a) (b)

Figure 4.14: (a) Top, SNR measured by recording 1000 times V_{SM} on a single pixel through the mechanical modulation approach, for different lock-in integration times T_C. Bottom, the noise represented by the standard deviation σ of V_{SM} (see equation 4.5). (b) V_{SM} as function of time recorded for T_C = 2s, on the top and T_C = 500 ms on the bottom. The sample was the silicon wafer shown in figure 4.22(a).

Figure 4.14(a) shows the SNR and the noise (represented by $\sigma_{V_{SM}}$) as function of T_C

obtained by the mechanical modulation approach. Figure 4.14(b) shows, as examples, the 1000 measurements of V_{SM} recorded for the highest SNR, $T_C = 500$ ms and the lowest, $T_C = 2$ s. The SNR is strictly influenced by $\sigma_{V_{SM}}$. The noise can be caused by laser voltage fluctuations, which can be reduced with averaging, and also by frequency instability of the laser caused by thermal drift for acquisitions over a time-scale of seconds [116]. Thermal drift can cause frequency changes in the order of several MHz, which in turn degrade the SNR for long acquisition time, as shown in figure 4.14(a) for $T_C > 1$s. It's worth noting that the SM signal amplitude, and hence SNR, is also extremely sensitive to the efficiency with which radiation is coupled back into the laser cavity, which will depend upon the exact alignment and curvature of the silicon wafer in each case, as well as the portion of radiation reflected and transmitted through the wafer. As expected the maximum SNR value with mechanical modulation obtained in this study is ~ 10 times lower than the maximum value found in [14] because only a small fraction of the THz beam is reflected. In fact, for example, the signal level in figure 4.14(b) is only $\sim 200\mu$V. However higher SNR means higher image quality, but this is often translated in long acquisition times. For example, in the mechanical modulation approach the highest SNR (SNR $\sim$ 30) is achieved for $T_C = 500$ ms. V_{SM} was measured 1000 times, leading to a total elapsed time for this measurement of $t_{pixel} = 5$ s. Hence it's clear that a good trade-off between T_C and desired image quality has to be chosen prior to the image acquisition. An example of the effect of T_C on the acquired image is shown in figure 4.15, which shows the THz image of a silicon wafer inclusion obtained for integration times of 10, 20, 50 and 500ms measuring V_{SM} only one time each pixel.

Despite the highest SNR being recorded at T_C= 500ms, figure 4.15 shows that T_C as small as 20ms is sufficient to extract sensible information out of the image. This value corresponds to an SNR ~ 10. By considering a number of pixels $40 \times 50 = 2000$ and excluding the computational time, the total elapsed time to acquire the figure with T_C= 20ms can be quantified to be ~ 40 seconds, but this represents a 2D image of the sample. A 3D image requires the scan of the sample also in the Z direction at each X-Y position, effectively increasing the total elapsed time [13]. On the other hand, the swept-frequency

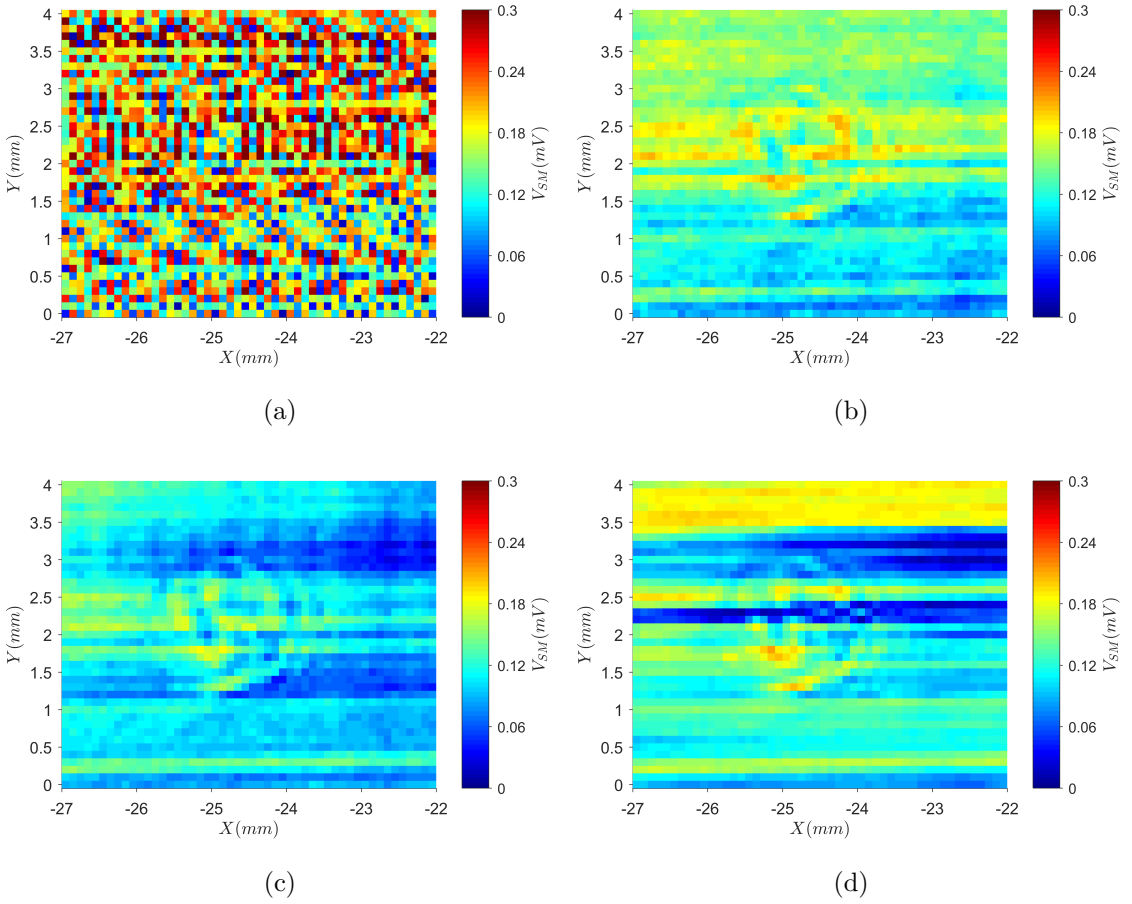

Figure 4.15: SM THz image of an impurity embedded in a silicon wafer, taken through mechanical approach for different lock-in T_C. respectively (a) 10ms, (b) 20ms, (c) 50ms, (d) 500ms. 40×50 pixels, 100 μm pixel size.

approach has the ability to acquire a 3D image by sweeping the QCL lasing frequency. The SNR measured as function of the number of waveform averages per pixel, N, for the swept-frequency approach is shown in figure 4.16(a). As already shown in the section 4.2, the magnitude and the phase values obtained through SFI are resolved by the complex FFT performed on the waveform recorded by a saw-tooth modulation superimposed on the laser voltage, which causes the lasing frequency to chirp (see figure 4.7 and 4.8).

As examples, in figure 4.16(b) the magnitude of the waveform V_{SM} recorded at the highest, N = 50, and the lowest, N = 1000, SNR are shown. In figure 4.16(a) also the noise, represented by the standard deviations, of the magnitude and the phase resolved by the complex

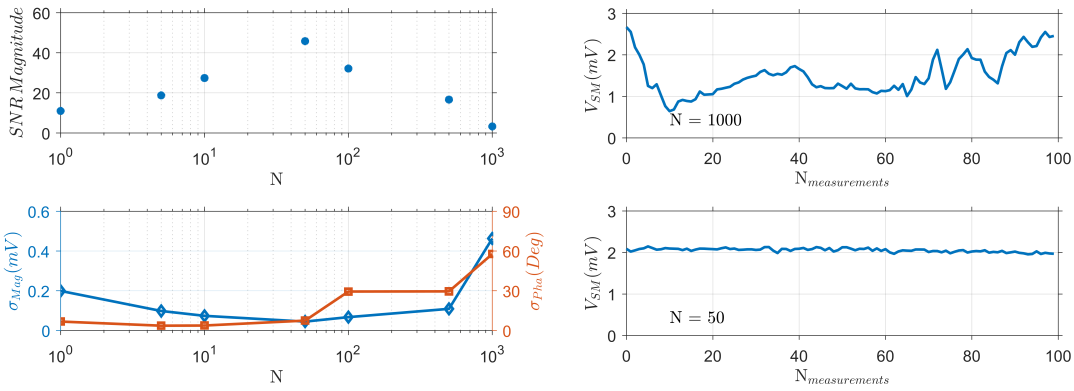

(a) (b)

Figure 4.16: (a) Top, SNR of the magnitude of the waveform measured through SFI by recording 100 times the waveform on a single pixel, for different N. Bottom, the noise represented by the standard deviation σ of the magnitude (left axis) and the phase (right axis) of the waveform measured through SFI. (b) V_{SM} as function of the number of measurements for N = 1000 on the top and N = 50 on the bottom. The sample was the silicon wafer shown in figure 4.22(a).

FFT performed on the waveform are shown. The SNR is influenced by voltage noise of SM waveforms, which is reduced by increasing the number of averages, but for long acquisition time the lasing frequency is affected by the thermal and current fluctuations that increase the standard deviations of both magnitude and phase of the waveform. Although the SNR obtained through the swept-frequency approach is also $\sim$10 times lower than the SNR obtained through mechanical modulation in the case of reflection from a metallic target [14], figure 4.16(a) demonstrates a higher SNR than the mechanical approach when the comparison is made using the same target. It has been already demonstrated that for N=1, the lowest acquisition time per pixel was found to be 259 ms with f_{Mod}=1kHz [14]; excluding the computational time, this corresponds to an acquisition $\sim$10 times slower than the mechanical approach with T_C = 20ms (see figure 4.15(b)). Nevertheless, it should be stressed that, the swept-frequency approach offers the capacity of reconstructing a 3D image of the sample with a high-depth resolution. Moreover it presents advantages in terms of the experimental set-up because it does not need stages capable of movement in the Z directions and does not require the use of a mechanical chopper, practically reducing the hardware needed. Furthermore by replacing the digital acquisition board with a faster

DAQ, the speed of SFI to record images can be drastically increased by using a higher f_{Mod}, such as 100 kHz.

4.4 Imaging Silicon Wafers for photovoltaic applications

Silicon is one of the technologically most important materials today. Its production, from the crystalline silicon ingot to the subsequent slicing into silicon wafers, requires a high grade of purity and therefore good quality control is highly desirable [30, 209, 210]. Consequently the imaging of silicon wafers can be an essential part of the wafer production process securing the quality of this delicate product. Current technologies, based on optical (at λ=193nm) or e-beam inspection, are bulky and slow [211, 212]. The imaging approach based on self-mixing in a THz-QCL has been used to acquire images of two kinds of silicon wafers relevant to the manufacture of photovoltaic cells; an unprocessed multicrystalline silicon wafer with thickness $\sim$250μm and a processed photovoltaic cell with thickness $\sim$700μm, each with a lateral dimension of 15.6 cm^2. Depending on the situation, both mechanical modulation and SFI were used to acquire the images exploiting the set-up shown in the section 4.2 (see figure 4.6).

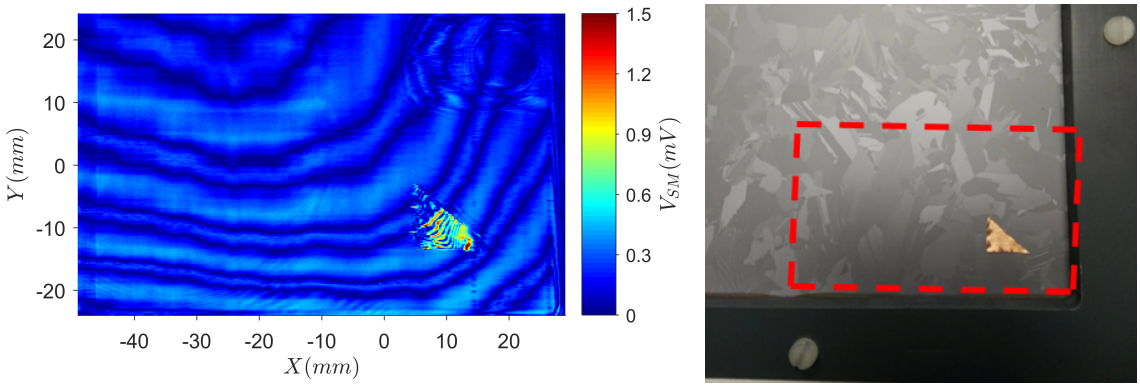

(a) (b)

Figure 4.17: (a) 2D THz image of unprocessed multicrystalline silicon wafer, 390 × 240 pixels ($X \times Y$), pixel size 200 μm. (b) A picture from a camera of the same wafer. The red rectangle highlights the SM scan zone

Figure 4.17(a) and 4.17(b) show, respectively, a THz image of the silicon wafer, acquired through mechanical modulation with T_C=20ms, and the corresponding picture taken from

a visible camera, with the red rectangle highlighting the THz scan area. This image was acquired in $\sim$ 31 minutes. The triangular piece of copper was used as a reference point and provides a stronger reflection than the silicon, since a fraction of the THz beam incident on the wafer surface is transmitted through the silicon. In this reflection image it can be seen that the THz image does not resolve grains and grain boundaries visible to the naked eye. The fringes visible in the THz image arise from the tilt and imperfect flatness of the wafer; each fringe represents a change in the external cavity length of $\lambda/2$. In fact, the top-right part of the THz image shows some circular fringes caused by some residual tension in the wafer, which could be created by the wafer holder seal pressing, in proximity of the scanning area, on the wafer surface.

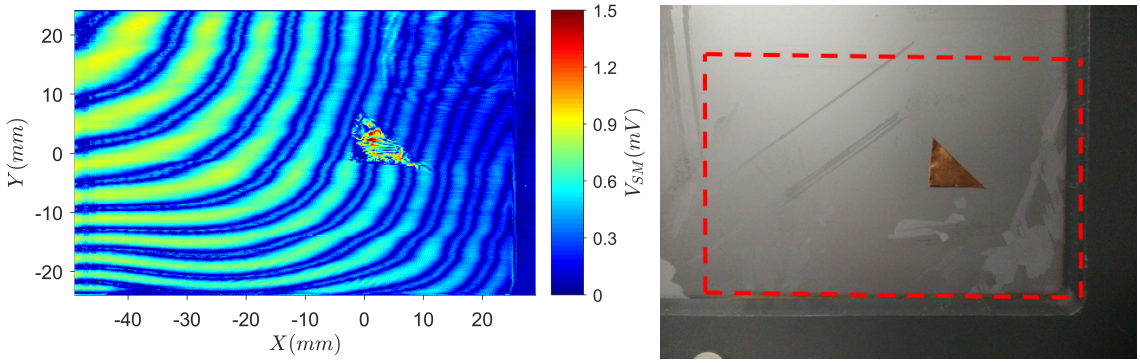

(a) (b)

Figure 4.18: (a) 2D THz image of a second unprocessed multicrystalline silicon wafer, 390×240 pixels ($X \times Y$), pixel size 200 μm. (b) A picture from a camera of the same wafer. The red rectangle highlights the SM scan zone

Similar results were obtained from a second unprocessed wafer, shown in Figure 4.18(a), which was acquired through mechanical modulation with T_C=20ms. Again, in this case the THz image does not resolve grains and grain boundaries and the fringes arise from tilt and imperfect flatness of the sample. In the top right corner, residual tension created by the seal warping the surface of the wafer can again be seen. Presumably, the grains cannot be resolved in the THz image because they have same refractive index in the THz region.

Figures 4.19(a) and 4.20(a) show the THz images acquired from the front and the reverse

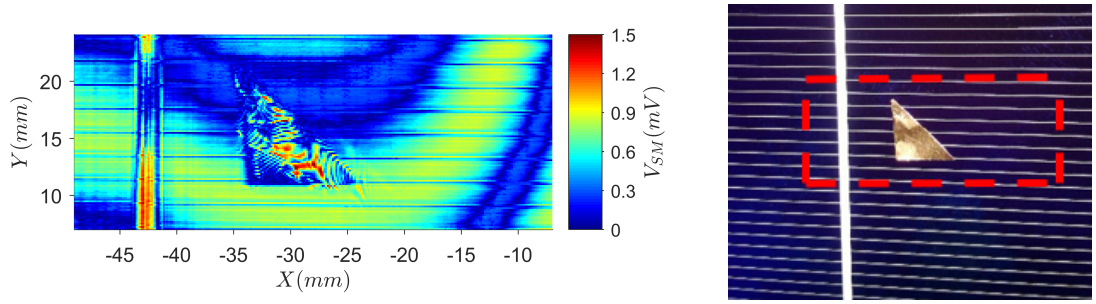

(a) (b)

Figure 4.19: (a) 2D THz image of a processed silicon wafer, 280×114 pixels ($X \times Y$), pixel size 150 μm.(b) A picture from a camera of the same wafer. The red rectangle highlights the SM scan zone

surface of the processed photovoltaic wafer, acquired through mechanical modulation with T_C=20ms. Here the coating on the front surface reflects the THz radiation, such that the SM signal obtained from the wafer surface is comparable with that obtained from the copper triangle. Fringes arising from the tilt and imperfect flatness of the wafer are again visible in these images.

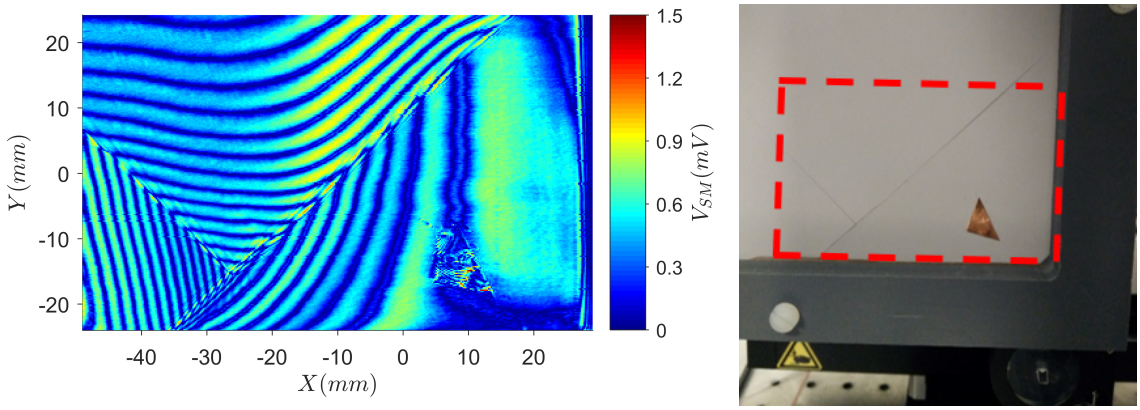

(a) (b)

Figure 4.20: (a) 2D THz image of the back of a processed silicon wafer, 390×240 pixels ($X \times Y$), pixel size 200 μm. (b) A picture from a camera of the same wafer. The red rectangle highlights the SM scan zone

Crucially, this high sensitivity to the morphology of the wafer surface allows the presence of cracks to be readily identified. This is demonstrated in Figure 4.20(a) (obtained through mechanical modulation with T_C=20ms), which clearly shows discontinuities in the fringes caused by two cracks in the wafer, which are also apparent on the corresponding visible

image shown in Figure 4.20(b).

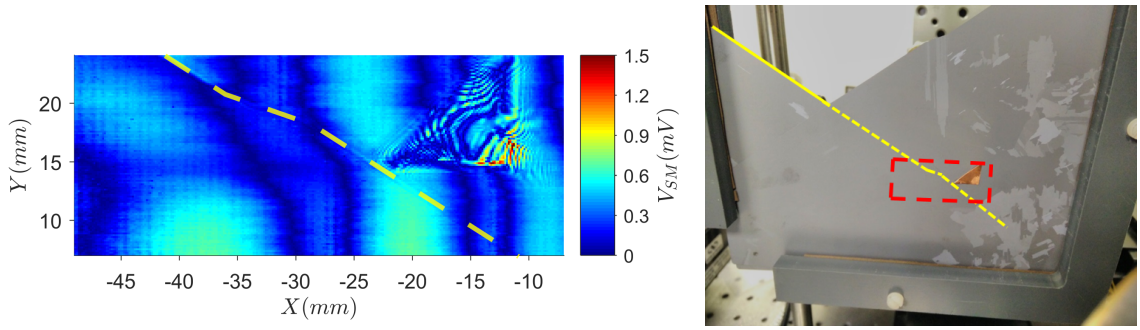

(a) (b)

Figure 4.21: (a) 2D THz image of 2 overlaid unprocessed silicon wafer, 280×114 pixels ($X \times Y$), pixel size 150 μm, obtained through mechanical modulation with T_C=20ms. (b) A picture from a camera of the same wafer. The red rectangle highlights the SM scan zone, the solid yellow line shows the visible wafer edge, the dashed yellow line shows the not visible edge placed behind the front one

The absorption of Silicon in the THz regime is well known from literature and has been extensively studied also for different doping concentrations, for both n- and p-type material [213–215]. Considering the low absorption of silicon around ~3.4 THz it is also possible using our technique to observe contrast arising from individual wafers when stacked together. By stacking 2 unprocessed silicon wafers as shown in Figure 4.21(b), the THz image (shown in Figure 4.21(a)) can resolve the edge of the second wafer placed behind the first one. The edge appears as a feature and also causes discontinuities in the fringes.

4.4.1 Imaging silicon wafers with impurities

The study of surface contaminations and impurities of silicon wafers has always been essential in integrated circuits manufacturing because contaminations can strongly modify and affect electronic and optical properties of semiconductors [216–222]. Moreover in the production of solar grade silicon such impurities are one of the major factors affecting the degradation of solar energy conversion efficiency [30]. Often the impurities present in a silicon ingot depends on the method of ingot fabrication.

Table 4.1 shows the maximum concentration of chemical impurities permitted in a silicon

Element	ppm	at/cm^3
O	1	5E16
C	1	5E16
B	0.5	2.5E16
P	0.025	1.25E15
As	0.025	1.25E15
Fe, Al, Cr, Ni, Ti, Mo, V, Cu, Zn	Summed max 0.1	5E15
Concentration of each not mentioned metal		<5E13

Table 4.1: Maximum level of chemical impurities present in a multicrystalline solar cell. Adapted from A. Muller [30]

ingot in order to achieve the desired level of solar conversion efficiency in a multicrystalline solar cell. In particular, a low level of transition metals is crucial. As such, a fast and high-resolution imaging system able to discriminate silicon wafers containing contaminations can be a useful toll for the screening of silicon wafers sliced from an ingot. Given the fast acquisition speeds that can be achieved through the self-mixing effect in a THz QCL, an imaging system based on this technique is well-suited for this purpose. Furthermore, due to its compact size, and because THz radiation is non-ionizing and hence safe for humans, such a system can readily be integrated in a wafer production chain. To demonstrate this capability images were acquired of an unprocessed polycrystalline silicon wafer containing an unknown impurity.

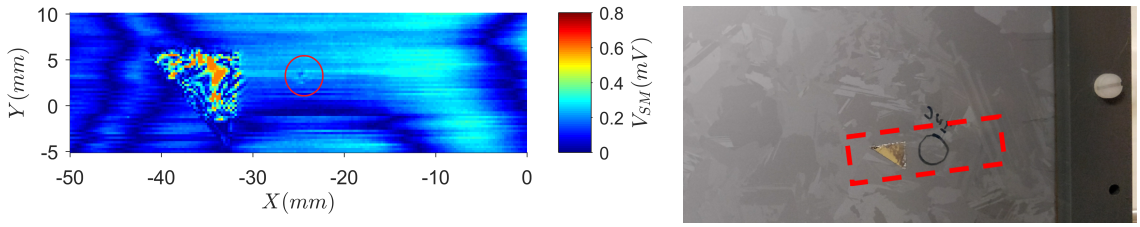

(a) (b)

Figure 4.22: (a) 2D THz image of unprocessed silicon wafer with an impurity embedded on the surface, highlighted by the red circle. 200×62 pixels ($X \times Y$), pixel size 250 μm. (b) A picture from a camera of the same wafer. The red rectangle highlights the SM scan zone.

Figure 4.22(a) shows a THz image, obtained through mechanical modulation with a T_C=50ms, of an unprocessed silicon wafer containing an impurity, which is invisible to the naked eye.

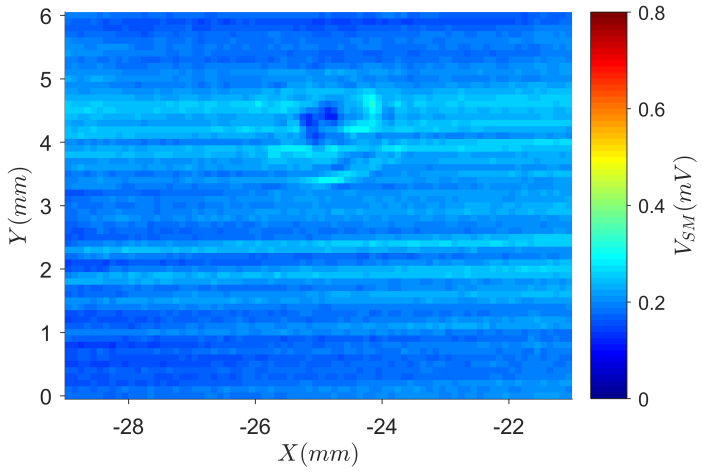

Figure 4.23: 2D THz image of the impurity embedded on the silicon surface. 80×60 pixels ($X \times Y$), pixel size 100 μm. Obtained through mechanical modulation with a T_C=50ms.

Figure 4.23 shows a zoomed-in THz image of the impurity shown in figure 4.22(a). The impurity has a direct effect on the surface structure of the wafer; the circular fringes suggest that the impurity is deforming the surface, creating residual tension, in a similar manner to the fringes created by the seal of the wafer holder shown in Figure 4.17(a) and 4.18(a). This effect is also visible in the images obtained through the swept-frequency approach, as shown in figure 4.24(a) and 4.24(b). Here the circular fringes are visible both in the magnitude and phase image. Due to the sensitivity to changes in surface morphology, the phase image, in particular, suggest that the impurity is bending the wafer surface, maybe to accommodate the contaminant.

In order to gain a better understanding of the impurity, figure 4.25(a) and 4.25(b) show the averaged self-mixing magnitude plotted along the X and Y directions, obtained between $Y = 1.5mm$ and $Y = 2.1mm$ and $X = -25.3mm$ and $X = -24.7mm$, respectively. Also shown, in figure 4.26(a) and 4.26(b), are the phase profiles plotted in the same range of X and Y. The magnitude images show a small decrease in signal, which can be attributed to a different reflectivity of the impurity with respect to the silicon wafer. Considering the different kind of contaminants, summarised in table 4.1, a metal can be excluded because

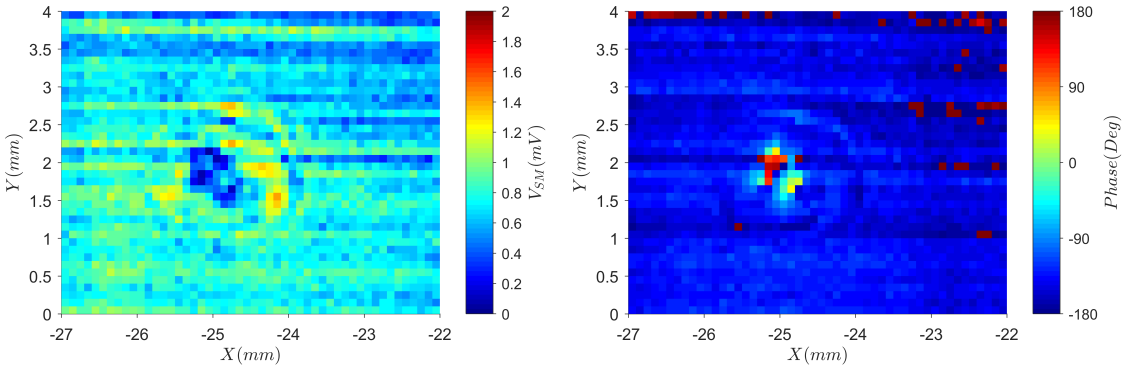

(a) (b)

Figure 4.24: (a) Magnitude and (b) Phase THz image of unprocessed silicon wafer with an impurity embedded on the surface taken through swept-frequency approach. 50×40 pixels ($X \times Y$), pixel size 100 μm.

that would have a higher reflectivity, resulting in a higher signal magnitude. However, discriminating between the other (non-metallic) impurities using this technique alone is difficult, and spectroscopic analysis might be needed to identify the kind of contaminant. On the other hand the phase profiles show a phase change of $\sim \pi$ ($\sim 180°$) between the impurity and the wafer surface. As already mentioned in Section 4.1, the depth resolution achieved in a similar system using the swept-frequency approach with a THz QCL has been estimated to be $\sim 0.1\mu m$. By considering that a change in phase is attributable to a change in external cavity length, and using a lasing wavelength of $\sim 87\mu m$ ($\sim 3.45THz$) in equation 4.1, it is possible to estimate that the impurity has deformed the wafer surface by $\sim 22\mu m$. This result is based on the assumption that the phase change on reflection at the silicon and the impurity is equal. But the materials can be different, with different permittivity, hence some of the measured phase change might be due to the different permittivity rather than different depth. Moreover another possibility might be that the impurity is $\sim 22\mu m$ below the surface.

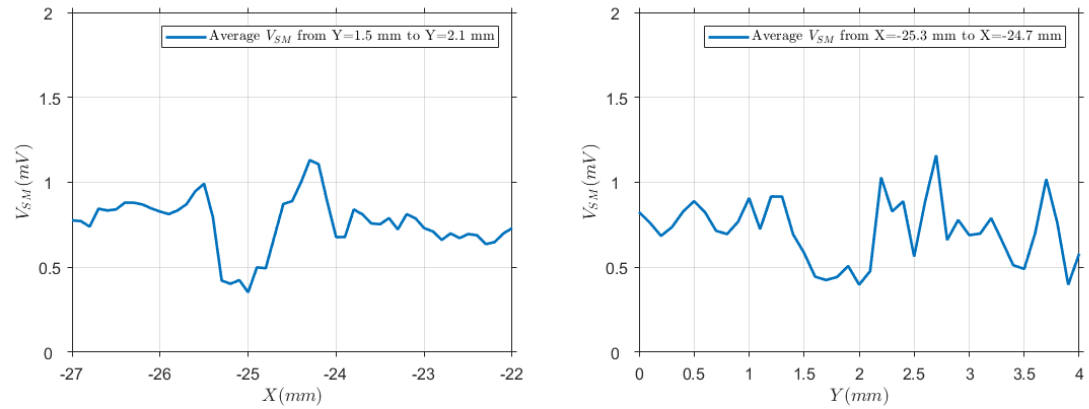

(a) (b)

Figure 4.25: (a) Averaged magnitude along X profile between $Y = 1.5mm$ and $Y = 2.1mm$. (b) Averaged magnitude along Y profile between $X = -25.3mm$ and $X = -24.7mm$. Data taken from figure 4.24(a).

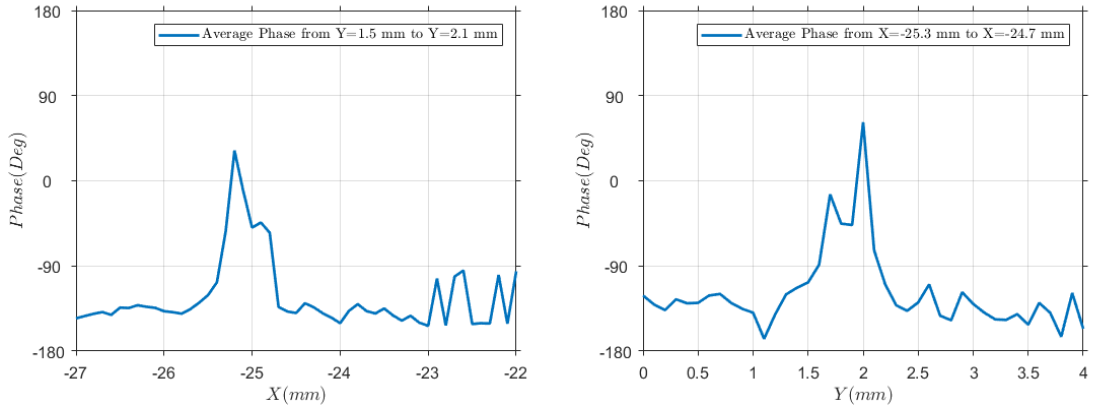

(a) (b)

Figure 4.26: (a) Averaged phase along X profile between $Y = 1.5mm$ and $Y = 2.1mm$. (b) Averaged phase along Y profile between $X = -25.3mm$ and $X = -24.7mm$. Data taken from figure 4.24(b).

4.4.2 Silicon Wafers in Transmission

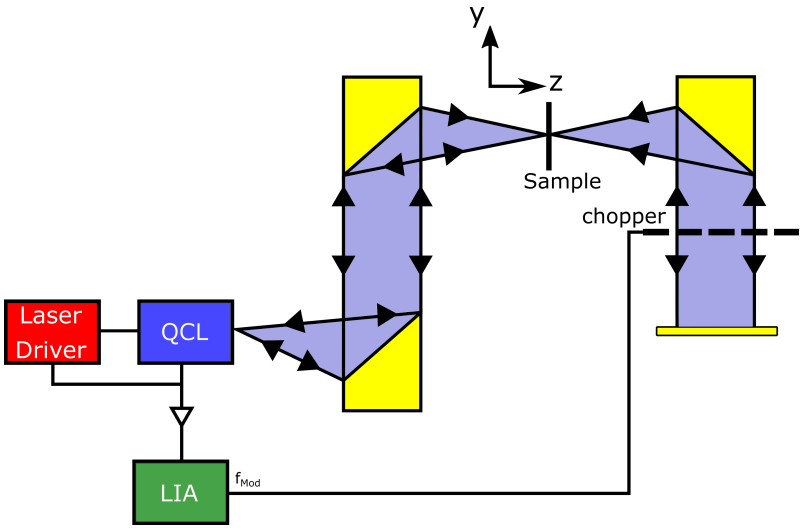

Figure 4.27: Experimental set-up for SM imaging in transmission in a THz QCL. LIA, lock-in amplifier.

Since a fraction of the THz beam is transmitted through the unprocessed wafer, it is also possible to record images using this transmitted component. Samples like the silicon wafers have low transmission but a weak reflection, therefore a larger signal is expected using a transmission geometry. This can be, in principle, translated in a image acquisition in transmission faster than in reflection. To demonstrate this new imaging modality, the system was subsequently modified as shown in figure 4.27. In addition to the original system configuration (Figure 4.6(a)) a second parabolic mirror was added on the reverse side of the sample. This parabolic mirror projects the transmitted beam onto a planar mirror which reflects the beam back to the QCL. In this way the beam undertakes a double-pass through the sample. The mechanical chopper was placed behind the sample along the transmitted beam path such that lock-in detection of the SM voltage at the chopper reference frequency allowed only the radiation transmitted through the sample to be resolved.

Figure 4.28(a) gives a demonstration of the THz imaging in a transmission geometry. In this case, since the processed photovoltaic wafer is covered by a reflective coating, as already shown in Figure 4.19(a), the transmitted THz signal is negligible. This allows to

understand how the reflected beam affects the image data acquired in transmission.

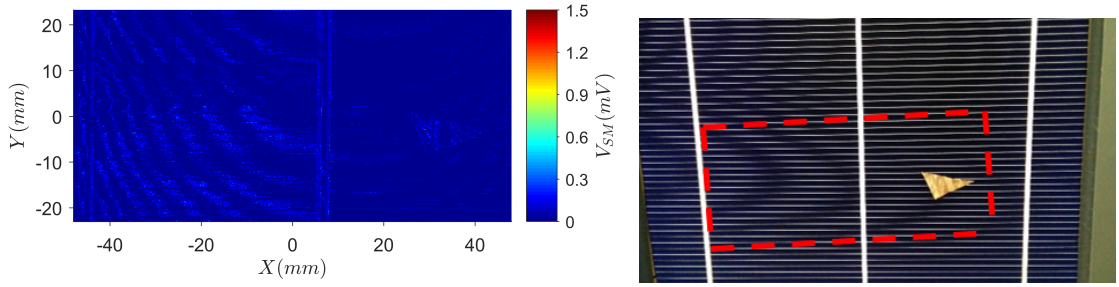

(a) (b)

Figure 4.28: (a) 2D THz image in transmission of a processed silicon wafer, 384×184 pixels ($X \times Y$), pixel size 250 μm, obtained with T_C=20ms. (b) A picture from a camera of the same wafer. The red rectangle highlights the SM scan zone.

The small signal that is visible in Figure 4.28(a), must originate from a small portion of THz radiation reflected from the surface of the photovoltaic wafer, which is re-injected into the laser cavity, despite using a lock-in detection and with the chopper being placed behind (with respect to the beam path) the sample. The scan of the sample gives a time-varying SM signal. A component of this signal must fall within the lock-in detection bandwidth and is therefore recorded by the LIA. In order to remove this effect, the sample should be tilted. This information is crucial to understand the limitation of the lock-in detection scheme, and how the tilt of the sample must be considered in the acquisition of the transmitted signal.

Referring to Figure 4.29, the maximum signal reflected from the sample is obtained when the sample surface is exactly at an angle $\theta = 90°$ with respect to the beam direction, because all the radiation reflected from the sample surface can be re-injected into the laser cavity. Following this idea, in the case of the transmission scheme shown in Figure 4.27, the maximum signal (transmitted + reflected) can be achieved when both sample surface and flat mirror are exactly at an angle θ_1 and $\theta_2 = 90°$ with respect to the beam direction. But in this scenario, the system cannot discriminate fully between reflected and transmitted signals because both of them are re-injected into the laser cavity. Nevertheless, by adding a small tilt only to the sample surface, such that $\theta_1 \neq 90°$, part of the beam reflected from the sample can be discriminated against since it is not be able to re-enter the

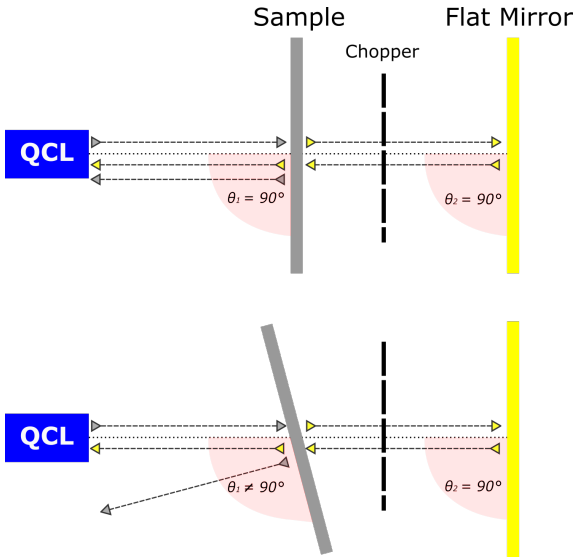

Figure 4.29: A simplified scheme to explain the effect of tilting the sample in SM transmission geometry. Grey arrows are the reflected THz beam, yellow arrows the transmitted beam.

laser cavity, allowing only the transmitted signal to be measured through the self-mixing effect. A simplified scheme of this effect is shown in Figure 4.29.

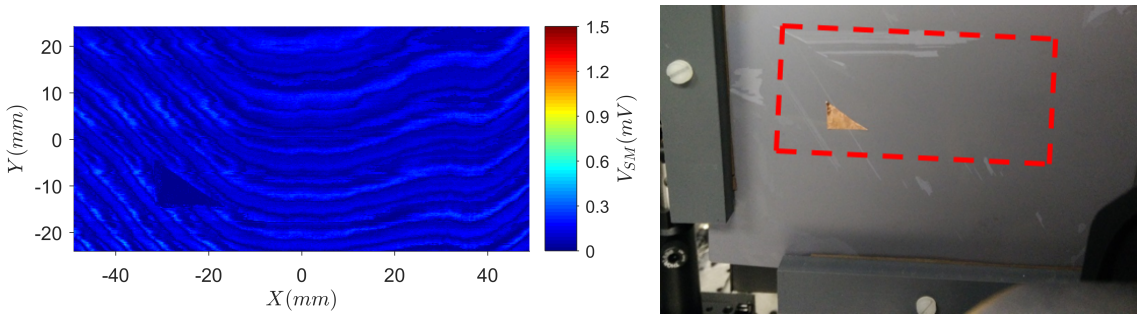

(a) (b)

Figure 4.30: (a) 2D THz image in transmission of unprocessed silicon wafer, 392 × 192 pixels ($X \times Y$), pixel size 250 μm, obtained with T_C=50ms. (b) A picture from a camera of the same wafer. The red rectangle highlights the SM scan zone.

Figure 4.30(a) shows a THz image of the unprocessed silicon wafer obtained using this transmission geometry. This example clearly demonstrates that only the SM signal arising from the transmitted radiation has been acquired; the signal corresponding to the position of the copper reference triangle is now comparable to $V_{SM} = 0$ V. This THz image and the THz image shown figure 4.23 allow a simple comparison between reflected and transmitted

SM signal, by averaging V_{SM} of all the pixels composing the images. Figure 4.23 shows an average reflected signal of V_{SM} ≈200μV, while figure 4.30(a) has an average transmitted signal of V_{SM} ≈100μV. Roughly an equivalent amount of 50% of the reflected beam is transmitted through an unprocessed silicon wafer ∼250μm thick.

To further demonstrate the ability to image silicon wafers in this transmission geometry, three pieces of unprocessed wafer were arranged as shown in figure 4.31(a). Figure 4.31(b) clearly shows the capability of the transmission system to distinguish the edges of all three silicon wafers. The region with no sample present shows the strongest SM signal, because all the THz radiation is transmitted. As expected, the signal decreases when the beam is transmitted through the front wafer; and with the addition of a subsequent wafer the signal is further reduced down to the weakest signal, which is obtained when the THz beam is transmitted through all the three wafers.

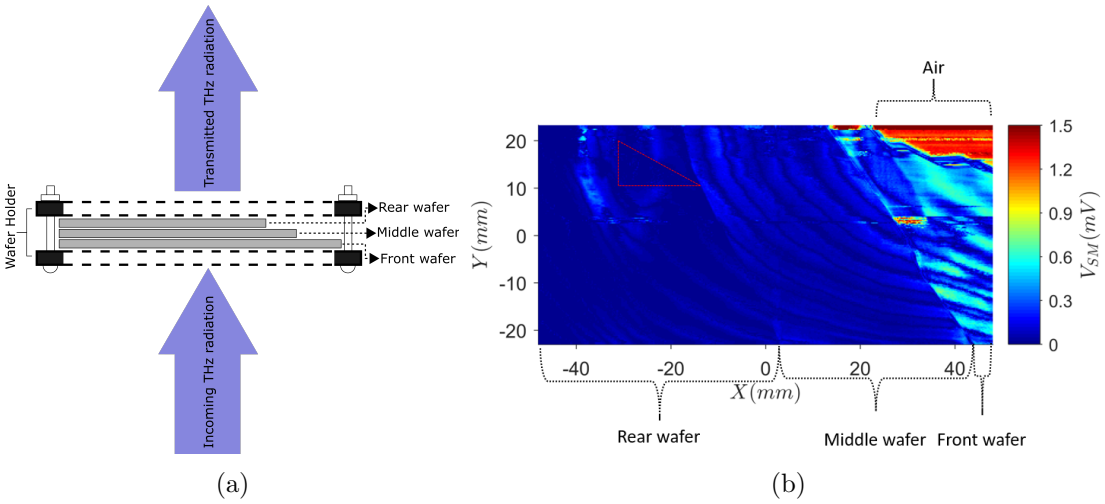

(a) (b)

Figure 4.31: (a) Top view schematic of the arrangement of the 3 wafers. (b) 2D THz transmission SM image of 3 stacked unprocessed silicon wafers. 384×184 pixels ($X \times Y$), pixel size 250 μm, obtained with T_C=20ms.

4.5 Imaging of Human Skin Tissue

The interest in THz imaging of biological samples has been growing considerably during the last decade thanks to the ability of THz radiation to provide information about materials not accessible through other parts of the electromagnetic spectrum. Polar molecules, like water, can strongly absorb THz radiation and this feature opens the possibility of studying the hydration level of skin tissues as well as skin affected by diseases such as melanoma [38, 170, 189–191, 193–196]. In this section THz imaging of healthy human skin tissue as well as skin containing melanoma will be demonstrated. The results shown in this section demonstrate that healthy skin can be distinguished from the skin containing melanoma. Furthermore the results are compared in order to provide more insight on the understanding of the THz response to the various layers of human skin.

4.5.1 Sample preparation and system calibration

All the samples (with and without melanoma) shown in this section were prepared following the same procedure described as follow. The sample was excavated from the patient at Leeds General Infirmary (LGI) teaching hospital. A piece of the sample was taken to be biopsied using the traditional medical techniques; within a few hours of the removal from the patient, the remaining part of the sample was wrapped in a gauze soaked in saline solution to prevent deterioration and placed in a sample jar to avoid drying out. At this stage, the sample was taken to the preparation laboratory and, using a scalpel, a measurement sample with dimensions approximately 20mm wide and 5mm thick, possibly containing different tissue types, was excised. In this part of the process an absorbent gauze was used to remove any excess (surface) liquid from the sample. In order to further remove any excess liquid, the sample was gently pressed between two further absorbent gauzes for approximately 30 minutes, until no obvious excess liquid was visible. The sample was then mounted in a cylindrical sample holder; the holder consisted of a quartz window on the top and a rear plastic window, between which the tissue sample was secured using a clamping screw. In order to absorb any excess liquid that might leave the sample during

the long experimental time, a piece of absorbent gauze was also placed between the sample and the rear plastic window as shown in figure 4.32.

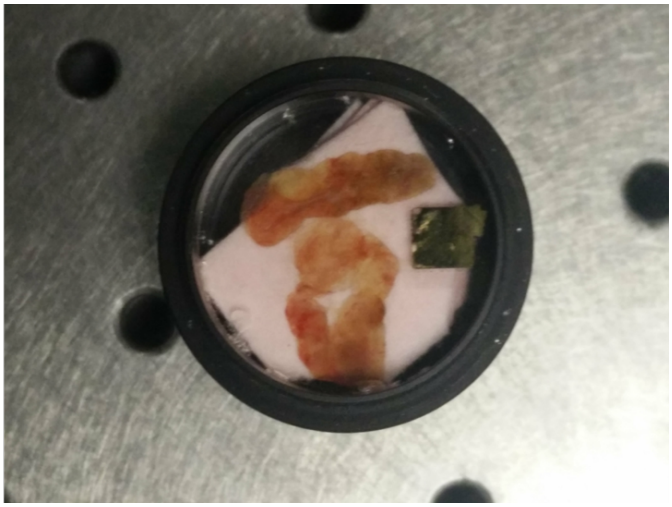

Figure 4.32: Camera photos of a benign skin sample used to calibrate the SM imaging system.

In some of the images shown in this section, a square of gold had been evaporated onto the quartz window and was used as a reference during the system alignment to remove any tilt of the sample with respect to the THz beam direction. Adjustment of the sample tilt and system calibration were carried out by acquiring preliminary images of a healthy skin tissue sample. As shown in figure 4.32 the visible image suggests that this sample contains only subcutaneous fat with no clear evidence of other skin layers.

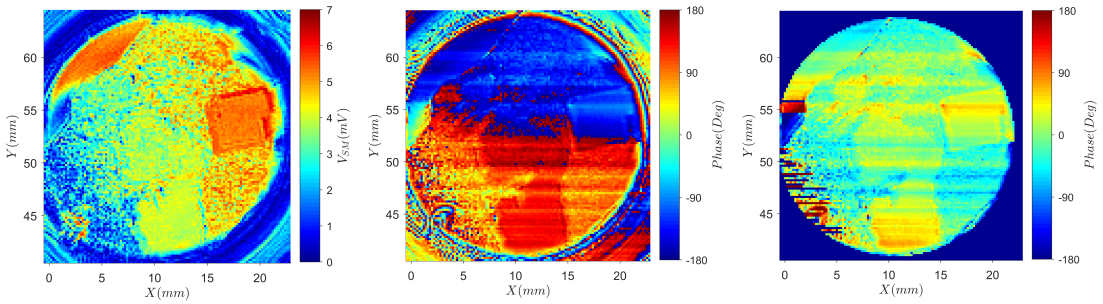

(a) (b) (c)

Figure 4.33: (a) Magnitude, (b) wrapped and (c) unwrapped phase of a benign skin sample, shown in figure 4.32, taken with THz-QCL SFI. 117×120 pixels ($X \times Y$), pixel size 200 μm.

Figure 4.33(a), 4.33(b) and 4.33(c) show, respectively, the THz magnitude, the raw phase and the unwrapped phase images of the sample shown in figure 4.32 obtained through SFI. As mentioned in the Section 4.2, in order to obtain the real phase images of this sample phase unwrapping of the images is necessary in post-processing to overcome the phase discontinuities [14]. The images confirm that the system is properly aligned and calibrated to provide good spatial resolution and to allow magnitude and phase to be extracted.

4.5.2 Healthy human skin

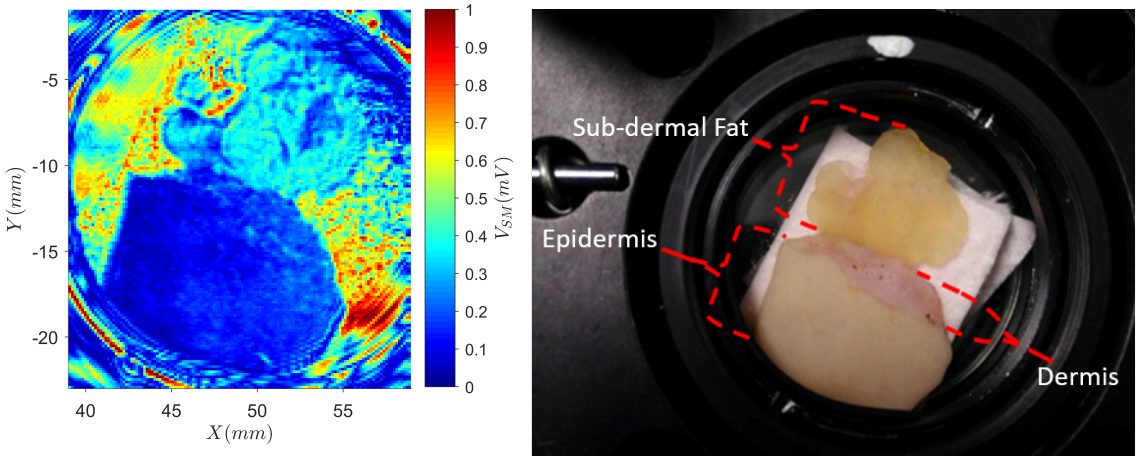

(a) (b)

Figure 4.34: (a) 2D THz image of a human skin tissue, acquired using the mechanical modulation approach with T_C=20ms. 133×147 pixels ($X \times Y$), pixel size 150 μm. (b) A picture from a camera specifying the different skin layers.

Figure 4.34(a) shows the THz image of a human skin sample acquired using the mechanical modulation approach. The comparison between the THz and the visible image demonstrates clear contrast in the THz image between the three skin layers shown in figure 4.34(b). In the THz image magnitude and phase are not separated by mixed together. In order to extract both magnitude and phase information, a swept-frequency image of the same sample was acquired.

Figure 4.35(a) shows the magnitude image obtained from this sample. Again, comparison with figure 4.34(b) shows clear contrast between different skin layers can be resolved using

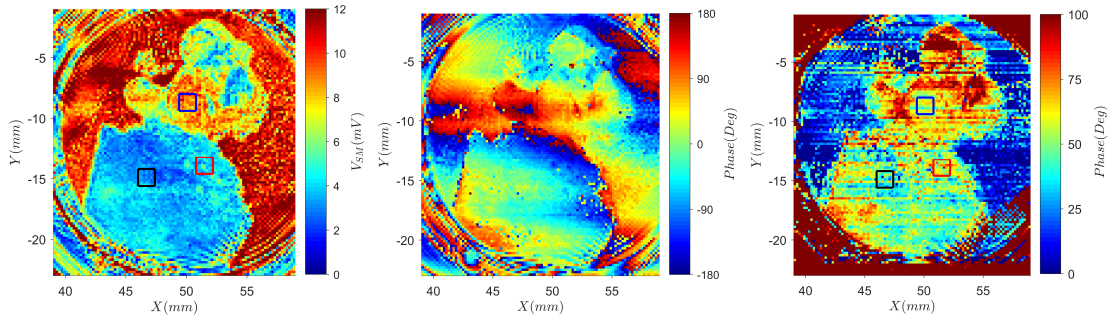

(a) (b) (c)

Figure 4.35: (a) Magnitude, (b) Raw and (c) Unwrapped phase of a human skin sample taken with THz-QCL SFI. The coloured squares select the pixels used for the analysis. 100×110 pixels ($X \times Y$), pixel size 200 μm.

this technique. Indeed it is possible to distinguish between the epidermis, dermis and sub-dermal fats, which each provide a different signal magnitude. This effect is due to the different reflectance caused by the different chemical composition (including water content) and physical structure of the skin layers. Figure 4.35(c) shows the result of the unwrapping performed on the raw phase image, shown in figure 4.35(b). Further analysis of this data has been possible by sampling magnitude and phase values of 64 pixels corresponding to the position of the different tissue types identified in the visible image, as shown in figure 4.35(a) by the coloured squares (black, red and blue squares). The magnitude-phase map for every pixel corresponding to each tissue type is shown in figure 4.36, and demonstrates a clear clustering of values. The spreading of the data in a single cluster originates from inhomogeneity of the sample caused by different density and structure of the sampled parts.

Figure 4.36 shows how the strongest magnitude (i.e. the stronger reflection) is recorded from the sub-dermal fat; epidermis shows a moderately stronger magnitude than dermis, but both are weaker than fat.

This result contrasts slightly with that reported in [170]. Through a SFI imaging approach using a THz QCL, but with the QCL lasing at $\sim 2.59THz$, they investigated a porcine tissue sample differentiated in layers, namely: epidermis, upper dermis, lower dermis, sub-dermal fat and muscle. In their experiments only the lower dermis appears to produce

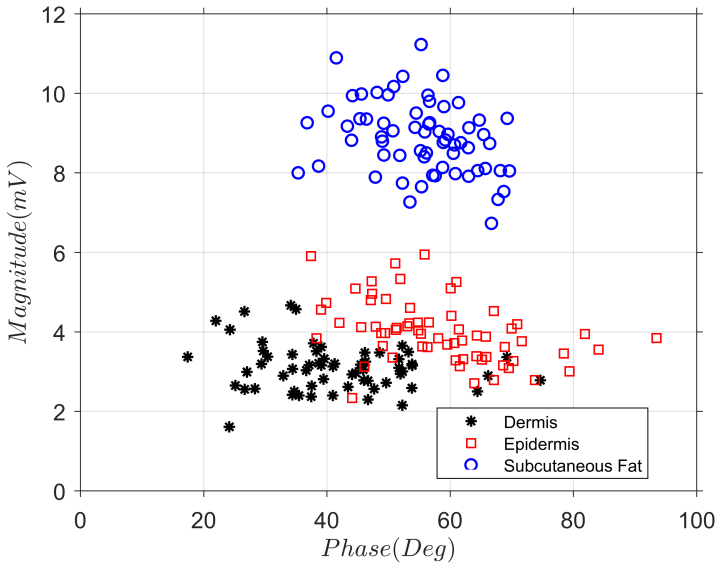

Figure 4.36: Magnitude vs phase graph. Each point is referred to a single pixel taken from the coloured squares in figures 4.35(a) and 4.35(c). Analysis was performed in collaboration with Dr J. Keeley.

a smaller SM signal magnitude than sub-dermal fat. Epidermis and upper dermis were clearly shown to give a stronger SM signal magnitude than fat, while muscle was shown to produce a comparable signal magnitude.

Of course, differences like lasing frequency may play a big role in this comparison as well as the different tissue nature and compositions (for example, porcine against human). Moreover dryness and maintenance of the sample can strongly influence the measurements. As such, more investigations are needed to provide a better understanding of the THz magnitude and phase obtained from complicated and inhomogeneous samples such as skin tissue.

4.5.3 Human skin cancer

A THz image of a human skin sample containing melanoma, acquired by the mechanical modulation approach, is shown in figure 4.37(a) and its corresponding camera photo in figure 4.37(b). In this case the sample contain a healthier area in the top fegion, and in the THz image it is clearly evident that the melanoma shows contrast with respect to

the healthy area. This is also evident in the images taken through the swept frequency approach, figure 4.38(a) and 4.38(b).

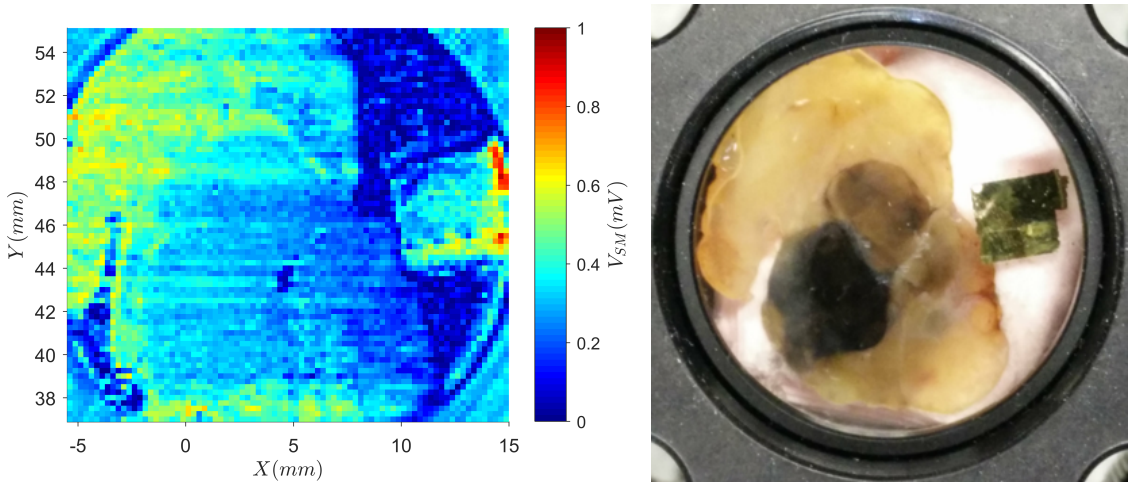

(a) (b)

Figure 4.37: (a) 2D THz image of the cancer sample, taken through the mechanical modulation approach with T_C=50ms. 82 × 73 pixels ($X \times Y$), pixel size 250 μm. (b) A picture from a camera of the same sample.

An evident difference in magnitude and phase can be noticed between regions of fat and melanoma. A cancerous layer is expected to have a high water content [38, 170, 189, 190, 193, 194]; different complex permittivity which is affected by the water content gives different magnitude and phase values [182, 204, 223]. This characteristic signature of cancereous tissues imaged by THz radiation in our experiments is shown in figure 4.39, which summarises the analysis conducted on figure 4.38(a) and 4.38(b). The coloured circles in figure 4.39 indicate the pixels (49 pixels in total) used for this analysis. Similarly to figure 4.36, figure 4.39 demonstrates a clear clustering of magnitude and phase values, in particular the weaker reflection from the melanoma area compared to the fat in the upper region of the sample. In this case also the signal measured from the gold is also included in the map and shows a higher magnitude than fat (and also the melanoma), confirming the results of the sample used for calibration (see figure 4.33(a)). Again, the spread of the magnitude and phase data in this map originates from inhomogeneity of the tissue.

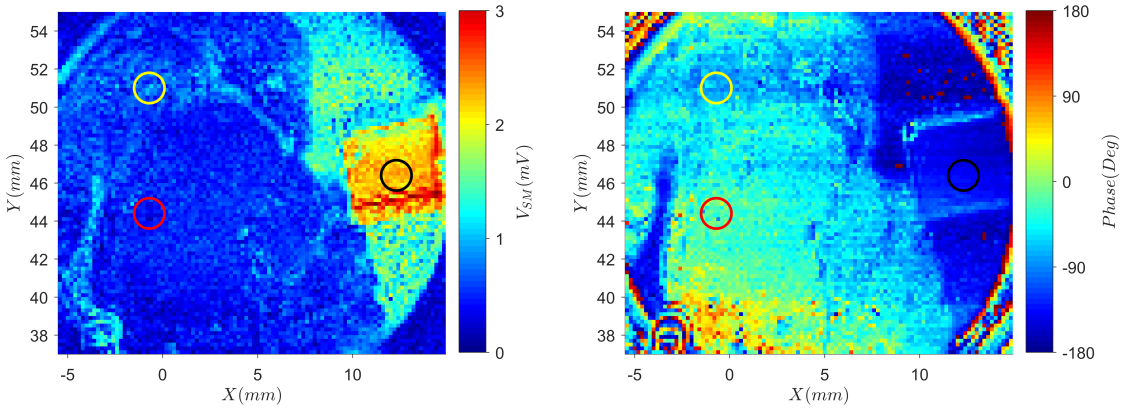

Figure 4.38: (a) Magnitude and (b) Unwrapped phase of a skin sample with melanoma, shown in figure 4.37(b), taken with THz-QCL SFI. The coloured circles select the pixels used for the analysis. 102×90 pixels ($X \times Y$), pixel size 200 μm.

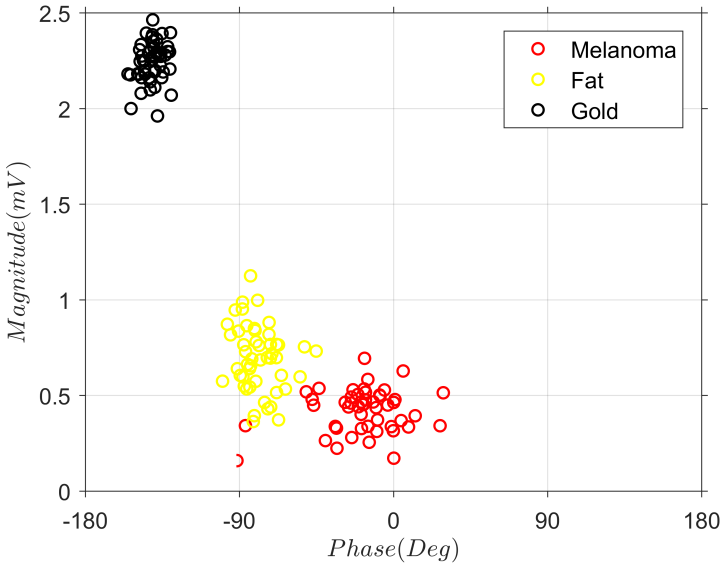

Figure 4.39: Magnitude vs phase graph. Each point is referred to a single pixel taken from the coloured circles in figures 4.38(a) and 4.38(b). The analysis was performed in collaboration with Dr J. Keeley.

4.6 Conclusions

In this chapter far-field THz imaging systems utilising the self-mixing effect in a QCL have been experimentally demonstrated by acquiring images of radically different samples (skin tissue and silicon wafers) and by evaluating functioning parameters of the systems. Two different acquisition schemes, namely using mechanical modulation of the THz beam and swept-frequency imaging enabling retrieval of magnitude and phase parameters, have been considered. By reconstructing an image of a gold-on-glass resolution target and evaluating the square wave MTF, a spatial resolution of $\sim 200\mu$m has been demonstrated. Considering a lasing frequency of ~ 3.4 THz ($\lambda \sim 90\mu m$) and assuming a potentially irregular beam profile, this resolution limit is consistent with that reported in the literature [3, 11, 13, 116, 120, 204, 205].

Moreover, the SNR has been characterised within the context of imaging silicon wafers for photovoltaic applications. The SNR values were measured to be $\sim$10$\times$ lower than those obtained previously using a metallic target [14], due to part of the THz beam being transmitted through the silicon wafers. However it has been demonstrated that the SNRs were satisfactory to image and retrieve information from silicon wafer samples.

The imaging systems have been applied to the acquisition of images of silicon wafers relevant to the manufacture of photovoltaic cells. In particular, the possibility to be applied to the detection of cracks, due to the phase changes occurring along the cracks, and also for the detection of impurities and defects has been demonstrated. In the latter case it has been possible to measure the deformation of the silicon wafer surface due to an embedded impurity, assuming that the phase change on reflection at the silicon and the impurity is equal. Furthermore the edges of three stacked silicon wafers have been retrieved when the system was modified to acquire only the THz radiation transmitted through the sample, opening the possibility of studying samples not only in reflection but also in transmission modalities.

Finally, the possibility of applying the imaging system to the study of human skin tissue, and for differentiating health and cancerous tissue has been demonstrated. By exploit-

ing both the swept-frequency and the mechanical modulation approach, three layers of a benign skin sample, namely dermis, epidermis and subcutaneous fat, have been clearly differentiated due to their different chemical composition. Contrast in both magnitude and phase between skin melanoma and subcutaneous fat has also been demonstrated due to the increased water content developed by the melanoma.

5 Near-Field imaging based on self-mixing in a THz QCL

In the standard imaging scheme based on self-mixing, the image resolution is limited by the beam spot size. It has been demonstrated in the Chapter 4 that a resolution limit of $\sim 200\,\mu m$ is possible by employing a THz QCL lasing at $f \sim 3.45\,THz$ ($\lambda \sim 87\,\mu m$). Overcoming the resolution limit can be achieved by utilizing a different technique. Near-field (NF) THz imaging techniques have shown great potential for different applications that require sub-wavelength resolution. Applications include THz near-field microscopy for mapping charge carriers in semiconductors and nanostructures [6, 224], investigation of THz plasmons waves in metamaterials, graphene or carbon micro-fibers devices [25, 26, 122, 225–228], THz waveguides characterisation [229, 230], and THz microscopy of bio-medical samples [231]. There are different types of THz near-field microscopes, but the scattering-type (or aperture-less) near-field microscopy (s-SNOM) and the aperture-type near-field microscopy (a-SNOM) have been mainly employed. The a-SNOM consists of placing a sub-wavelength aperture in order to restrict the illuminating beam spatially or limit the detection area in the near-field. The main limitation is the poor transmission through the aperture because most of the radiation is reflected from the aperture plane; the fraction of transmitted beam also scale as d^3, where d is the hole size (see figure 5.1) hence a reduced size leads to a drastic beam attenuation. Consequently the detection sensitivity and spatial resolution are limited too [7, 154, 232]. In a similar way, near-field imaging can be achieved by placing the source or detector in close proximity of the sample under analysis [233–235] but this approach has been revealed to be experimentally challenging. THz s-SNOM imaging, instead, has shown promising results achieving subwavelength resolution, independent of the light wavelength [232], on the order of $\lambda/1000$ [122, 155, 185]. This chapter will first describe different attempts to set up a bespoke s-SNOM system and will then discuss the set-up and results obtained through a commercially available s-SNOM/AFM (atomic force microscope) platform made by the company Neaspec GmbH and equipped with a THz QCL source.

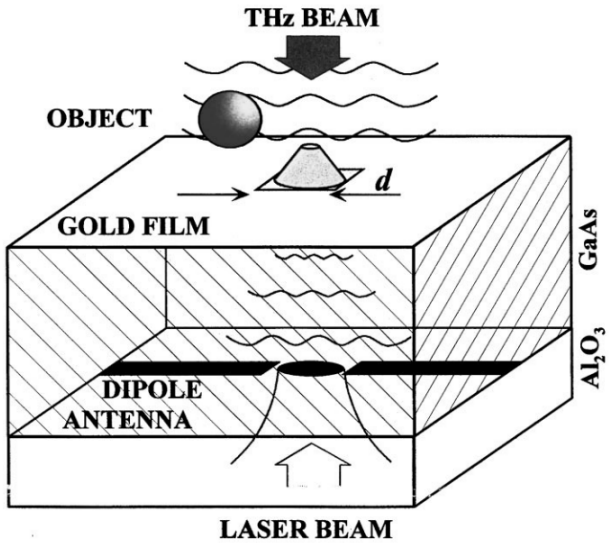

Figure 5.1: A schematic diagram of a probe used in aperture-type SNOM. Adapted from O. Mitrofanov [7].

5.1 Scattering-type scanning near-field optical microscope (s-SNOM)

Scattering near-field microscopy consists of a scattering probe, generally a metallic tip of an atomic force microscope (AFM), placed in close proximity to the sample surface. The probe is illuminated by incoming light (E_{in}) and the scattered (E_{out}) and back-scattered (E_{b-scat}) radiations can be collected in the far-field (see figure 5.2). The light is focused onto the tip of the probe which establishes the near-field interaction with the sample surface; the interaction modifies E_{out} and E_{b-scat}, as will be described in section 5.4. The collected scattered fields will contain information about the surface properties acquired with a spatial resolution given by the size of the tip and the tip-sample relative distance. To aid detection of the weak scattered field, the probe is dithered in order to allow lock-in amplification at the tip tapping frequency [185, 232].

The metallic tip is illuminated by a radiation which polarizes the tip creating a dipole which is mirrored in the sample surface. As a consequence the field scattered by the tip will have information about the complex permittivity of the tip and the sample. To describe optical radiation in near-field interaction it is possible to consider the light only

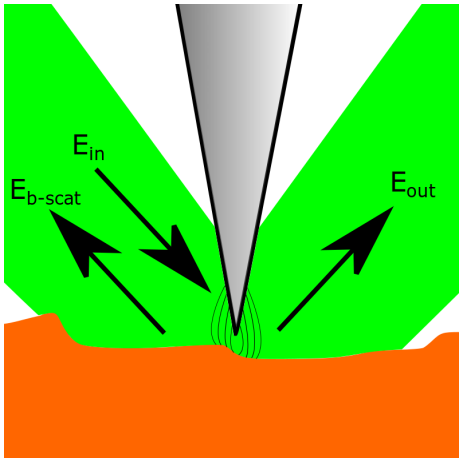

Figure 5.2: Near-field interaction when a sharp tip, illuminated by an incoming radiation (E_{in}), is in close proximity to the sample surface. Scattered (E_{out}) and back-scattered (E_{b-scat}) radiation can be collected.

as a wave, allowing the possibility to use a classical field theory based on Maxwell's equations. However, this does not exclude the possibility to use a more comprehensive quantum theory when the sample is considered as a quantum material, like molecules, 2D materials or quantum dots [236]. This would yield semi-classical theories depending on the kind of sample under investigation.

The light confinement in a near-field microscope is a key information to understand. For example in nano-plasmonic experiments based on near-field, the plasmonic resonances created by the tip at specific light wavelength, have shown the possibility to confine light at smaller wavelength compared to the original light wavelength [143, 236].

Another key component of near-field microscopy is the resolution. The peculiarity is to improve the resolution dictated by the diffraction of the beam waist. In a near-field microscope, the resolution is imposed by the tip-sample distance and the tip size, hence it allows to achieve resolutions well below the light wavelength [236]. Despite there are different techniques to estimate the spatial resolution, in this chapter, a 83nm spatial resolution will be demonstrated by using a 80% - 20% criterion with a metallic tip with 20 nm radius of curvature.

5.1.1 THz s-SNOM microscope based on self-mixing detection

The THz QCL consisted of 14 μm-thick GaAs/AlGaAs 9-well hybrid active region lasing at ∼3.45 THz which was processed into a semi-insulating surface-plasmon ridge waveguide with dimensions of 1.8 mm x 150 μm (see figure 2.25(a) and figure 2.26(a)). The QCL was cooled using a continuous-flow L-He cryostat and kept at the temperature of 20 ± 0.01 K. A laser driver was used to drive the laser at the constant current of 420mA.

The set-up was adapted from the usual self-mixing scheme, consisting of a pair of 2-inch-diameter f/2 parabolic mirrors which focused the THz beam from the QCL onto the sample surface; the reflected beam is reinjected into the laser facet creating a perturbation in the QCL which can be measured by monitoring its voltage, V_{SM}. In this case, the second parabolic mirror was mounted with an angle $\theta \approx 50^{\circ}$ with respect to the needle axis. The tip was placed on a three axis (x-y-z) piezo stage (Newport NPXYZ100SG) capable of nanometer ($\sim 4nm$) movements and the sample was vertically mounted on 3 motorized line translation stages, each of them enabling motion in a single direction, with a resolution of 1.5 μm in x-y (Newport ILS150CC) and 0.001 μm in z (Newport XMS160). The piezo stage ensured nanometric control of the tip translation as well as enabling the tip sinusoidal oscillation in the z direction. The probe tip was a standard Pt:Ir scanning tunnelling microscopy (STM) probe made by UNISOKU, with shaft diameter of 0.5 mm and tip radius of curvature of 1 μm. The modulated THz near-field response caused by the oscillation of the tip were measured as a change to V_{SM} on the QCL terminals. Since only the scattered field was measured, a very small fraction of the original THz beam is measured, hence lock-in amplification is needed to measure voltage changes on the order of tens of μV.

5.1.2 Seeking for the THz focus

The near-field interaction occurs when the tip-sample surface distance is comparable to the radius of curvature of the probe, d∼1μm. However, the tip first needs to be placed within the THz beam focus and the method to do so consisted of 3 main steps. In order to

locate the initial beam focus, the tip was removed and a metallic reflective angled mirror ($\theta \approx 50°$) was placed at the focus. The position of this mirror was optimised to maximise V_{SM}, as shown in figure 5.3(a).

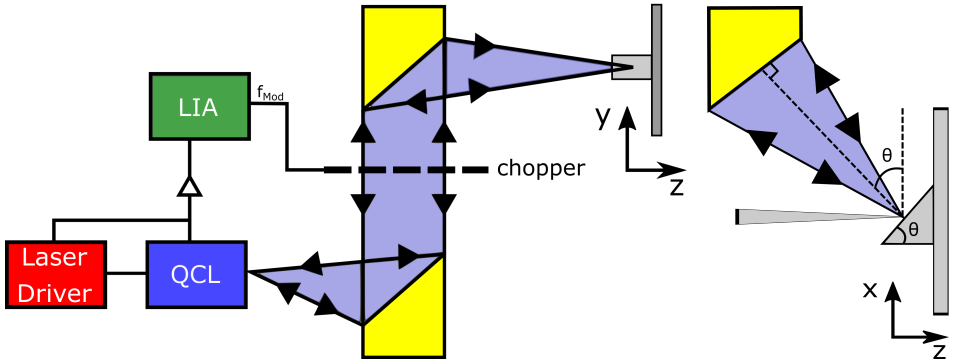

(a) (b)

Figure 5.3: (a) Vertical view of the scheme used for maximisation of V_{SM} in the THz near-field set-up. (b) Horizontal view of the metallic angled mirror used to maximise self-mixing signal. QCL stands for Quantum Cascade Laser, LIA for Lock-in Amplifier. Yellow polygons represent f/2 parabolic mirrors.

The tip, placed on the piezo stage, was then brought in proximity of the mirror's reflecting face and moved along Y and X directions in order to find its position within the THz beam (see figure 5.3(b)). In order to locate the centre of the focus in the Y-direction, the tip was scanned laterally across the front of the metallic mirror. As the tip blocks more of the central lobe of the THz beam, V_{SM} decreases, and as the tip leaves the beam focus, V_{SM} increases. The position where V_{SM} is at a minimum is the centre of the focus in Y. With the Y position of the tip acquired, the optimum X-position then needs to be located. In order to achieve this, a translation of the tip towards the mirror, can be employed. As such, when the tip enters the focus of the beam V_{SM} begins to decrease. This decrease will continue until the tip completely blocks the beam from the metallic mirror, so the amount of reflected power is at a minimum. This decrease has a characteristic S shape due to the approximately Gaussian beam shape. The focus for X is taken as the central location of this S-curve. The experimental results are shown in figure 5.4.

Referring to the axis direction defined in figure 5.3, the tip was first moved with steps of

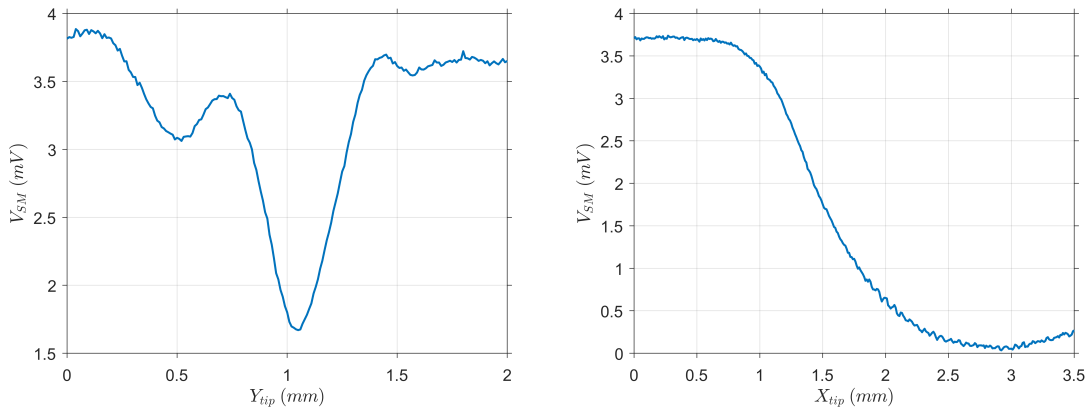

(a) (b)

Figure 5.4: Experimental data showing V_{SM} drops caused by the blocking of the THz beam with the tip when is moved, in proximity of the metal prism within the beam, along (a) Y and (b) X relative directions, with reference to figure 5.3. The tip movement step was 10 μm, the QCL was driven at 420 mA and kept at a constant T=20 $\pm$ 0.01 K, chopper frequency $f_{chopper} = 220Hz$.

10 μm along Y over a distance of Δ Y_{tip}=2 mm. Figure 5.4(a) shows first a small decrease of V_{SM} at $Y_{tip} = 0.49mm$ that might be caused by the tip shaft, probably due to side lobes of the beam profile [237], and a second larger decrease at Y_{tip}=1.05 mm, attesting the Y position of the tip within the beam. The tip was then kept at Y_{tip}=1.05 mm and translated over a distance Δ X_{tip}=3.5 mm, where the starting point X_{tip}=0mm indicates that the beam was not blocked by the tip (see figure 5.4(b)). In this case V_{SM} decreased to a null signal ($V_{SM} \sim 0$ mV) because the tip shaft was entirely blocking the beam.

As the X position is slightly more difficult to quantify from these measurements (since the change from tip to shaft blocking the beam will cause non-linear changes in the amount of beam being blocked), a more thorough way of quantifying the beam focus, in not only X but also Z, is to perform a mapping of the field scattered from only the tip. In order to perform this the mirror was removed and the set-up was modified by introducing a tip piezo stage controller to impose a sinusoidal dithering of the tip with frequency f_{tip}=90 Hz and amplitude 2μm to the tip, as shown in figure 5.5. This allowed lock-in detection of the component of V_{SM} due to by the tip.

The mapping of the THz beam is shown in figure 5.6. The results shows V_{SM} oscillating

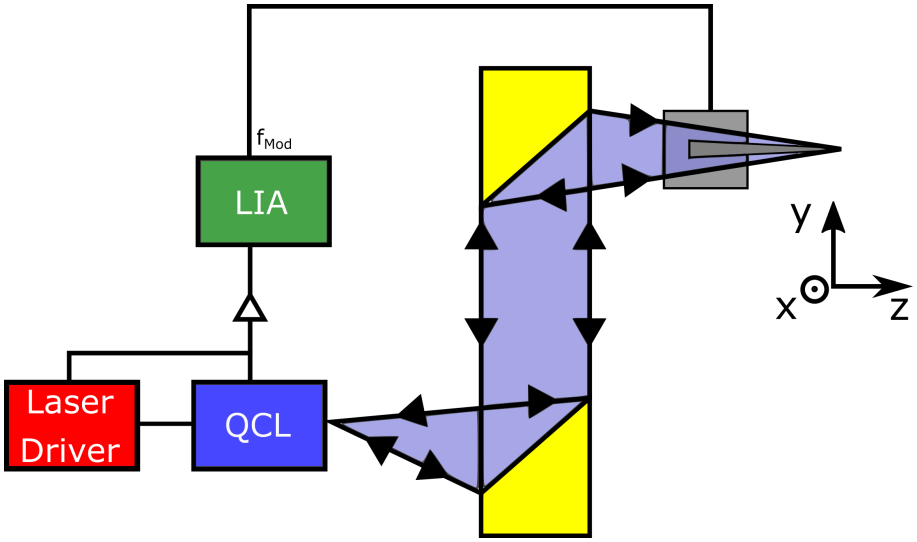

Figure 5.5: Experimental self-mixing set-up used to map the THz beam reflected exclusively from the tip.

between maximum and minimum values, where the focal point was identified by the fringe yielding the biggest amplitude. The blue dashed lines in the figure 5.6 show the outline of the beam profile deduced from these measurements. From these results the relative tip positions giving the biggest signal amplitude have been identified as $Z_{tip} \sim 1.5$ mm and $X_{tip} \sim 3.4$ mm, with $Y_{tip} \sim 1.05$ mm.

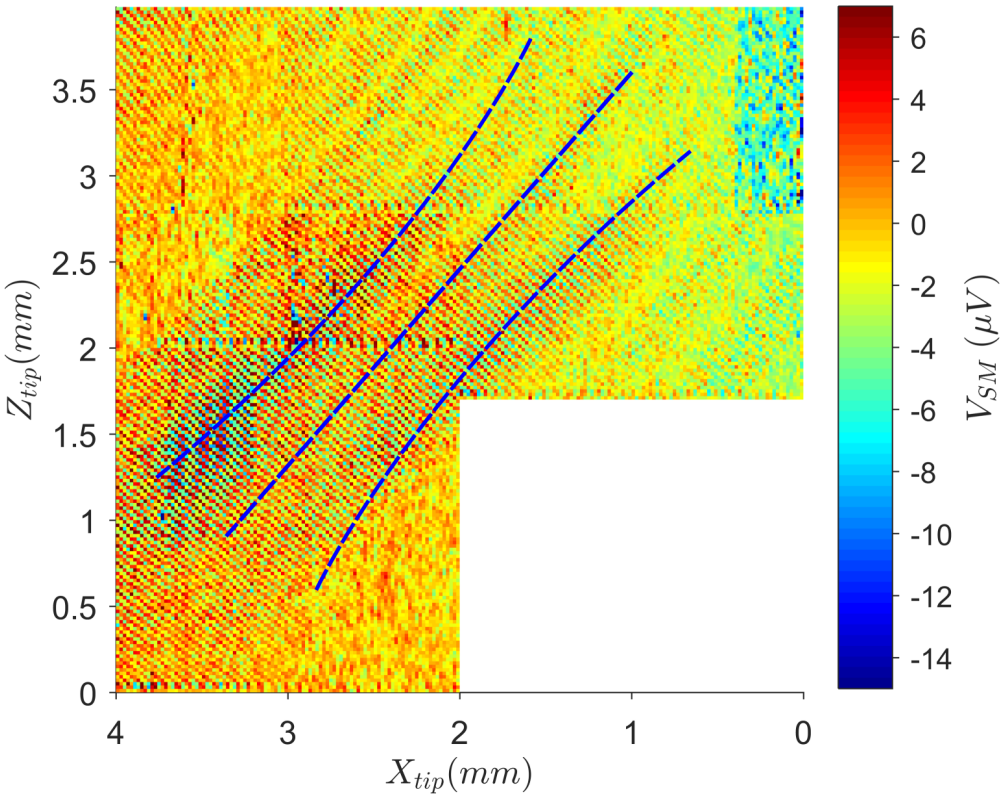

Figure 5.6: THz beam mapped through V_{SM}, blue dashed line used to guide the eye. The tip movement step was 20 μm, the QCL was driven at 420mA and kept at a constant T=20 ± 0.01 K, tip dither frequency f_{tip}=90Hz and amplitude 2μm.

5.1.3 Surface approach

As already previously mentioned, the NF interaction occurs when the tip-sample distance is comparable to the radius of curvature of the tip, which in this case was r$\sim$ 1μm. Experimentally, this interaction could be identified as a drastic enhancement of V_{SM} when the tip is in close proximity of the sample. The sample consisted of a gold-coated mirror mounted on a mechanical translation stage. V_{SM} was measured while the tip, placed within the THz beam focus, was dithered at 110 Hz with an amplitude of 2μm and the sample was moved towards the tip in the same direction of the tip modulation (Z), as shown in figure 5.7(a).

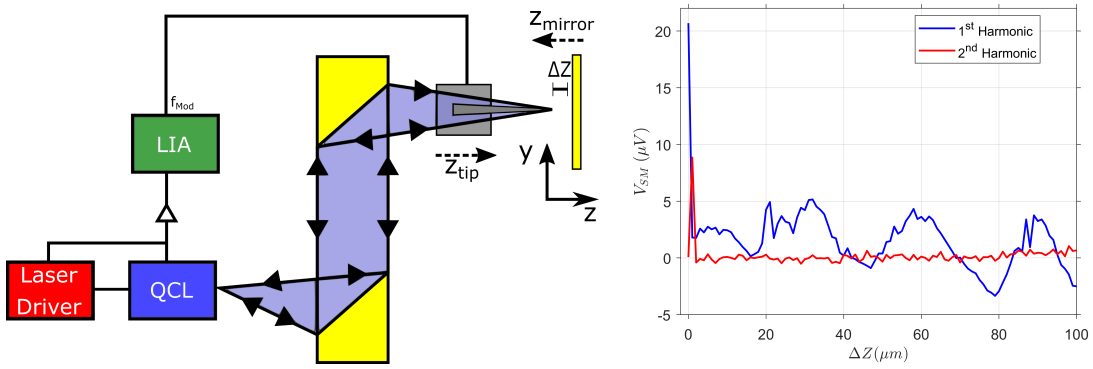

(a) (b)

Figure 5.7: (a) Experimental self-mixing set-up used to measure the NF enhancement. (b) Experimental V_{SM} demodulated at the 1^{st} and 2^{nd} harmonic of the tip frequency, showing the NF enhancement when ΔZ$\approx$1μm. ΔZ step was 1 μm, the QCL was driven at 420mA and kept at a constant T=20$\pm$0.01 K, tip dither frequency f_{mod}=110Hz and amplitude 2μm. LIA T_c=2s and sensitivity 10μV.

Figure 5.7(b) shows the experimental V_{SM} demodulated at the 1^{st} and 2^{nd} harmonic of the tip frequency, f_{tip}=110Hz, and plotted as function of the tip-sample distance, ΔZ. The NF enhancement occurred at ΔZ$\approx$1μm as expected. In this scheme, the gold mirror was approached towards the tip, which was constantly kept within the THz beam focus. While ΔZ decreased, the total round trip distance between laser facet and sample decreased by twice the translation distance; this translated as a phase change of the scattered field resulting in an unwanted oscillation of V_{SM}. At large tip-sample distance a background

non-zero signal of V_{SM} demodulated at the 1^{st} harmonic was due to unwanted reflections from the tip shaft; these effects has been also reported in [185]. Demodulation of V_{SM} at the 2^{nd} harmonic efficiently suppressed the background signal, but also decreased the detectable signal. Most of the NF imaging applications make use of signal demodulated at the second or higher harmonics in order to avoid unwanted reflections and to extract clear information about the sample [6, 26, 122, 155, 224–226]. The tip dithering frequency was previously optimized by recording V_{SM} at the NF enhancement position for different modulation frequencies, as shown in figure 5.8.

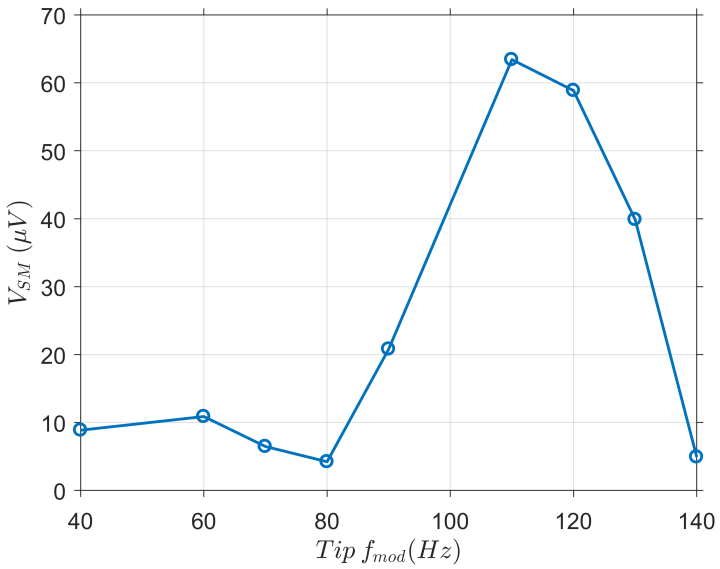

Figure 5.8: V_{SM} recorded at the NF interaction point for different tip modulation frequencies.

This optimization consisted of evaluating the f_{mod} that yielded the highest V_{SM}, which in this case was f_{mod}=110Hz. Typically, higher modulation frequencies are preferred since they lead to a reduction in noise due to higher averaging, but in this case the upper limit of the tip modulation frequency for a full 2μm oscillation was limited by the inertia of the piezo stage.

In traditional SNOM, incoherent detection is typically employed and in order to resolve the magnitude and phase of the scattered field, an external interferometer is required [6, 26, 224]. On the other hand, self-mixing detection, applied to s-SNOM is intrinsically

coherent, being a homodyne detection scheme. This means that it is possible to retrieve phase and magnitude information by changing the round trip distance of the beam. In order to demonstrate this effect the surface approach measurements explained above were repeated for different tip and gold mirror positions in the beam.

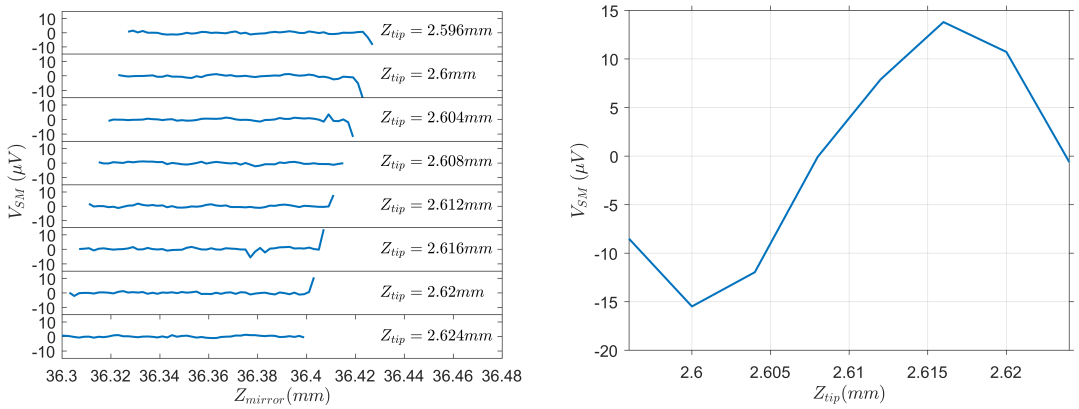

(a) (b)

Figure 5.9: (a) Series of surface approaches for different tip and mirror position. (b) V_{SM} recorded at the NF enhancement for different tip-mirro positions. The QCL was driven at 420mA and kept at a constant T=20 ± 0.01 K, tip dither frequency f_{mod}=110Hz and amplitude 2μm. LIA T_c=2s and sensitivity 10μV.

The experiments consisted of repeating the approach curve as shown in figure 5.7(b), but changing both the tip position and the starting position of the mirror by 4 μm for each measurements. In this case V_{SM} was recorded as a function of the relative position of the mirror, as shown in figure 5.9(a). The near-field enhancements show a clear oscillation between negative and positive V_{SM} due to the phase change of the scattered signal. An interferometric fringe can be recorded by plotting the NF-enhanced V_{SM} as function of Z_{tip}, as shown in figure 5.9(b).

5.1.4 Limitation of surface approach technique

The approach explained in the previous section unfortunately suffered from one big limitation. In order to acquire a NF image, the tip-sample distance needed to be kept at the position corresponding to the NF enhancement ($\Delta Z \leq 1\mu$m in this case) for each pixel. The system lacked a feedback circuit to control and keep ΔZ constant and so any micrometer

vibration could influence and degrade the signal, making it unstable. The factors causing these kinds of vibrations could be multiple and often are impossible to be taken into account because they come from the environment. Nevertheless in order to investigate how the signal could be drastically affected, the NF-enhanced V_{SM} was recorded over a time lapse of 10000 seconds (approximately the time needed to acquire a full image), by keeping the tip and gold mirror at the same position and with the QCL at the constant experimental conditions.

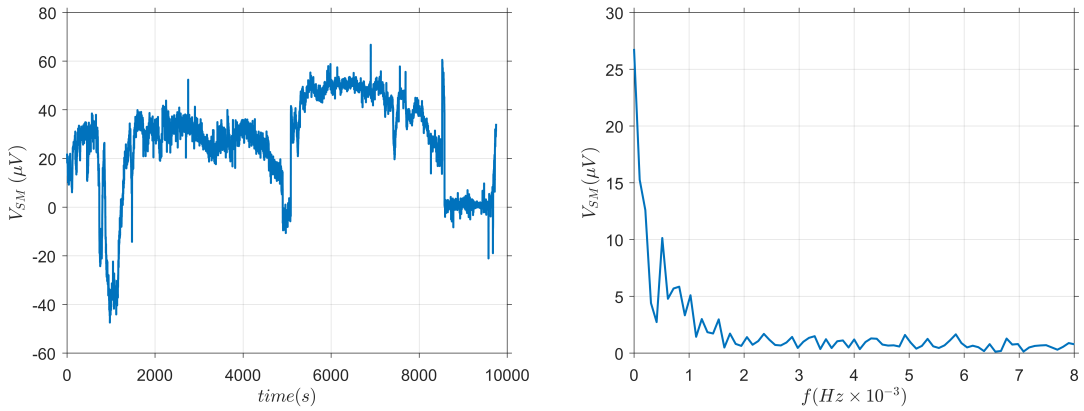

(a) (b)

Figure 5.10: (a) The NF enhanced V_{SM} recorded over a time lapse of 10000 seconds with 1 second sampling rate, by keeping tip and gold mirror at the same position and the QCL at the same experimental conditions. (b) Magnitude of the FFT performed on the signal shown in (a).

From figure 5.10 it is easy to note the huge drift of V_{SM} and the causes were most probably related to vibrations coming from the surrounding environment. The magnitude of the FFT performed on the V_{SM} (see figure 5.10(b)) reveals noise at extremely low frequencies, but this is also dictated by the the 1 second sampling rate which cut out all the frequencies greater than 1 Hz. This demonstrated the absolute need of a feedback loop circuit which would control and keep the tip-sample distance constant at any time, independent of the environmental influence. A possible solution to this issue can be found in [122]. The authors have attached the tip to a quartz resonant tuning fork (QTF), where the resonance is based on the piezoelectric effect. In this case any modification to frequency, amplitude and phase of the tuning fork translates into a change of voltage/current which provides

the feedback mechanism to keep the tip-sample distance constant.

5.2 THz s-SNOM based on commercial Neaspec neaSNOM AFM platform

Atomic force microscopy (AFM) is a technique used to measure the topography of a sample by measuring the atomic forces through the deflection of an elastic mechanical probe. The probe is a sharp tip, generally metallic with a radius of curvature from a few to tens of nanometers, attached to a cantilever which is vibrating at its own resonance frequency. In order to perform imaging the sample is raster-scanned using a piezo-electric stage, while the probe is maintained at a constant distance from the sample surface. An atomic force microscope already implements a feedback loop circuit to control and maintain the probe-sample distance and this makes it the perfect candidate to be used for s-SNOM. The feedback loop in a standard AFM usually employs a laser beam which is directed to the cantilever where the probe-tip is placed. The deflection of the cantilever is tracked by the reflected beam pointed to a photo-detector that acquires vertical and lateral motion of the probe. Subsequently a circuit corrects the position of the piezo stage where the sample is held, accordingly. Neaspec GmbH has created and patented this kind of system, called the neasNOM Microscope, which can simultaneously map the topography and, if equipped with a light source and appropriate detector, record a NF optical signal thanks to a built in lock-in amplifier.

Here, in a similar way to the previous set-up, the neasNOM has been arranged allowing self-mixing detection using a THz QCL, by aligning and focusing the THz beam onto the tip apex of the AFM probe (see figure 5.11). The THz QCL consisted of 14 μm-thick GaAs/AlGaAs 9-well hybrid active region lasing at $\sim$3.45 THz which was processed into a semi-insulating surface-plasmon ridge waveguide with dimensions of 1.8 mm x 150 μm. The QCL was cooled using a continuous-flow L-He cryostat and kept at the temperature of 20 $\pm$ 0.01 K. A laser driver was used to drive the laser at different constant currents. Performance and spectral characteristics of the THz QCL were previously tested (see figure 2.25(a) and 2.26(a)).

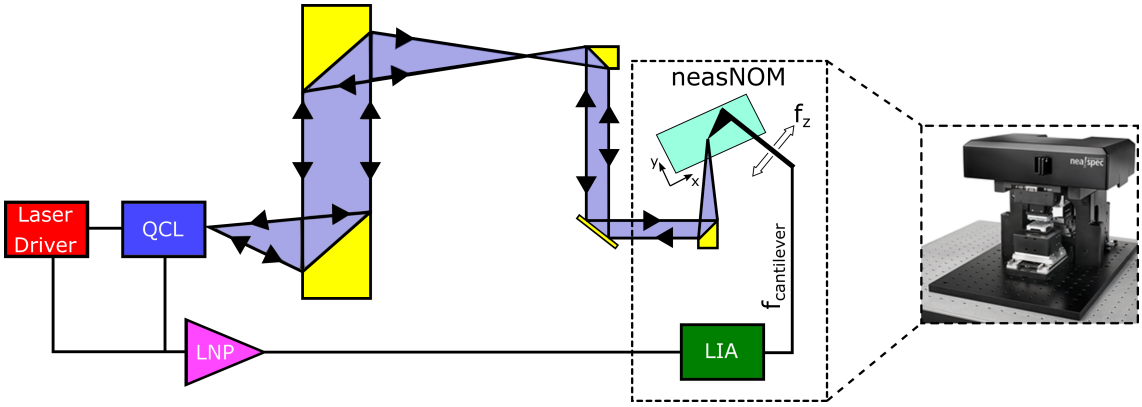

Figure 5.11: Schematic of the neaSNOM microscope arranged in the self-mixing scheme. The beam of a THz QCL lasing at ∼3.45 THz was focused on the tip apex of the neaSNOM probe trough a series of parabolic and flat mirrors. By following the beam path from the QCL, the first two gold polygons indicate 2" diameter f/2 parabolic mirror, the third was a 1/2" diameter f/1 parabolic mirror which projected the beam to a parabolic mirror internal to the microscope thanks to an external flat mirror. The internal parabolic mirror, in turn, focused the beam onto the tip apex. V_{SM} was first pre-amplified with a low noise pre-amplifier (LNP) and then measured by the microscope internal lock-in amplifier (LIA) locked to the intrinsic resonance frequency of the cantilever. The sample could be raster scanned thanks to the microscope piezo-electric stage. Right a real photo of the neaSNOM.

5.2.1 System alignment

A 2 mW He:Ne visible red laser (λ=633nm) was used as a pilot laser in order to align the system. The red laser beam was scattered through a diffuser so that it could reproduce the divergence of the QCL THz beam; this was mounted with the diffuser at the intended position of the lasing facet of the QCL. The alignment procedure consisted of firstly aligning the two 2" diameter f/2 parabolic mirrors and then the 1/2" diameter f/1 parabolic mirror. The most critical and difficult optic to align was the small 1/2" diameter f/1 parabolic mirror, and so after being reflected a laser target was used to check the diameter, shape and direction of the projection of the beam over a distance of few meters between the mirror and the target, as shown in figure 5.12.

After achieving a sufficiently collimated beam, a flat gold mirror was then added to the path of the projected beam to reflect it to the neaSNOM internal parabolic mirror. The internal parabolic mirror was at a fixed angle Θ ∼60° with respect to the stage sample. In a similar way to the previous set-up, a metallic prism was fabricated with its reflecting

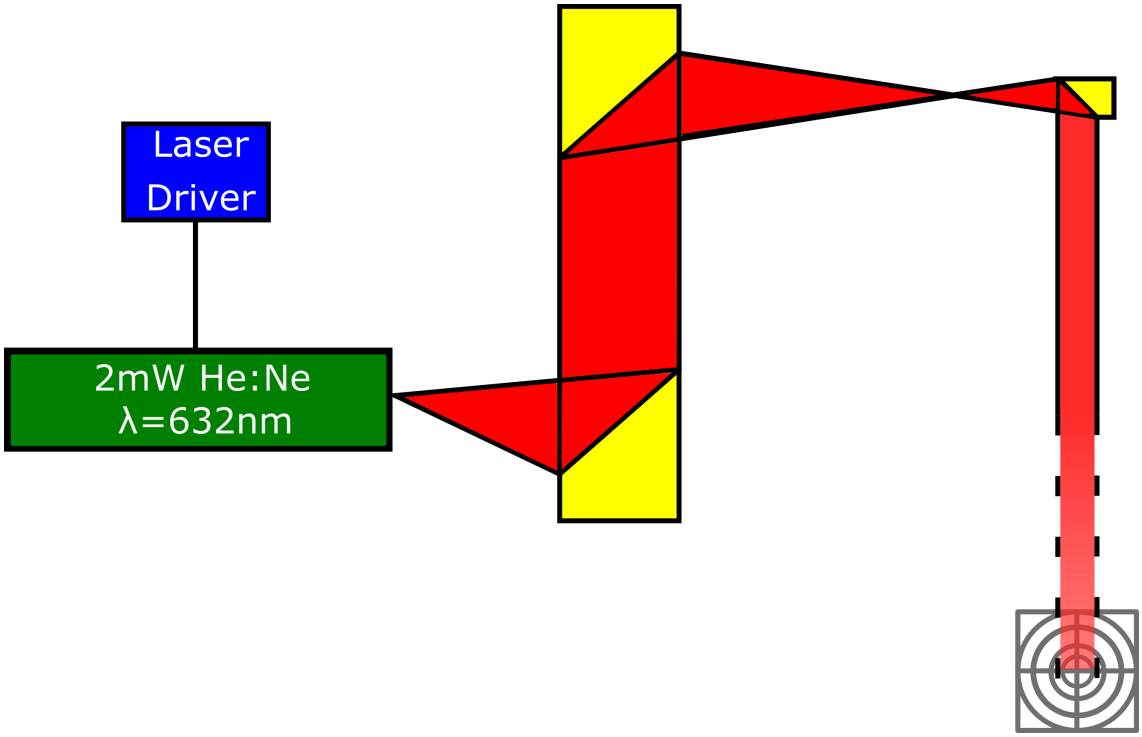

Figure 5.12: Schematic of the first step of neasNOM microscope alignment. The beam of 2 mW He:Ne visible red laser (λ=633nm) was scattered through a small aperture to reproduce the divergence of the THz QCL beam. By following the beam path from the He:Ne, the first two gold polygons were 2" diameter f/2 parabolic mirror, the third was a 1/2" diameter f/1 parabolic mirror. The beam was projected on a laser target to check shape and direction.

face at the same angle Θ ~60° and placed on the microscope sample stage. Thanks to the microscope's internal camera and to the controller of the internal parabolic mirror, its position could be adjusted until the red laser spot appeared on the prism. All the mirrors in the system were also adjusted to make the multiple spots reflected back to the front-face of the He:Ne laser converge into a single spot hitting the scattering diffuser. The probe tip was then approached towards the prism until its apex started scattering the red laser spot, as observed using the microscope camera (see figure 5.13).

The He:Ne laser was then removed and replaced by the QCL, as shown in figure 5.14. Without the probe tip engaged to the surface of the metal prism, V_{SM} was measured due to the beam reflected by the prism and reinjected into lasing facet of the QCL. Hence the system was modified by introducing a chopper to modulate the beam at f_{Mod} ~220Hz

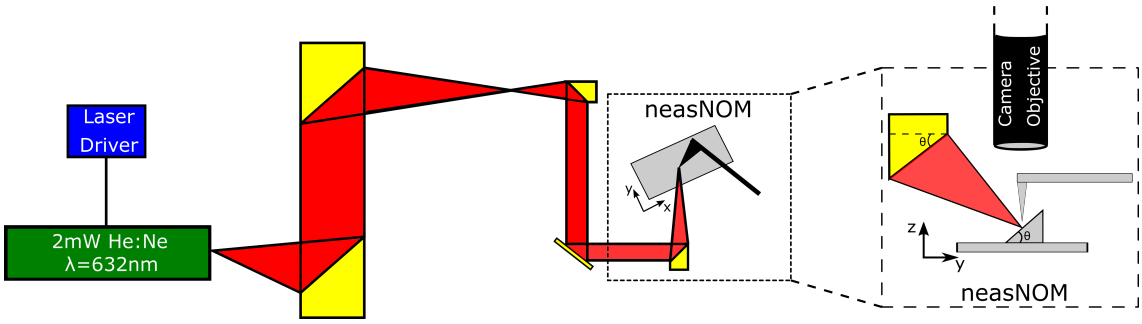

Figure 5.13: Schematic of the second step of neasNOM microscope alignment. The beam of 2 mW He:Ne visible red laser (λ=633nm) was scattered through a small aperture to reproduce the divergence of the THz QCL beam. By following the beam path from the He:Ne, the first two gold polygons were 2" diameter f/2 parabolic mirror, the third was a 1/2" diameter f/1 parabolic mirror that projected the beam to the microscope internal parabolic mirror thanks to a flat mirror. A metal prism with its reflecting face at the same Θ angle as the internal mirror was used to check the position of the spot.

which was used as a reference for lock-in detection. A self-mixing signal on the order of V_{SM} ~2mV ensured the correct alignment of the system.

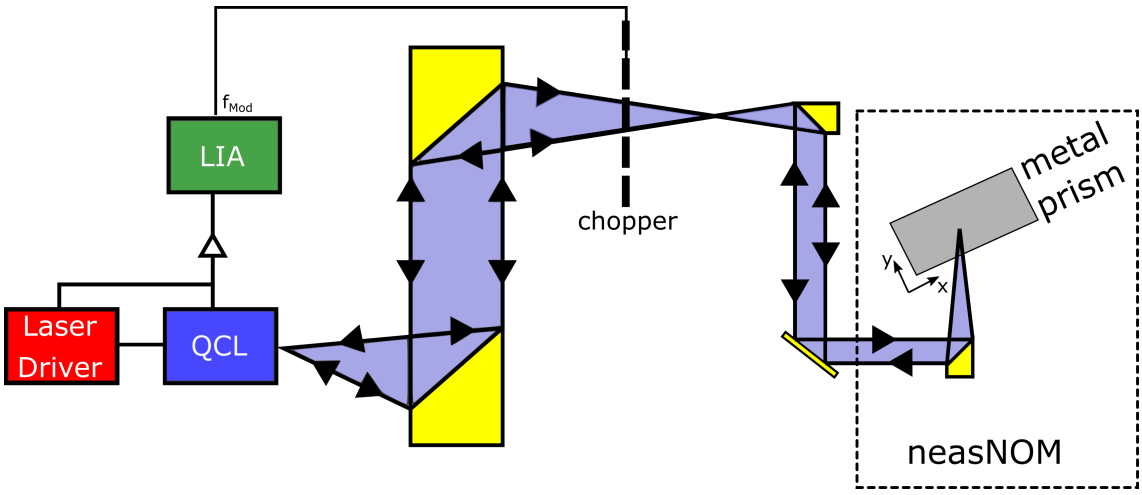

Figure 5.14: Schematic of the third step of neasNOM microscope alignment. V_{SM} was evaluated only by the reflection of the beam from the metal prism, placed onto the sample stage of the neaSNOM, and reinjected into the QCL facet.

Finally, after removing the prism, the system was modified as shown in figure 5.11, by introducing a low noise preamplifier (LNP) in order to pre-amplify (with a gain of 2×10^3) the small V_{SM} arising from the beam weakly scattered by the probe tip apex and reinjected into the QCL facet. V_{SM} was then measured by the microscope internal lock-in amplifier

(LIA) locked to the intrinsic resonant frequency of the cantilever.

5.2.2 THz-s-SNOM System Characterization

In order to understand the capabilities of the neaSNOM system when equipped with a THz QCL source a set of experiments were carried out to fully characterize the system. THz near-field enhancement was first demonstrated by recording a surface approach curve using a gold sample. By operating the neaSNOM in tapping mode with tip tapping frequency $f_{tapping}$ ~60kHz and amplitude A_{tip}=23nm, the THz self-mixing signal demodulated up to the 5^{th} harmonic was recorded as function of tip-sample separation in the range d=0-100nm and with a resolution of $1nm$, as shown figure 5.15. In this context the probe tip had a

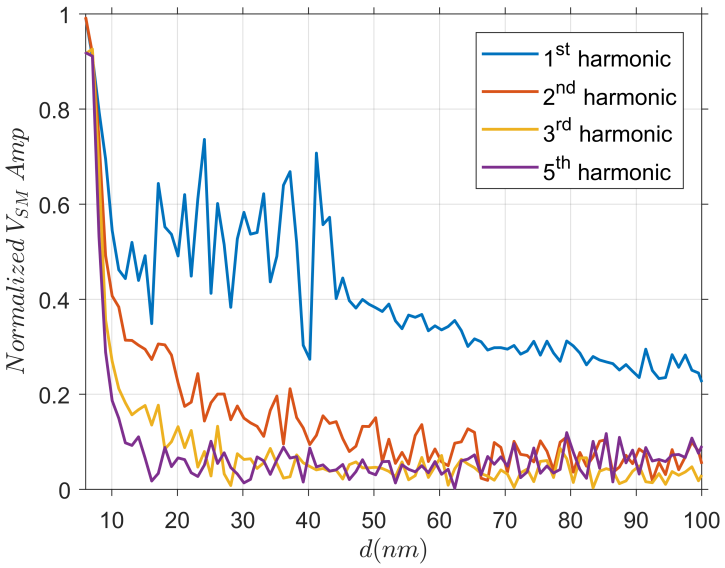

Figure 5.15: Approach curves on gold. Normalized V_{SM} amplitude recorded, in tapping mode, as function of the tip-sample separation by the internal LIA of the microscope. Demodulation of the signal up to the 5^{th} harmonic clearly demonstrated the background signal suppression. $f_{tapping}$ ~60kHz, A_{tip}=23nm, approach resolution 1nm, T_C=1s. The QCL was driven at 420mA, with a lasing frequency of ~3.45THz and kept at a constant T=20±0.01 K.

radius of curvature r_{tip} ~20nm. As already previously mentioned, NF enhancement occurs when the tip-sample distance is comparable to the tip's radius of curvature. The approach curves clearly demonstrated this effect, in fact the strongest NF signal enhancement occurs

for Z<20nm. Moreover, the 1^{st} harmonic data shows a background signal corresponding to ∼20% of the NF-enhanced V_{SM} amplitude, acquired by the internal lock-in amplifier of the microscope. Demodulation of the signal at higher harmonics efficiently demonstrated the suppression of the background signal, which was attributed to unwanted reflections from the sample or to beam scattering by the tip shaft. In this case, oscillations of the signal were not observed due to the much shorter approach distance compared to the previous set-up (100nm vs 100μm).

The spatial resolution of the microscope was evaluated by imaging a test sample of 50nm-thick Au on Si, fabricated through standard e-beam lithography. Images of topography (height) (see figure 5.16(b)), and V_{SM} amplitude demodulated at the 3^{rd} harmonic, a_3, (see figure 5.16(a)) were recorded simultaneously.

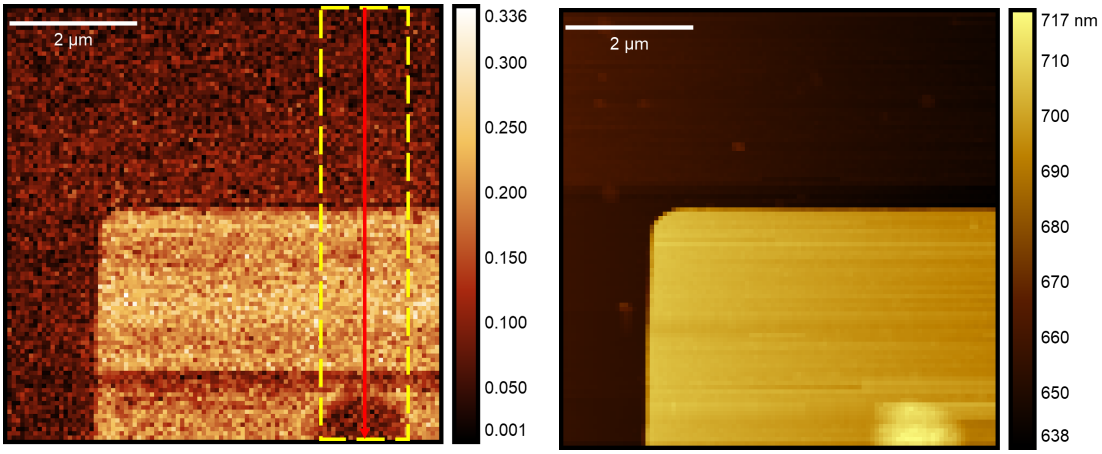

(a) (b)

Figure 5.16: 7μm×7μm (a) THz NF image of a Au corner on Si, vertical scale is the V_{SM} amplitude a_3. The red arrow indicates the direction line used for the resolution evaluation, by averaging 20 rows as shown in the yellow rectangle. (b) Topography of the same sample. $f_{tapping}$ ∼60kHz, A_{tip} ≈23nm, pixel size 70nm, T_C=200ms. The QCL was driven at 420mA, with a lasing frequency of ∼3.45THz and kept at a constant T=20±0.01K.

The THz image clearly shows a contrast between Si and Au, due to the difference of material permittivity. By averaging 20 columns of the image, as shown in figure 5.16(a), a profile of a_3 and height were obtained. The THz profile has been fit with an edge response

function (ERF) [14, 38] given by equation 5.1,

$$I(y) = \frac{I_0}{2}\Big(A + erf(2\sqrt{\ln 2}\frac{(y - y_0)}{w})\Big). \tag{5.1}$$

Here I_0 is the full beam intensity, y is the position, y_0 is the center position of the step, w is the width at half maximum of I(y) derivative and A is a free fit parameter which yielded, $A = 2.0218$.

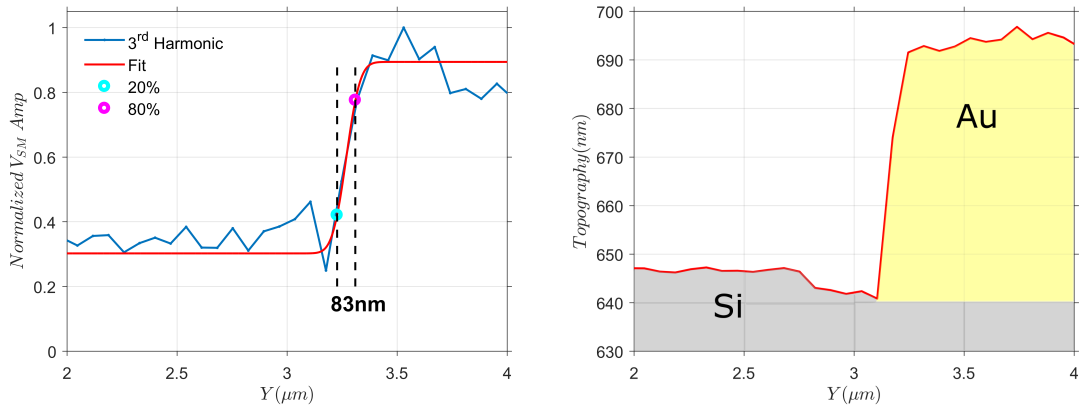

(a) (b)

Figure 5.17: (a) Normalized THz profile obtained by averaging 20 columns of image as shown in figure 5.16. Red curve is the fit obtained by equation 5.1. (b) Height profile obtained in the same conditions. Line scan resolution was dictated by the pixel size of 70nm.

The resolution was calculated by using the 20% - 80% criterion applied to ERF fit. The distance between 80% and 20% of the maximum signal yielded a spatial resolution of R=83nm, which corresponded to a sub-wavelength resolution better than $\lambda/1000$ (for λ ~87μm). This value is similar to that achieved with similar conditions in the THz regime by other groups, also exploiting different detection systems [26, 38, 122, 155].

The tip tapping amplitude has a direct physical relation with the resolution. In the above case a resolution of 83nm has been achieved by using a A_{tip} ≈23nm, but a higher A_{tip} would have yielded a higher resolution. The physical explanation has to be found in the NF interaction area between tip apex and sample surface, as shown in figure 5.18.

In the tapping mode operation, the tip is constantly kept oscillating between a maximum

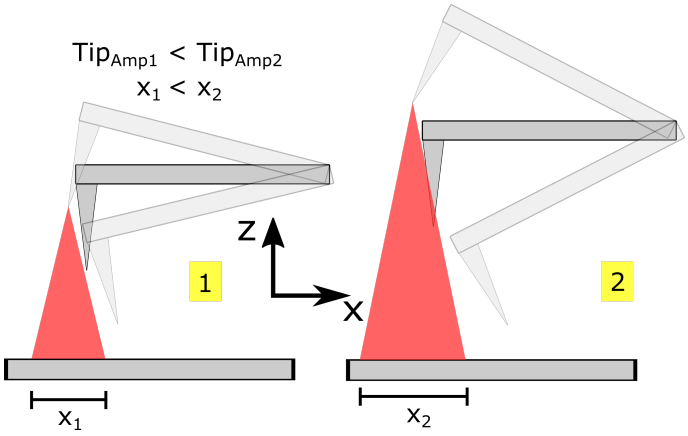

Figure 5.18: 2D Schematic used to explain the relation between tip tapping amplitude and resolution. A higher tip tapping amplitude yields a higher resolution because the NF field interaction area becomes bigger.

and a minimum position. By assuming the NF interaction occurs within a cone of interaction between tip apex and sample surface, where the cone apex coincides with the tip apex and the base coincides with sample surface area, a higher tapping amplitude would create a bigger interacting sample area. The SNR (see equation 5.2) of the acquisition will be also affected; a larger interacting area would make the tip less sensitive to the local surface effects. In order to demonstrate how the tapping amplitude affects the resolution, the same 20% - 80% criterion was applied to the ERF fit of the line scans (averaging over 10 columns) obtained using the same 50nm-thick Au on Si test sample, obtained with 3 different tip tapping amplitudes, as shown in figure 5.19. Also the SNR of the measurements has been calculated respectively for Si and Au in order to demonstrate the effect of the tapping amplitude on the signal-to-noise ratio of the measurements. The experiments have demonstrated the two effects: a direct relation between resolution and tip tapping amplitude, and a direct relation between SNR and tapping amplitude. It's worth mentioning that the difference of resolution obtained between figure 5.17(a) and the top panel of figure 5.19(a) are attributable to different experimental conditions related to tip that is subjected to wear. However the experiment conditions have been maintained the same for the three sets of data shown in figure 5.19(a).

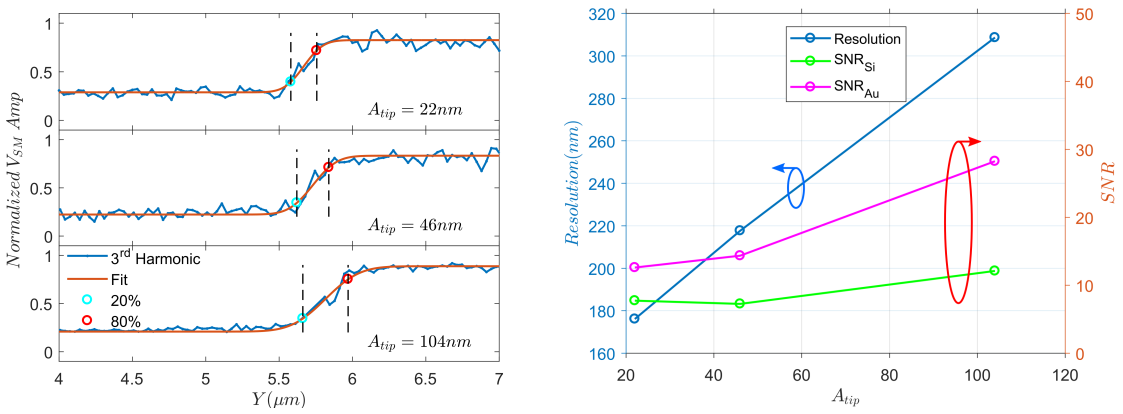

(a) (b)

Figure 5.19: (a) Normalized THz profiles obtained by averaging 10 rows of the line scan for 3 different tip tapping amplitudes. Red curves are the fit obtained by equation 5.1. (b) Resolution and SNR as function of A_{tip}. Line scan pixel size was 30nm. $f_{tapping}$ ~85kHz, T_C=200ms. The QCL was driven at 420mA, with a lasing frequency of ~3.45THz and kept at a constant T=20±0.01 K.

Optimization of the image acquisition time constant, T_C, was carried out by evaluating the SNR for a series of 2μm×2μm images of the same 50nm-thick Au on Si test sample, as shown figure 5.20. Two areas corresponding Si and Au, respectively, have been selected, as shown in figure 5.21(a). For each of these the SNR has been calculated using equation 5.2,

$$SNR = \frac{\mu_3}{\sigma_3}, \tag{5.2}$$

where μ_3 and σ_3 are respectively the average and standard deviation of the amplitude signal, a_3, for the selected areas. From the experiments a clear contrast between Au and Si was visible for $T_C \geq$50ms and this corresponded to a SNR ratio between the two materials, $\frac{SNR_{Au}}{SNR_{Si}}$>1, as shown from the plot in figure 5.21(b).

From the results shown in this section it has been possible to select the ideal experimental conditions to acquire images with clear contrast between the materials under analysis. By focusing the attention on the time constant, T_C could also be directly related to the total time elapsed to acquire an image; for example, all the images shown in figure 5.20 were 80px×80px with 25nm pixel size. While the image with T_C=5ms took 32 seconds

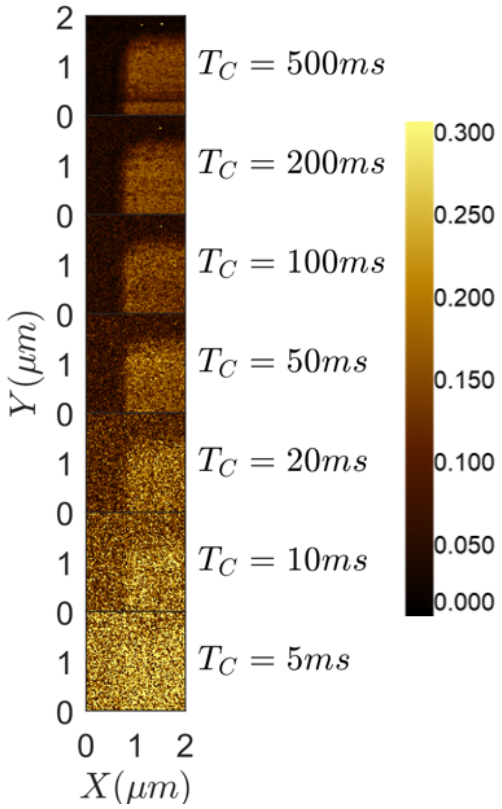

Figure 5.20: Series of NF images of 50nm-thick Au corner on Si, acquired at different T_C. Vertical scale is V_{SM} amplitude demodulated at the 3^{rd} harmonic, a_3. Pixel size was 25nm. $f_{tapping}$ ~85kHz, A_{tip} ≈23nm. The QCL was driven at 420mA, with a lasing frequency of ~3.45THz and kept at a constant T=20±0.01K.

to be fully acquired, the image with T_C=500ms took 100 times longer, slightly less than 1 hour. Long acquisitions might introduces different types of experimental difficulties (such as thermal drift of the lasing frequency or mechanical drift of the optics), hence a good trade-off between image quality and elapsed time needed to be found. In this particular case a T_C=200ms was selected as the best trade-off that ensured clear contrast and reasonable elapsed time (~ 20 minutes).

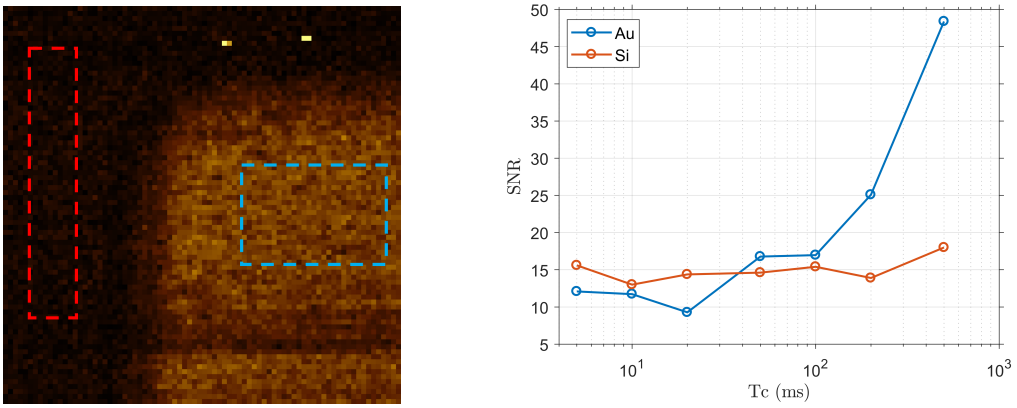

(a) (b)

Figure 5.21: (a) Au (blue) and Si (red) areas selected for SNR evaluation. (b) Calculated SNR as function of T_C. Referring to figure 5.20 a clear contrast between Au and Si is visible when $SNR_{Au}/SNR_{Si}>1$.

5.3 Stepped-frequency self-mixing in a THz QCL applied to s-SNOM

As shown in Chapter 2, the lasing frequency of a THz QCL, in stable experimental conditions, is strictly dependent on the driving current. This allows the possibility to record phase and amplitude, in the near-field, entirely through electrical means, i.e. it is possible to sweep V_{SM} through an interferometric fringe by simply stepping the laser driving current. Indeed, a similar approach has been previously demonstrated in the far-field [116] (see also Chapter 4) by sweeping V_{SM} through a series of interferometric fringes by applying a chirp to the laser driving current. In order to demonstrate the validity of this stepped-frequency approach in the near-field, figure 5.22 compares V_{SM}, obtained through the swept-frequency approach in far-field using a gold mirror as a target, with V_{SM} obtained by stepping the QCL driving current, with the use of s-SNOM. For these measurements the QCL was kept at a constant T=20±0.01 K, and V_{SM} was recorded every 1mA between 550mA and 623mA; for the near-field measurements V_{SM} was demodulated at the 4^{th} harmonic of the tip tapping frequency, $f_{tapping}$ ~60kHz and A_{tip} ≈32nm.
From figure 5.22, the good agreement between V_{SM} obtained from far-field and near-field measurements is evident. Furthermore from the near-field data both phase and amplitude of the scattered field could be extracted, and these are specific to the sample under illumi-

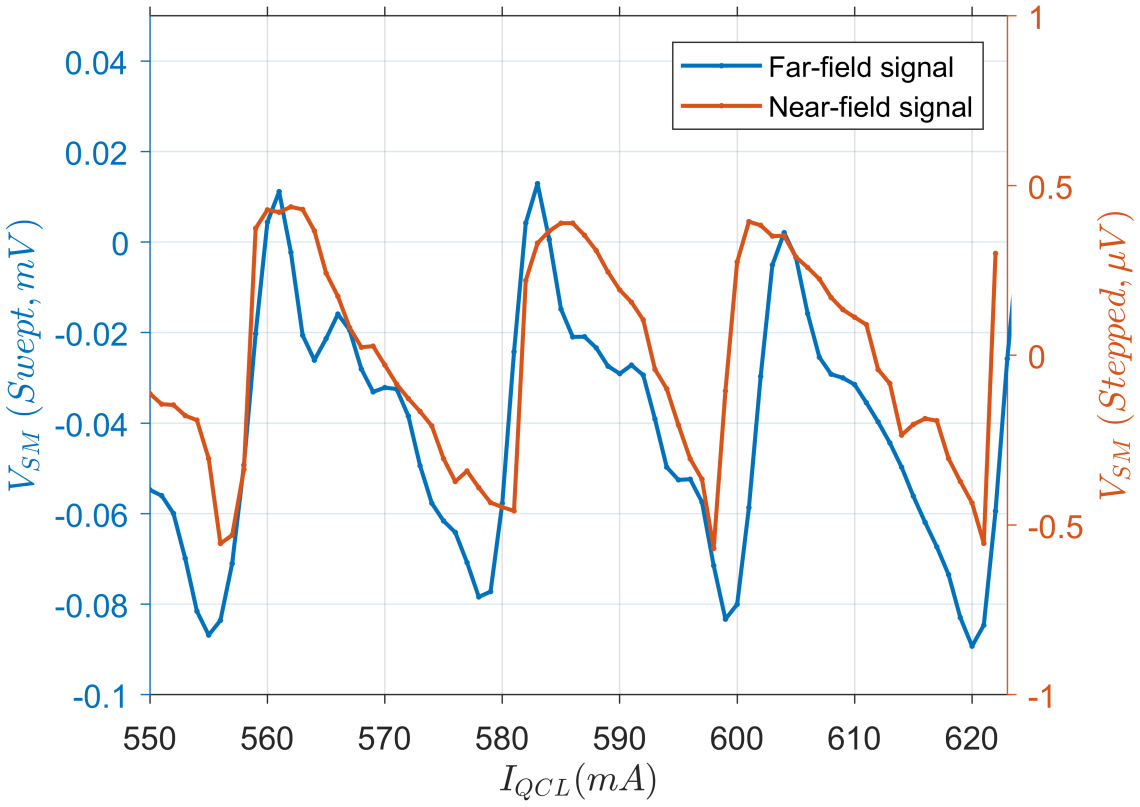

Figure 5.22: Blue data: Swept-frequency V_{SM} signal measured using reflection from gold mirror in far-field. Red data: equivalent V_{SM} signal, demodulated at the 4^{th} harmonic, measured using scattering from the probe tip of s-SNOM. The 2 curves were obtained from the same THz QCL. Code created by Dr. James Keeley.

nation, as described by the finite-dipole (FD) model. It's worth mentioning that the slight different periodicity between the data arises from different external cavity length used for the measurements; moreover the near-field signal is much smaller than the reflected far-field signal.

As already previously mentioned in this chapter, traditional s-SNOM requires an interferometer to resolve phase and amplitude of the scattered signal [6, 26, 224]. This is not the case for the SM scheme because it is intrinsically coherent; retrieving phase and amplitude of a signal by changing the round trip distance, L_{ext}, has been previously demonstrated in the literature [155] and also in this chapter as shown in figure 5.9. However, these approaches are slow and require the use of electro-mechanical stages. Here, an all-electrical

approach has been developed, keeping all the components positions stable and simply stepping the laser driving current (I_{QCL}).

5.4 Theory of s-SNOM based on self-mixing detection

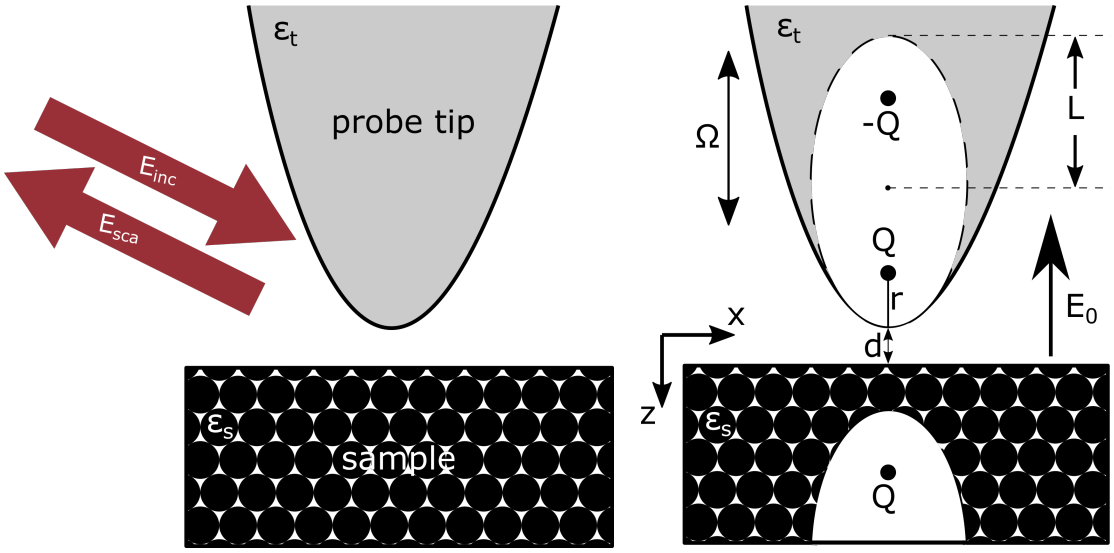

Figure 5.23: (a) The probe tip is assumed as an elongated tip illuminated by an incident wave E_{inc} from the side; the scattered wave E_{scat} is detected. (b) In the finite-dipole (FD) model the tip is assumed as a spheroid in a uniform electric field E_0. E_{inc} polarizes the tip, ε_t, which mirrors the dipole into the sample, ε_s. The tip, with radius of curvature r kept a distance d from the sample surface, is dithered with frequency Ω.

Section 5.5 is dedicated to experimental results in which coherent THz-s-SNOM signals are related to complex permittivity of samples, and in order to understand these results the origin of the NF signal requires to be understood theoretically. The probe tip, with radius of curvature r and permittivity ε_t, held at distance d from the sample surface is illuminated by an incident field, E_{inc}. The field E_{inc} polarizes the tip, inducing a dipole which is mirrored in the sample, with permittivity ε_s. The point dipole model threats the needle tip as a sphere [152, 185], but this assumption in some cases is a limit to understand the experimental data; the finite-dipole was later developed to better explain the experimental data. According to the finite-dipole (FD) model the tip is described as a spheroid which has an effective length L and an apex radius r and it is subject to a uniform

electric field E_0. The scattered field, E_{sca}, is proportional to the effective polarizability, α_{eff} as described by following the relation,

$$\frac{E_{sca}}{E_{inc}} \propto (1 + r_p)^2 \alpha_{eff}, \tag{5.3}$$

where r_p is the Fresnel reflection coefficient for p-polarized light and α_{eff} [155, 238, 239] is given by the equation 5.4,

$$\alpha_{eff} = r^2 L \frac{L(\varepsilon_t - 1)(2L\sqrt{1 - \frac{r}{L}} + r \ln \frac{(1-\sqrt{1-\frac{r}{L}})^2)}{\frac{r}{L}})}{2L\sqrt{1 - \frac{r}{L}}((L - r\varepsilon_t) - rL(\varepsilon_t - 1) \ln \frac{(1-\sqrt{1-\frac{r}{L}})^2}{\frac{r}{L}})} \cdot \\ \cdot \left(2 + \frac{(gL - r - d)\beta \ln \frac{L}{d+\frac{3r}{4}}}{(d - gL + \frac{3r}{4})\beta \ln \frac{L}{d+\frac{r}{2}}} + L \ln \frac{L}{\frac{r}{4}}\right). \tag{5.4}$$

Here $\beta = (\varepsilon_s - 1)/(\varepsilon_s + 1)$ is the surface response function of the sample and g is a complex factor which takes account of the total charge induced in the spheroid. It's important to note that in this context the apex-sample surface distance d is a function of time and oscillates with frequency Ω and amplitude given by the tip tapping amplitude, A_{tip}. As such d(t) is then given by,

$$d(t) = b + A_{tip} \cos(\Omega t), \tag{5.5}$$

where b is the minimum tip-sample distance during the oscillation. The proportionality of the ratio of the scattered field, E_{sca}, to the incident field, E_{inc} has been written in equation 5.3 by following the FD model; at the same time the scattering efficiency [155, 238, 239], $\sigma(t)$=E_{sca}/E_{inc}, can be expressed as a complex quantity represented in terms of amplitude and phase, σ(t)=s(t)$e^{i\varphi(t)}$. Here, s(t) and φ(t) have a strong non-linear dependence on time through d(t) which depends on the tapping frequency Ω (see equation 5.5). Hence E_{sca} can be expanded as a harmonic series, i.e. a sum over the n-th harmonic of Ω, in which s_n and φ_n are, respectively, the amplitude and phase components of the scattering

efficiency demodulated at the n-th harmonic of the tapping frequency Ω. E_{sca} can be expressed following equation 5.6.

$$E_{sca}(t) = \sigma(t)E_{inc} = s(t)e^{i\varphi(t)}E_{inc} = E_{inc}\sum_n s_n e^{i\varphi_n}e^{in\Omega t}. \tag{5.6}$$

The two parameters s_n and φ_n are strictly dependent on the sample material and can be related to its complex permittivity, ε_s, via the FD model. In the FD model a $\varphi_n \approx 0$ is expected for a non resonant sample, for example for materials that do not exhibit optical phonon resonance peaks in their complex permittivity ($\varepsilon_s(\nu) = \varepsilon_s(\nu)' + i\varepsilon_s(\nu)''$) within the region of the lasing frequency; this has been previously demonstrated by employing a QCL lasing at 2.5 THz to acquire NF images of a Black Phosphorus (BP) on SiO_2 sample [155] using the SM scheme. Both BP and SiO_2 do not show any evidence of phase contrast in the images and this is in agreement with the FD model, since in both cases optical phonon resonances fall in the mid-IR regime. On the other hand, the same group has demonstrated a clear phase contrast by employing a resonant polar crystal of caesium bromide (CsBr), which exhibits a strong phonon resonance in the range 2.2 – 3.3 THz. They measured a phase difference $\Delta\varphi \approx 150°$ between CsBr and a 100nm thick gold layer deposited on it, as expected from the model. They found good agreement between experimental data and theory by using the values $L = 530nm$ and $g = 0.98e^{0.08i}$ in the FD model (see equation 5.4).

In order to obtain the components s_n and φ_n experimentally, we can note that $V_{SM}(t)$ is proportional to the scattered field $E_{sca}(t)$. Following equation 5.6, and by analogy with equation 3.21, this allows the following relation to be written [116, 151, 232],

$$V_{SM}(t) \propto E_{sca}(t) \propto s(t)\cos\left(\frac{4\pi L_{ext}\nu}{c} + \varphi(t)\right) = \sum_n s_n \cos\left(\frac{4\pi L_{ext}\nu}{c} + \varphi_n\right)\cos(n\Omega t) \tag{5.7}$$

The self-mixing voltage demodulated at the n–th harmonic of the tapping frequency can

thus be seen to be,

$$V_{SM,n} \propto s_n \cos\left(\frac{4\pi L_{ext}\nu}{c} + \varphi_n\right), \tag{5.8}$$

where ν is given by the modified excess phase equation (EPE),

$$\frac{4\pi L_{ext}(\nu_0 - \nu)}{c} = C \sin\left(\frac{4\pi\nu L_{ext}}{c} + \varphi_n + \arctan(\alpha)\right), \tag{5.9}$$

with the lasing frequency without feedback at driving current I given by,

$$\nu_0 = \nu' + k(I - I'), \tag{5.10}$$

where ν' is the lasing frequency without feedback at current I'.

5.5 Experimental results and comparison to the FD model

In order to demonstrate the ability of our all-electrical s-SNOM approach to quantify changes in both the amplitude and phase of the scattered THz field arising from the permittivity of materials, samples containing two crystals, SiO_2 and potassium bromide (KBr), were imaged using our technique. These materials are expected to be respectively a non-resonant and a resonant sample in the THz range. KBr, in particular, is an ionic crystal and its optical phonon-polariton dispersion has been previously determined by time-domain spectroscopy in reflection mode [17]. This has allowed retrieval of its complex permittivity ($\varepsilon(\nu) = \varepsilon^I(\nu) + i\varepsilon^{II}(\nu)$), as shown in figure 5.24(a). $\varepsilon(\nu)$ of KBr can be described in the harmonic approximation by [17],

$$\varepsilon^I(\nu) = \varepsilon_\infty \frac{(\nu_{LO}^2 - \nu^2)(\nu_{TO}^2 - \nu^2) + \gamma^2\nu^2}{(\nu_{TO}^2 - \nu^2)^2 + \gamma^2\nu^2}, \tag{5.11}$$

$$\varepsilon^{II}(\nu) = \varepsilon_\infty \frac{(\nu_{LO}^2 - \nu_{TO}^2)\gamma\nu}{(\nu_{TO}^2 - \nu^2)^2 + \gamma^2\nu^2}, \tag{5.12}$$

where ν_{TO} is the transversal optical phonon frequency, ν_{LO} is the longitudinal optical phonon frequency, γ is the damping parameter and ε_∞ is the high frequency dielectric constant. Also the SiO_2 phonon dispersion has been previously determined by reflection

and transmission spectroscopy [18] giving a good estimation of its permittivity in the THz region, as shown in figure 5.24(b).

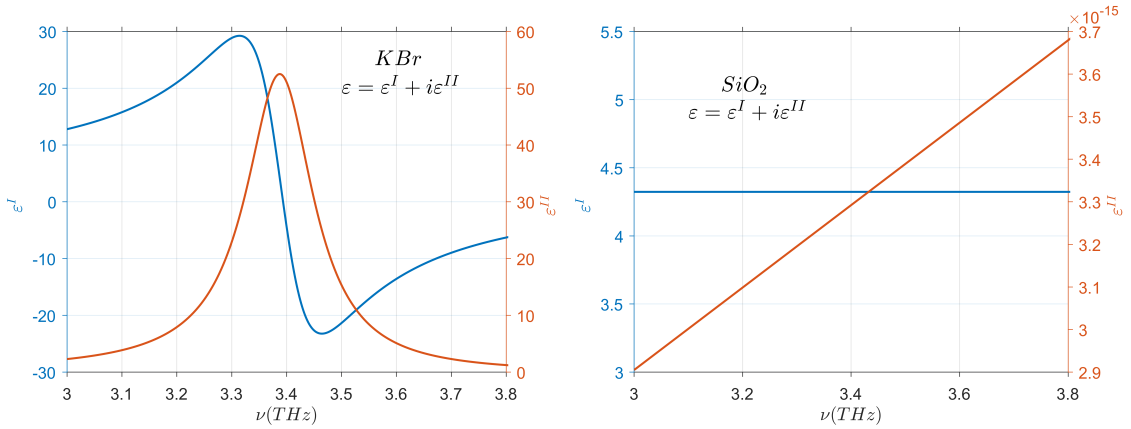

(a) (b)

Figure 5.24: The complex permittivity as function of the frequency ν, $\varepsilon_s(\nu) = \varepsilon_s^I(\nu) + i\varepsilon_s^{II}(\nu)$, of (a) KBr, data adapted from F. Brunner [17], and (b) SiO_2, data adapted from W.G. Spitzer [18].

Samples were prepared by evaporating a layer of Au with thickness 100nm and 50nm, respectively on SiO_2 and KBr substrates. For SiO_2, the Au area was defined through standard optical lithography. Instead, since KBr is freely soluble in water, it could not be processed in any water-based solution; for this reason the Au area was defined using Kapton tape as a mask. The Kapton tape's resistance to high temperature makes it a good candidate to tolerate the Au thermal evaporation without degradation, but on the other hand created a poorer edge definition compared to the Au on SiO_2.

This section is dedicated to the comparison of the experimental NF signals to that described by the SM model incorporating the FD model. The amplitude a_{sub} and the phase p_{sub} of the SM signal for the 2 substrate materials have been measured in the THz-s-SNOM system, shown in figure 5.11, at different laser driving currents (I_{QCL}). The V_{SM} signal for each image was obtained by the relation $V_{SM}=a_n \cos(p_n)$ and fit to $V_{SM,n}$ (see equation 5.8) through the excess-phase equation, (see equation 5.9) and the tuning coefficient k of the QCL (see equation 5.10), to generate synthetic self-mixing signals through a concise algorithm [19], allowing s and φ to be determined and correlated to the values

obtained from Au. The QCL used in this work consisted of 14 μm-thick GaAs/AlGaAs 9-well hybrid active region lasing at ~3.45 THz which was processed into a semi-insulating surface-plasmon ridge waveguide with dimensions of 1.8 mm × 150 μm. The QCL was cooled using a continuous-flow L-He cryostat, kept at the temperature of 20±0.01 K and driven at different constant I_{QCL}.

5.5.1 Experimental results for Au on SiO_2

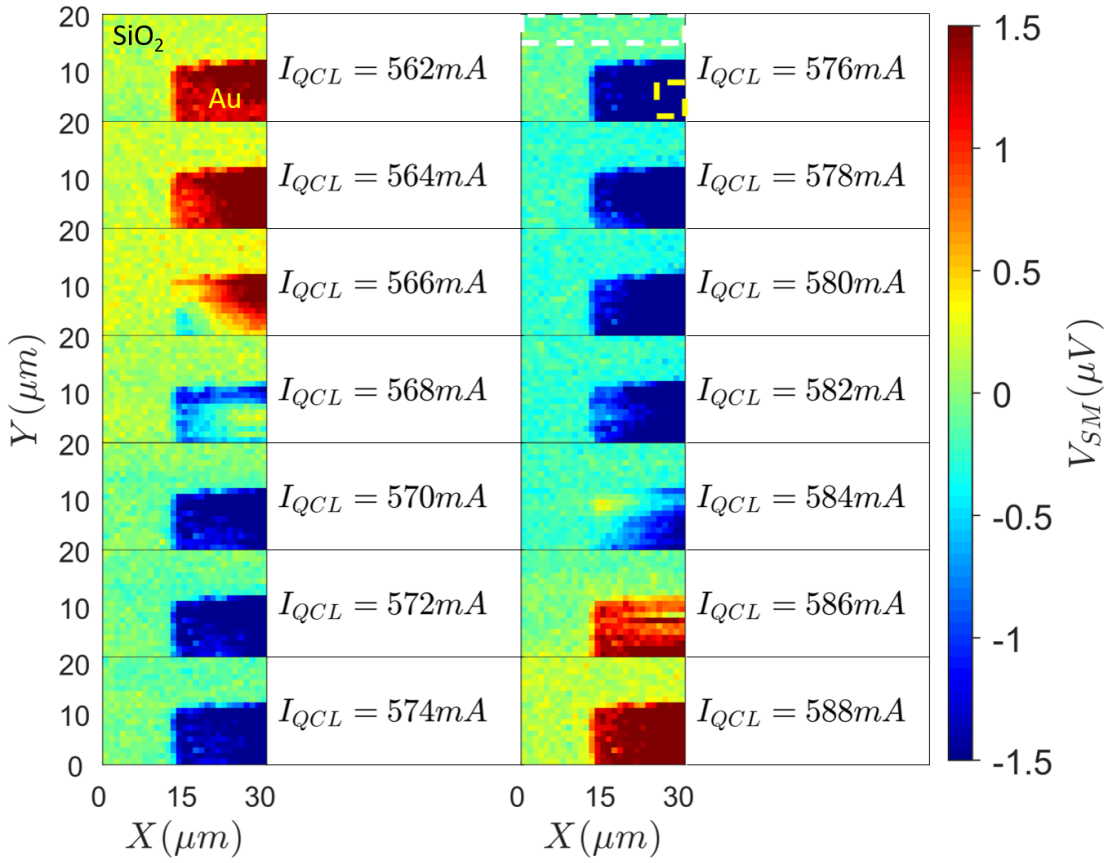

Figure 5.25: Series of NF images, n=1, of Au on SiO_2 obtained at different I_{QCL}. While the SM signal on SiO_2 varied only of small amount, the signal of Au had much larger $+V_{SM}$/$-V_{SM}$ swing. The dashed rectangle in the top right image indicates the areas where the data has been extracted. The images were 20μm×30μm with pixel size 1μm. $f_{tapping} \approx$ 60kHz, $A_{tip} \approx$25nm, T_c=200ms. Code created by Dr. James Keeley.

The approach used for this sample of 100nm-thick Au on SiO_2 consisted of firstly maximizing the the NF signal amplitude (a_1) by focusing the beam on the gold area of the

sample. An area of 20μm×30μm was been selected for the raster-scan, paying attention to cover a corner of Au with the rest covering the SiO_2. The same area was scanned with I_{QCL} ranging between 560mA and 600mA in steps of 2mA. This corresponded to a QCL lasing frequency tuning of ∼100MHz, as shown in the Chapter 2. For brevity, figure 5.25 shows the images obtained only between 562 mA$\leq I_{QCL} \leq$588 mA. These images were obtained by the combination of amplitude, a_1, and phase, p_1, following the relation $V_{SM}=a_1\cos(p_1)$. Evident contrast between Au and SiO_2 is visible and this is attributable to the permittivity difference between the two materials. While the V_{SM} of SiO_2 varies only of small amount with changing driving current, the signal from Au had much larger swing. However the SM signal oscillates between a maximum and a minimum values for each material, as expected from equation 5.8.

In order to perform a numerical analysis, typical signal values were extracted by averaging the pixels in the rectangular areas (yellow for the Au and white for the SiO_2) as shown in the top right images of figure 5.25. The data was fitted to the SM equations (equation 5.8 and 3.30) and compared to the predictions of the FD model (equations 5.4, 5.3 and 5.6) for the materials under analysis. The interferometric fringes obtained through the SM fitting algorithm show a sinusoidal form due to the small feedback parameter C and the linewidth enhancement factor α, being for Au, $C_{Au}=1\times10^{-7}$ and α_{Au}=-2.1061 and for SiO_2, $C_{SiO_2}=1\times10^{-7}$ and α_{SiO_2}=-2.2631. While the values of C are in line with the very weak feedback regime [14], similar values are obtained for α since the same QCL was used for the measurements. Likewise, comparable tuning coefficients k, $k_{Au}=6.65\cdot10^6$ Hz/mA and $k_{SiO_2}=6.45\cdot 10^6$Hz/mA were obtained from the fits. The phase difference and the ratio of amplitudes extracted from these fits are $\varphi_{Au} - \varphi_{SiO_2} \approx 30^\circ$ and $s_{Au}/s_{SiO_2} \approx 9.1$, respectively.

These values were then compared with those predicted by the FD model. For this, the permittivity of the tip, ε_t, was retrieved by the Drude model applied to platinum, Pt, which is a good approximation considering that the tip was made of an alloy Pt:Ir; similarly, the permittivity of Au was retrieved by application of the Drude model. In this work the FD model has been computed using $L = 500nm$ and $g = 1e^{i0.1}$, in equation 5.4. The model

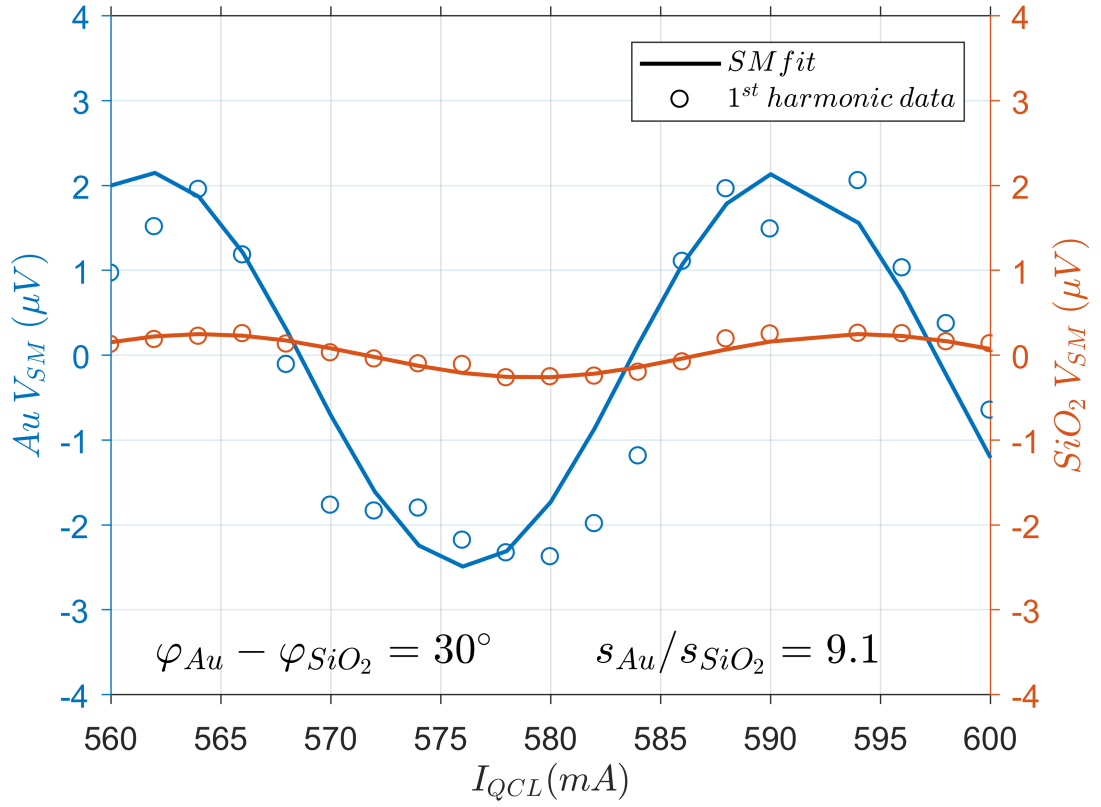

Figure 5.26: Interferometric fringes obtained for Au (left y-axes) and SiO_2 (right y-axes) out of the NF images shown in figure 5.25. The SM fit was performed by following the algorithm of R. Kliese [19]. $\varphi_{Au} - \varphi_{SiO_2}$ ≈30° and s_{Au}/s_{SiO_2} ≈9.1 could be extracted by the SM fit. The data point at I_{QCL}=592mA has been removed due to an experimental mistake.

predicts an amplitude ratio, $s_{Au}/s_{SiO_2} \approx 12$ and a phase difference $\varphi_{Au} - \varphi_{SiO_2}$ ≈11°, as shown in figure 5.27. Whilst the ratio of amplitudes agrees well with the experimental results, there is a slight difference between the phase differences obtained from the model and experimental data. This can be attributed to the experimental approach adopted. The SM signals, which are V_{SM} demodulated at the 1^{st} harmonic of the tip frequency, are subjected to a background signal which affected the SiO_2 data more prominently. Indeed as already previously stated by Cvitkovic et al [238], random and systematic errors can affect the phase in case the signal amplitude is low and, in particular, if the near-field signal is weak the measured phase can be strongly altered by the unsuppressed part of the background scattering. The data shown might be affected by the aforementioned issue,

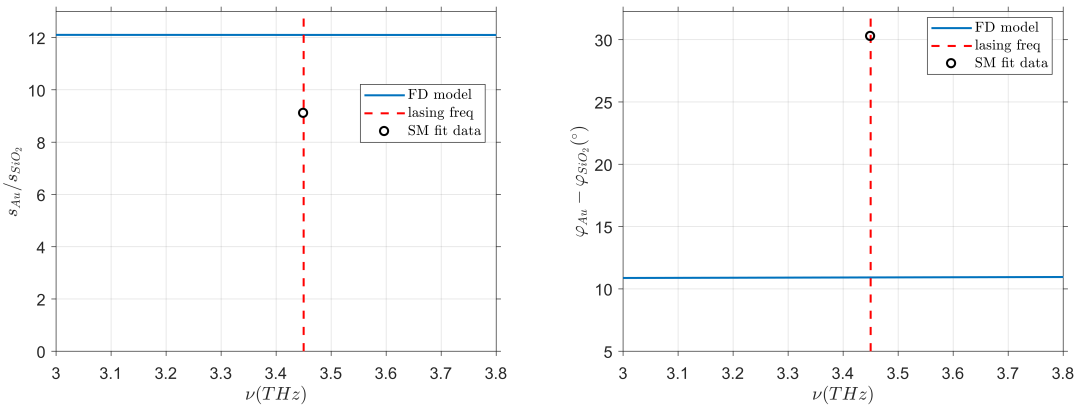

(a) (b)

Figure 5.27: Comparison between FD model and data extracted from the SM fit shown in figure 5.26. (a) Amplitude ratio, and (b) phase difference. Red dashed line indicates the QCL lasing frequency.

because SiO_2 produced a much smaller signal amplitude compared to the Au. In order to overcome this issue the experimental procedure for the KBr sample was changed and will be explained in the next section.

5.5.2 Experimental results for Au on KBr

The different approach adopted for the KBr sample consisted of firstly maximizing the SM signal (a_1) measured on the substrate. Images 1μm×1μm (10px×10px) were then acquired with I_{QCL} ranging between 550mA and 606mA in steps 2mA, making sure that the scan area only consisted of KBr. Secondly, equivalent 1μm×1μm images were acquired on the Au driving the laser over the same range of I_{QCL}. These images were acquired using $f_{tapping}$ ≈60kHz, A_{tip} ≈160nm and T_C=300ms. With this approach experimental errors due to, for example, laser temperature drift could be minimized since the acquisition of only 100 pixels was quicker than for the larger images acquired in the the previous approach (600 pixels). The interferometric fringes obtained through plotting the average $V_{SM}=a_1\cos(p_1)$ as a function of I_{QCL} are shown in figure 5.28.In this case the fitted fringes show a non-sinusoidal behaviour due to larger the feedback parameter C and the linewidth enhancement factor α, being for Au, C_{Au} = 1.00 and α_{Au}=-2.8987, and for

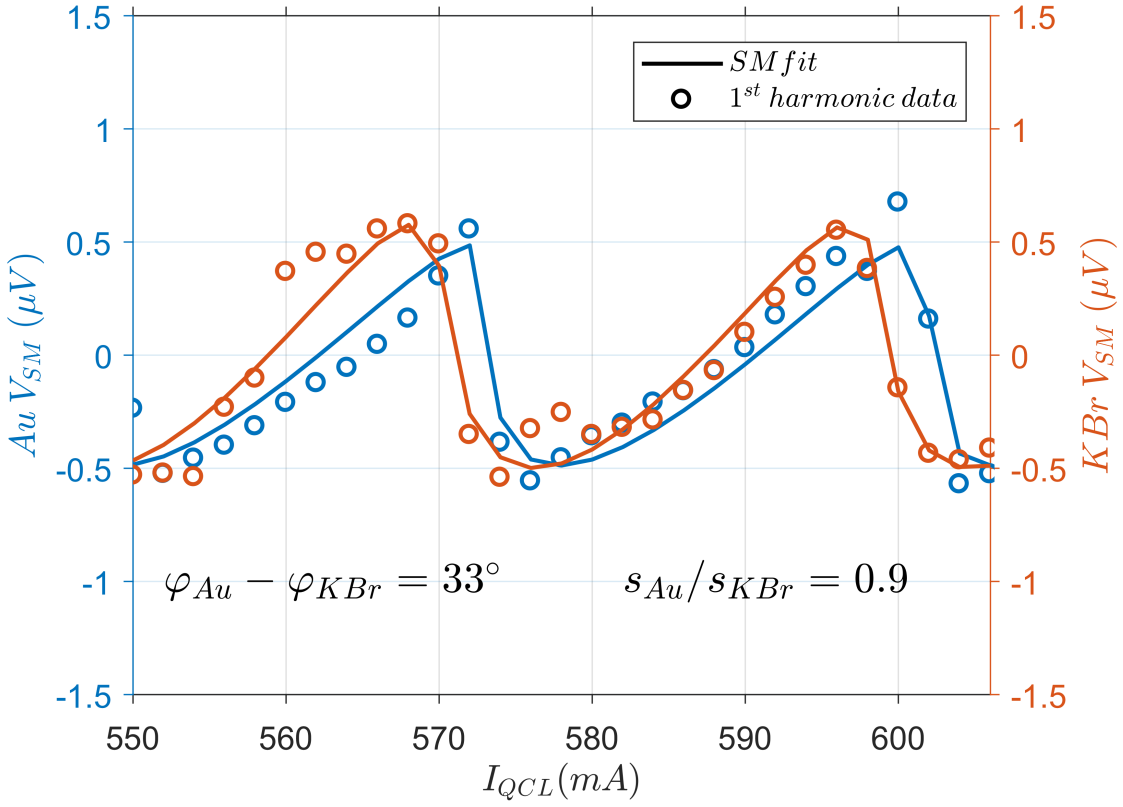

Figure 5.28: Interferometric fringes obtained for Au (left y-axes) and KBr (right y-axes) by averaging V_{SM} obtained from separate 1μm×1μm images of the two materials. The SM fit has been performed by following the algorithm of R. Kliese [19]. A $\varphi_{Au} - \varphi_{KBr}$ ≈33° and s_{Au}/s_{KBr} ≈0.9 could be extracted by the SM fit.

KBr, C_{KBr}=0.76 and α_{KBr}=-2.2133. While the values of C differ are in line with weak feedback regime of self-mixing [14], similar values are obtained for α since the same QCL was used for the measurements. Likewise, comparable tuning coefficients k, k_{Au}=6.73·10^6 Hz/mA and k_{SiO_2}=6.75·10^{6}Hz/mA were obtained, which are congruent with the values obtained from the previous sample. The phase difference and ratio of amplitudes extracted from these fits are $\varphi_{Au} - \varphi_{KBr}$ ≈33° and s_{Au}/s_{KBr} ≈0.9. In this case, both the phase difference and amplitude ratio are in good agreement with the FD model using L=500nm and g=1e$^{i0.1}$, as shown in figure 5.29. Specifically, the FD model for Au/KBr sample predicts a phase difference $\varphi_{Au} - \varphi_{KBr}$ ≈38° and the amplitude ratio s_{Au}/s_{KBr} ≈1.3 at the QCL lasing frequency, in accordance with the phonon resonance of KBr in the

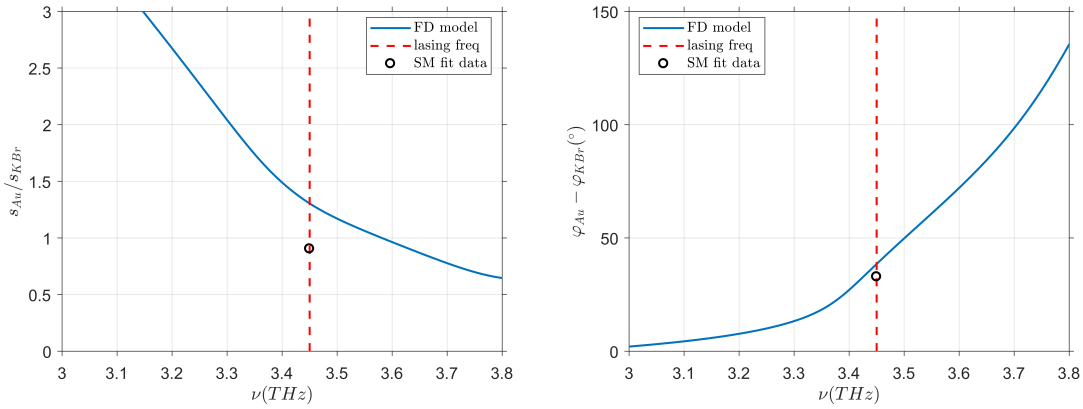

(a) (b)

Figure 5.29: Comparison between FD model and data extracted from the SM fit shown in figure 5.28. (a) Amplitude ratio, and (b) phase difference. Red dashed line indicates the QCL lasing frequency.

THz range as shown in figure 5.24(a). The slight discrepancy might still arise due to the experimental approach as well as the presence of background signal, considering the use of the 1^{st} harmonic data. Nevertheless, the all-electrical experimental approach described here opens the possibility to a new technique for extracting fundamental information of materials, including the complex permittivity, with a subwavelength resolution that can be potentially applied to many materials exhibiting resonant phenomena.

5.6 Possible implementation in the neaSNOM controller software

All the experiments using the stepped frequency SM approach applied to THz-s-SNOM were performed by manually changing the I_{QCL} for every image acquisition. The software of the neaSNOM did not provide direct control of I_{QCL} or any component external to the microscope, practically making the presence of the user essential. In order to increase the imaging rates, LabVIEW programs could be developed to automate changing the laser driving current while performing imaging of samples. Currently this isn't possible due to the lack of drivers available to control the neaSNOM, but Neaspec are currently developing drivers to allow this. As such, potential solutions in the form of flowcharts are presented for two potential imaging methods. These proposals considered two different manners in

order to acquire V_{SM} data: the pixel-by-pixel and the current-by-current approach. The

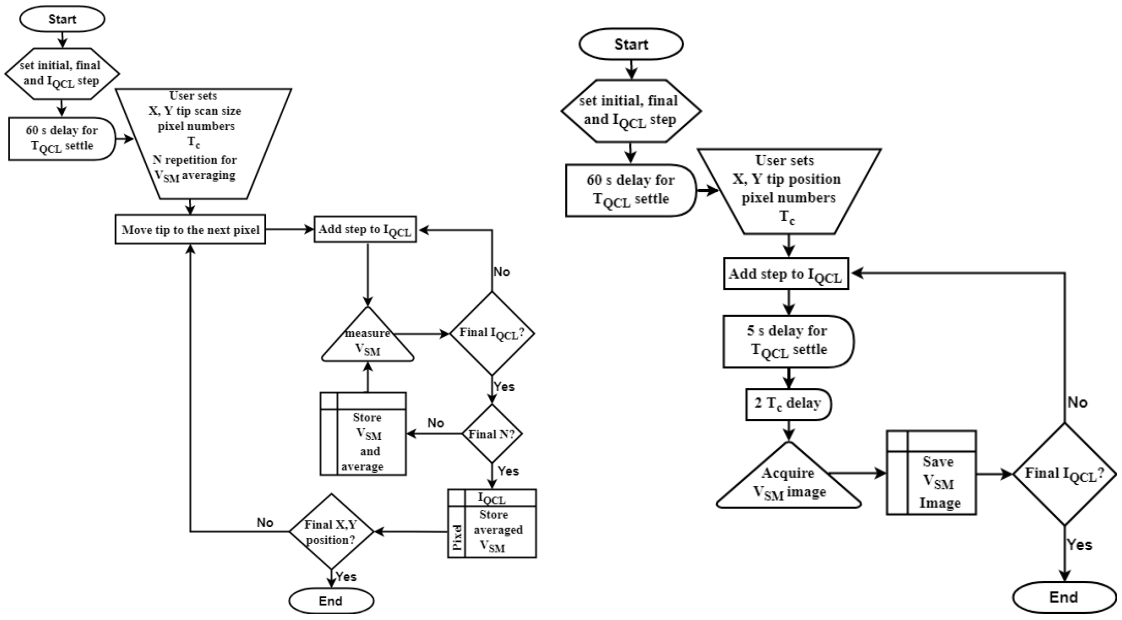

Figure 5.30: Flowchart of programs proposed to be implemented to the neaSNOM controller software. 5.30(a) pixel-by-pixel and (b) current-by-current approach.

pixel-by-pixel approach (see figure 5.30(a)), as the name suggests, acquires the V_{SM} fringes pixel by pixel. The user begins by entering the initial and final currents, and the current step, as well as the area to image, the imaging T_C and the number N of V_{SM} acquisition to be averaged. The code would run, setting the initial QCL driving current, and allowing 60 seconds for the QCL temperature to stabilise. The QCL temperature could also be read from the temperature controller to improve this function. The idea is that the software controls the entire I_{QCL} ramp on the first pixel storing the averaged (after average of N acquisitions) V_{SM} data at every current ramp; then the tip moves to the second pixel and continues imposing the current ramp for every chosen pixel. In this case the measurement time per current point would be determined by the T_C. For example, for T_C=1ms and 100 current points, the acquisition time per current ramp would be 100ms. This corresponds to a current stepping rate of 10Hz, which is enough to avoid the temperature of the QCL to be stabilised at every acquisition. Subsequently, by averaging 50 times (N) the acquisition, the total elapsed time would be 5s per pixel. The current-by-current approach (see figure

5.30(b)) instead would acquire the entire image before changing the laser current to the next value, similar to the method used in this chapter. One advantage of the pixel-by-pixel approach is it would avoid the sample drift caused by the repeated stage/tip movements in every image acquisition and would reduce tip degradation due to moving across the sample surface. Moreover the pixel-by-pixel approach would be faster than the current-by-current approach because it would avoid the 5s delay for the T_{QCL} stabilisation needed at every I_{QCL} value.

In order further improve the measurement procedure a radically different approach is here proposed. Instead of acquiring images of the samples under analysis, a better method would consist of exclusively recording approach curves. Measuring V_{SM} at the position of NF enhancement for each I_{QCL} would make the experiments less subjected to systematic errors caused by sample drift and QCL temperature drift. Also possible contaminations due to sample fabrication would have a smaller impact on the measurements. Similarly to the previous flowcharts, a block diagram for a program that acquires only approach curves is proposed in figure 5.31.

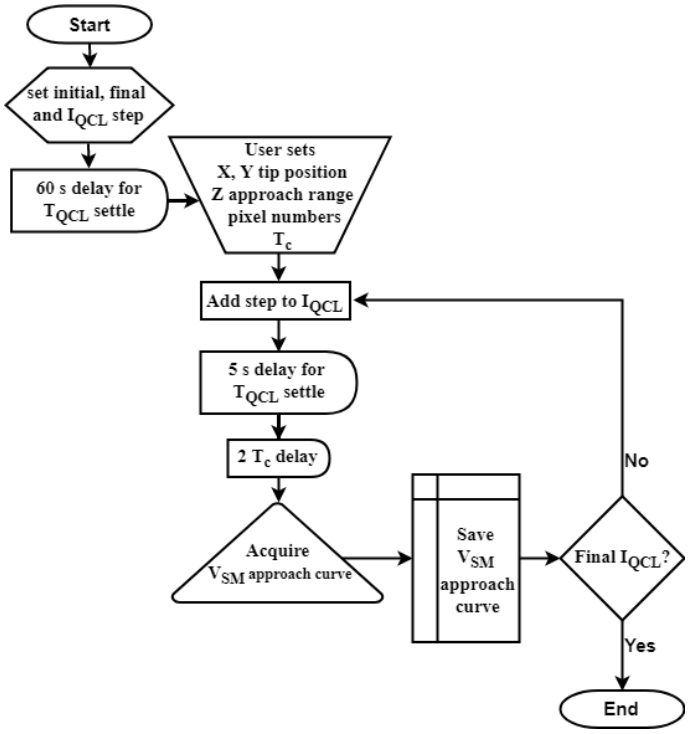

Figure 5.31: Proposed flowchart of a program that acquires approach curves for all the range of chosen I_{QCL}.

5.7 Conclusions

In this chapter, two different experimental systems for NF microscopy based on SM detection in a THz QCL have been presented. Despite the approach curves showing a NF enhancement of the SM signal demodulated up to 2^{nd} harmonic of the tip tapping frequency, the bespoke system suffered limitations given by the poor control of tip-sample surface distance (d). Considering that the NF enhancement occurs when d is comparable to the tip radius of curvature, the possibility to acquire an image is strictly related to the ability of the system to maintain d constant during the acquisition. Despite this approach have shown to work previously [185], the mentioned problem prevented the acquisition of images in this work. As such, a solution based on the implementation of a feedback circuit loop is proposed, similar to the work reported by R. Degl'Innocenti et al in [122].

The second system exploited a commercially available s-SNOM/AFM platform called neaSNOM made by the company Neaspec GmbH, which was operated using the SM

detection scheme. Acquisition of V_{SM} demodulated up to the 5th harmonic and with a subwavelength imaging resolution of 83nm ($\sim \lambda/1000$) has been demonstrated by employing a QCL based on a hybrid structure and lasing at ∼3.45THz. The system was characterized, and a clear dependence of the resolution on the tip tapping amplitude has been demonstrated. In order to select the ideal experimental parameters, the same image was acquired with different integration times, T_c; a good contrast between Au and Si was found for T_c=50ms, but T_c=200ms was selected as the best trade-off to ensure clear contrast and reasonable acquisition time.

Exploiting the dependence of the QCL lasing frequency on I_{QCL} a stepped-frequency SM scheme was developed enabling coherent NF imaging measurements of the phase φ_n and amplitude s_n of a specific sample, using an all-electrical approach. The possibility to retrieve complex permittivity information of materials has been demonstrated by using two different samples, Au/SiO_2 and Au/KBr. The results have been compared to prediction of the FD model in which the metallic tip is modelled as a spheroid which mirrors the dipole, created by the incident beam, into the sample. While the Au/KBr sample has shown a really good agreement with the theory, a slight discrepancy in the measured phase contrast was found for the Au/SiO_2 sample, which has been attributed to the experimental conditions and the influence of the background signal, as suggested also by Cvitkovic *et al* [238].

Future development of THz-s-SNOM based on SM detection in QCLs could benefit from a broader QCL frequency tuning and consequently a wider frequency range to investigate fundamental properties of materials. Possible applications will range from imaging biomaterials to the investigation of quantum or plasmonic devices where the subwavelength resolution of the s-SNOM is an essential feature to understand the nano world phenomena.

6 THz near-field imaging of graphene

Since Novoselov K. et al introduced the mechanical exfoliation method to produce large areas of graphene with relatively high quality [240], the interest of the research community in this material has grown exponentially. Due to its intriguing electronic and optical properties the emerging applications of this material are wide ranging. For example, graphene field effect transistors with astonishingly high mobility have shown ambipolar behaviour making it a material with the potential to replace silicon electronics in the future [240–242]. It has also been employed for the production of ultrafast lasers [241, 243, 244]. Since it's a transparent material, it can be used not only as an electrode for solar cells, replacing the more expensive Indium tin oxide (ITO), but also as a touch screen electrode [245–247]. Thanks to its semi-metal nature graphene has also been employed in photodetectors for mid-IR and THz light [248–252]. Graphene has also shown the possibility to support tunable propagating plasmons in the mid-IR and THz ranges [25, 26, 28, 142, 143, 145, 253–255]. Furthermore, it has been integrated in a metal resonator, and by electrically tuning its Fermi energy has been used as a THz light modulator [256] and also as a broadband optical modulator [244].

This chapter is dedicated to the study and imaging of graphene sheets through THz-s-SNOM employing a THz quantum cascade laser with a particular focus on the possibility of imaging propagating plasmons in graphene using THz radiation. To date this has been demonstrated only thermo-electrically [26] or in the time-domain through an aperture-type SNOM approach [25].

The chapter first presents the relevant theory and describes the modelling of surface plasmons in graphene taking into account two possible substrate materials, silicon dioxide SiO_2 and hexagonal boron nitride h-BN. The model is further developed to simulate THz-s-SNOM employing s-SNOM tips of different size. Subsequently, Section 6.3 will discuss the processing of graphene samples and finally Section 6.4 the acquired THz NF images, supported by Raman spectra, will be shown and discussed.

6.1 Theory and Modelling

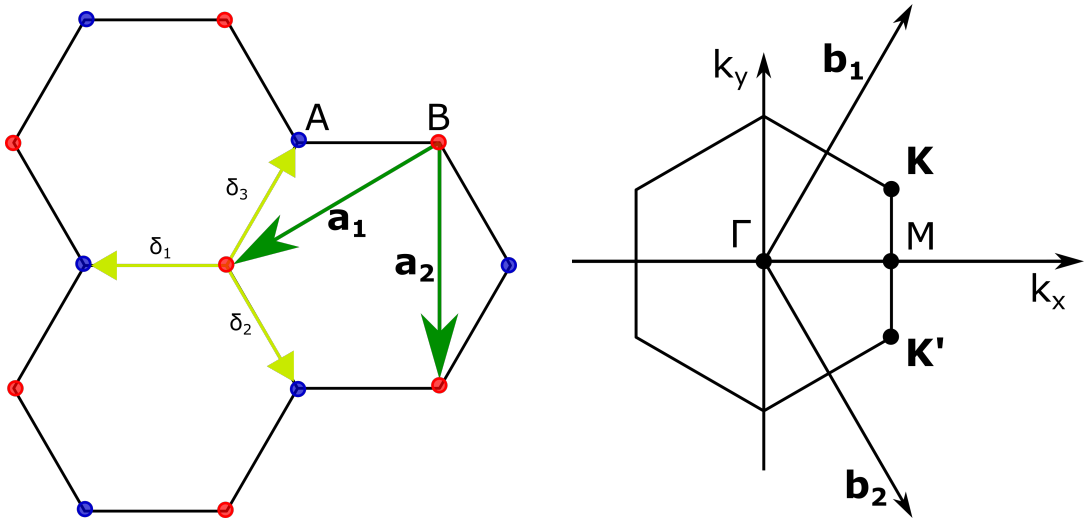

(a) (b)

Figure 6.1: (a) Graphene honeycomb lattice and (b) its Brillouin Zone. In (a) $\mathbf{a}_1$ and $\mathbf{a}_2$ are the lattice unit vectors indicating a triangular lattice; δ_1, δ_2 and δ_3 are the nearest-neighbor vectors. In (b) the dirac points are K and K'.

Graphene is a single atomic layer of graphite [257]. Carbon atoms in graphene are arranged in a honeycomb structure, as shown in fig. 6.1(a). The unit cell consists of two atoms basis structured in a triangular lattice, with lattice vectors, $\mathbf{a}_1$ = a/2(3, $\sqrt{3}$) and $\mathbf{a}_2$ = a/2(3, -$\sqrt{3}$), where a ≈ 1.42 Å is the carbon-carbon distance. The three nearest-neighbour vectors in real space are δ_1 = a/2(1, $\sqrt{3}$), δ_2 = a/2(1, -$\sqrt{3}$) and δ_3 = -a(1, 0). The next six second-nearest neighbours are at $\delta_1' = \pm a_1$, $\delta_2' = \pm a_2$ and $\delta_3' = \pm(a_2\text{-}a_1)$ [240, 257, 258]. Figure 6.1(b) also shows the reciprocal lattice, in which the vectors are defined as $\mathbf{b}_1$ = 2π/3a(1, $\sqrt{3}$) and $\mathbf{b}_2$ = 2π/3a(1, -$\sqrt{3}$). The K and K' points at the corner of the Brillouin zone (BZ) in the reciprocal lattice are called Dirac points and their position are given by **K** = (2π/3a,2π/3$\sqrt{3}$a) and **K'** = (2π/3a,-2π/3$\sqrt{3}$a). The band structure of graphene can be derived by the tight-binding model which shows a unique characteristic around the Dirac points K and K'. At K and K' the energy dispersion has a linear relationship with the momentum and can be described by the simple relation $E_n(p) = nv_f p$, where $v_f \approx 10^6$ m/s (≈ c/300) is called the Fermi velocity and n = ± 1 for the valence (-) or conduction (+)

band [21, 240, 257–260]. Experimental studies have confirmed that electron transport in graphene is governed by Dirac's relativistic equation where the charges have been shown to be massless dirac fermions, sustaining the thesis of a linear energy dispersion and a c/300 fermi velocity [21, 258]. In the absence of doping the Fermi energy of graphene lies at E_F = 0 eV and electrons are all confined in the valence band. There are no free electrons and the electrical conductivity is at the lowest value; this point is called the charge neutrality point (CNP). In the presence of photons direct interband excitations of valence electrons and the creation of hole-electron pair can occur at all photons frequencies, which makes graphene a 0 eV band gap material. The presence of dopants in the graphene can alter this status in two different ways. In the first case, a dopant can move E_F to positive values ($E_F > 0$ eV) making electrons occupy part of the conduction band, which automatically excludes some optical transitions due to the Pauli exclusion principle. With large doping, CB electrons are unbound from the static potential and will be free to move, making graphene behave in a similar way to a metal, but with the presence of an energy band gap. In this case the conductivity will be higher than the $E_F = 0$ eV case. In the other case, a dopant can move E_F to negative values ($E_F < 0$ eV), again excluding some optical transitions and hence creating an energy band gap. In this case the conductivity will again be higher than for $E_F = 0$ eV, but due to the hole concentrations instead of electrons [21, 240, 257–260]. These 3 cases are well explained in figures 6.2(a), 6.2(b) and 6.2(c).

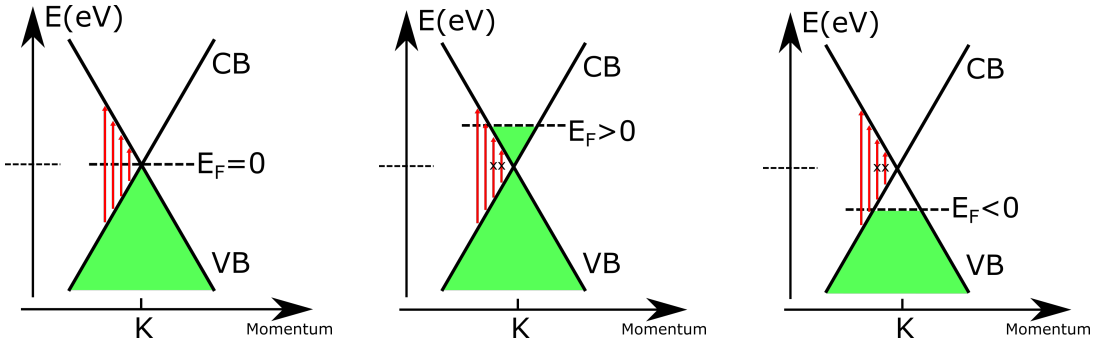

Figure 6.2: Theoretical energy bands of graphene for (a) $E_F = 0$ eV, (b) $E_F > 0$ eV and (c) $E_F < 0$ eV. Red arrows indicate possible and excluded (**X**) optical interband transitions. Green area indicates the band occupied by the electrons. CB and VB respectively stands for Conduction and Valence band.

From the experimental point of view, doping can be achieved in different ways: self-doping caused by the presence of defects due to the processing of graphene [22, 258, 261–264] or by the adsorption of molecules or nanoparticles (NPs) [22, 23, 264–270]; and doping due to field-effect [20, 21, 242, 251, 252, 269, 271, 272].

Doping due to the field effect is caused by the effect of an electric field applied perpendicularly to the graphene surface. It is a well known effect and is the basis of every field effect transistor. In a conventional Si field-effect transistor the application of an electric field perpendicularly to the Si channel shifts the Si Fermi level at the Si/oxide(or dielectric) interface, making the bands bend; as a consequence an increase (or decrease) of carrier concentration in the conduction band will occur. This, in turn, modifies the conductivity depending on the nature of the channel (n-channel or p-channel). As already mentioned, the conductivity of graphene has a minimum at its CNP and increases independently by applying either a positive or a negative electric field. The channel is one atomic layer of carbons and the Fermi level will be tuned depending on the applied electric field. The graphene field effect transistor has shown an ambipolar behaviour because the conduction is established both for electrons and holes and has been experimentally demonstrated with both the top and back-gated geometry, as shown in figures 6.3(b) and 6.4(b) [20, 21, 242, 251, 252, 269, 271, 272].

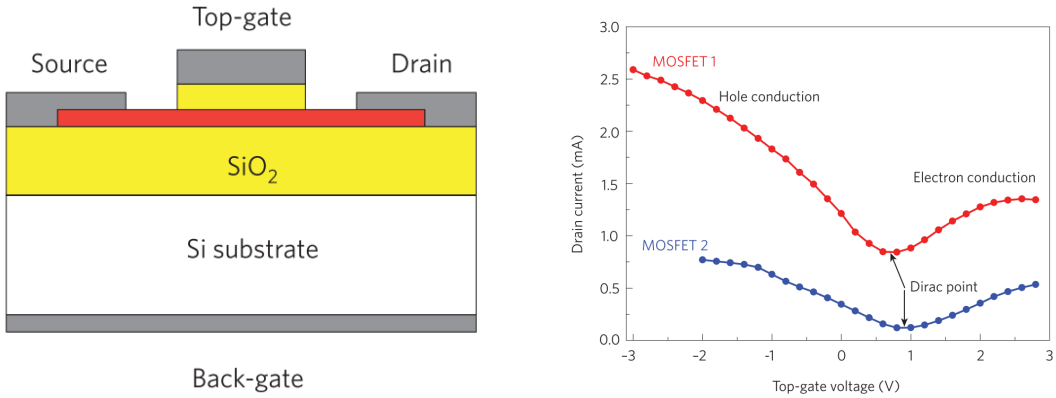

(a) (b)

Figure 6.3: (a) Top-gated MOSFET based on graphene channel transfered on a SiO_2/Si substrate. (b) Drain Current vs Top Gate Voltage characteristic showing the ambipolar nature of a graphene channel. Adapted from Schwierz [20]

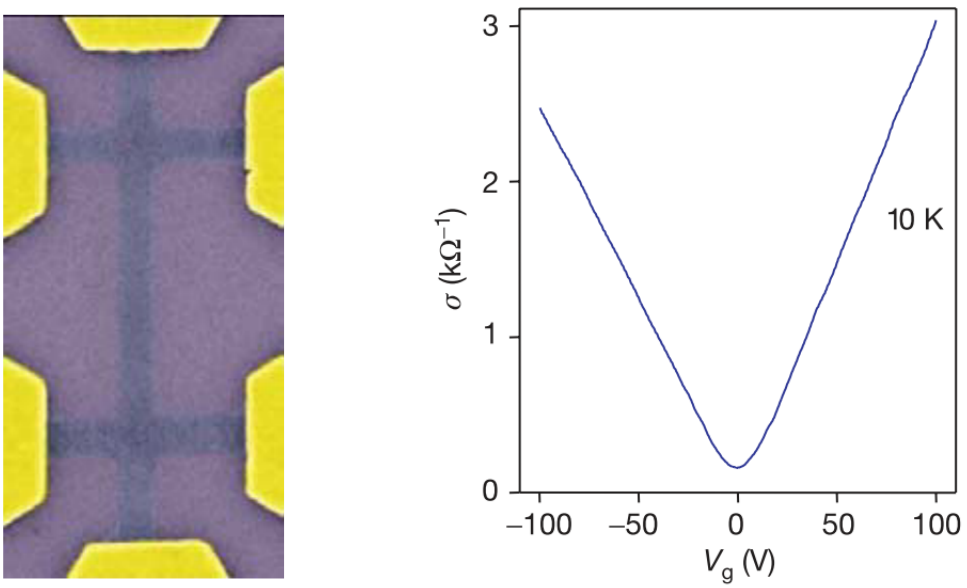

(a) (b)

Figure 6.4: (a) Scanning electron microscope image of a back-gated graphene transistor (the width of the central wire is 0.2 μm). (b) Changes in graphene's conductivity σ as a function of gate voltage V_g, at 10 K. Adapted from Novoselov [21]

Self-doping and doping due to the adsorption of molecules have a static effect on the Fermi level of graphene, meaning they mainly affect the CNP of the graphene sample. Experimental observations have demonstrated, for example, how doping graphene with nitrogen atoms during its synthesis can alter the CNP [22], and consequently also the sample mobility. It's worth mentioning that doping graphene during its synthesis means that dopant atoms can substitute the carbon atoms in the graphene structure. This is different to adsorption, where ligands, molecules or nanoparticles bond to the carbon atoms on the surface of graphene, without altering its structure. For example, it has been demonstrated that ligand-bound nanoparticles such as iron oxide, titanium dioxide or cadmium selenide, which act as charge reservoir, can strongly affect the CNP and charge mobility [23]. These effects are shown in figures 6.5(a), 6.5(b) and 6.5(c).

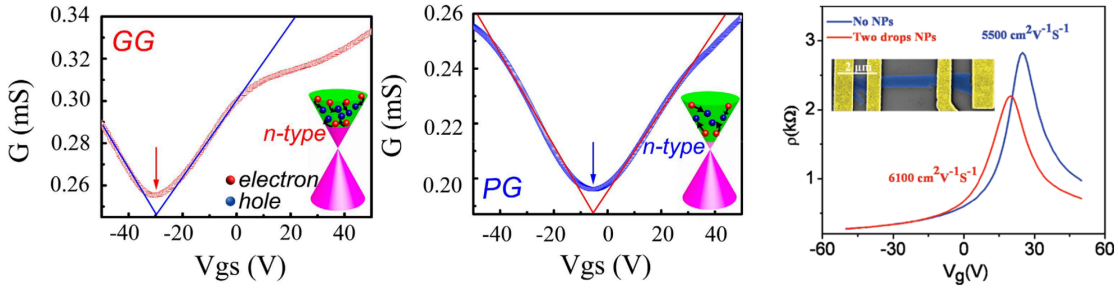

(a) (b) (c)

Figure 6.5: (a) Conductance (G) as a function of gate voltage (V_{gs}) for graphitic nitrogen dopant (GG) with G_{min} at - 30 V, V_{ds} = 1 V. Inset is energy band of the GG, the red and blue spheres represent the electron and hole, respectively. (b) Conductance (G) as a function of gate voltage (V_{gs}) for pyrrolic nitrogen dopant (PG) with G_{min} at - 5.2 V, V_{ds} = 1 V. Inset is energy band of the PG. (a) and (b) adapted from Zhang [22]. (c) Resistivity vs gate voltage for pristine graphene (blue) and the same device receiving two drops of NP solution (red). Inset shows the scanning electron micrograph of a pristine graphene device. Adapted from Wang [23]

6.1.1 Surface Plasmons in Graphene

The reason of imaging propagating plasmons on graphene is related to the possibility of applying this material for antenna devices. The confinement of the light to smaller (than the original) wavelength provided by the plasmonic resonance on the graphene surface open the possibility to have antennas based on graphene able to efficiently detect a broader range of wavelength by simply tuning the graphene fermi energy [143, 273], due to the semi-metal behaviour of this material. Moreover from a near-field image of propagating plasmons, their wavelength can be directly measured making the plasmon wavelength calculation effectively easy [143]. As mentioned in the previous section, for high doping, graphene has free carriers and so can be considered as a semi-metal due to the presence of an energy gap, which gives the possibility of interband transitions. Acting as a metal, its optical conductivity $\sigma(\omega)$ can be described by a generalized Drude model with the addition of a term that accounts of these interband transistions [24, 27, 142, 253, 259, 274–277], as will be discussed in Section 6.1.2.

The standard Drude model is used commonly to describe metal-light interactions and to explain conduction in metals. The optical response of a material can, in general, be

explained by its dielectric function $\varepsilon(\omega)$, which is strongly dependent of the light frequency, ω. Metals described by the Drude model are approximated as fixed cores (the atoms nuclei) surrounded by a gas of quasi-free electrons, which give rise to conduction in the metal. In this perspective the metal dielectric function can be written as [277, 278],

$$\varepsilon(\omega) = \varepsilon_\infty\left(1 - \frac{\omega_p^2}{\omega^2 + i\gamma\omega}\right), \tag{6.1}$$

where ω_p is the bulk plasma frequency, γ is the damping constant and ε_∞ is the high frequency dielectric offset; ω_p is characteristic of each metal and usually lies in the UV range of the electromagnetic spectrum and is given by the expression,

$$\omega_p = \sqrt{\frac{ne^2}{m_e\varepsilon_0}}, \tag{6.2}$$

where n is the carrier concentration, e is the electron charge, m_e is the electron effective mass and ε_0 the vacuum permittivity. When $\omega < \omega_p$, the real part of $\varepsilon(\omega)$ is negative and no radiation can propagate through the metal. For $\omega > \omega_p$ the metal becomes transparent and radiation can propagate [277, 278].

In order to understand the interaction between light and graphene, attention also needs to be given to the excitation of the surface plasmons (SPs). SPs are p-polarized electromagnetic (EM) waves trapped at the interface between a conductor (for example a metal with dielectric function $\varepsilon(\omega)$) and a dielectric (with dielectric constant ε_r); these are transverse magnetic (TM) modes caused by collective oscillations of surface charges bound to the interface, which are solutions of Maxwell's equation[277, 278]:

$$\nabla \times \nabla \times \boldsymbol{E}(\boldsymbol{r},\omega) - \frac{\omega^2}{c^2}\varepsilon(\omega)\boldsymbol{E}(\boldsymbol{r},\omega) = 0, \tag{6.3}$$

where $\mathbf{E}(\mathbf{r},\omega)$ is the oscillating electric field propagating along the vector $\mathbf{r}$. By considering that above the metal surface (defined at x=0) this electric field decays exponentially, it is possible to write E(x>0) $\propto e^{-Kx}$. At the same time, in the metal the field propagates with wavevector K_m, and so E(x<0) $\propto e^{K_m x}$, where x is the direction normal to the

metal surface. The wavevectors K and K_m can be expressed as $K = \sqrt{K_{SP}^2 - \varepsilon_r(\omega^2/c^2)}$, $K_m = \sqrt{K_{SP}^2 - \varepsilon(\omega)(\omega^2/c^2)}$. Then by matching the boundary conditions for the TM polarization, it is possible to obtain the relation,

$$1 = -\frac{\varepsilon(\omega)K}{\varepsilon_r K_m}. \tag{6.4}$$

Finally, by substituting K and K_m in equation 6.4 and solving for K_{SP}, the SP wavevector can be described by the dispersion relation [24, 259, 277, 278]:

$$K_{SP} = \frac{\omega}{c}\sqrt{\frac{\varepsilon_r\varepsilon(\omega)}{\varepsilon_r + \varepsilon(\omega)}}, \tag{6.5}$$

in which ω is the light frequency, c the speed of light and $\varepsilon(\omega)$ is given by equation 6.1 for a bulk metal. From equation 6.5 it is possible to note how the expression diverges to the value $K_{SP} \gg \omega/c$ for certain frequencies. These are the frequencies where $\varepsilon(\omega) = -\varepsilon_r$ which gives rise to an interesting peculiarity of SPs. Namely, they are able to confine EM waves far below the diffraction limit. Indeed, $\varepsilon(\omega) < -\varepsilon_r$ is a necessary condition for the existence of SPs, and this is why metals are usually used [24, 259, 277, 278] in optical experiments. Figure 6.6 shows the SP dispersion relation at the interface of Si/Ag [24]. Around the SP resonance (where $\omega/\omega_{sp} = 1$) the SP wavevector is much larger than the wavevector propagating in Si (the dielectric), and hence the SP wavelength is much smaller than the wavelength of light propagating in the dielectric.

Now by considering a thin slab of metal of thickness d, the permittivity (dielectric function) can be re-written in terms of the optical conductivity following the relation [24, 259, 277, 278],

$$\varepsilon(\omega) = 1 + \frac{i\sigma_v}{\omega\varepsilon_0} \tag{6.6}$$

In equation 6.6, σ_v is the volume conductivity related to the expression $\mathbf{J}_v = \sigma_v\mathbf{E}$. In the case of a very thin metal, $d{\cdot}K_m \ll 1$, currents are uniform at the metal surface and $\mathbf{J}_s = \sigma_s\mathbf{E} = \mathbf{J}_v \cdot d$, where $\sigma_s = \sigma_v \cdot d$ is the surface conductivity. Consequently it is possible to

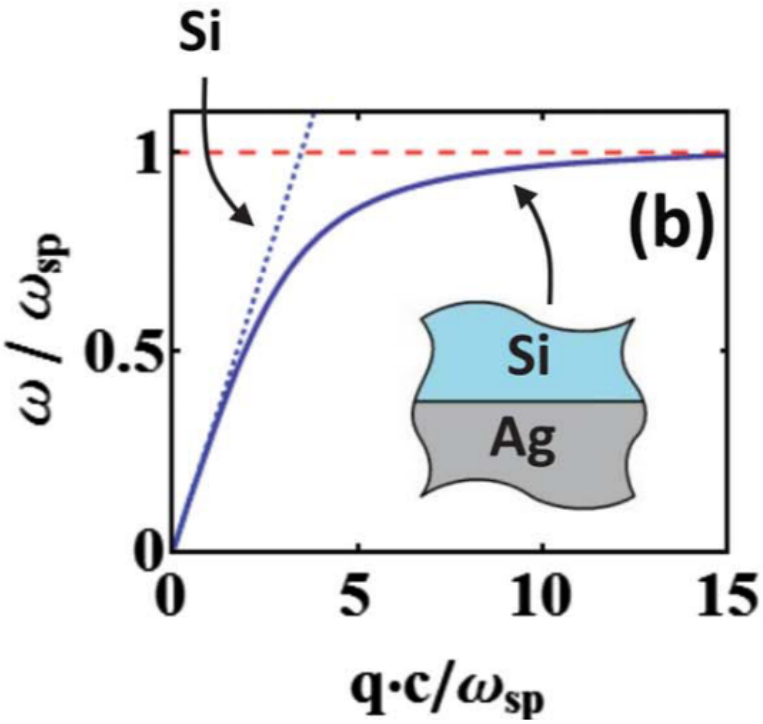

Figure 6.6: SPs dispersion curve (solid blue line) for Ag-Si interfaces; dotted blue is the light line in Si; dashed red line denotes the SP resonance. Adapted from Jablan [24]

obtain the dispersion relations as function of the surface conductivity:

$$K_{SP} = \frac{2i\omega\varepsilon_0\varepsilon_r}{\sigma_s} \tag{6.7}$$

Graphene can be considered essentially as a 2D electronic system. It is usually placed on a dielectric substrate (with dielectric constant ε_r) and if not specified is surrounded by air as depicted in figure 6.7.

Similarly to the case of metals, TM modes can be found by assuming that the electric field decays exponentially in the direction normal to the graphene surface and has the form:

$$E_z = A\exp^{iqz-Q_1x}, \quad E_y = 0, \quad E_x = B\exp^{iqz-Q_0x}, \quad for \quad x > 0, \tag{6.8}$$

$$E_z = C\exp^{iqz+Q_1x}, \quad E_y = 0, \quad E_x = D\exp^{iqz+Q_0x}, \quad for \quad x < 0, \tag{6.9}$$

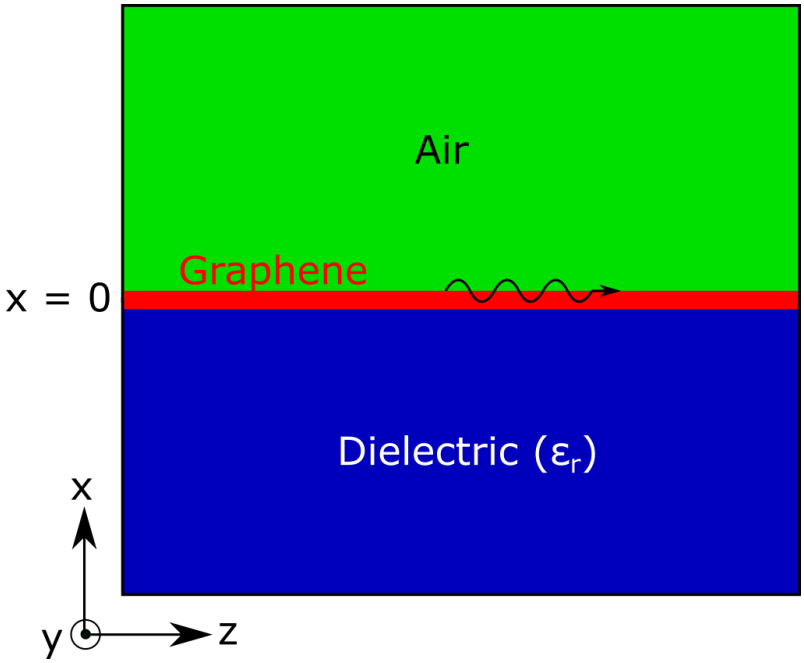

Figure 6.7: Schematic of the graphene system and TM plasmon modes

where q is the SP wavevector. Inserting these expressions into Maxwell's equations and matching the boundary conditions it is possible to obtain the dispersion relation for p-polarized EM waves on the graphene surface,

$$\frac{\varepsilon_r}{\sqrt{q^2 - \frac{\varepsilon_r \omega^2}{c^2}}} + \frac{1}{\sqrt{q^2 - \frac{\omega^2}{c^2}}} = -\frac{\sigma(\omega, q) i}{\omega \varepsilon_0} \tag{6.10}$$

In the electrostatic regime (q$\gg \omega$/c), equation 6.10 can be reduced to:

$$q \approx Q_0 \approx Q_1 \approx \frac{i\varepsilon_0(\varepsilon_r + 1)\omega}{\sigma(\omega, q)} \tag{6.11}$$

Equation 6.11 represents the dispersion relation of plasmons on the graphene surface [24, 27, 142, 143, 253, 259]. Furthermore by adding to the optical conductivity an explicit dependence on the wavevector, and not only on the frequency, the possibility of nonlocal effects can be taken into account, where the mean free path of the electrons can be smaller than q^{-1}. It is worth mentioning that even though the dispersion relations for plasmons in graphene and SPs in metals (equations 6.7 and 6.11, respectively) have a similar form,

they are qualitatively different because electrons in graphene are frozen in the transverse direction [21, 240, 257–260, 279]. Moreover, while for conventional metals the bulk plasma frequency, ω_p, shows a dependence $\propto \mathrm{n}^{1/2}$, with the carrier concentration (see equation 6.2), in graphene, due to Landau interband damping, this dependence becomes $\propto \mathrm{n}^{1/4}$, by following the relation given by equation 6.12 [249].

$$\omega_p = \sqrt{\frac{eE_F q}{2\pi\hbar^2\varepsilon_0\varepsilon_r}}, \tag{6.12}$$

where E_F is the fermi energy of graphene. This proportionality can be seen by using the simple relations given by the Drude model, $\mathrm{n}=\mathrm{k}_F^2/\pi$ and $\mathrm{m}_e=\mathrm{E}_F/\mathrm{v}^2$ [249].
In order to calculate the plasmon dispersion relation in graphene, an expression for the conductivity is needed.

6.1.2 The conductivity of Graphene

Thanks to the semi-metal nature of graphene, it is possible to adopt a semi-classical model which does not account for the dependence of the conductivity on the wave vector. This model leads to a Drude-like expression [24, 253, 259, 277, 280] in the form:

$$\sigma_D(\omega) = \frac{e^2 E_F}{\pi\hbar^2}\frac{i}{\omega + i\tau^{-1}}, \tag{6.13}$$

where e is the elementary charge, E_F the Fermi energy and τ is the relaxation time (RT). The RT is a parameter linked to the losses due to electron impurity, electron defects, and electron-phonon scattering. Equation 6.13 assumes a temperature $\mathrm{T} \approx 0$, which is a good approximation for high doping for which $\mathrm{E}_F \gg \mathrm{k}_B\mathrm{T}$. By combining equations 6.13 and 6.11 a direct equation for the plasmon dispersion relation is obtained:

$$q(\omega) = \frac{\pi\hbar^2\varepsilon_0(\varepsilon_r+1)}{e^2 E_F}\Big(1 + \frac{i}{\tau\omega}\Big)\omega^2 \tag{6.14}$$

The effect of losses can be represented by a dimensionless number called the plasmon propagation constant (PP), which can be interpreted as the propagation distance of plasmons

on the graphene surface before they vanish, expressed as a number of plasmon wavelengths by the following relation,

$$PP = \frac{\Re q}{2\pi \Im q}. \tag{6.15}$$

Using equation 6.14 we obtain the following expression for PP, which shows a direct relation with the RT:

$$PP = \frac{\omega\tau}{2\pi}. \tag{6.16}$$

An estimation of the relaxation time, τ, can be obtained by DC mobility measurements if the photon energy is below the interband transition ($\hbar\omega$<2E$_F$) and if ω<ω_{Oph}, which is optical phonon threshold of graphene ($\hbar\omega_{Oph} \approx 0.2eV$ [254]). In this case RT can be expressed as [24, 253, 259],

$$\tau_{DC} = \frac{\mu E_F}{e v_F}, \tag{6.17}$$

where μ is the DC mobility and v$_F$ is the Fermi velocity, which is the velocity associated with the Fermi energy according to the relation, E$_F$=$\frac{1}{2}$mv$_F^2$. It's important to emphasize that in this regime ($\hbar\omega$<2E$_F$ and ω<ω_{Oph}), scattering from impurities and defects are the major limiting processes affecting the relaxation time [24, 259]. Excitation of hole-electron pairs is not expected because ω is well below the frequency of interband transitions and the phonon frequency (intraband transitions). Therefore, the major factor limiting RT, and in turn PP, will be the DC mobility determined by these scattering processes.

However, for ω greater than or equal to 2E$_F$ electron transitions can occur, and hence the losses increases. In order to account for interband transitions a self-consistent linear response theory, called the Random Phase Approximation (RPA), with the relaxation time approximation introduced by Mermin [277, 281] (for finite τ) can be employed. Within the RPA the electric susceptibility of graphene is given by [24, 143, 253, 259, 276, 280, 282]

$$\chi(q,\omega) = \frac{e^2}{q^2}\Pi(q,\omega), \tag{6.18}$$

where

$$\Pi(q,\omega) = \frac{4}{\Omega}\sum_{\boldsymbol{k},n_1,n_2} \frac{f(E_{n_2,\boldsymbol{k}+\boldsymbol{q}}) - f(E_{n_1,\boldsymbol{k}})}{\hbar\omega + E_{n_1,\boldsymbol{k}} - E_{n_2,\boldsymbol{k}+\boldsymbol{q}}} \times \left|\langle n_1,\boldsymbol{k}|e^{-i\boldsymbol{q}\boldsymbol{r}}|n_2,\boldsymbol{k}+\boldsymbol{q}\rangle\right|^2, \tag{6.19}$$

in which $f(E) = (e^{E-E_F/k_BT}+1)^{-1}$ is the Fermi-Dirac distribution and n_x represents the band indices. In equation 6.19 the factor 4 arises from the degeneracies of 2 valleys and 2 spins. In the RPA-RT approach the effect of defects, impurities and phonons scattering are taken into account through the RT [281]; moreover conservation of electron number is assumed. In this perspective the susceptibility can be written as,

$$\chi_\tau(q,\omega) = \frac{(1+i/\omega\tau)\chi(q,\omega+i/\tau)}{1+(i/\omega\tau)\chi(q,\omega+i/\tau)/\chi(q,0)}. \tag{6.20}$$

The conductivity is then obtained by the relation,

$$\sigma_I(q,\omega) = -i\omega\chi_\tau(q,\omega). \tag{6.21}$$

By solving equation 6.21 in the limit q→0 and for T=0, it is possible to derive an expression for the contribution to the conductivity of graphene, in the RPA approximation, which considers the interband transitions,

$$\sigma_I(\omega) = \frac{e^2}{4\hbar}\Big(\theta(\hbar\omega-2E_F) - \frac{i}{\pi}ln\left|\frac{2E_F+\hbar\omega}{2E_F-\hbar\omega}\right|\Big), \tag{6.22}$$

where the step function, θ is defined as,

$$\theta(\hbar\omega-2E_F) = \begin{cases} 0,\ \hbar\omega < 2E_F \\ 1,\ \hbar\omega \geq 2E_F \end{cases} \tag{6.23}$$

As a result the total conductivity of graphene is given by summing equation 6.13 and 6.22, $\sigma = \sigma_D + \sigma_I$, which yields,

$$\sigma(\omega) = \frac{e^2 E_F}{\pi\hbar^2}\frac{i}{\omega + i\tau^{-1}} + \frac{e^2}{4\hbar}\left(\theta(\hbar\omega - 2E_F) - \frac{i}{\pi} ln\left|\frac{2E_F + \hbar\omega}{2E_F - \hbar\omega}\right|\right) \tag{6.24}$$

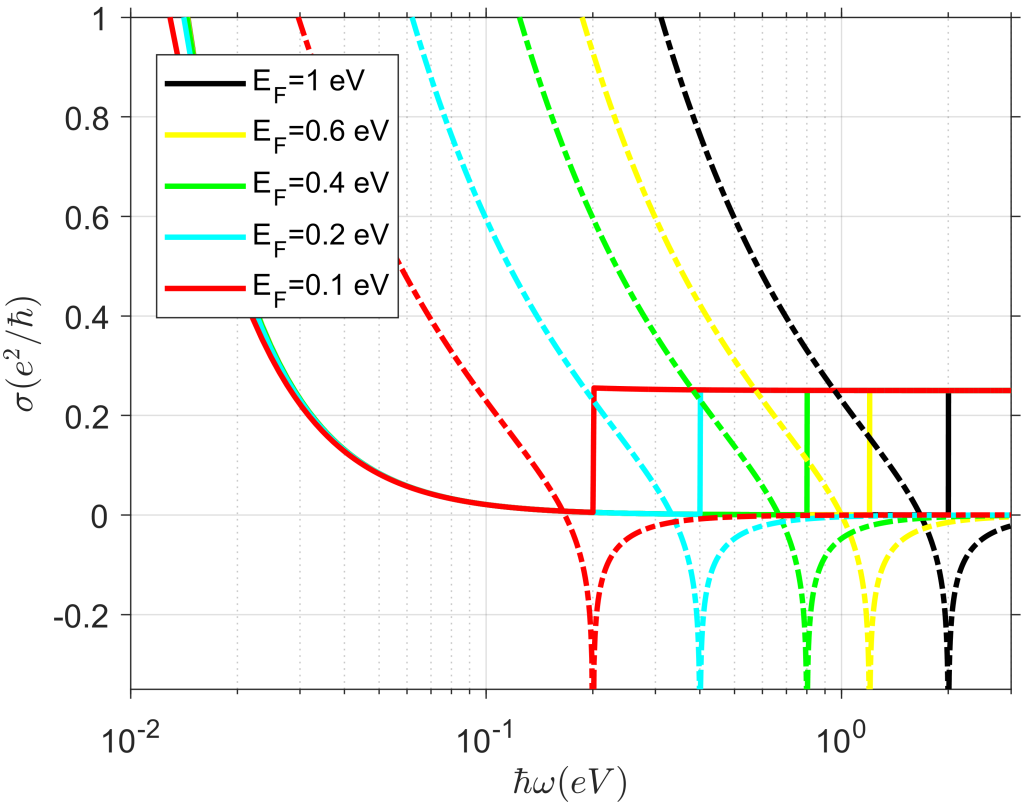

Figure 6.8: Real (solid curve) and Imaginary (dashed curve) parts of graphene conductivity obtained by the RPA-RT approximation for different doping level (E_F)

Figure 6.8 shows the real and imaginary parts of the conductivity of graphene obtained from equation 6.24, for different doping levels, and assuming an electron mobility μ=10000 cm^2/Vs. From the graph can be seen that the imaginary part of the conductivity becomes negative for frequencies around $2E_F$. In this region there are no solutions to the dispersion relation and consequently graphene cannot support TM modes. For $\hbar\omega > 2E_F$ the real part reaches the universal value of $\sigma_0 = e^2/4\hbar$ [24, 253] which indicates a loss process; electrons are excited by the incident photons from the valence to the conduction band. This effect

has been experimentally confirmed, with only 2.3% of white light being absorbed by a single layer of graphene [283]. The behaviour of the real and imaginary parts of the conductivity has also been verified experimentally with infrared spectromicroscopy, by studying the transmission and reflectance of a graphene device under different applied gate voltages [276]. For T>0 the effect of a non-zero temperature is to marginally smooth the steep increase of the real part of the conductivity and also to smooth the negative peak of the imaginary part occurring in proximity of the interband transition at $2E_F$ [24, 253, 259, 280].

From equation 6.11 and 6.24 the real part of the plasmon wavevector can be evaluated as a function of the incident photon energy, allowing the plasmon dispersion relation to be plotted for different doping levels.

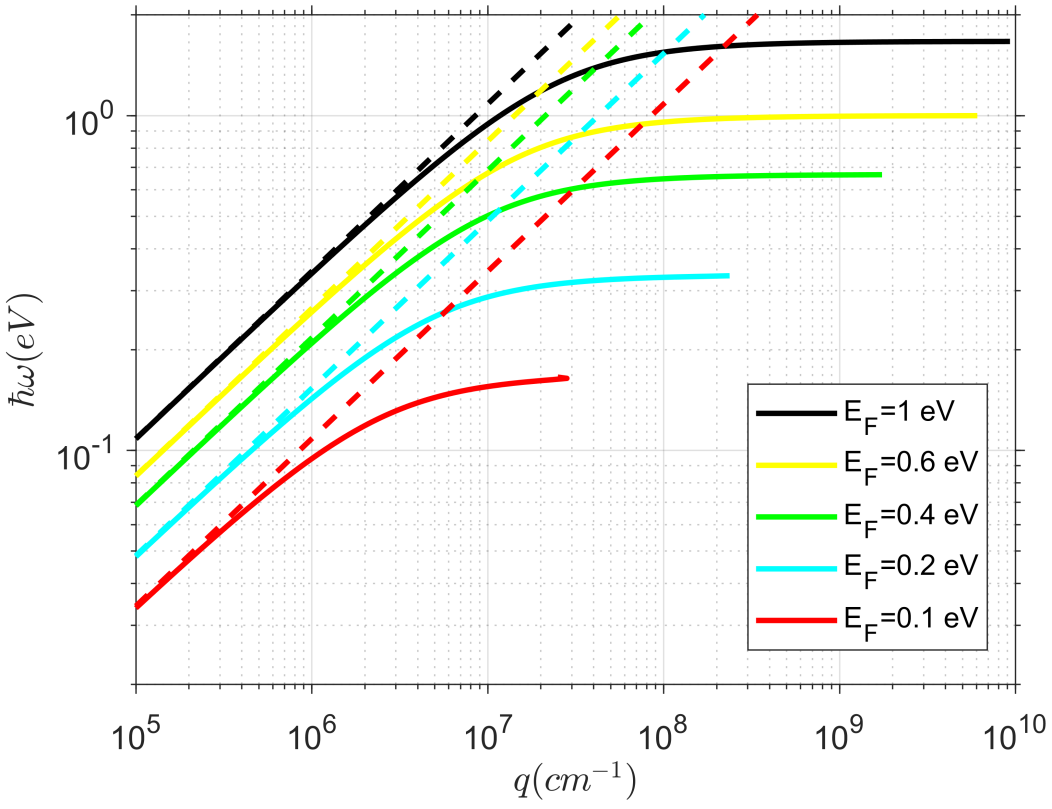

Figure 6.9: Graphene plasmon dispersion relation for different doping levels. ε_r=3.9 is assumed, which corresponds to the SiO_2 dielectric constant. Logarithmic scale. Solid curves are obtained by considering the effect of $\sigma=\sigma_D+\sigma_I$, dashed curves by considering only the effect of σ_D.

This is plotted on a logarithmic scale in figure 6.9 assuming a value ε_r=3.9, which is the permittivity of SiO_2. SiO_2 is one of the substrates considered in this study and is also commonly used for the fabrication of graphene based devices [21, 142, 143, 240, 242, 258, 261, 268, 284]. As predicted from equation 6.14, for small $\hbar\omega$, all the curves in figure 6.9 show a quadratic dependence of the wave vector q on the light frequency (dashed curves). This behaviour, which is typical of 2D electron gases [253], is due to the effect of the Drude component of the conductivity σ_D (equation 6.13). However, when $\hbar\omega$ approaches the interband transition energy a logarithmic dependence is observed. From the complex wavevector it is possible to extract a value of the plasmon wavelength using the relation $\lambda_P = 2\pi/\Re q$. From an experimental point of view this relation is also useful, because it allows the SP wavevector to be directly extracted from an image of the resonance of propagating graphene plasmons. The complex wavevector also allows the parameter PP to be calculated according to equation 6.15.

Figure 6.10 shows the parameter PP evaluated as function of the incident photon energy. The dashed curves represent PP when only the Drude component of conductivity (σ_D, equation 6.13) is taken into account; solid curves when the full conductivity σ=σ_D+σ_I is considered. In the latter case, PP reaches high values (>100 for E_F=1eV), but decrease sharply when $\hbar\omega$ approaches $2E_F$ due to the formation of electron-hole pairs because of interband transitions. However, in both cases PP increases as E_F increases and this is attributed to the increment of carrier concentrations in the conduction band, with the consequent increase of RT, τ. It is also evident how the incident photon energy plays a major role on the propagation of the graphene plasmons. For this current study, the interest is focused on the understanding of the graphene plasmon response stimulated by THz light, which corresponds to photon energies on the order of a few tens of meV (3 THz = 12.4 meV). In this regime PP is very short and the differences between σ and σ_D are negligible. In the mid-IR and near-IR regimes (from hundreds of meV to 1 eV) the differences are more relevant because of the interband transitions, the losses from which need to be taken into account. Moreover, the assumptions made for the RT ($\omega < \omega_{Oph}$) are no longer valid because transitions of graphene optical phonons might occur [254] and

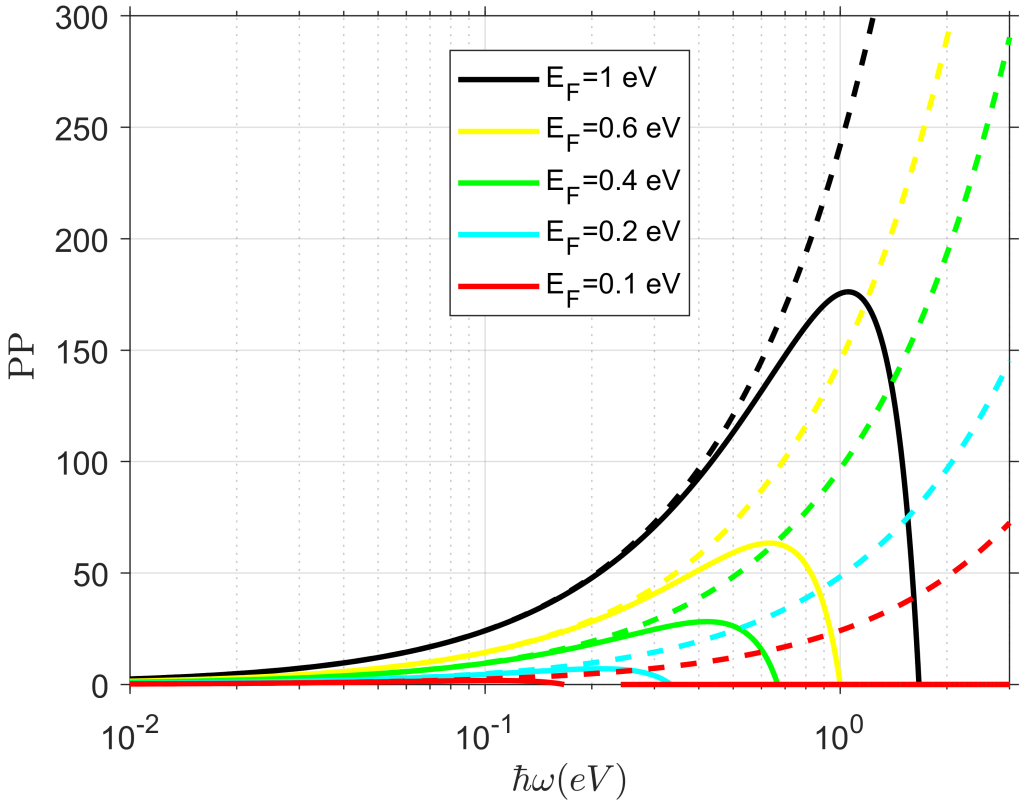

Figure 6.10: Plasmon propagation as function of the incident photon energy; ε_r=3.9 is assumed. Solid curves are obtained by considering the effect of σ=σ_D+σ_I, dashed curves by considering only the effect of σ_D.

electron-phonon scattering has to be considered in the model. In the THz regime, however, it is valid to consider scattering by impurities and defects as the major processes limiting PP. Indeed, due to the linear dependence of PP on μ, the DC mobility in equation 6.17 is the significant factor affecting PP in graphene under THz light at fixed E_F. As an example, figure 6.11 shows PP as function of μ obtained at $\hbar\omega = 12.4meV$ (3 THz) for $E_F = 0.4$ eV. At $\mu \approx 10000cm^2/Vs$, PP ≈ 1, which is roughly ten times lower than PP obtained at $\hbar\omega = 100meV$.

The mobility in graphene depends strongly on the properties of the substrate/environment and different studies have revealed the crucial role of the substrate optical phonon modes on the damping of graphene plasmons [142, 254]. In the models presented above the effect of the substrate has been accounted for using the static dielectric constant ε_r (3.9 for

SiO_2). This is a limitation because the dependence of ε on ω is not negligible and can have a strong impact on the properties of a graphene sheet deposited onto the substrate. For example SiO_2 exhibits numerous phonon modes in the mid-IR region [18] that cannot be ignored when building a model to describe the near-field interaction between a s-SNOM tip and a graphene sample.

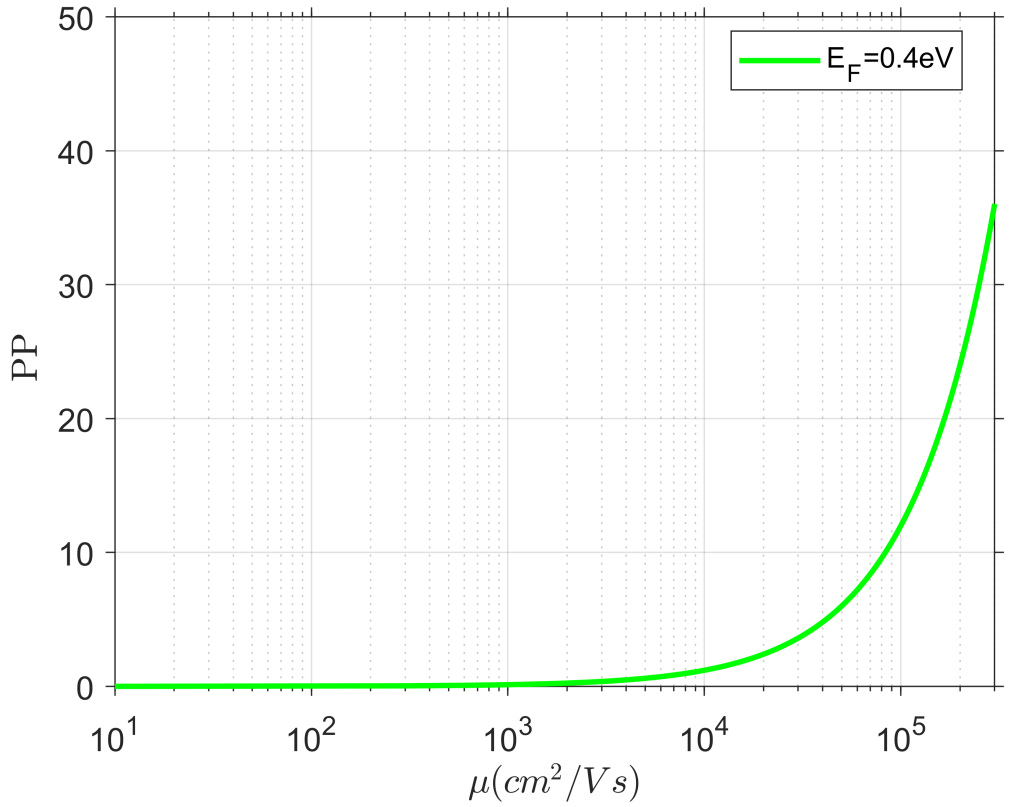

Figure 6.11: Plasmon propagation in grahene as function of DC mobility μ obtained at 3 THz for E_F = 0.4eV; ε_r=3.9 is assumed.

6.1.3 Near-Field interaction with graphene

In scattering-type near-field microscopy (s-SNOM) a near field interaction occurs when a metallic nanometric tip (with radius of curvature a), polarized by the incoming light, is approached to a polar or conducting surface. The evanescent field created by the light at the tip is altered when the tip-sample distance is comparable to a. In turn, the polarization of the tip is also affected [152] and to quantify this interaction the Fresnel

reflection coefficient is employed [142, 146, 253, 254]. The Fresnel reflection coefficient for p-polarized light $r_p(q,\omega)$ is defined as the ratio of the amplitude of the reflected p-polarized field Er to that of the incoming p-polarized field E_i. Specifically in the case of graphene, the Fresnel reflection coefficient is given by equation 6.25. In order to account for the substrate phonon modes and their coupling with graphene plasmons, the full complex dielectric function of the substrate needs to be considered.

$$r_p(q,\omega) = \frac{\varepsilon_r(\omega)\varepsilon_0 Q_0 - \varepsilon_0 Q_1 + \left(\frac{4\pi Q_0 Q_1 \sigma}{\omega}\right)}{\varepsilon_r(\omega)\varepsilon_0 Q_0 + \varepsilon_0 Q_1 + \left(\frac{4\pi Q_0 Q_1 \sigma}{\omega}\right)}. \tag{6.25}$$

In equation 6.25 ε_0 is the dielectric constant of vacuum, $\varepsilon_1(\omega) = \varepsilon_r(\omega)\varepsilon_0$ is the complex dielectric function of the substrate, $Q_i = \sqrt{\varepsilon_{r,i}(\omega/c)^2 - q^2}$ are the out-of-plane components of momenta, and σ is the conductivity of graphene obtained from equation 6.24. It is worth mentioning that the reflection coefficient, $r_p(q,\omega)$, describes all the dynamics of the interaction between light and electrons at graphene-substrate interface in the near-field as well as far-field. The charges in graphene are driven by the radial component of the field scattered by the tip; these charges, in turn, modify the polarization of the tip. In this study the apex of the metallic tip is approximated as a point dipole. The tip is identified by its radius of curvature, a ,and the distance between the effective dipole and the tip apex, b, as shown in figure 6.12. This distance b has been found to provide good agreement with experimental data when b=0.7a [142]. In s-SNOM experiments the tip is oscillated in the direction normal to the sample surface with amplitude Δx and frequency Ω, figure 6.12.

As such the distance between the dipole and the sample surface is a function of time, and can be defined as,

$$d(t) = b + \Delta x(1 - cos(\Omega t)). \tag{6.26}$$

Equation 6.26 and the reflection coefficient of equation 6.25, r_p, can be used to calculate

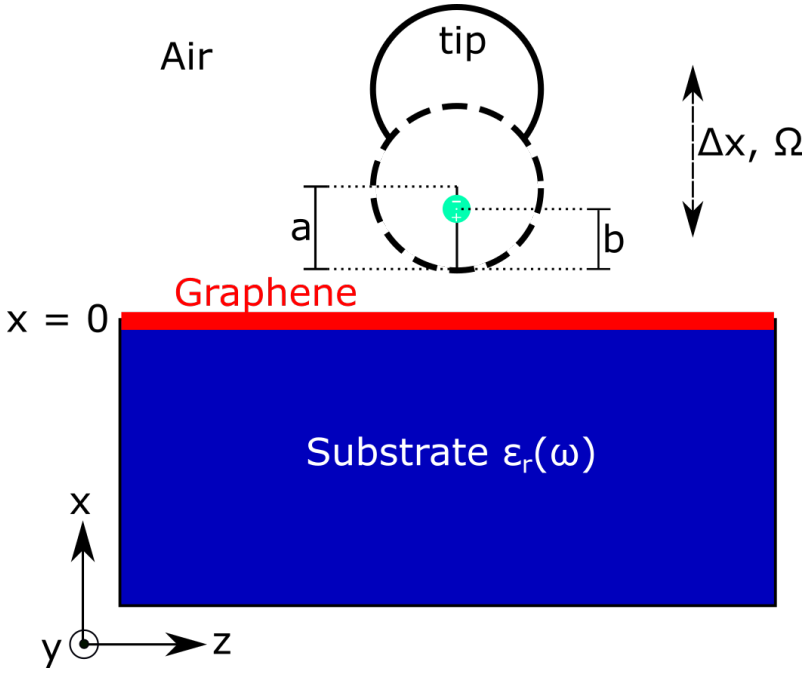

Figure 6.12: Schematic of the s-SNOM oscillating tip

a tip-sample coupling function G [142] as follow,

$$G(d,\omega) = \int_0^\infty dq q^2 e^{-2qx_d} r_p(q,\omega). \tag{6.27}$$

Due to the presence of d(t), the weight function q^2e^{-2qd} is function of time, and its time averaged result $<q^2e^{-2qd}>_t$, called the coupling weight function (CWF), has a bell shape and yields a maximum value around q∼1/a. In this way, the shape of the tip makes available a large range of in-plane (surface) momenta q (centered around q∼1/a) in the near-field system. This is an important parameter for modelling because it gives the access to a range of momenta that can be probed depending on the curvature radius of the tip, a. For example, figure 6.13(a) shows the CWF for a=20nm and Δx=40nm, and figure 6.13(b) instead shows CWF obtained for a=1μm, Δx=200nm. In the first case, CWF attains a peak value at q∼5.21×10^5cm^{-1} which corresponds to a∼20nm; in the second case, CWF has a peak value at q∼1.16×10^4cm^{-1} which corresponds to a∼1μm.

Finally by using tip-sample coupling function G it is possible to compute the near-field signal, demodulated at the n-th harmonic, as a function of the incoming photon energy,

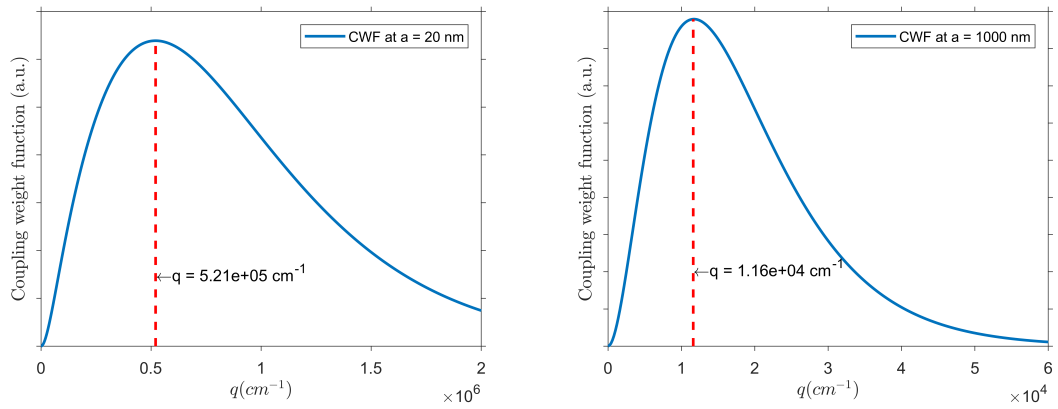

(a) (b)

Figure 6.13: Coupling weight function (CWF) obtained (a) for a=20nm and Δx=40nm, (b) for a=1 μm and Δx=200nm. q shown in the graphs is the momenta at CWF peak.

using [142]

$$s_n e^{i\phi_n} \propto \int_0^{2\pi} \frac{e^{in\phi} d\phi}{1 - G(d,\omega)a^3}, \tag{6.28}$$

in which $s_n(\omega)$ is the amplitude and $\phi_n(\omega)$ is the phase of the near field signal obtained for graphene. This expression is also valid for the substrate alone, by considering its reflection coefficient in the form

$$r_p(q,\omega) = \frac{\varepsilon_r(\omega)\varepsilon_0 Q_0 - \varepsilon_0 Q_1}{\varepsilon_r(\omega)\varepsilon_0 Q_0 + \varepsilon_0 Q_1}. \tag{6.29}$$

This model takes account of the different phonon modes of the substrate by introducing its complex dielectric function and reveals how substrate phonons couple with graphene plasmon modes. The dependence of the NF signal on the graphene relaxation time (τ) and doping level (E_F) are included through the expression for the conductivity, σ (equation 6.24). A discussion of the NF interactions simulated for two different substrates and for different graphene E_F is given in the next section by plotting the results of the model with a particular focus on the parameters r_p, $s_n e^{i\phi_n}$ and a.

6.1.4 Model results and discussion

As previously mentioned the main interest of this study is related to near-field interaction with graphene under THz illumination. As such, the discussion will be focus on this frequency range.

According to the CWF shown in figures 6.13(a) and 6.13(b), the in-plane momenta that contribute strongly to the near-field coupling are those around the peak CWF. As such, the near-field signal computed using equation 6.28 will be strong if and only if the dispersion curve obtained from r_p intersect the principle momenta given by the radius of curvature of the tip, i.e. q$\sim$1/a.

The substrates considered in this work are silicon dioxide, SiO_2, and hexagonal boron nitride, h-BN. Complex dielectric functions have been obtained from literature, respectively from [18] for SiO_2 and from [140] for h-BN. For SiO_2 all the bulk optical phonon modes are considered, although usually only the surface phonon mode is the dominant mode affecting the near-field interaction [142, 253, 254].

h-BN is 2D crystalline material with a similar structure to graphene (a honeycomb lattice). It is an anisotropic material, which means that its complex dielectric function is different depending on the crystallographic direction, $\varepsilon_x = \varepsilon_y \neq \varepsilon_z$; the total permittivity is calculated by the equation $\varepsilon = \sqrt{\varepsilon_x \times \varepsilon_z}$ [140]. It is usually placed underneath graphene in a heterostructure because it has much lower surface roughness compared to SiO_2; this is done with the aim of increasing charge mobility by limiting the scattering from Coulomb impurities and corrugations [271, 285, 286]. In fact h-BN has only 1.7% of lattice mismatch with graphene [287] and graphene is sometimes encapsulated between two layers of h-BN in order to screen it from the environment [26, 141, 288, 289]. In the experimental section of this study h-BN is used as a layer between SiO_2 and graphene.

In order to encapsulate the strength of the interaction between photons and plasmonic modes, figure 6.14 plots the imaginary part of r_p for $E_F = 0.1$, 0.2, and 0.4 eV, for the case of graphene on SiO_2. The black dashed line corresponds to the plasmon wavevector obtained from equation 6.11 using the SiO_2 dielectric constant ε_r=3.9 and considering only

the Drude component of the conductivity. The blue dashed line, instead, marks the q for which the CWF has a maximum value, for a=20nm, $\Delta x = 40$nm. It is immediately clear how the plasmon wave vector (black dashed line) follows the dispersion of $\Im r_p$ but does not reproduce the changes in $\Im r_p$ caused by the phonon modes of SiO_2. This is expected because of the use of the static dielectric constant of SiO_2 in the calculation of the Drude plasmon wave vector.

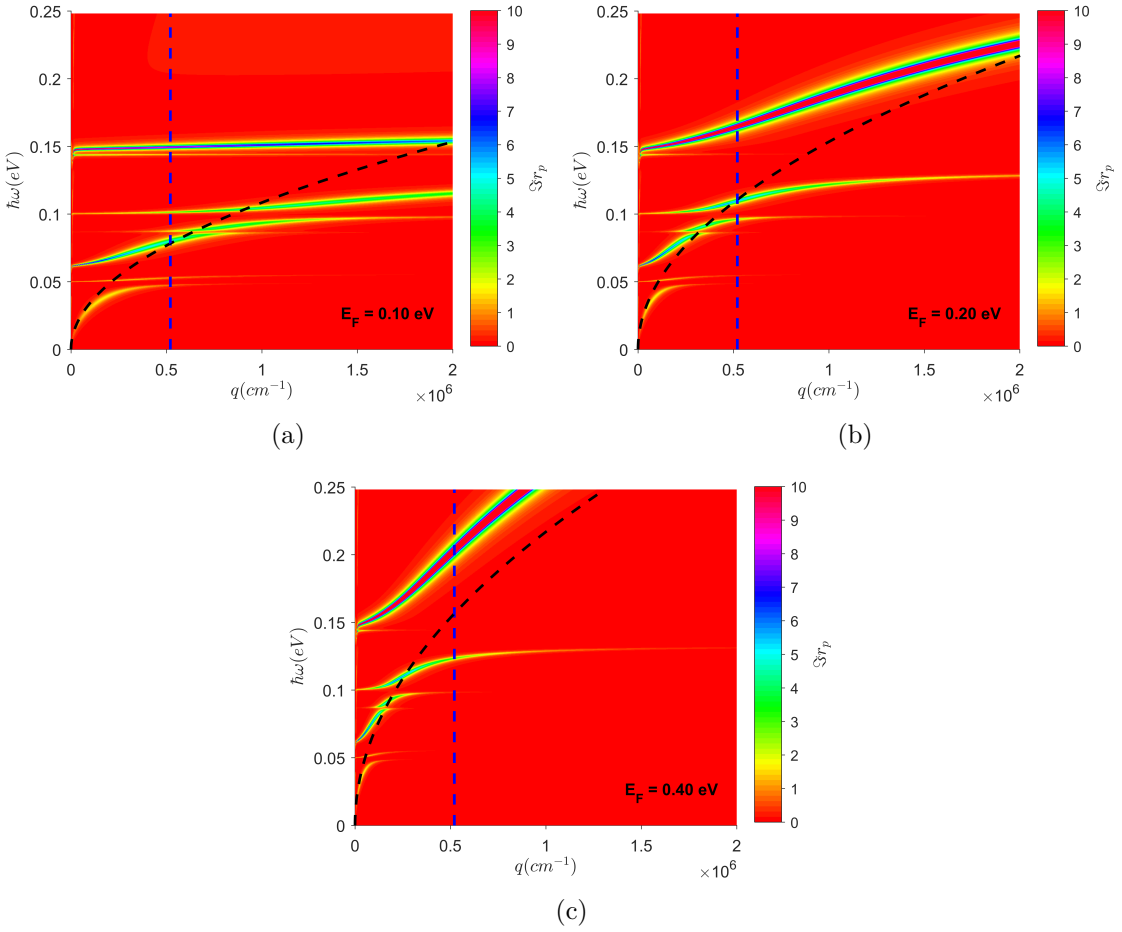

Figure 6.14: Imaginary part of r_p, from equation 6.25, for graphene on SiO_2 obtained at (a) E_F=0.1 eV, (b) E_F=0.2 eV, (c) E_F=0.4 eV. The black dashed line corresponds to the wavevectors q calculated from equation 6.11 considering only the Drude component of the conductivity and using ε_r=3.9 for the substrate. The blue vertical dashed line marks the dominant q, as shown in figure 6.13(a)

The near-field signal demodulated at harmonic n=3, calculated, from equation 6.28 and plotted as a function of photon energy, is shown in figure 6.15 for different E_F. Also

shown is the near-field signal for the case of SiO_2 alone. The graphs demonstrate how the range of momenta, q, provided by the CWF of the tip (figure 6.13(a)), couple well with graphene for photon energies between $\hbar\omega$ ~0.05eV and $\hbar\omega$ ~0.2eV. This is expected by considering the different points of intersection between the available momenta (blue dashed line) and the dispersions of r_p in figure 6.14. The peaks in the near-field amplitude and phase in the case of SiO_2 are related to the phonon modes of the substrate. The peaks of the signal for graphene, instead, are split in two different branches: the first branch up to $\hbar\omega$ ~0.125eV is linked directly to the intrinsic graphene plasmon, and the second branch, at $\hbar\omega$>0.125eV, is linked to the substrate phonon; this behaviour has been experimentally verified by nano-spectroscopy conducted on the Graphene/SiO_2 interface by employing different light sources able to cover the photon energies in question [142]. Another important characteristic to note is the blue shift of the signal peaks with increasing E_F. The two branches clearly experience a shift to higher photon energies. Interestingly the blue curve in figure 6.15 (E_F=0.1eV) has a minor peak in amplitude and a steady change of phase at $\hbar\omega$=0.2eV, corresponding to the inter-band transition when photons are absorbed.

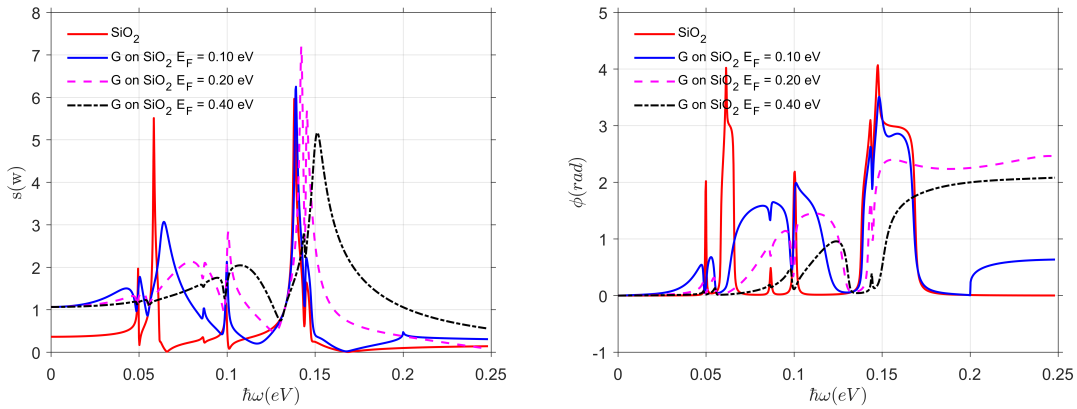

(a) (b)

Figure 6.15: (a) Amplitude and (b) Phase of the near-field signal obtained from equation 6.28 for different E_F of graphene (G) on SiO_2 by considering a=20nm, $\Delta x = 40$nm. Signal is demodulated at the 3rd harmonic. Red line corresponds to the near-field signal of only SiO_2.

Figure 6.16, shows the imaginary part of r_p for E_F = 0.1, 0.2, and 0.4 eV, for the case

of graphene on h-BN. Also plotted is the plasmon wave-vector calculated from the Drude component of the conductivity using ε_r=5.9 [290] (black dashed line), as well as q corresponding to the maximum CWF for a=20nm, Δx = 40nm (blue dashed line). The plasmon wave vector follows the $\Im r_p$ dispersion well, but again does not reproduce the changes in $\Im r_p$ due to the substrate phonons even in this case.

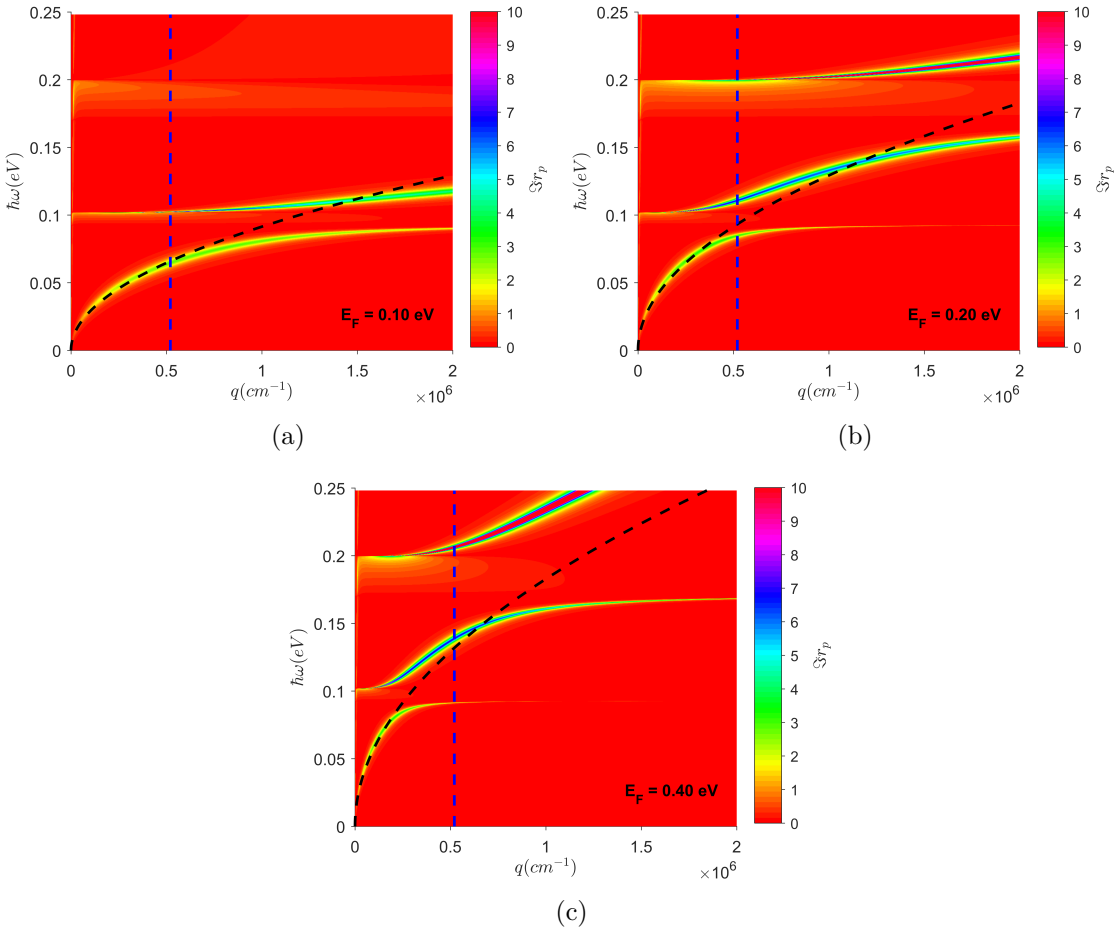

Figure 6.16: Imaginary part of r_p, from equation 6.25, for graphene on h-BN obtained at (a) E_F=0.1 eV, (b) E_F=0.2 eV, (c) E_F=0.4 eV. The black dashed line corresponds to the wavevectors q calculated from equation 6.11 considering only the drude component of the conductivity and using ε_r=5.9 for the substrate. The blue vertical dashed line marks the dominant q, as shown in figure 6.13(a)

The computed amplitudes and phases of the near-field signal are shown in figure 6.17 as a function of the photon energy. The blue shift of the graphene peaks with increasing E_F is evident also for this system.

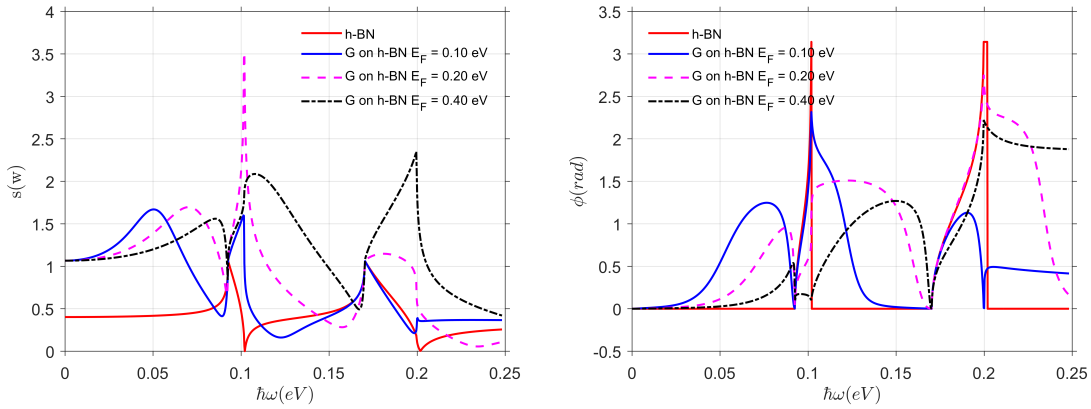

(a) (b)

Figure 6.17: (a) Amplitude and (b) Phase of the near-field signal obtained from equation 6.28 for different E_F of graphene (G) on h-BN by considering a=20nm, $\Delta x = 40$nm. Signal is demodulated at the 3rd harmonic. Red line corresponds to the near-field signal of only h-BN.

It is evident from figures 6.15 and 6.17 that the use of a tip with radius of curvature a=20nm and Δx= 40nm provides the momenta, q, the couples better with mid-IR photons, compared to the THz photons. In order to gain a better understanding of the near-field response in the THz regime (for photon energies $\hbar\omega$<0.05eV) a different radius of curvature of the tip should be employed. It has been shown in the previous section that using a=1μm and Δx= 200nm creates a peak in the CWF around q$\sim 1.16\times10^4$cm^{-1}. This value is smaller than the previous value and thus will intersect the dispersion of $\Im r_p$ at lower photon energies, as shown in figures 6.18 and 6.20 respectively for h-BN and SiO_2 substrates.

As expected, the amplitude and phase of the near-field signal show, now, a stronger signal in the region $\hbar\omega$<0.05eV. In this region there are no substrate optical phonon modes and so the signal does not show damping or enhancement caused by them; as a consequence, the blue shift due to the increase of E_F is more evident in figure 6.19 than figure 6.17. One more evident feature is the increase of the amplitude and phase of the signal due to the increment of E_F. In the region where $\hbar\omega$>0.05eV the amplitude and phase of the signal for graphene/h-BN closely follows the signal for h-BN alone, which is expected due to poor coupling of the in-plane momenta with the sample. Interestingly, for the same

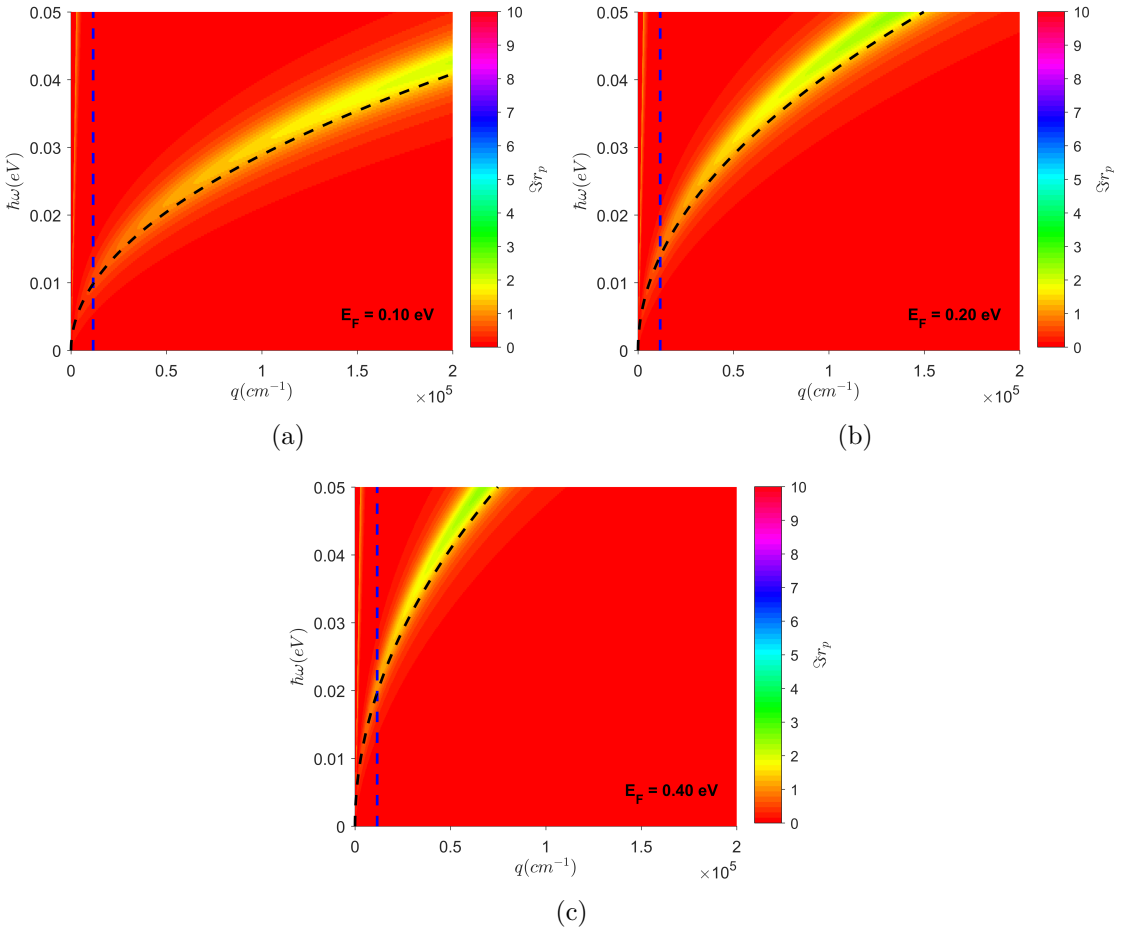

Figure 6.18: Imaginary part of r_p, from equation 6.25, for graphene on h-BN obtained at (a) E_F=0.1 eV, (b) E_F=0.2 eV, (c) E_F=0.4 eV. The black dashed line corresponds to the wavevectors q calculated from equation 6.11 considering only the drude component of the conductivity and using ε_r=5.9 for the substrate. The blue vertical dashed line marks the dominant q, as shown in figure 6.13(b)

reason, the blue curve in figure 6.19 (graphene at E_F=0.1eV) does not show any significant signal when the photon energies approach the inter-band transition at $\hbar\omega$=0.2eV.

Figure 6.21 shows the near-field signal obtained by the use of the larger tip for graphene on SiO_2. Even in this case the major near-field resonance is in the region $\hbar\omega < 0.05eV$; the absence of substrate phonon modes again prevent damping and the only enhancement is due to the increase of E_F. Also the blue shift of the resonance peaks with increasing E_F is evident even in this case.

Finally it is interesting to compare the amplitude of the signal optimized for mid-IR

photons (photon energy 0.05eV<$\hbar\omega$<0.1eV in figure 6.17(b)) with the amplitude of the signal optimized for THz photons (photon energy $\hbar\omega$ ∼0.01eV in figure 6.19(a)), for h-BN substrate. In the first case the amplitude yields s∼1.7, while in the latter case s∼1. The experiments, employing the larger tip a=1μm, are expected to provide similar amplitude of the signal when compared to the mid-IR results, which employed the smaller tip, extracted from the literature.

Section 6.4 will be dedicated to presenting and discussing experimental images of graphene on SiO_2 and on h-BN acquired through the use of a commercially available s-SNOM system produced by the company Neaspec, coupled with a quantum cascade laser lasing at f∼3.45THz ($\hbar\omega$=12.4meV). The purpose of this study is to explore the possibility of mapping the propagation of plasmons which are expected to exhibit a resonance depending on the geometry of the sample. It will be explained how the small value of PP prevents the formation of plasmons because of the poor quality of the sample, which can influence the charges mobility. A way will be suggested with the aim of observing the resonance of propagating plasmons in the THz regime.

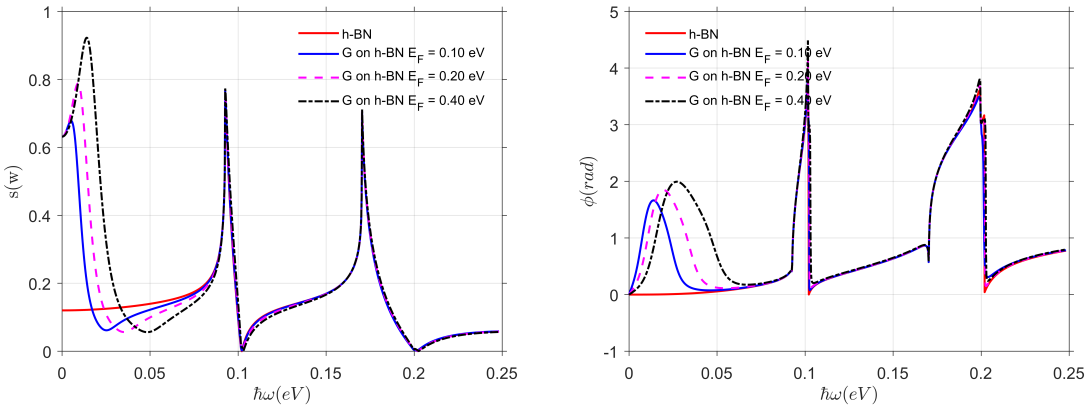

(a) (b)

Figure 6.19: (a) Amplitude and (b) Phase of the near-field signal obtained from equation 6.28 for different E_F of graphene (G) on h-BN by considering a=1μm, $\Delta x = 200$nm. Signal is demodulated at the 3rd harmonic. Red line corresponds to the near-field signal of only h-BN.

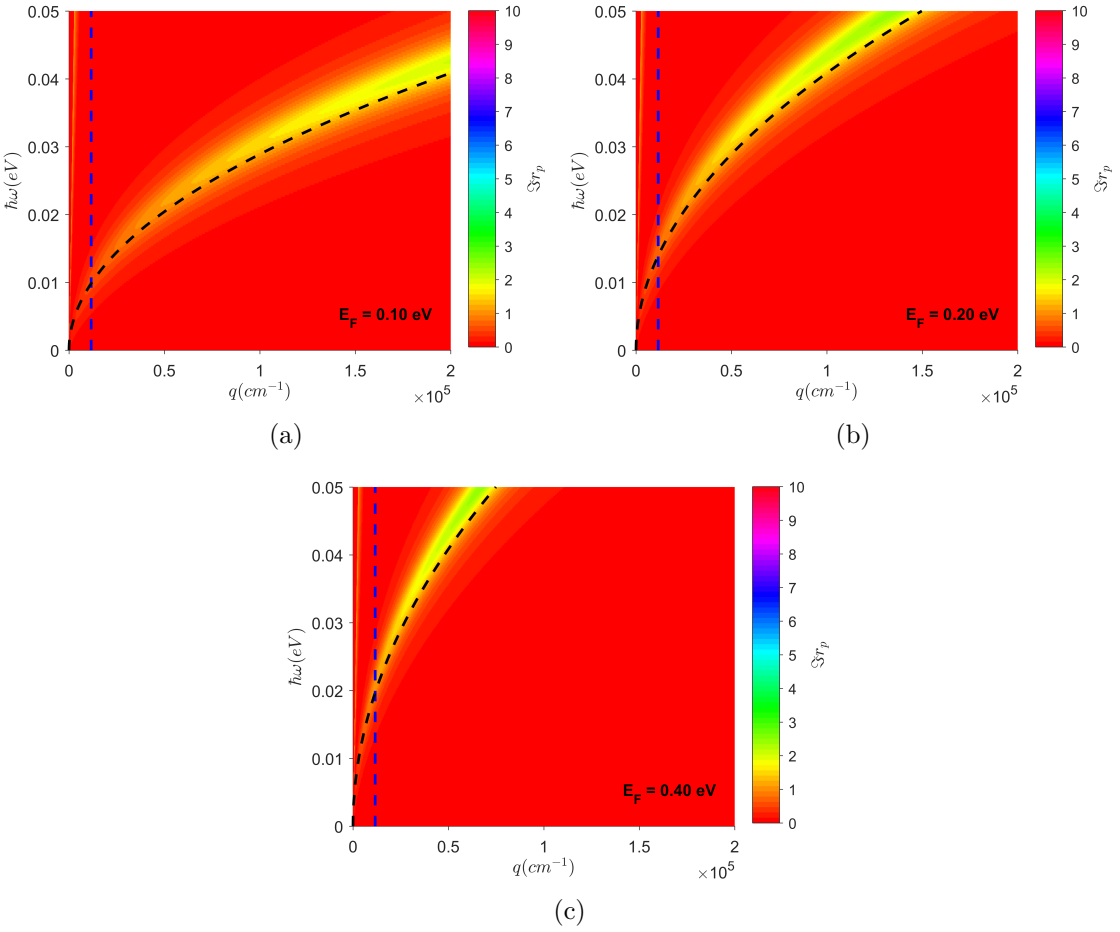

Figure 6.20: Imaginary part of r_p, from equation 6.25, for Graphene on SiO_2 obtained at (a) E_F=0.1 eV, (b) E_F=0.2 eV, (c) E_F=0.4 eV. The black dashed line corresponds to the wavevectors q calculated from equation 6.11 considering only the drude component of the conductivity and using ε_r=3.9 for the substrate. The blue vertical dashed line marks the dominant q, as shown in figure 6.13(b)

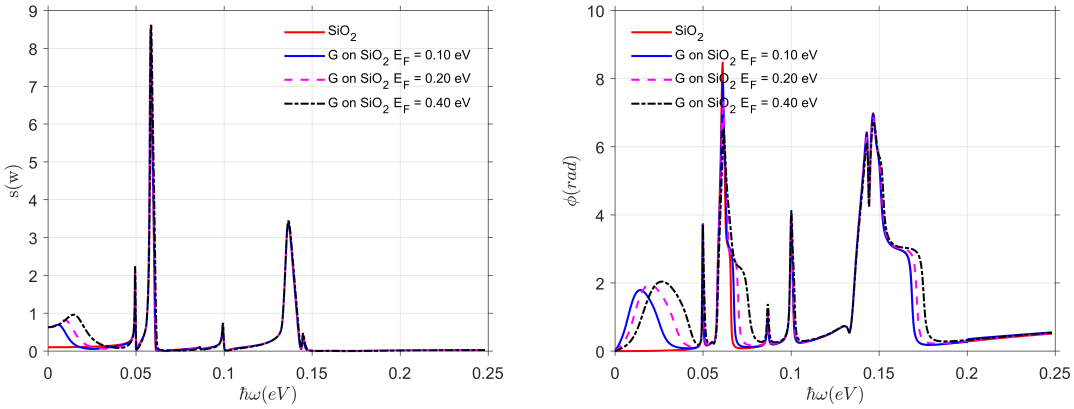

(a) (b)

Figure 6.21: (a) Amplitude and (b) Phase of the near-field signal obtained from equation 6.28 for different E_F of graphene (G) on SiO_2 by considering a=1μm, Δx = 200nm. Signal is demodulated at the 3rd harmonic. Red line corresponds to the near-field signal of only SiO_2.

6.2 Propagating plasmons in graphene from literature

Surface plasmon waves on graphene has been studied experimentally in the THz and mid-IR ranges through the use of near-field systems equipped with different laser sources. Of remarkable interest are the studies conducted in the THz regime. In [25] the authors present near-field image of different graphene structures (bow-ties, ribbons and mesas) epitaxially grown on a SiC substrate. They employed an aperture-type near-field microscope based on THz time-domain spectroscopy in order to map the temporal evolution of the surface plasmon waves excited at the edge of the graphene structures by THz plane waves (figure 6.22). They demonstrated reduced or enhanced transmission of THz waves depending on the ribbon width and the orientation of the graphene ribbons with respect to the electric field polarization. Of exceptional interest is also the study conducted in [26]. Here, the authors employed a sophisticated graphene photodetector in which the graphene is encapsulated between two sheets of h-BN. With a split-gate architecture they could tune the carriers concentrations (and fermi energy) selectively in two different areas of the graphene, and effectively establish a p-n junction between the two gates. Real-space images of propagating acoustic terahertz plasmons, excited by focusing the beam of a gas laser onto the tip of a scattering-type near-field microscope, have been acquired using a thermo-electrical detection mechanism. Images were created by measuring the photocurrent at one of the sensor contacts as a function of the tip position, as shown figure 6.23.

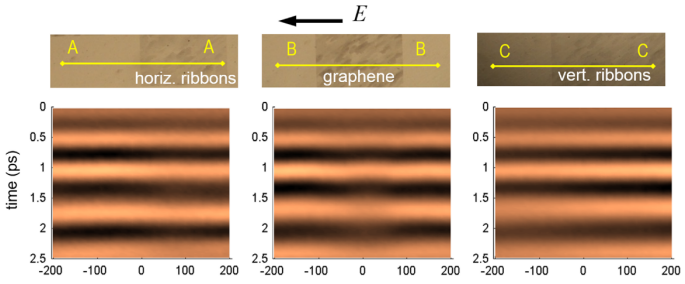

Figure 6.22: Near-field THz space-time map measured for a 200μm×200μm graphene mesa (middle) and 1 μm wide graphene ribbons oriented parallel (left) and perpendicular (right) to the electric field polarization. Top row shows optical images of the sample; bottom row the detected THz field E(x,t). Adapted from O. Mitrofanov [25].

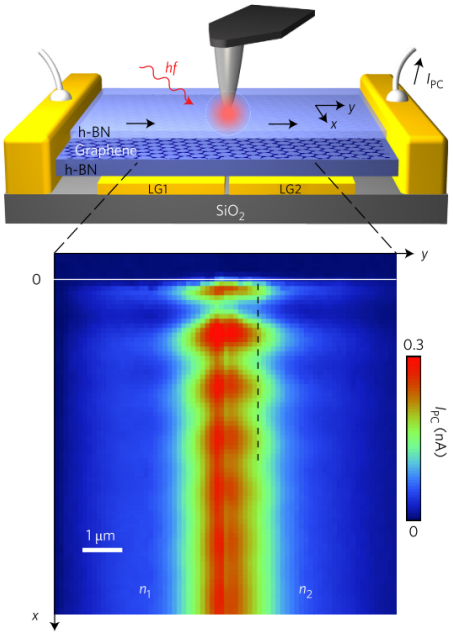

Figure 6.23: Image at the top: Schematic of the experimental setup. Bottom: Image of the photocurrent, I_{PC} recorded at f=2.52 THz. n_1 and n_2 represent the different carrier concentrations established by the two gates. Adapted from P. Alonso-González [26].

Mid-IR plasmons in graphene have also been extensively studied in the literature; the concept is that the tip illuminated by the light acts to launch plasmons on graphene through the in-plane momenta provided by the tip. The plasmons propagates until being reflected from sample edges or defects, establishing a spatial resonance [27, 28, 140–146]. The mid-IR graphene plasmon resonances have been imaged both optically and thermo-electrically. Propagating plasmons on graphene encapsulated between two films of h-BN have been imaged in [140]. In [141], by employing the same scheme as shown in figure 6.23 with a mid-IR continuous-wave laser, the group emphasizes the possibility of thermo-electrically measuring the plasmon propagation rather than using optoelectronic materials. In [27, 142–145] the groups have studied different properties of propagating mid-IR plasmons in graphene. Within these studies they have verified the coupling of the graphene plasmons with the substrate optical phonons [142] and also demonstrated the tuning of the plasmon properties by changing the gate voltage in a FET-architecture [143]. Of particular interest the plasmon confinement in graphene ribbons with various

widths [144, 145] and in tapered graphene ribbons has been studied by exciting plasmons with different light frequencies [27], as shown in figure 6.24. In [28] the authors have studied the effect of temperature on the plasmon lifetime which is related to the plasmon propagation, showing how a decrease of sample temperature brings an increases in the plasmon propagation, as shown in figure 6.25.

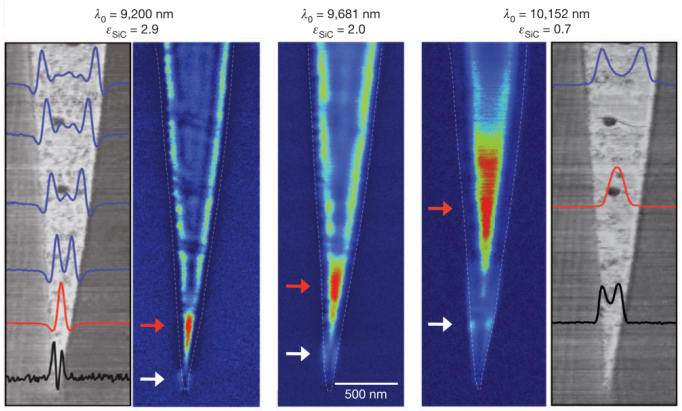

Figure 6.24: Images of a tapered graphene ribbon. The topography (obtained by AFM) is shown in greyscale in the leftmost and rightmost panels, and outlined by dashed lines in the central, coloured panels, which are the mid-IR near-field optical images taken at source wavelengths stated at the top. The line traces in the leftmost and rightmost panels are extracted from the near-field images for λ_0=9200nm and λ_0=10152nm. Red and white arrows indicate the resonant localized modes. Adapted from J. Chen [27].

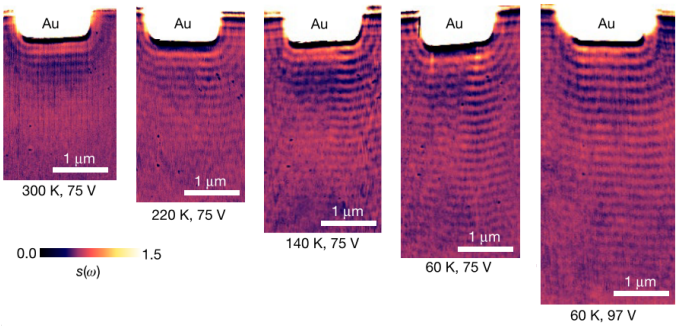

Figure 6.25: Nanoscale mid-IR images of the normalized scattering amplitude s acquired at sequential sample temperatures and gate voltages. A gold electrode (labelled Au at the top of the images) functions as an antenna that emits graphene plasmons. Adapted from G. Ni [28].

6.3 Fabrication of the graphene samples

Two types of samples have been fabricated for this study: the first sample consists of commercially available CVD (Chemical Vapour Deposition) graphene on Cu which has been transferred onto a SiO_2/Si(n+) wafer, with thickness 285nm, 525μm respectively. The second sample was a CVD graphene/CVD h-BN heterostructure on a SiO_2/Si(p+) wafer, with thickness 285nm, 525μm respectively already fabricated by the commercial supplier. The shape of the samples has been defined through optical lithography and the details of processing and fabrication will be given in section 6.3.

6.3.1 Graphene on SiO_2

The fabrication started with the substrate preparation. After cleaving samples with dimension 10 mm by 10 mm from a 6-inch-diameter SiO_2/Si(n+) wafer, they were cleaned in an ultrasonic bath of isopropyl alcohol (IPA), acetone and water at 100 % power for 5 mins each. Standard S-1813 positive photoresist was spin-coated on each sample at a speed of 5000 rpm for 30 seconds, ensuring a resist thickness of $\sim$1.2μm. Then the samples were soft-baked on a hotplate at 115°C for 2 minutes and the edge beads were manually removed using a cleanroom cotton bud soaked in acetone. The adopted approach was to create on the SiO_2 surface a pattern of labelled thin metal crosses, with width 2 μm and spacing 75 μm, and covering an entire area of 1 mm by 1 mm, in order to visually choose the best area of graphene after transfer onto the substrate. The edge beads removal is a standard clean-room procedure which guarantees a good contact between the lithographic mask and the exposed area of the sample. The mask was a standard chromium mask previously designed and fabricated (by a commercial supplier), which is shown in figure 6.26(a). The samples were exposed to a UV lamp (λ=310nm @ 6.7 mW/cm^2) through the substrate mask for 8 seconds in a Karl Suss MJB3 mask aligner and subsequently developed in a standard MF-319 developer for 20 seconds. Then, 15-20 nm of Chromium was evaporated on the developed sample using an Edwards auto 306 thermal evaporator and then left overnight in acetone in order to lift-off the undesired metallic part. The

fabricated pattern is shown in figure 6.26(b).

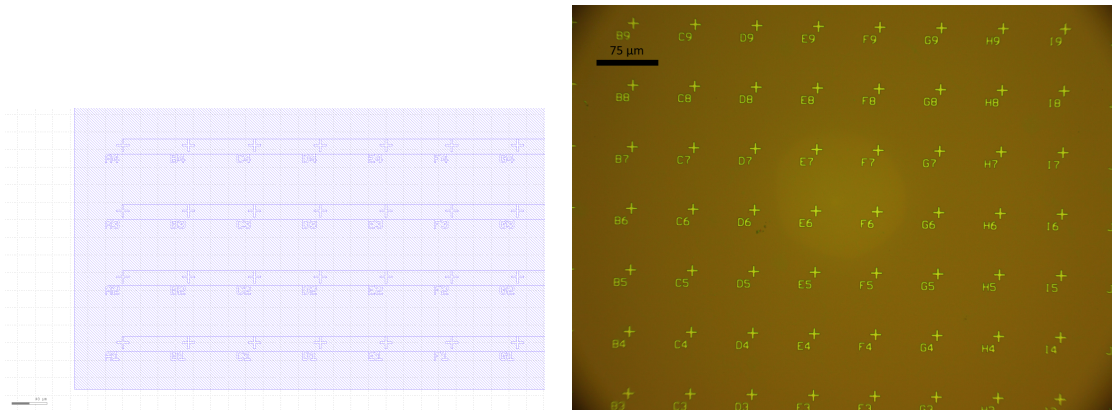

(a) (b)

Figure 6.26: (a) Design of photolithography mask used for crosses pattern definition on SiO_2/Si(n+), exported from the software KLayout. (b) Optical microscope photo of the pattern of labelled Cr crosses evaporated on SiO_2.

A 4-inch-diameter circular foil of CVD-grown graphene on copper (Cu) was purchased. The processing started by cleaving a $\sim$ 20 mm by 20mm piece of foil. Poly-methyl methacrylate (PMMA) 495K A8 was then spin-coated at 2000 rpm for 30 seconds on the top side of the foil, and consequently it was soft-baked at 180°C for 2 minutes. PMMA/G/Cu foil was then cleaved into pieces small enough to fit the dimensions of the sample substrate. $FeCl_3$ solution is usually employed for Cu etching, but it is a slow process ($\sim$ 24 hours for completion) and has often shown unwanted contamination. In this case, the transfer process consisted of etching the Cu layer underneath the PMMA/G in a acid solution 1(1HNO_3:3HCL):1H_2O_2:1H_2O [291]. This ensured a much faster etching ($\sim$ 2 minutes) and consequently much less contamination of the graphene. The PMMA/G/Cu pieces (with the PMMA side facing the top) were placed floating on the acid solution. Once the Cu was etched away the PMMA/G samples were transferred to 3 consecutive distilled H_2O baths, for 10 minutes each, in order to clean the graphene. Finally PMMA/G was transferred to the previously prepared substrates. The PMMA/G/SiO_2 sample was, then, firstly left to dry in air for 2 hours and then baked at 180°C for 5 minutes. In figure 6.27 an optical photo of a sample before and after baking is shown.

This final baking ensured a complete evaporation of water at the interface G/SiO_2, and

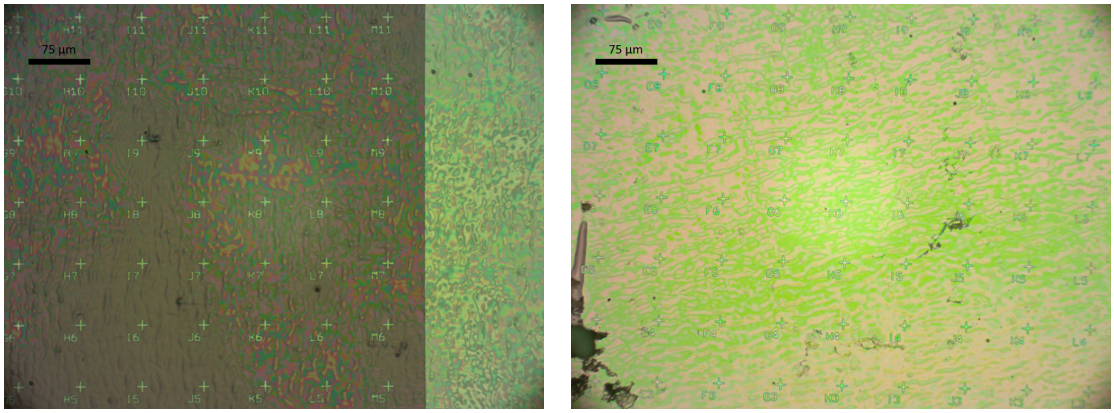

(a) (b)

Figure 6.27: Optical microscope photo of the post-transferred PMMA/G/SiO_2, (a) pre and (b) post baking it at 180°C for 5 minutes

established a better adhesion of the graphene to the substrate. PMMA was then removed by leaving the samples in an acetone bath for 3-4 hours. Once the PMMA was removed the best graphene area was chosen through visual inspection using an optical microscope. The choice was driven by searching for a region where the graphene had a continuous layer with no contaminations.

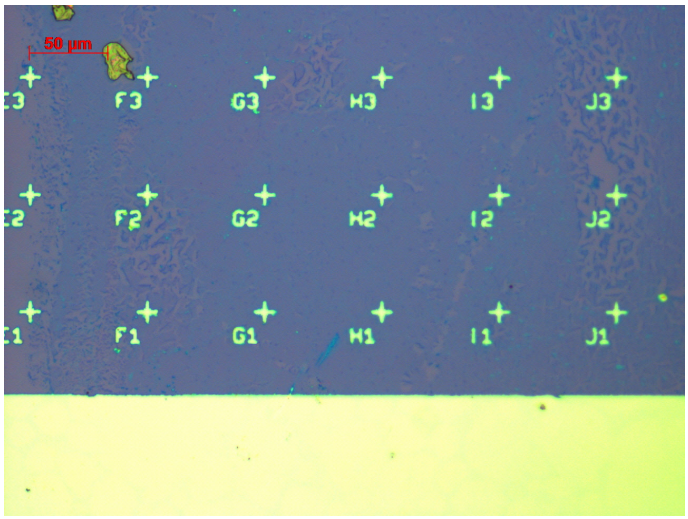

Figure 6.28: Optical microscope photo of the best graphene area chosen from a sample after the transfer process.

Figure 6.28 shows one of the chosen ares of graphene. Specifically for this sample, it is possible to note the presence of non continuous graphene in the right and left side of the

sample but the squared region between G2, H2, G1 and H1 contained a continuous and uncontaminated layer.

The geometry of the sample was then defined by optical lithography. Photoresist S-1813 was spin-coated at 5000 rpm for 30 seconds on the sample, then soft-baked on a hot plate for 1 minute at 115°C. A standard Cr photolithographic mask was designed and then fabricated by the commercial supplier; the sample geometries defined on the mask were designed following expectations based on the theory presented in section 6.1 and a detailed explanation will be given in section 6.4. The sample was exposed in the mask aligner for 6 seconds at 6.5mW/cm^2 UV lamp power and then developed in MF-319 developer for 30 seconds. The unwanted graphene was removed using an oxygen plasma asher operated for 1 minute at 50 W of RF power. The unwanted chromium was removed by soaking the sample in a standard chromium etchant solution for 30 seconds. Finally the photoresist was removed in acetone and the results are shown in figure 6.29(b).

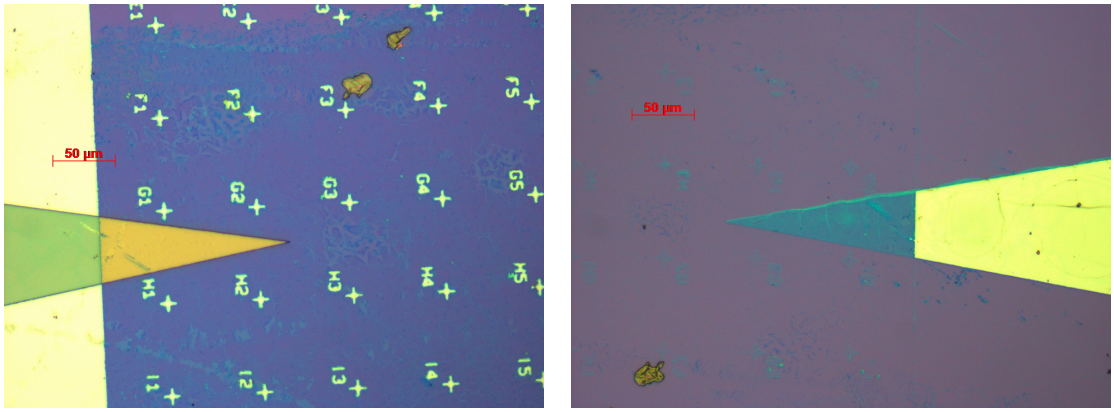

(a) (b)

Figure 6.29: Optical microscope photo of (a) post-developed lithographically defined graphene area. (b) After graphene and chromium etching

In some cases the fabrication of metal contacts on graphene was needed for electrical testing. This part of the processing included using a bilayer of photoresist in order to ensure a highly precise definition of the metal contacts. First a layer of LOR A3 photoresist was spin-coated on the sample at 3000 rpm, ensuring a thickness of $\sim$ 300 nm. This was hard-baked at 200°C for 5 minutes. A second layer of S-1813 was then spin-coated at

5000 rpm for 30 seconds, before removing the edge beads and a second bake at 115°C. The contacts were defined by optical lithography exposing the sample for 13 seconds at 3 mW/cm^2 UV lamp power. A layer of 100-nm-thick of Ti/Au (10 nm / 90 nm) was evaporated by thermal evaporation and lift-off was completed by soaking the sample in a standard 1165 Remover at 70°C for 5 minutes. Figure 6.30 shows optical microscope images taken after the development of the photoresist and after Ti/Au evaporation on the contacts areas.

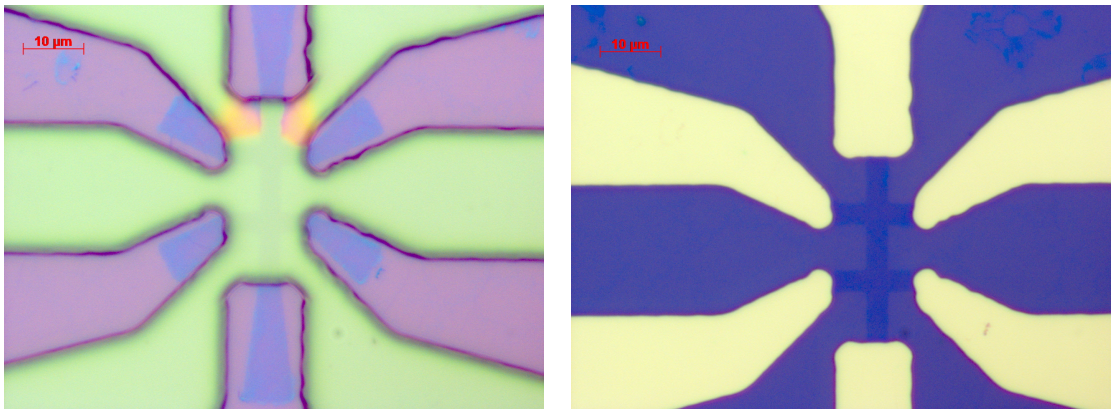

(a) (b)

Figure 6.30: Optical microscope photo of (a) post-developed lithographically defined graphene contacts and (b) post Ti/Au evaporation.

6.3.2 Graphene on h-BN/SiO$_2$

The samples of the heterostructure G/*h-BN* transferred on $SiO_2/Si(p+)$ wafer were purchased from a commercial supplier. The supplier ensured a 98% coverage of the substrate by the heterostructure and a continuous layer of graphene with minor holes and organic residues; the graphene is specified to be single layer for 95% of the sample area with islands of multi-layer graphene for the remaining 5%. Graphene geometries were defined by optical lithography using the Maskless Aligner - MLA 150 produced by Heidelber instruments. The MLA 150 employs a 375 nm laser source, does not require any photolithographic Cr mask, and is suited for feature resolution down to 1 μm. The supplied software is capable of accepting electronic versions of geometries and the plate, where the sample is placed,

will move following them with high precision and speed. The fabrication procedure followed the standard process already adopted for G transferred on SiO_2. Photoresist S-1813 was spin-coated at 5000 rpm for 30 seconds and then the sample was soft-baked at 115°C for 1 minute on a hot plate. Exposure in the mask less aligner used dose of 90 mJ/cm^2.

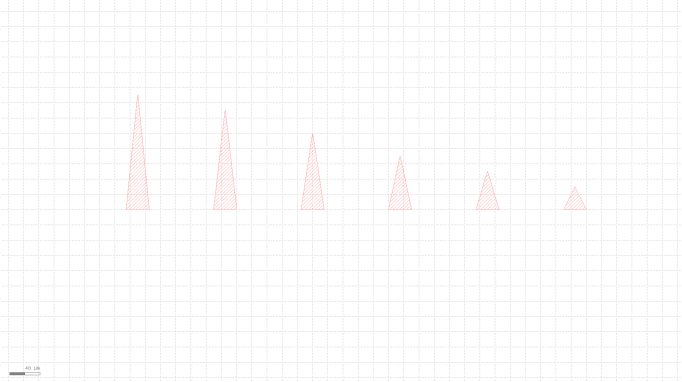

Figure 6.31: Design used in the mask less aligner for G/h-BN definition on SiO_2/Si(p+), exported from the software KLayout.

The sample design, exported from the software KLayout, is shown in figure 6.31. After exposure the sample was developed in MF-319 developer for 30 seconds and finally the unwanted graphene has been etched away in the oxygen plasma asher operated at 50 W of RF power for 1 minute. Figure 6.32 shows the results post-development and post-etching of graphene.

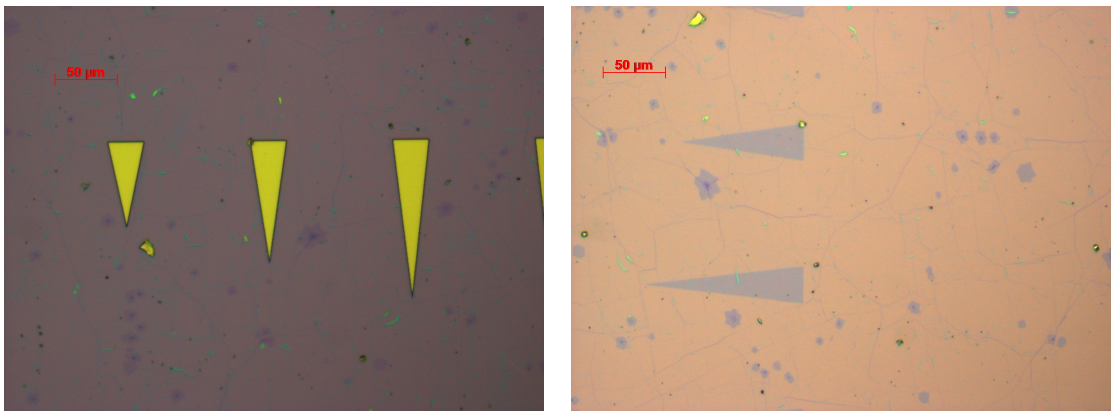

(a) (b)

Figure 6.32: Optical microscope photo of G/h-BN (a) after resist development and (b) after graphene etching.

Section 6.4 will be dedicated to the results and discussion of THz near-field imaging of the different fabricated graphene samples, which have also been characterised through Raman spectroscopy in order to verify the quality and the single layer nature of the samples. Raman measurements were performed using a Horiba LabRam HR microscope equipped with a green laser (λ=532.01nm) with power 40 mW and a beam spot size, given by a 50 $\times$ objective lens, of $sim5\mu$m. The spectral resolution was set to 2 cm^{-1} and all the Raman peaks were fitted with a Lorenztian function.

6.4 Results and discussion

The aim of the study presented here is to explore the possibility of imaging THz plasmons in graphene using an s-SNOM system equipped with a THz QCL source. For this work, and following the expectations based on the theory presented in section 6.1, two different tip sizes have been used. As stated by the supplier (www.rmnano.com), the tips are made of an alloy Pt:Ir and have radius r = 20 nm and r = 1 μm, both having length l=80μm$\pm$20% and a resonant frequency Ω $\sim$60kHz. Throughout the discussion, the tip with r=20nm will be referred to as the small tip and the tip with r=1μm as the large tip. The apparatus for this study consisted of an s-SNOM microscope made by the company Neaspec equipped with a THz QCL source. The QCL consisted of a 14 μm-thick 9-wells GaAs/AlGaAs active region processed in a semi-insulating surface plasmon (SISP) ridge waveguide with dimension 1.8 mm$\times$150 μm, with a lasing frequency ν $\sim$3.45 THz ($\hbar\omega$ $\sim$14.2meV, λ_0 $\sim$87μm), which was previously characterized as shown in figures 2.25(a) and 2.26(a); the schematic is exactly as shown in figure 5.11. The laser was driven with a constant current of 420 mA and kept at a constant temperature of 20$\pm$0.01 K using a continuous flow L-He cryostat. THz near-field images of each sample were acquired from the SM signal demodulated at 3Ω, using a 200 ms (small tip) or 300 ms (large tip) integration time per pixel. The NF signal was first maximized by aligning the QCL in order to acquire images from the top of a SM fringe. Considering that the tip remains stationary and that the sample is moved along the direction of the beam path (the longitudinal direction) throughout the acquisition, this ensured that any tilt of the sample will not cause any decrease of the signal.

Based on the theory presented in section 6.1, a plasmon propagating on graphene on a SiO_2 substrate (ε_r=3.9) at ∼3.45 THz should yield a plasmon wavelength λ_p ∼3.5μm (extracted from the plasmon dispersion relation shown in figure 6.9) in the case of E_F = 0.1 eV and a DC mobility of μ = 10000 cm^2/Vs.

6.4.1 CVD graphene/SiO_2 with the small tip

The first set of samples (namely **C706_5_1** and **C706_5_2**) consisted of CVD graphene grown on Cu which has been transferred on the same SiO_2/Si(n+) substrate and processed into tapered ribbons through optical lithography. These samples were imagined with the small tip using a tapping frequency Ω ∼63.3kHz and amplitude Δz∼27nm. As in the literature the choice of tapered ribbons is dictated by the fact that in triangular geometries, propagating plasmons should show localized resonant modes as shown in figure 6.24.
THz images and AFM topographies obtained from sample **C706_5_1** with a pixel size of 300nm×333nm for the body and 500nm×250nm for the tip of the triangle, are shown in figures 6.33 and 6.34, respectively. The Raman spectra along with the optical image taken from the Raman microscope are shown in figure 6.35.

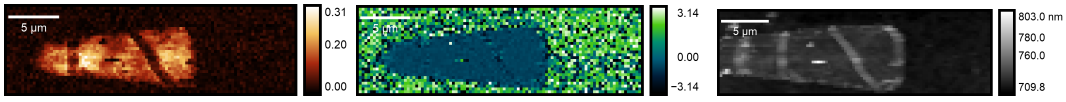

(a) (b) (c)

Figure 6.33: **C706_5_1** triangle body. THz near-field image of tapered ribbon of G/SiO_2 acquired using the small near-field tip, demodulated at 3Ω. (a) Amplitude, vertical scale a(ω). (b) Phase, vertical scale p(rad). (c) AFM topography. 100×30 pixels with pixel size 300nm×333nm.

The Raman spectrum of `C706_5_1` shows the classic G and 2D peaks of graphene [292–294] which have been fitted with a Lorentzian function. The fit of the 2D mode has a Raman shift peak at 2694 ± 2 cm^{-1} and its full widths at half maximum (FWHM) is 37 cm^{-1}. The fit of the G peak instead has a peak at 1583 ± 2 cm^{-1} and its FWHM is 16 cm^{-1}. From the shapes, the positions and the relative intensity of these two peaks the single layer nature of this sample can be attested [293, 294]. From the G peak it is possible

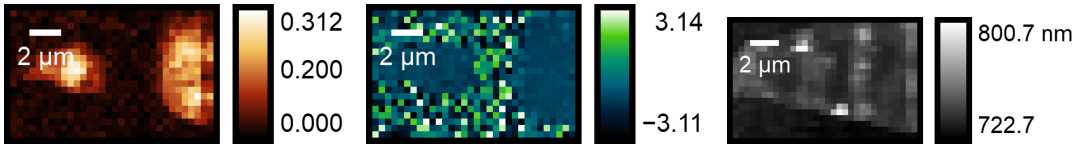

(a) (b) (c)

Figure 6.34: **C706_5_1** triangle tip. THz near-field image of tapered ribbon tip G/SiO_2 acquired using the small near-field tip, demodulated at 3Ω. (a) Amplitude, vertical scale a(ω). (b) Phase, vertical scale p(rad). (c) AFM topography. 32×20 pixels with pixel size 500nm×250nm.

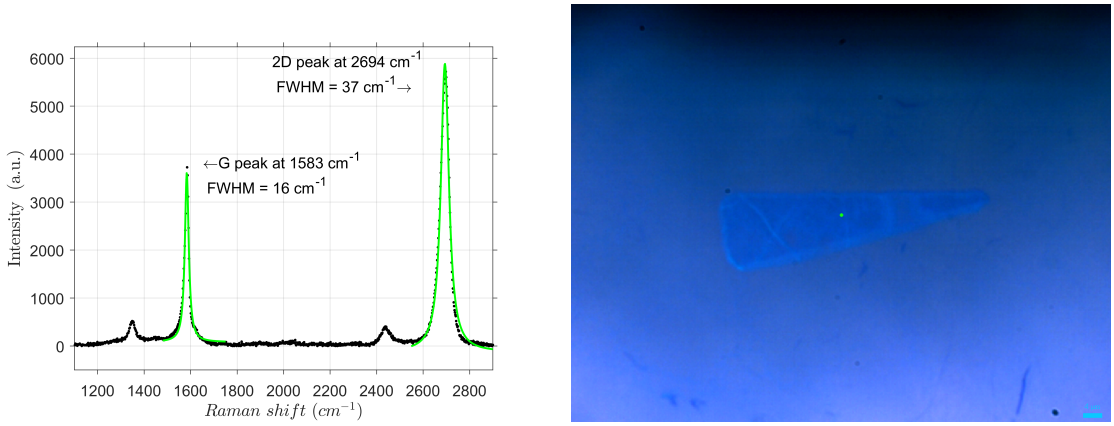

(a) (b)

Figure 6.35: **C706_5_1**.(a) Raman spectrum with fitted G and 2D peaks. (b) Optical image taken from the Raman microscope. The green dot indicates the position where the Raman spectrum has been acquired.

to evaluate the carrier concentration of the sample. By taking into account the error given by the precision of the spectrum and by following the nonadiabatic Kohn anomaly theory, the G peak position reveals a carrier concentration $n \sim 1.5 \times 10^{12} cm^{-2}$ [292, 295]. Although this value might not be accurate, it can provide a general understanding of the set of samples under investigation. The topographies (figures 6.33(c) and 6.34(c)) suggest a sample containing some contaminations due to the processing. In particular, it is possible to notice oblique lines higher than graphene in the topography (see figure 6.33(c)); these lines show an almost null signal in the THz near-field amplitude, suggesting their origin is due to contaminants on the graphene surface.

The THz image obtained from the triangle tip (figure6.34(a)) clearly shows a null signal in the middle area as well. However, its topography (see figure 6.34(c)) does show the

presence of graphene, so in this case the null signal is attributable to a graphene area predominated by defects. Although the Raman spectrum should reveal the presence of defective graphene, it should be noted that the Raman laser was not positioned on this area of defects when the spectrum was acquired.

The THz near field images do not show any clear evidence of propagating plasmon. Nevertheless, clear contrast between the substrate and the graphene is visible in the amplitude images, which is expected from the theory (see figure 6.15(a)). In order to compare the results with theory (see figure 6.15(b)), similarly to Chapter 5, the amplitude and the phase image are combined following the relation, V_{SM}=$a_3$cos(p_3) and the result is shown in figure 6.36. The experimental ratio of $s_{3,G}/s_{3,SiO_2}$ is obtained by averaging the amplitude of V_{SM} in the squared areas as shown in figure 6.36. The theory predicted a ratio of amplitudes between G and substrate, $s_{3,G}/s_{3,SiO_2}(\omega) \sim 3$ which is in agreement to the experimental ratio which yields $s_{3,G}/s_{3,SiO_2}(\omega) \sim 5$. The phase cannot be compared because the stepped-frequency approach was not adopted for these measurements.

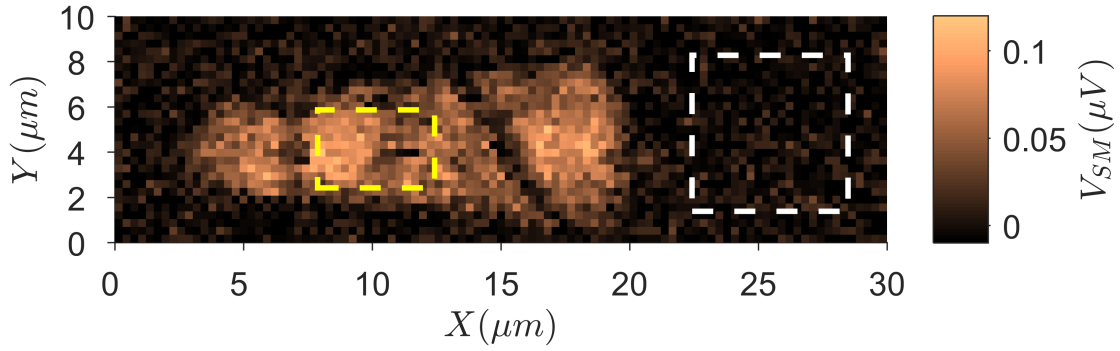

Figure 6.36: **C706_5_1** THz near-field image obtained following the relation V_{SM}=$a_3$cos(p_3), in which a_3 is figure 6.33(a) and p_3 is figure 6.33(b). The image size is 100×30 pixels. The square indicates the areas where $s_{exp}(\omega)$ was averaged.

The slight discrepancies between the experimental and theoretical amplitude ratios can be attributed to a temperature effect, which is assumed T=0K in the theory. At ambient temperature, T=295K, the carrier concentration of graphene increases and this can explain the larger V_{SM} measured from the experiments [296, 297].

C706_5_2 is a sample fabricated from the same CVD graphene on Cu as the previous

sample `C706_5_1`, and transferred onto the same SiO_2/Si(n+) substrate. They only differ in the region of graphene chosen for lithography, but they have been processed at the same time. THz near-field images of this sample with a pixel size of 310nm×333nm are shown in figure 6.37. The AFM topographiy is shown in figure 6.37(c) and the Raman spectrum along with the optical image taken from the Raman microscope are shown in figure 6.38.

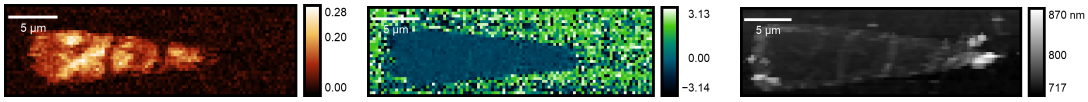

(a) (b) (c)

Figure 6.37: **C706_5_2** graphene tapered ribbon. THz near-field image of tapered ribbon of G/SiO_2 acquired by using the small near-field tip, demodulated at 3Ω. (a) Amplitude, vertical scale $a(\omega)$. (b) Phase, vertical scale $p(rad)$.(c) AFM topography. 100×30 pixels with pixel size 310nm×333nm.

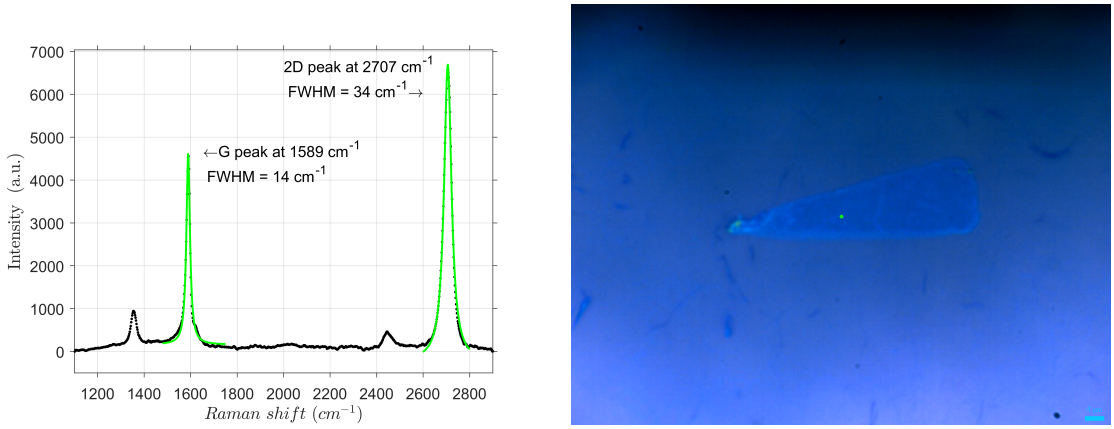

(a) (b)

Figure 6.38: **C706_5_2**.(a) Raman spectrum with fitted G and 2D peaks. (b) Optical image taken from the Raman microscope. The green dot indicates the position where the Raman spectrum has been acquired.

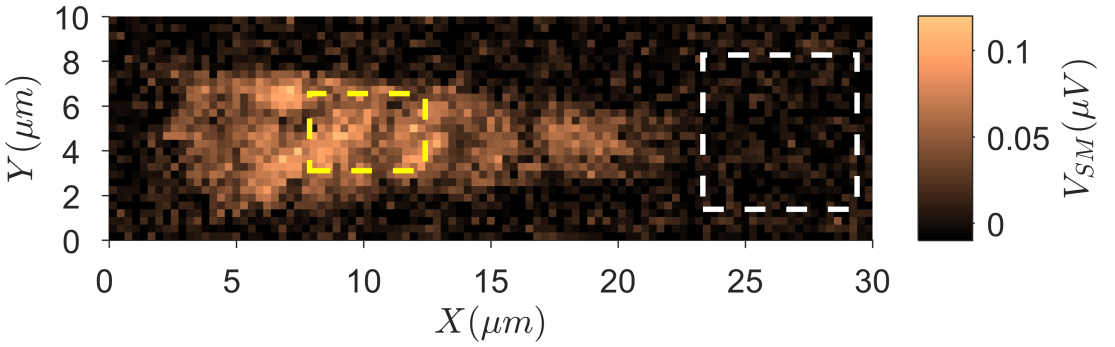

Figure 6.39: **C706_5_2** THz near-field image obtained following the relation V_{SM}=$a_3$cos(p_3), in which a_3 is figure 6.37(a) and p_3 is figure 6.37(b). The image size is 100×30 pixels. The squares indicate the areas where $s_{exp}(\omega)$ was averaged.

In this case the G peak of the Raman spectrum for `C706_5_2` reveals a carrier concentration n∼2×10^{12}cm^{-2} [292] comparable to the carrier concentration of `C706_5_1`. Considering that E_F and carrier concentration are directly related, this sample hence suggests a comparable doping to the previous sample. The 2D peak attests again the monolayer nature of this sample [293, 294]. The topography reveals the presence of contamination which is again translated as a decrease of amplitude in the THz image. Also in this case the ratio of amplitudes between substrate and graphene $s_{3,G}/s_{3,SiO_2}(\omega) \sim 5$ is obtained by averaging the values of the pixels as shown in figure 6.39. Similarly to `C706_5_1`, the discrepancies between theory and experiments are attributed to the temperature effect. It is notable that despite `C706_5_2` having a slightly higher doping than `C706_5_1` there is no appreciable difference in the measured signal. This is expected from the theory (see figure 6.15), because $s(\omega)$ does not vary significantly at $\hbar\omega$=14meV with an increase of E_F. Again, no propagating plasmons are visible in the THz near-field images of this sample.

6.4.2 CVD graphene/SiO_2 with the large tip

The next set of samples under analysis are CVD graphene grown on Cu and transferred on SiO_2/Si(n+). These samples (**C803_3_2**, **C803_1_2** and **C803_1_1**) have been processed in tapered ribbons and imaged using the large near field tip

THz near-field images for sample `C803_3_2` are shown in figure 6.40. These were acquired

using a 37 nm of tapping amplitude and a tapping frequency $\Omega \sim 57$ kHz. The AFM topography is shown in figure 6.40(c) and the Raman spectrum along with the optical image taken from the Raman microscope are shown in figure 6.41.

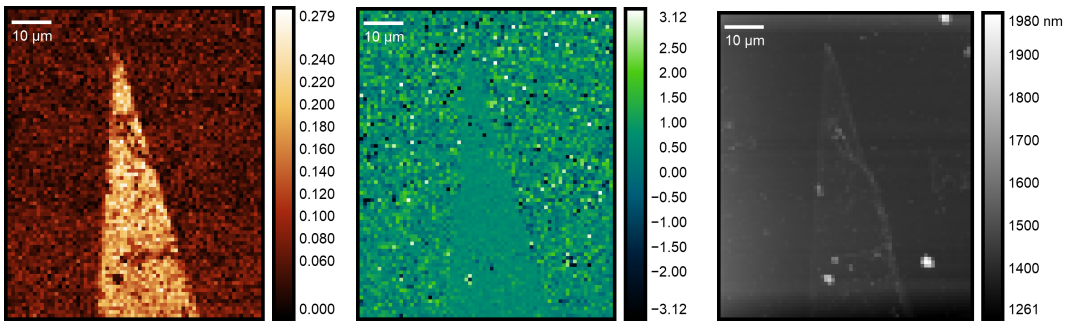

(a) (b) (c)

Figure 6.40: **C803_3_2** graphene tapered ribbon. THz near-field image of tapered ribbon of G/SiO_2 acquired by using the large near-field tip, demodulated at 3Ω. (a) Amplitude, vertical scale a(ω). (b) Phase, vertical scale p(rad). (c) AFM topography. 70×85 pixels with pixel size 1μm×1μm

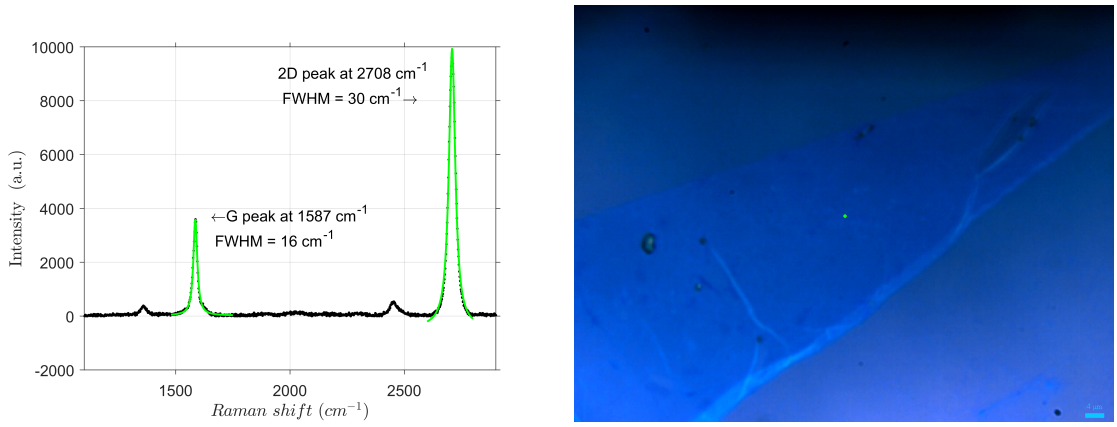

(a) (b)

Figure 6.41: **C803_3_2**.(a) Raman spectrum with fitted G and 2D peaks. (b) Optical image taken from the Raman microscope. The green dot indicates the position where the Raman spectrum has been acquired.

The 2D peak of the Raman spectrum of `C803_3_2` confirms the single layer nature of this sample. The G peak ,instead, indicates a carrier concentration n$\sim 2\times 10^{12}$cm^{-2} [292]. The topography (see figure 6.40(c)), as well as the optical microscope image (see figure 6.41(b)), reveal the presence of a defect close to apex and another defect near the base of

the triangle. Again, these defects are not confirmed by the Raman spectrum, because the Raman laser was not positioned on this area of defects when the spectrum was acquired. Nevertheless, a corresponding decrease in the THz signal is observed, similarly to the contamination in the previous samples.

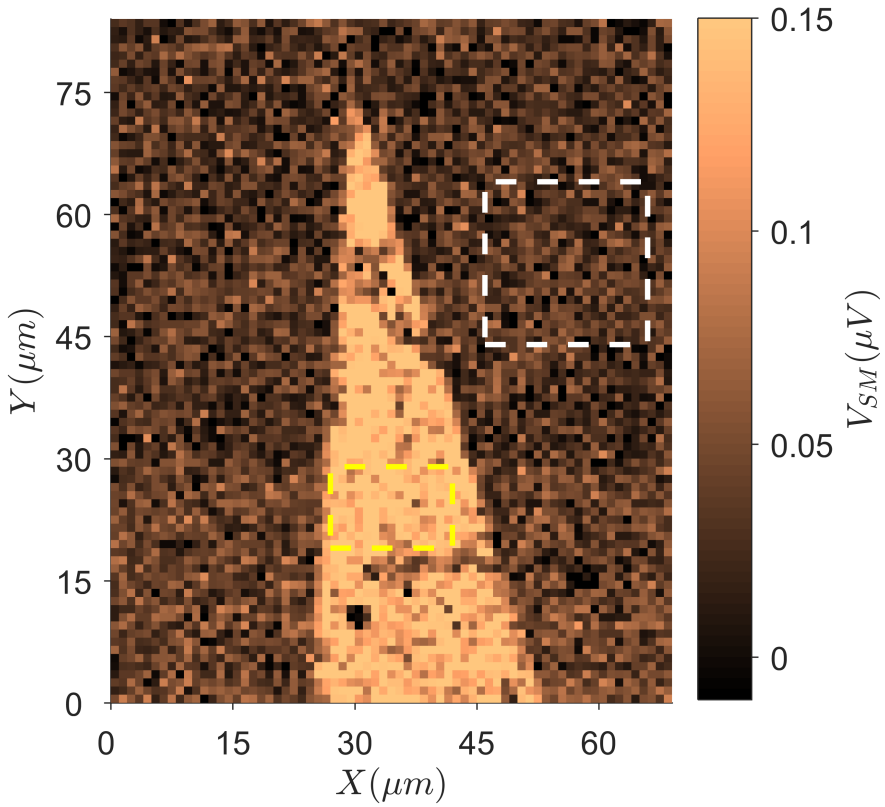

Figure 6.42: **C803_3_2** THz near-field image obtained following the relation V_{SM}=$a_3$cos(p_3), in which a_3 is figure 6.40(a) and p_3 is figure 6.40(b). The image size is 70×85 pixels. The squares indicate the areas where $s_{exp}(\omega)$ was averaged.

By averaging the V_{SM} signal of the pixels in the rectangles shown in figure 6.42 a ratio $s_{3,G}/s_{3,SiO_2}(\omega) \sim 4$ can be extracted. In this case the theory predicts a strong variation of this ratio depending on the Fermi energy on the sample, because the use of the large tip enhances the near-field signal of the graphene at low photon energies (see figure 6.21). The theoretical ratio of amplitudes varies between $s_{3,G}/s_{3,SiO_2}(\omega) \sim 2$, at E_F=0.1eV, to $s_{3,G}/s_{3,SiO_2}(\omega) \sim 10$, at E_F=0.4eV. Since the measurements were conducted at room temperature, it is possible to assume a temperature effect similar to the previous samples

which causes a slight increase of the V_{SM} signal for the graphene. This assumption and the result can suggest a Fermi energy for this sample of $E_F \sim 0.15$eV. Direct estimation of the Fermi energy for this sample through electrical measurements is not possible, but the results obtained from the sample `C803_1_2` give an interesting insight.

THz near-field images of this sample are shown in figure 6.43. These were acquired with the large tip using a 47 nm tapping amplitude and a tapping frequency $\Omega \sim 57kHz$. The AFM topographiy is shown in figure 6.43(c) and the Raman spectrum along with the optical image taken from the Raman microscope are shown in figure 6.44.

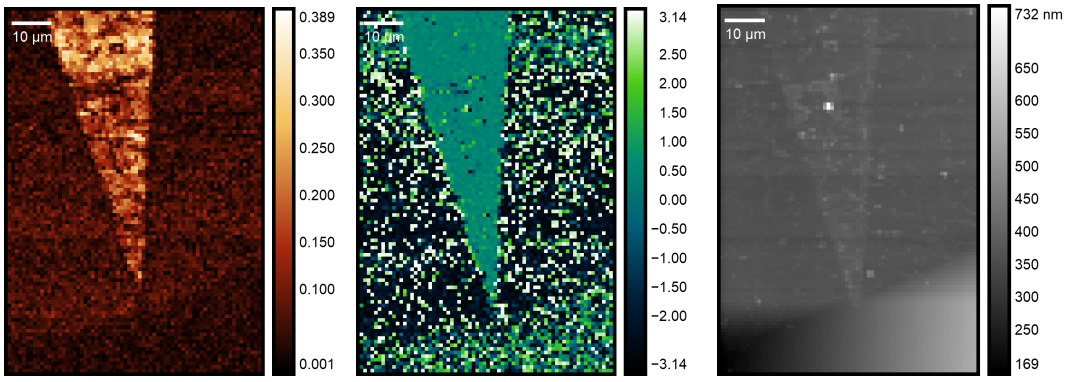

(a) (b) (c)

Figure 6.43: **C803_1_2** graphene tapered ribbon. THz near-field image of tapered ribbon of G/SiO_2 acquired by using the large near-field tip, demodulated at 3Ω. (a) Amplitude, vertical scale a(ω). (b) Phase, vertical scale p(rad). (c) AFM topography. 70×100 pixels with pixel size 1μm×1μm.

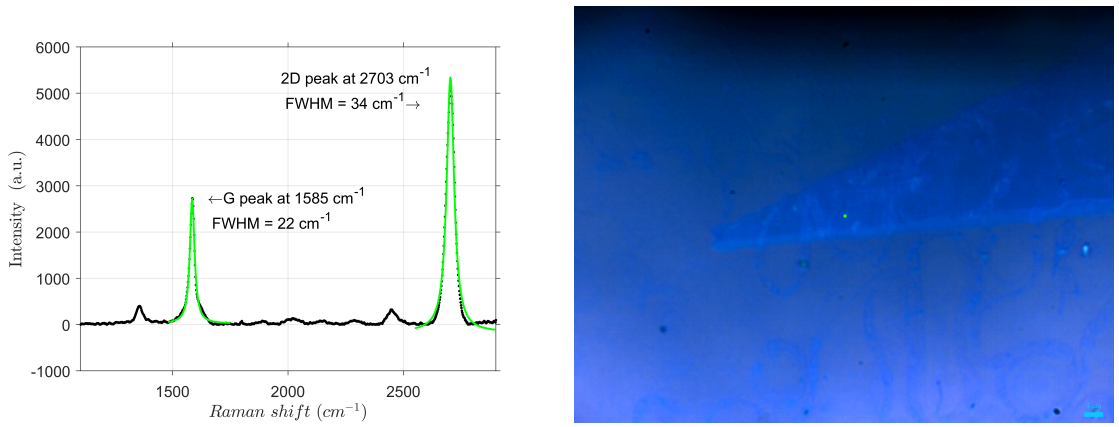

(a) (b)

Figure 6.44: **C803_1_2**.(a) Raman spectrum with fitted G and 2D peaks. (b) Optical image taken from the Raman microscope. The green dot indicates the position where the Raman spectrum has been acquired.

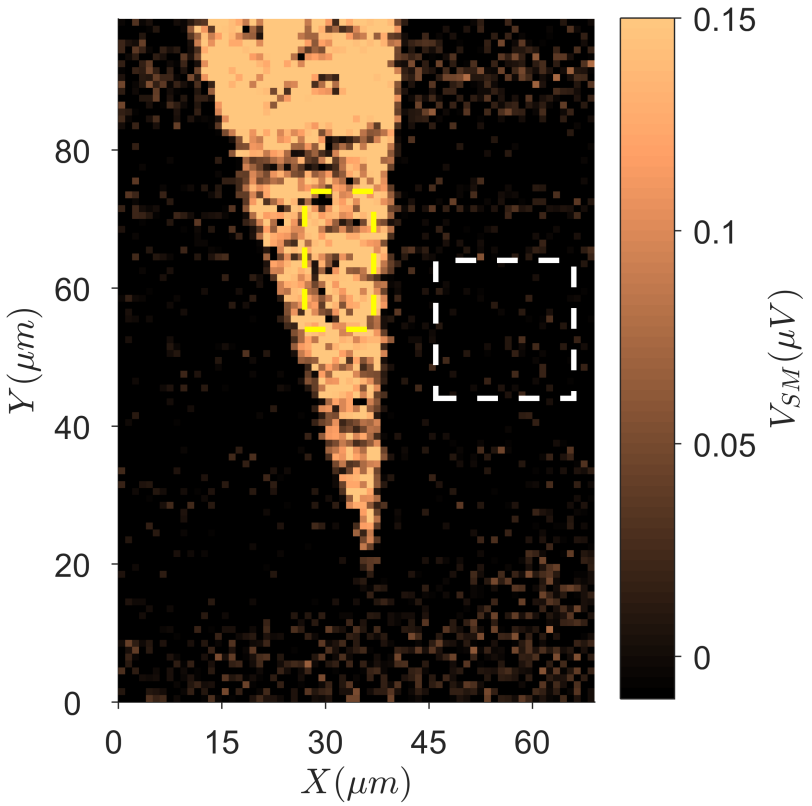

Figure 6.45: **C803_1_2** THz near-field image obtained following the relation V_{SM}=$a_3$cos(p_3), in which a_3 is figure 6.43(a) and p_3 is figure 6.43(b). The image size is 70×100 pixels. The squares indicate the areas where $s_{exp}(\omega)$ was averaged.

The Raman spectrum of C803_1_2 (see figure 6.44(a)) confirms the sample as single layer graphene [293, 294]. In this case the carrier concentration can be estimated to be n$\sim 2\times 10^{12}$cm^{-2} from the G peak [292]. This attests a similar doping level compare to the previous sample C803_3_2. By averaging the V_{SM} signal of the pixels in the rectangles shown in figure 6.45 a ratio $s_{3,G}/s_{3,SiO_2}(\omega) \sim 3$ can be extracted. Despite this sample has similar doping level compared to the sample C803_3_2, a lower V_{SM} signal can be acquired from the graphene. Considering the same experimental conditions as the previous sample, this effect is attributable to the defects on C803_1_2, which are also visible in the THz images and the AFM topography (see figure 6.43). The presence of defects lower the acquirable signal, in turn making the averaging lower.

THz near-field images of C803_1_1, shown in figure 6.46, have been acquired using 300ms integration time, 55 nm of tapping amplitude and demodulated at 3Ω, whith tapping frequency $\Omega \sim 57kHz$ of the big tip. AFM topographiy is shown in figure 6.46(c) and Raman spectrum with the optical image taken from the Raman microscope are shown in figure 6.47.

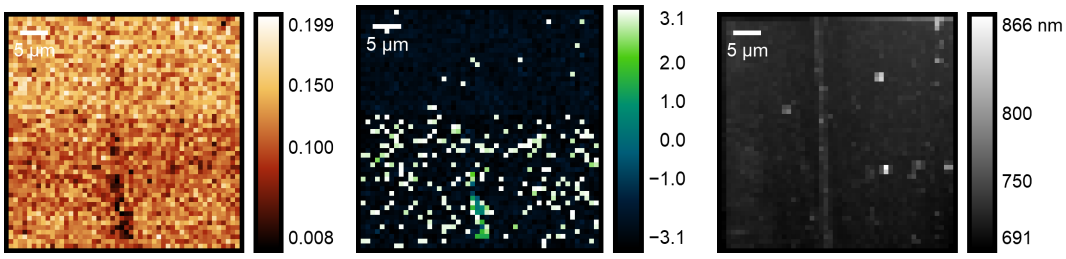

(a) (b) (c)

Figure 6.46: **C803__1__1** graphene tapered ribbon. THz near-field image of tapered ribbon of G/SiO_2 acquired by using the large near-field tip, demodulated at 3Ω. (a) Amplitude, vertical scale a(ω). (b) Phase, vertical scale p(rad). (c) AFM topography. 50×50 pixels with pixel size 1μm×1μm.

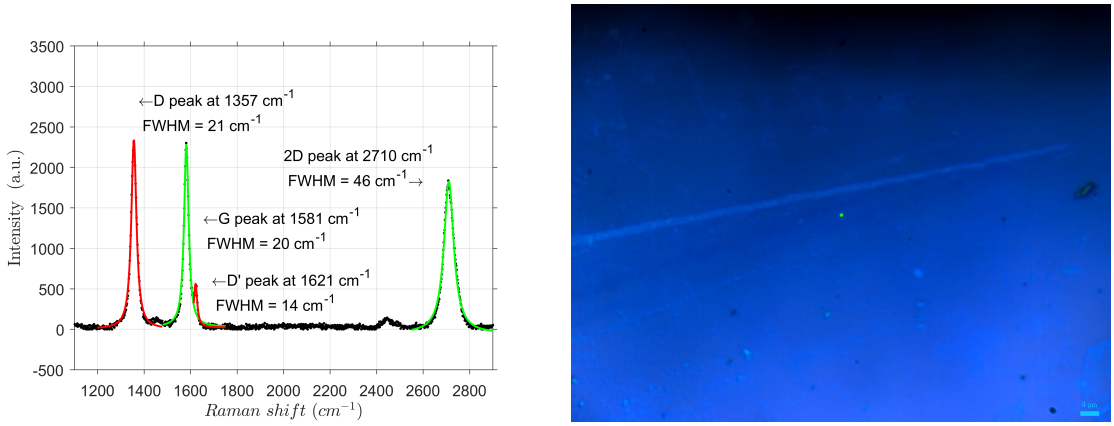

(a) (b)

Figure 6.47: **C803_1_1**.(a) Raman spectrum with fitted D, D', G and 2D peaks. (b) Optical image taken from the Raman microscope. The green dot indicates the position where the Raman spectrum has been acquired.

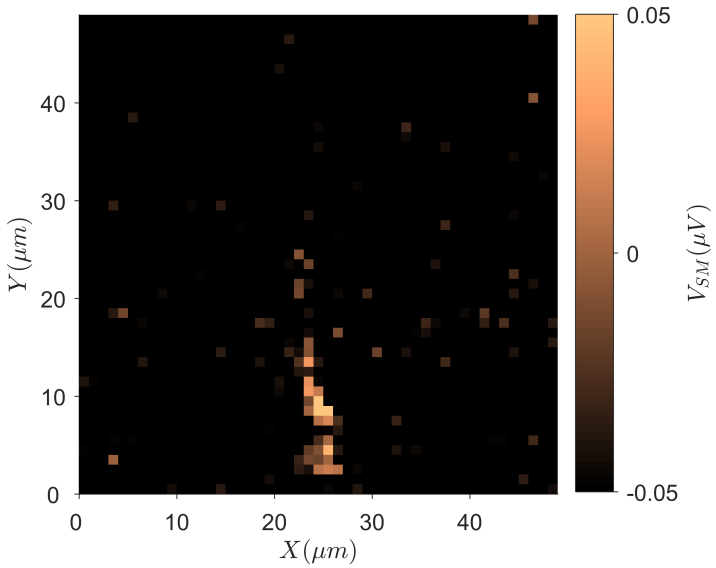

Figure 6.48: **C803_1_1** THz near-field image obtained following the relation V_{SM}=$a_3$cos(p_3), in which a_3 is figure 6.43(a) and p_3 is figure 6.43(b). The image size is 50×50 pixels.

The Raman spectrum of `C803_1_1` reveals the presence of accentuated D and D' peaks. These two peaks are associated with disorder in graphene; in particular by evaluating the ratio of intensities between D and D', $I(D)/I(D')$, it is possible to understand the nature of the defects causing disorder [298]. In this case the ratio is I(D)/I(D')≈4.15. According to [298] a ratio of this value would indicate defects in between graphene vacancy-like defects and graphite boundariy-like defects. However, in the case of graphite being present, the 2D peak of the Raman spectrum would be wider, with also the possibility of fitting it with 2 Lorentzian peaks [293, 294], and this is not the case for this sample. Despite the optical microscope images (see figure 6.47(b)) showing the presence of graphene, the AFM topography (see figure 6.46(c)), which extends over a 50 μm × 50 μm area, has only depicted an edge of the tapered ribbon. Hence, the AFM topography and the Raman spectrum suggest that this sample is affected by a significant presence of vacancies, which are missing atoms in the graphene crystalline structure. The impact of disorder in graphene has been studied by [286] and their calculations suggest that plasmon-losses in graphene are dominated by disorder, and that the plasmon lifetime (or relaxation time, RT) is shorter than the DC relaxation time, τ_{DC}. This would drastically impact on the near-field signal, because large plasmon losses would translate directly to a reduced signal. . In fact, the THz near-field images in figures 6.46 and 6.48 have an almost null response; only a small part of the ribbon edge is visible at the bottom of the amplitude image, which backs up this assertion. These assumptions need to be carefully verified trough other experiments which will be suggested in the conclusions. It's worth comparing the results obtained using the small tip and the results obtained using the large tip with the theory. Considering an energy photons of 14meV and using the small tip, the theory predicted no visible differences in the amplitude ratio between graphene and substrate increasing the E_F. On the other hand the use of the large tip would make this ratio increase by increasing the E_F. In our measurements this effect is not directly evident because of the use of different samples. A near-field study of a field-effect transistor based on a graphene channel, using a large tip would make these differences more accentuated, because the fermi energy could be tuned accordingly. Finally, despite the use of a large tip, no propa-

gating plasmons are visible in the THz near-field images of these samples.

6.4.3 CVD graphene/CVD h-BN/SiO_2

The next sample (namely **G_hBN_1**) is a sample of G/h-BN/SiO_2/Si(p+) which has been processed in a tapered ribbon through optical lithography using a maskless aligner. The reason of imaging this sample is related to the lower surface roughness compared to SiO_2 which should lead to considerably higher mobility [26, 28, 140, 271]. THz near-field images of `G_hBN_1` are shown in figure 6.49. These images were acquired using the small tip with a 381 nm tapping amplitude and a tapping frequency Ω ~68kHz. The AFM topography is shown in figure 6.49(c) and the Raman spectrum along with the optical image taken from the optical microscope are shown in figure 6.50.

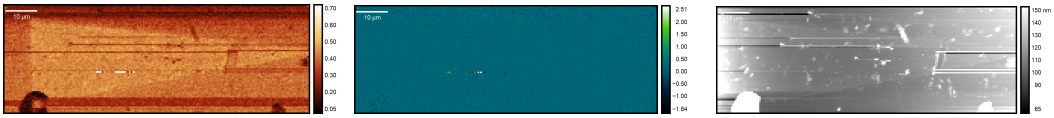

(a) (b) (c)

Figure 6.49: **G_hBN_1** graphene tapered ribbon. THz near-field image of tapered ribbon of G/h-BN acquired by using the small near-field tip, demodulated at 3Ω. (a) Amplitude, vertical scale a(ω). (b) Phase, vertical scale p(rad). (c) AFM topography. 200×70 pixels with pixel size 500nm×500nm

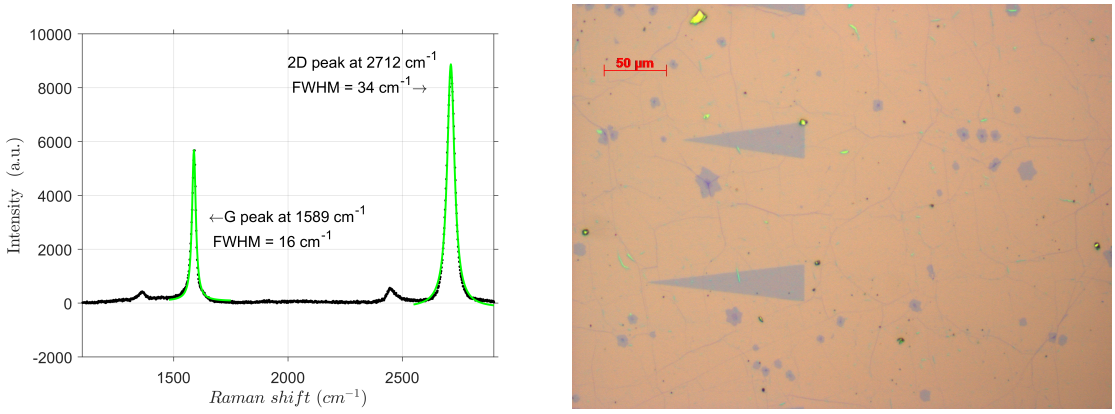

(a) (b)

Figure 6.50: **G_hBN_1**.(a) Raman spectrum with fitted G and 2D peaks. (b) 20× Optical image taken from the optical microscope.

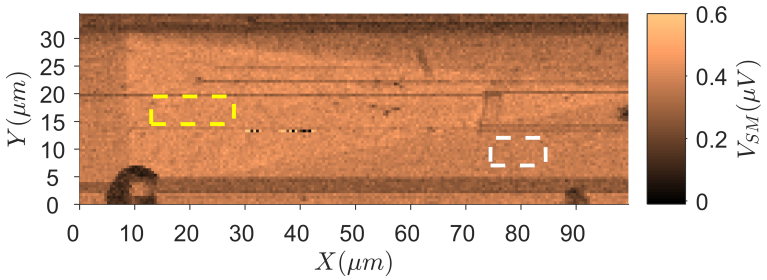

Figure 6.51: **C803_1_1** THz near-field image obtained following the relation V_{SM}=$a_3$cos(p_3), in which a_3 is figure 6.49(a) and p_3 is figure 6.49(b). The image size is 200×70 pixels. The rectangles indicate the areas where $s_{exp}(\omega)$ was averaged.

The raman spectrum of `G_hBN_1` reveals the single layer nature of the graphene on this sample and a carrier concentration of n∼3×10^{12}cm^{-2}. In this case, by averaging the V_{SM} signal of the pixels in the rectangles shown in figure 6.51 a ratio $s_{3,G}/s_{3,SiO_2}(\omega)$ ∼ 1 can be extracted. The theory predicted an amplitudes ratio of ∼ 3 independently of the value of E_F (see figure 6.17(a)). The difference between amplitudes in the theory and the experiment might be related to the temperature effect which impacts on electron-phonon coupling in the graphene. In fact, in [288, 299], the authors emphasize that at room temperature scattering from acoustic phonons is the dominant limiting factor in h-BN/G/h-BN stacks. Moreover, in this sample, graphene is not encapsulated but is always facing the environment on the top side, and this might be the source of different contaminants which could have a negative impact on the results. These two effects together could have prevented the observation of propagating plasmons in the THz near-field images of this sample.

6.5 Conclusions

In conclusion, in this study, the NF imaging of graphene samples using s-SNOM has been presented, and the possibility to image propagating plasmons on graphene has been explored. All the samples have shown no evidence of propagating plasmons, which is not unexpected considering the theoretical predictions, which suggest poor plasmon propagation

in the THz range (see figure 6.10). In order to increase plasmon propagation in the THz range, a possible pathway to be undertaken would be through the use of graphene samples with larger mobility, as shown in figure 6.11. To do so an encapsulation of graphene in two layers of h-BN can drastically increase the mobility, because of the low substrate surface roughness which would avoid charge traps or Coulomb contaminations, but also because the layer covering the top side would screen the graphene from the environment. Also an exfoliated graphene sample, rather than a CVD-grown sample, would have a higher mobility [20]. Another possibility to increase the mobility would be the creation of a quasi-suspended graphene sheet as shown in [254], by the introduction of polymer nano-particles dispersed on the substrate to lift the graphene layer. An increase of mobility can also be achieved by using cryogenic temperatures. In the theory a temperature $T = 0$ has been assumed, although the samples were at room temperature. It has been demonstrated how a low temperature can increase the plasmon propagation (see figure 6.25, [28]), due to a reduction of the eletron-phonon interaction. Hence, an interesting study would be the analysis of imaging graphene in the THz range at cryogenic temperatures. This approach could reveal interesting insights explaining the electron-phonons interaction in more depth. Another interesting study would be the analysis of disorder in graphene. Following the suggestion in [298], control of the defect concentration in graphene can be achieved in a simple oxygen plasma asher at fixed pressure and fixed RF power, by simply changing the ashing time from 1 to 300 seconds. THz near field imaging of graphene samples with controlled defect concentrations might reveal other interesting properties related to the plasmon lifetime which have been experimentally studied only in the mid-IR range [286]. THz near-field imaging, AFM and Raman measurements together are powerful tools to analyse 2D systems, such as graphene because they can be mutually used to study structural and electronic properties. In a study of disorder in graphene, for example, Raman spectroscopy would be needed to analyse the type of defects responsible for the disorder, which can be confirmed by AFM topography, and THz near-field imaging would reveal the electronic properties directly related to them.

7 Concluding Remarks

The following section summarises the results shown throughout this thesis and discusses potential future work.

7.1 Terahertz Quantum Cascade Lasers

In this chapter the general functioning of a THz QCL was explained. The processing of a wafer into THz QCL based on the structure adapted from the proposed one by [171] and fabricated in a SISP waveguide has been shown. Characterisation of the THz QCL through its LIV curve and spectrum are in agreement with the literature in terms of optical power (∼20mW at 10K in pulsed and ∼13mW at 30K in CW) and lasing frequency (∼3.3-3.5THz). Furthermore single mode emission of ∼3.445THz in CW mode thanks to a photonic lattice with a π-phase adjusted incorporated in it was achieved as in [9], making this QCL the perfect candidate for self-mixing imaging or near-field imaging based on self-mixing. In the next chapters the single mode emission and the continuous frequency tuning of the aforementioned QCL will be exploited to take images and demonstrate the possibility to retrieve information about permittivity of materials.

7.2 Self-mixing in THz QCLs

In this chapter the theory describing the self-mixing effect in lasers has been explained. The three-mirror model allowed the derivation of two fundamental equations (3.21 and 3.30) useful to describe the behaviour of a QCL under optical feedback. In particular, the aim of this chapter was to provide insight of how it is possible to exploit the self-mixing effect in a THz QCL to extract both the amplitude and phase of the field reflected from a remote target, which can be related to sample properties such as the complex permittivity. Furthermore, the detection sensitivity of an LFI scheme based on a THz-frequency QCL has been quantified. The measurements demonstrated that variations on the laser voltage induced by OF to the laser can be resolved with the reinjection of powers as low as ∼-125 dB of the emitted power, which corresponds to a NEP for the used scheme

of $\sim$1.4 pW/$\sqrt{Hz}$. By estimating the reinjection losses this value corresponds to NEP $\sim$1 fW/$\sqrt{Hz}$, demonstrating the high suitability of the SM effect to applications that require the detection of weakly scattered THz radiation, such as THz-s-SNOM.

7.3 THz imaging (far field) based on Self-Mixing in a QCL

In this chapter far-field THz imaging systems utilising the self-mixing effect in a QCL have been experimentally demonstrated by acquiring images of radically different samples (skin tissue and silicon wafers) and by evaluating functioning parameters of the systems. Two different acquisition schemes, namely using mechanical modulation of the THz beam and swept-frequency imaging enabling retrieval of magnitude and phase parameters, have been considered. By reconstructing an image of a gold-on-glass resolution target and evaluating the square wave MTF, a spatial resolution of $\sim 200\mu$m has been demonstrated. Considering a lasing frequency of ~ 3.4 THz ($\lambda \sim 90\mu m$) and assuming a potentially irregular beam profile, this resolution limit is consistent with that reported in the literature [3, 11, 13, 116, 120, 204, 205].

Moreover, the SNR has been characterised within the context of imaging silicon wafers for photovoltaic applications. The SNR values were measured to be $\sim$10$\times$ lower than those obtained previously using a metallic target [14], due to part of the THz beam being transmitted through the silicon wafers. However it has been demonstrated that the SNRs were satisfactory to image and retrieve information from silicon wafer samples.

The imaging systems have been applied to the acquisition of images of silicon wafers relevant to the manufacture of photovoltaic cells. In particular, the possibility to be applied to the detection of cracks, due to the phase changes occurring along the cracks, and also for the detection of impurities and defects has been demonstrated. In the latter case it has been possible to measure the deformation of the silicon wafer surface due to an embedded impurity, assuming that the phase change on reflection at the silicon and the impurity is equal. Furthermore the edges of three stacked silicon wafers have been retrieved when the system was modified to acquire only the THz radiation transmitted through the sample, opening the possibility of studying samples not only in reflection but also in transmission

modalities.

Finally, the possibility of applying the imaging system to the study of human skin tissue, and for differentiating health and cancerous tissue has been demonstrated. By exploiting both the swept-frequency and the mechanical modulation approach, three layers of a benign skin sample, namely dermis, epidermis and subcutaneous fat, have been clearly differentiated due to their different chemical composition. Contrast in both magnitude and phase between skin melanoma and subcutaneous fat has also been demonstrated due to the increased water content developed by the melanoma.

7.4 Near-Field imaging based on self-mixing in a THz QCL

In this chapter, two different experimental systems for NF microscopy based on SM detection in a THz QCL have been presented. Despite the approach curves showing a NF enhancement of the SM signal demodulated up to 2^{nd} harmonic of the tip tapping frequency, the bespoke system suffered limitations given by the poor control of tip-sample surface distance (d). Considering that the NF enhancement occurs when d is comparable to the tip radius of curvature, the possibility to acquire an image is strictly related to the ability of the system to maintain d constant during the acquisition. Despite this approach have shown to work previously [185], the mentioned problem prevented the acquisition of images in this work. As such, a solution based on the implementation of a feedback circuit loop is proposed, similar to the work reported by R. Degl'Innocenti et al in [122].

The second system exploited a commercially available s-SNOM/AFM platform called neaSNOM made by the company Neaspec GmbH, which was operated using the SM detection scheme. Acquisition of V_{SM} demodulated up to the 5th harmonic and with a subwavelength imaging resolution of 83nm ($\sim \lambda/1000$) has been demonstrated by employing a QCL based on a hybrid structure and lasing at ~3.45THz. The system was characterized, and a clear dependence of the resolution on the tip tapping amplitude has been demonstrated. In order to select the ideal experimental parameters, the same image was acquired with different integration times, T_c; a good contrast between Au and Si was found for T_c=50ms, but T_c=200ms was selected as the best trade-off to ensure clear

contrast and reasonable acquisition time.

Exploiting the dependence of the QCL lasing frequency on I_{QCL} a stepped-frequency SM scheme was developed enabling coherent NF imaging measurements of the phase φ_n and amplitude s_n of a specific sample, using an all-electrical approach. The possibility to retrieve complex permittivity information of materials has been demonstrated by using two different samples, Au/SiO_2 and Au/KBr. The results have been compared to prediction of the FD model in which the metallic tip is modelled as a spheroid which mirrors the dipole, created by the incident beam, into the sample. While the Au/KBr sample has shown a really good agreement with the theory, a slight discrepancy in the measured phase contrast was found for the Au/SiO_2 sample, which has been attributed to the experimental conditions and the influence of the background signal, as suggested also by Cvitkovic *et al* [238].

Future development of THz-s-SNOM based on SM detection in QCLs could benefit from a broader QCL frequency tuning and consequently a wider frequency range to investigate fundamental properties of materials. Possible applications will range from imaging biomaterials to the investigation of quantum or plasmonic devices where the subwavelength resolution of the s-SNOM is an essential feature to understand the nano world phenomena.

7.5 THz near-field imaging of graphene

In conclusion, in this study, the NF imaging of graphene samples using s-SNOM has been presented, and the possibility to image propagating plasmons on graphene has been explored. All the samples have shown no evidence of propagating plasmons, which is not unexpected considering the theoretical predictions, which suggest poor plasmon propagation in the THz range (see figure 6.10). In order to increase plasmon propagation in the THz range, a possible pathway to be undertaken would be through the use of graphene samples with larger mobility, as shown in figure 6.11. To do so an encapsulation of graphene in two layers of h-BN can drastically increase the mobility, because of the low substrate surface roughness which would avoid charge traps or Coulomb contaminations, but also because the layer covering the top side would screen the graphene from the environment. Also

an exfoliated graphene sample, rather than a CVD-grown sample, would have a higher mobility [20]. Another possibility to increase the mobility would be the creation of a quasi-suspended graphene sheet as shown in [254], by the introduction of polymer nano-particles dispersed on the substrate to lift the graphene layer. An increase of mobility can also be achieved by using cryogenic temperatures. In the theory a temperature $T = 0$ has been assumed, although the samples were at room temperature. It has been demonstrated how a low temperature can increase the plasmon propagation (see figure 6.25, [28]), due to a reduction of the eletron-phonon interaction. Hence, an interesting study would be the analysis of imaging graphene in the THz range at cryogenic temperatures. This approach could reveal interesting insights explaining the electron-phonons interaction in more depth. Another interesting study would be the analysis of disorder in graphene. Following the suggestion in [298], control of the defect concentration in graphene can be achieved in a simple oxygen plasma asher at fixed pressure and fixed RF power, by simply changing the ashing time from 1 to 300 seconds. THz near field imaging of graphene samples with controlled defect concentrations might reveal other interesting properties related to the plasmon lifetime which have been experimentally studied only in the mid-IR range [286]. THz near-field imaging, AFM and Raman measurements together are powerful tools to analyse 2D systems, such as graphene because they can be mutually used to study structural and electronic properties. In a study of disorder in graphene, for example, Raman spectroscopy would be needed to analyse the type of defects responsible for the disorder, which can be confirmed by AFM topography, and THz near-field imaging would reveal the electronic properties directly related to them.

Bibliography

[1] G. P. Williams, "Filling the THz gap - High power sources and applications," *Reports on Progress in Physics*, vol. 69, no. 2, pp. 301–326, 2006.

[2] N. Rothbart, H. Richter, M. Wienold, L. Schrottke, H. T. Grahn, and H. W. Hubers, "Fast 2-D and 3-D terahertz imaging with a quantum-cascade laser and a scanning mirror," *IEEE Transactions on Terahertz Science and Technology*, vol. 3, no. 5, pp. 617–624, 2013.

[3] P. Dean, M. U. Shaukat, S. P. Khanna, S. Chakraborty, M. Lachab, A. Burnett, G. Davies, and E. H. Linfield, "Absorption-sensitive diffuse reflection imaging of concealed powders using a terahertz quantum cascade laser," *Optics Express*, 2008.

[4] A. A. Danylov, T. M. Goyette, J. Waldman, M. J. Coulombe, A. J. Gatesman, R. H. Giles, X. Qian, N. Chandrayan, S. Vangala, K. Termkoa, W. D. Goodhue, and W. E. Nixon, "Terahertz inverse synthetic aperture radar (ISAR) imaging with a quantum cascade laser transmitter," *Optics express*, vol. 18, no. 15, pp. 16264–72, 2010.

[5] M. Ravaro, V. Jagtap, G. Santarelli, C. Sirtori, L. H. Li, S. P. Khanna, E. H. Linfield, and S. Barbieri, "Continuous-wave coherent imaging with terahertz quantum cascade lasers using electro-optic harmonic sampling," *Applied Physics Letters*, vol. 102, no. 9, pp. 1–5, 2013.

[6] A. J. Huber, F. Keilmann, J. Wittborn, J. Aizpurua, and R. Hillenbrand, "Terahertz near-field nanoscopy of mobile carriers in single semiconductor nanodevices," *Nano Letters*, vol. 8, no. 11, pp. 3766–3770, 2008.

[7] O. Mitrofanov, I. Brener, R. Harel, J. D. Wynn, L. N. Pfeiffer, K. W. West, and J. Federici, "Terahertz near-field microscopy based on a collection mode detector," *Applied Physics Letters*, vol. 77, no. 22, p. 3496, 2000.

[8] B. S. Williams, "Terahertz quantum-cascade lasers," *Nature Photonics*, vol. 1, no. 9, pp. 517–525, 2007.

[9] I. Kundu, P. Dean, A. Valavanis, L. Li, Y. Han, E. H. Linfield, and A. G. Davies, "Frequency Tunability and Spectral Control in Terahertz Quantum Cascade Lasers with Phase-Adjusted Finite-Defect-Site Photonic Lattices," *IEEE Transactions on Terahertz Science and Technology*, vol. 7, no. 4, pp. 360–367, 2017.

[10] S. Donati, "Developing self-mixing interferometry for instrumentation and measurements," *Laser and Photonics Reviews*, vol. 6, no. 3, pp. 393–417, 2012.

[11] P. Dean, A. Valavanis, J. Keeley, K. Bertling, Y. L. Lim, R. Alhathlool, A. D. Burnett, L. H. Li, S. P. Khanna, D. Indjin, T. Taimre, A. D. Rakić, E. H. Linfield, and A. G. Davies, "Terahertz imaging using quantum cascade lasers - A review of systems and applications," *Journal of Physics D: Applied Physics*, vol. 47, no. 37, 2014.

[12] P. Dean, Y. L. Lim, A. Valavanis, R. Kliese, M. Nikolić, S. P. Khanna, M. Lachab, D. Indjin, Z. Ikonić, P. Harrison, A. D. Rakić, E. H. Linfield, and a. G. Davies, "Terahertz imaging through self-mixing in a quantum cascade laser.," *Optics letters*, vol. 36, no. 13, pp. 2587–9, 2011.

[13] P. Dean, A. Valavanis, J. Keeley, K. Bertling, Y. Leng Lim, R. Alhathlool, S. Chowdhury, T. Taimre, L. H. Li, D. Indjin, S. J. Wilson, A. D. Rakić, E. H. Linfield, and A. Giles Davies, "Coherent three-dimensional terahertz imaging through self-mixing in a quantum cascade laser," *Applied Physics Letters*, vol. 103, no. 18, pp. 2011–2015, 2013.

[14] J. T. Keeley, *Self-Mixing in Terahertz Quantum Cascade Lasers*. PhD thesis, University of Leeds, 2016.

[15] Y. Ren, R. Wallis, D. S. Jessop, R. Degl'Innocenti, A. Klimont, H. E. Beere, and

D. A. Ritchie, “Fast terahertz imaging using a quantum cascade amplifier,” *Applied Physics Letters*, vol. 107, no. 1, pp. 1–6, 2015.

[16] M. Wienold, T. Hagelschuer, N. Rothbart, L. Schrottke, K. Biermann, H. T. Grahn, and H. W. Hübers, “Real-time terahertz imaging through self-mixing in a quantum-cascade laser,” *Applied Physics Letters*, vol. 109, no. 1, 2016.

[17] F. D. J. Brunner, A. Schneider, P. Guenter, and P. G\"{u}nter, “A terahertz time-domain spectrometer for simultaneous transmission and reflection measurements at normal incidence,” *Optics Express*, vol. 17, no. 23, pp. 20684–20693, 2009.

[18] W. G. Spitzer and D. A. Kleinman, “Infrared lattice bands of quartz,” *Physical Review*, vol. 121, no. 5, pp. 1324–1335, 1961.

[19] R. Kliese, T. Taimre, A. A. A. Bakar, Y. L. Lim, K. Bertling, M. Nikoli, J. Perchoux, T. Bosch, and A. D. Raki, “Solving self-mixing equations for arbitrary feedback levels : a concise algorithm,” *Applied Optics*, vol. 53, no. 17, pp. 3723–3736, 2014.

[20] F. Schwierz, “Graphene transistors,” *Nature Nanotechnology*, vol. 5, no. 7, pp. 487–496, 2010.

[21] K. S. Novoselov, A. K. Geim, S. V. Morozov, D. Jiang, M. I. Katsnelson, I. V. Grigorieva, S. V. Dubonos, and A. A. Firsov, “Two-dimensional gas of massless Dirac fermions in graphene,” *Nature*, vol. 438, no. 7065, pp. 197–200, 2005.

[22] J. Zhang, C. Zhao, N. Liu, H. Zhang, J. Liu, Y. Q. Fu, B. Guo, Z. Wang, S. Lei, and P. A. Hu, “Tunable electronic properties of graphene through controlling bonding configurations of doped nitrogen atoms,” *Scientific Reports*, vol. 6, no. 4, pp. 1–10, 2016.

[23] D. Wang, X. Liu, L. He, Y. Yin, D. Wu, and J. Shi, “Manipulating graphene mobility and charge neutral point with ligand-bound nanoparticles as charge reservoir,” *Nano Letters*, vol. 10, no. 12, pp. 4989–4993, 2010.

[24] M. Jablan, H. Buljan, and M. Soljačić, "Plasmonics in graphene at infrared frequencies," *Physical Review B - Condensed Matter and Materials Physics*, vol. 80, no. 24, pp. 1–7, 2009.

[25] O. Mitrofanov, W. Yu, R. J. Thompson, Y. Jiang, Z. J. Greenberg, J. Palmer, I. Brener, W. Pan, C. Berger, W. A. De Heer, and Z. Jiang, "Terahertz near-field imaging of surface plasmon waves in graphene structures," *Solid State Communications*, vol. 224, pp. 47–52, 2015.

[26] P. Alonso-González, A. Y. Nikitin, Y. Gao, A. Woessner, M. B. Lundeberg, A. Principi, N. Forcellini, W. Yan, S. Vélez, A. J. Huber, K. Watanabe, T. Taniguchi, F. Casanova, L. E. Hueso, M. Polini, J. Hone, F. H. Koppens, and R. Hillenbrand, "Acoustic terahertz graphene plasmons revealed by photocurrent nanoscopy," *Nature Nanotechnology*, vol. 12, no. 1, pp. 31–35, 2017.

[27] J. Chen, M. Badioli, P. Alonso-González, S. Thongrattanasiri, F. Huth, J. Osmond, M. Spasenović, A. Centeno, A. Pesquera, P. Godignon, A. Zurutuza Elorza, N. Camara, F. J. G. de Abajo, R. Hillenbrand, and F. H. L. Koppens, "Optical nano-imaging of gate-tunable graphene plasmons," *Nature*, pp. 3–7, 2012.

[28] G. X. Ni, A. S. McLeod, Z. Sun, L. Wang, L. Xiong, K. W. Post, S. S. Sunku, B. Y. Jiang, J. Hone, C. R. Dean, M. M. Fogler, and D. N. Basov, "Fundamental limits to graphene plasmonics," *Nature*, vol. 557, no. 7706, pp. 530–533, 2018.

[29] G. Agnew, A. Grier, T. Taimre, Y. L. Lim, K. Bertling, Z. Ikonić, A. Valavanis, P. Dean, J. Cooper, S. P. Khanna, M. Lachab, E. H. Linfield, A. G. Davies, P. Harrison, D. Indjin, and A. D. Rakić, "Model for a pulsed terahertz quantum cascade laser under optical feedback," *Optics Express*, vol. 24, no. 18, p. 20554, 2016.

[30] A. Müller, M. Ghosh, R. Sonnenschein, and P. Woditsch, "Silicon for photovoltaic applications," *Materials Science and Engineering B: Solid-State Materials for Advanced Technology*, vol. 134, no. 2-3 SPEC. ISS., pp. 257–262, 2006.

[31] C. Sirtori, "Bridge for the terahertz gap," *Nature*, vol. 417, no. 6885, pp. 132–133, 2002.

[32] G. Davies and E. H. Linfield, "Bridging the terahertz gap," *Physics World*, vol. 17, no. 4, pp. 37–41, 2004.

[33] B. B. Hu and M. C. Nuss, "Imaging with terahertz waves," *Optics Letters*, vol. 20, no. 16, p. 1716, 1995.

[34] P. H. Siegel, "Terahertz Technology," *IEEE Trans. Microw. Theory Tech.*, vol. 50, no. 3, pp. 910–928, 2002.

[35] A. G. Davies, A. D. Burnett, W. Fan, E. H. Linfield, and J. E. Cunningham, "Terahertz spectroscopy of explosives and drugs," *Materials Today*, vol. 11, no. 3, pp. 18–26, 2008.

[36] M. Tonouchi, "Cutting-edge terahertz technology," *Nature Photonics*, vol. 1, pp. 97–105, 2007.

[37] J. F. Federici, B. Schulkin, F. Huang, D. Gary, R. Barat, F. Oliveira, and D. Zimdars, "THz imaging and sensing for security applications-explosives, weapons and drugs," *Semicond. Sci. Technol.*, vol. 20, pp. S266–S280, jul 2005.

[38] S. M. Kim, F. Hatami, J. S. Harris, A. W. Kurian, J. Ford, D. King, G. Scalari, M. Giovannini, N. Hoyler, J. Faist, and G. Harris, "Biomedical terahertz imaging with a quantum cascade laser," *Applied Physics Letters*, 2006.

[39] V. P. Wallace, A. J. Fitzgerald, S. Shankar, N. Flanagan, R. Pye, J. Cluff, and D. D. Arnone, "Terahertz pulsed imaging of basal cell carcinoma ex vivo and in vivo," *British Journal of Dermatology*, vol. 151, no. 2, pp. 424–432, 2004.

[40] A. Burnett, W. Fan, P. Upadhya, J. Cunningham, H. Edwards, T. Munshi, M. Hargreaves, E. Linfield, and G. Davies, "Complementary spectroscopic studies of materials of security interest," *Optics/Photonics in Security and Defence, Stockholm, Sweden*, vol. 6402, 2006.

[41] J. Chen, Y. Chen, H. Zhao, G. J. Bastiaans, and X.-C. Zhang, "Absorption coefficients of selected explosives and related compounds in the range of 0.1-2.8 THz," *Optics Express*, vol. 15, no. 19, p. 12060, 2007.

[42] W. S. Holland, J. S. Greaves, B. Zuckerman, R. A. Webb, C. McCarthy, I. M. Coulson, D. M. Walther, W. R. Dent, W. K. Gear, and I. Robson, "Submillimetre images of dusty debris around nearby stars," *Nature*, vol. 392, no. 6678, pp. 788–791, 1998.

[43] H. M. Pickett, "THz spectroscopy of the atmosphere," *Optoelectronics' 99-Integrated Optoelectronic Devices*, vol. 3617, no. January, pp. 2–6, 1999.

[44] R. Hoogeveen, P. Yagoubov, A. Maurellis, V. Koshelets, S. Shitov, U. Mair, and M. Krocka, "New cryogenic heterodyne techniques applied in TELIS : the balloon borne THz and submm limb sounder for atmospheric reaearch," *Infrared Spaceborne Remote Sensing XI*, vol. 5152, pp. 347–355, 2003.

[45] K. C. Huang and Z. Wang, "Terahertz terabit wireless communication," *IEEE Microwave Magazine*, vol. 12, no. 4, pp. 108–116, 2011.

[46] T. Löffler, T. Bauer, K. J. Siebert, H. G. Roskos, A. Fitzgerald, and S. Czasch, "Terahertz dark-field imaging of biomedical tissue," *Optics Express*, vol. 9, no. 12, p. 616, 2009.

[47] A. Novikova, D. Markl, J. A. Zeitler, T. Rades, and C. S. Leopold, "A non-destructive method for quality control of the pellet distribution within a MUPS tablet by terahertz pulsed imaging," *European Journal of Pharmaceutical Sciences*, vol. 111, pp. 549–555, 2018.

[48] C. Pei, H. Lin, D. Markl, Y. C. Shen, J. A. Zeitler, and J. A. Elliott, "A quantitative comparison of in-line coating thickness distributions obtained from a pharmaceutical tablet mixing process using discrete element method and terahertz pulsed imaging," *Chemical Engineering Science*, vol. 192, pp. 34–45, 2018.

[49] L. Li, L. Chen, J. Freeman, M. Salih, P. Dean, A. Davies, and E. Linfield, "Multi-Watt high-power THz frequency quantum cascade lasers," *Electronics Letters*, vol. 53, no. 12, pp. 799–800, 2017.

[50] L. Li, L. Chen, J. Zhu, J. Freeman, P. Dean, A. Valavanis, A. Davies, and E. Linfield, "Terahertz quantum cascade lasers with >1 W output powers," *Electronics Letters*, vol. 50, no. 4, pp. 309–311, 2014.

[51] C. W. Berry, M. R. Hashemi, and M. Jarrahi, "Generation of high power pulsed terahertz radiation using a plasmonic photoconductive emitter array with logarithmic spiral antennas," *Applied Physics Letters*, vol. 104, no. 8, 2014.

[52] A. V. Räisänen, "Frequency multipliers for millimeter and submillimeter wavelengths," *Proceedings of the IEEE*, vol. 1, no. 11, pp. 1842–1852, 1992.

[53] A. Maestrini, J. Ward, J. Gill, H. Javadi, E. Schlecht, G. Chattopadhyay, F. Maiwald, N. R. Erickson, and I. Mehdi, "A 1.7-1.9 THz local oscillator source," *IEEE Microwave and Wireless Components Letters*, vol. 14, no. 6, pp. 253–255, 2004.

[54] D. Saeedkia and S. Safavi-naeini, "Terahertz Photonics: Optoelectronic Techniques for Generation and Detection of Terahertz Waves," *Journal of Lightwave Technology*, vol. 26, no. 15, p. 2409, 2008.

[55] A. G. Davies, E. H. Linfield, and M. B. Johnston, "The development of terahertz sources and their applications," *Physics in Medicine and Biology*, vol. 47, no. 21, pp. 3679–3689, 2002.

[56] W. Shi, Y. J. Ding, N. Fernelius, and K. L. Vodopyanov, "Efficient, tunable, and coherent 0.18-5.27 Thz source based on GaSe crystal," *Optics Letters*, vol. 27, no. 16, pp. 1454–1456, 2002.

[57] G. Mourou, C. V. Stancampiano, A. Antonetti, and A. Orszag, "Picosecond microwave pulses generated with a subpicosecond laser-driven semiconductor switch," *Applied Physics Letters*, vol. 39, no. 4, pp. 295–296, 1981.

[58] D. H. Auston, K. P. Cheung, and P. R. Smith, "Picosecond photoconducting Hertzian dipoles," *Applied Physics Letters*, vol. 45, no. 3, pp. 284–286, 1984.

[59] T. Edwards, D. Walsh, M. Spurr, C. Rae, M. Dunn, and P. Browne, "Compact source of continuously and widely-tunable terahertz radiation.," *Optics Express*, vol. 14, no. 4, p. 1582, 2006.

[60] B. Ferguson and X. C. Zhang, "Materials for terahertz science and technology," *Nature Materials*, vol. 1, no. 1, pp. 26–33, 2002.

[61] G. P. Williams, "FAR-IR/THz radiation from the Jefferson Laboratory, energy recovered linac, free electron laser," *Review of Scientific Instruments*, vol. 73, no. 3, pp. 1461–1463, 2002.

[62] J. Faist, F. Capasso, D. L. Sivco, C. Sirtori, H. A. L., and A. Y. Cho, "Quantum Cascade Laser," *Science*, vol. 264, no. April, p. 553, 1994.

[63] R. Köhler, A. Tredicucci, F. Beltram, H. E. Beere, E. H. Linfield, A. G. Davies, D. A. Ritchie, R. C. Iotti, and F. Rossi, "Terahertz semiconductor-heterostructure laser," *Nature*, vol. 417, no. 6885, pp. 156–159, 2002.

[64] T. S. Hartwick, D. T. Hodges, D. H. Barker, and F. B. Foote, "Far infrared imagery," *Applied Optics*, vol. 15, no. 8, p. 1919, 1976.

[65] P. K. Cheo, "Far-infrared laser system for detection of defects in polyethylene-insulated power cables," *Optics Letters*, vol. 2, no. 2, p. 42, 1978.

[66] P. Dean, A. Valavanis, J. Keeley, K. Bertling, Y. L. Lim, R. Alhathlool, A. D. Burnett, L. H. Li, S. P. Khanna, D. Indjin, T. Taimre, A. D. Rakić, E. H. Linfield, and A. G. Davies, "Terahertz imaging using quantum cascade lasers - A review of systems and applications," *Journal of Physics D: Applied Physics*, vol. 47, no. 37, 2014.

[67] J. E. Bjarnason, T. L. J. Chan, A. W. M. Lee, M. A. Celis, and E. R. Brown,

"Millimeter-wave, terahertz, and mid-infrared transmission through common clothing," *Appl. Phys. Lett.*, vol. 85, no. 4, p. 519, 2004.

[68] J. A. Zeitler, P. F. Taday, D. A. Newnham, M. Pepper, K. C. Gordon, and T. Rades, "Terahertz pulsed spectroscopy and imaging in the pharmaceutical setting - a review," *J. Pharm. Pharmacol.*, vol. 59, pp. 209–223, feb 2007.

[69] J. A. Zeitler, Y. Shen, C. Baker, P. F. Taday, M. Pepper, and T. Rades, "Analysis of Coating Structures and Interfaces in Solid Oral Dosage Forms by Three Dimensional Terahertz Pulsed Imaging," *Journal of pharmaceutical sciences*, vol. 92, no. 2, p. 330, 2007.

[70] T. Yasui, T. Yasuda, K.-i. Sawanaka, and T. Araki, "Terahertz paintmeter for noncontact monitoring of thickness and drying progress in paint film," *Appl. Opt.*, vol. 44, p. 6849, nov 2005.

[71] M. Lu, J. Shen, N. Li, Y. Zhang, C. Zhang, L. Liang, and X. Xu, "Detection and identification of illicit drugs using terahertz imaging," *J. Appl. Phys.*, vol. 100, no. 10, p. 103104, 2006.

[72] T. Löffler, T. May, A. Alcin, B. Hils, C. A. Weg, and H. G. Roskos, "Continuous-wave terahertz imaging with a hybrid system," *Conference on Lasers and Electro-Optics, 2007, CLEO 2007*, vol. 091111, pp. 1–4, 2007.

[73] I. S. Gregory, W. R. Tribe, C. Baker, B. E. Cole, M. J. Evans, L. Spencer, M. Pepper, and M. Missous, "Continuous-wave terahertz system with a 60 dB dynamic range," *Applied Physics Letters*, vol. 86, no. 20, pp. 1–3, 2005.

[74] H. Richter, M. Greiner-Bär, S. G. Pavlov, A. D. Semenov, M. Wienold, L. Schrottke, M. Giehler, R. Hey, H. T. Grahn, and H.-W. Hübers, "A compact, continuous-wave terahertz source based on a quantum-cascade laser and a miniature cryocooler," *Optics Express*, vol. 18, no. 10, p. 10177, 2010.

[75] E. Bründermann, M. Havenith, G. Scalari, M. Giovannini, J. Faist, J. Kunsch, L. Mechold, and M. Abraham, "Turn-key compact high temperature terahertz quantum cascade lasers: imaging and room temperature detection," *Optics Express*, vol. 14, no. 5, p. 1829, 2006.

[76] J. Darmo, V. Tamosiunas, G. Fasching, J. Kroll, K. Unterrainer, M. Beck, M. Giovannini, J. Faist, C. Kremser, and P. Debbage, "Imaging with a Terahertz quantum cascade laser," *Optics Express*, vol. 12, no. 9, p. 1879, 2004.

[77] P. Dean, N. K. Saat, S. P. Khanna, M. Salih, A. Burnett, J. Cunningham, E. H. Linfield, and A. G. Davies, "Dual-frequency imaging using an electrically tunable terahertz quantum cascade laser," *34th International Conference on Infrared, Millimeter, and Terahertz Waves, IRMMW-THz 2009*, vol. 17, no. 23, pp. 156–159, 2009.

[78] A. W. M. Lee, B. S. Williams, S. Kumar, Q. Hu, and J. L. Reno, "Real-Time Imaging Using a 4.3-THz Quantum Cascade Laser and a 320 240 Microbolometer Focal-Plane Array," *IEEE PHOTONICS TECHNOLOGY LETTERS*, vol. 18, no. 13, pp. 1–3, 2006.

[79] B. N. Behnken, G. Karunasiri, D. R. Chamberlin, P. R. Robrish, and J. Faist, "Real-time imaging using a 2.8 THz quantum cascade laser and uncooled infrared microbolometer camera," 2008.

[80] S. Barbieri, J. Alton, H. E. Beere, E. H. Linfield, D. A. Ritchie, S. Withington, G. Scalari, L. Ajili, and J. Faist, "Heterodyne mixing of two far-infrared quantum cascade lasers by use of a point-contact Schottky diode," *Optics Letters*, vol. 29, no. 14, p. 1632, 2004.

[81] A. Barkan, F. K. Tittel, D. M. Mittleman, R. Dengler, P. H. Siegel, G. Scalari, L. Ajili, J. Faist, H. E. Beere, E. H. Linfield, A. G. Davies, and D. A. Ritchie, "Linewidth and tuning characteristics of terahertz quantum cascade lasers," *Optics Letters*, vol. 29, no. 6, p. 575, 2004.

[82] A. A. Danylov, T. M. Goyette, J. Waldman, M. J. Coulombe, A. J. Gatesman, R. H. Giles, W. D. Goodhue, X. Qian, and W. E. Nixon, "Frequency stabilization of a single mode terahertz quantum cascade laser to the kilohertz level," *Optics Express*, vol. 17, no. 9, p. 7525, 2009.

[83] D. A. Kleiman and P. P. Kisliuk, "Discrimination Against Unwanted Orders in the Fabry-Perot Resonator," *The Bell System Technical Journal*, vol. 50, pp. 453–462, 1962.

[84] H. Kogelnick and C. K. N. Patel, "ode Suppression and Single Frequency Operation in Gaseous Optical Masers," *IRE, Proc.l*, vol. 50, pp. 2365–2366, 1962.

[85] D. M. Clunie and N. H. Rock, "The laser feedback interferometer," *J. Sci. Instrum.*, vol. 41, pp. 489–492, 1964.

[86] C. B. Wheeler and S. J. Fielding, "Interferometry using a laser as radiation source , amplifier and detector," *J. Phys. E.*, vol. 5, pp. 101–103, 1972.

[87] M. I. Nathan, W. P. Dumke, G. Burns, F. H. Dill, G. Lasher, F. H. Dill, and G. Lasher, "STIMULATED EMISSION OF RADIATION FROM GaAs pn JUNCTIONS," *Applied Physics Letters*, vol. 1, p. 62, 1962.

[88] T. M. Quist, R. H. Rediker, R. J. Keyes, and W. E. Krag, "SEMICONDUCTOR MASER OF GaAs," *Applied Physics Letters*, vol. 1, no. 4, p. 91, 1962.

[89] R. N. Hall, G. E. Fenner, J. D. Kingsley, and T. J. Soltys, "Coherent Light Emission From GaAs Junctions," *Physical Review Letters*, vol. 9, no. 9, pp. 366–368, 1962.

[90] A. P. Bogatov, P. G. Eliseev, L. P. Ivanov, A. S. Logginov, M. A. Manko, and K. Y. Senatorov, "Study of the Single-Mode Injection Laser," *IEEE Journal of Quantum Electronics*, vol. 9, no. 2, pp. 392–394, 1973.

[91] H. Bachert and S. Raab, "The Influence of External Optical Coupling on the Threshold Current Density of GaAs Injection Lasers," *Phys. Status Solidi*, vol. 29, no. 2, pp. 175–178, 1968.

[92] R. Lang and K. Kobayashi, "External Optical Feedback Effects on Semiconductor Injection Laser Properties," *IEEE Journal of Quantum Electronics*, vol. 16, no. 3, pp. 347–355, 1980.

[93] J. H. Churnside, "Laser Doppler velocimetry by modulating a CO2 laser with backscattered light," *Applied Optics*, vol. 23, no. 1, p. 61, 1984.

[94] S. Shinohara, A. Mochizuki, H. Yoshida, and M. Sumi, "Laser Doppler velocimeter using the self-mixing effect of a semiconductor laser diode," *Applied Optics*, vol. 25, no. 9, pp. 1417–1419, 1986.

[95] M. H. Koelink, F. F. M. de Mul, A. L. Weijers, J. Greve, R. Graaff, A. C. M. Dassel, and J. G. Aarnoudse, "Fiber-coupled self-mixing diode-laser Doppler velocimeter : technical aspects and flow velocity profile disturbances in water and blood flows," *Applied Optics*, vol. 33, no. 24, p. 5628, 1994.

[96] M. H. Koelink, M. Slot, F. F. M. de Mul, J. Greve, R. Graaff, A. C. M. Dassel, and J. G. Aarnoudse, "Laser Doppler velocimeter based on the self-mixing effect in a fiber-coupled semiconductor laser: theory," *Applied Optics*, vol. 31, no. 18, p. 3401, 1992.

[97] F. F. M. de Mul, M. H. Koelink, A. L. Weijers, J. Greve, J. G. Aarnoudse, R. Graaff, and A. C. M. Dassel, "A semiconductor laser used for direct measurement of the blood perfusion of tissue," *IEEE Transactions on Biomedical Engineering*, vol. 40, no. 2, p. 208, 1993.

[98] C. Zakian, M. Dickinson, and T. King, "Particle sizing and flow measurement using self-mixing interferometry with a laser diode," *Journal of Optics A: Pure and Applied Optics*, vol. 7, pp. 445–452, 2005.

[99] M. Norgia, S. Member, A. Pesatori, and L. Rovati, "Low-Cost Optical Flowmeter With Analog Front-End Electronics for Blood Extracorporeal Circulators," *IEEE*

Transactions on instrumentation and measurement, vol. 59, no. 5, pp. 1233–1239, 2010.

[100] S. Donati, G. Giuliani, and S. Merlo, "Laser Diode Feedback Interferometer for Measurement of Displacements without Ambiguity," *IEEE Journal of Quantum Electronics*, vol. 31, no. 1, p. 113, 1995.

[101] R. Kliese, Y. L. Lim, K. Bertling, A. A. A. Bakar, T. Bosch, and A. D. Raki, "Self-mixing displacement sensing using the junction voltage variation in a GaN laser," *2008 Conf. Optoelectron. Microelectron. Mater. Devices*, pp. 23–25, 2008.

[102] Y. Leng Lim, P. Dean, M. Nikoli, R. Kliese, S. P. Khanna, M. Lachab, A. Valavanis, D. Indjin, Z. Ikoni, P. Harrison, E. H. Linfield, A. Giles Davies, S. J. Wilson, and A. D. Raki, "Demonstration of a self-mixing displacement sensor based on terahertz quantum cascade lasers," *Applied Physics Letters*, vol. 99, no. 8, pp. 1–4, 2011.

[103] F. P. Mezzapesa, L. L. Columbo, G. D. Risi, M. Brambilla, and M. Dabbicco, "Nanoscale Displacement Sensing Based on Nonlinear Frequency Mixing in Quantum Cascade Lasers," *IEEE Journal on Selected Topics in Quantum Electronics*, vol. 21, no. 6, 2015.

[104] M. Norgia and S. Donati, "A Displacement-Measuring Instrument utilizing self-mixing interferometry," *IEEE TRANSACTIONS ON INSTRUMENTATION AND MEASUREMENT*, vol. 52, no. 6, pp. 1765–1770, 2003.

[105] N. Servagent, F. Gouaux, and T. Bosch, "Measurements of displacement using the self-mixing interference in a laser diode," *J. Opt.*, vol. 29, pp. 168–173, 1998.

[106] G. Berkovic and E. Shafir, "Optical methods for distance and displacement measurements Optical methods for distance and displacement measurements," *Advances in Optics and Photonics*, vol. 4, pp. 441–471, 2012.

[107] F. Gouaux, N. Servagent, and T. Bosch, "Absolute distance measurement with an optical feedback interferometer," *Applied Optics*, vol. 37, p. 6684, 1998.

[108] T. Bosch, N. Servagent, R. Chellali, and M. Lescure, "Three-Dimensional Object Construction Using a Self-Mixing Type Scanning Laser Range Finder," *IEEE TRANSACTIONS ON INSTRUMENTATION AND MEASUREMENT*, vol. 47, no. 5, pp. 1326–1329, 1998.

[109] T. Gensty, J. Von Staden, M. Peil, W. Elsaber, G. Giuliani, and C. Mann, "Investigations of the Linewidth of Intersubband Quantum Cascade Lasers," *2006 IEEE 20th Int. Semicond. Laser Conf.*, pp. 65–66, 2006.

[110] Y. Yu, J. Xi, J. F. Chicharo, and T. Bosch, "Toward Automatic Measurement of the Linewidth-Enhancement Factor Using Optical With Weak Optical Feedback," *IEEE Journal of Quantum Electronics*, vol. 43, no. 7, pp. 527–534, 2007.

[111] M. Ishihara, T. Morimoto, S. Furuta, K. Kasahara, N. Akikusa, K. Fujita, and T. Edamura, "Linewidth enhancement factor of quantum cascade lasers with single phonon resonance-continuum depopulation structure on Peltier cooler," *Electronics Letters*, vol. 45, no. 23, 2009.

[112] A. Villafranca, G. Giuliani, S. Donati, and I. Garces, "Investigation on the linewidth enhancement factor of multiple longitudinal mode semiconductor lasers," *Proc. SPIE*, vol. 6997, no. 1, 2008.

[113] M. Wang and G. Lai, "Self-mixing microscopic interferometer for the measurement of microprofile," *Optics Communications*, vol. 238, no. 4-6, pp. 237–244, 2004.

[114] A. Bearden, M. P. O'Neill, L. C. Osborne, and T. L. Wong, "Imaging and vibrational analysis with laser-feedback interferometry," *Optics Letters*, vol. 18, no. 3, p. 238, 1993.

[115] B. Ovryn and J. H. Andrews, "Phase-shifted laser feedback interferometry," *Optics Letters*, vol. 23, no. 14, p. 1078, 1998.

[116] J. Keeley, P. Dean, A. Valavanis, K. Bertling, Y. L. Lim, R. Alhathlool, T. Taimre, L. H. Li, D. Indjin, A. D. Rakić, E. H. Linfield, and A. G. Davies, "Three-dimensional

terahertz imaging using swept-frequency feedback interferometry with a quantum cascade laser," *Optics Letters*, vol. 40, no. 6, p. 994, 2015.

[117] T. Bosch, N. Servagent, R. Chellali, and M. Lescure, "A scanning range finder using the self-mixing effect inside a laser diode for 3-D vision," *IEEE Instrumentation and Measurement Tec. Conf.*, vol. 1, pp. 226–231, 1996.

[118] E. Gagnon and J.-F. Rivest, "Laser range imaging using the self-mixing effect in a laser diode," *IEEE TRANSACTIONS ON INSTRUMENTATION AND MEASUREMENT*, vol. 48, no. 3, pp. 693–699, 1999.

[119] S. Shinohara, H. Uda, Y. Ichioka, H. Yasui, H. Yoshida, H. Ikeda, and M. Sumi, "Detection of mesa spots and indents on slowly moving object surface by laser-light beam scanning," *SICE '95. Proc. 34th SICE Annu. Conf. Int. Sess. Pap.*, pp. 1167–1170, 1995.

[120] P. Dean, M. U. Shaukat, E. H. Linfield, and A. G. Davies, "Three-dimensional characterisation of the non-Gaussian focused beam from a terahertz quantum cascade laser," *Conference on Lasers and Electro-Optics, 2007, CLEO 2007*, pp. 9–10, 2007.

[121] F. Zenhausern, M. P. O'Boyle, and H. K. Wickramasinghe, "Apertureless nearfield optical microscope," *Applied Physics Letters*, vol. 65, p. 1623, 1994.

[122] R. Degl'Innocenti, R. Wallis, B. Wei, L. Xiao, S. J. Kindness, O. Mitrofanov, P. Braeuninger-Weimer, S. Hofmann, H. E. Beere, and D. A. Ritchie, "Terahertz Nanoscopy of Plasmonic Resonances with a Quantum Cascade Laser," *ACS Photonics*, vol. 4, no. 9, pp. 2150–2157, 2017.

[123] E. Betzig and J. K. Trautman, "Near-Field Optics Microscopy, Spectroscopy, and Surface Modification Beyond the Diffraction Limit," *Science*, vol. 257, no. July, pp. 189–195, 1992.

[124] U. Durig, D. W. Pohl, and F. Rohner, "Near-field optical-scanning microscopy," *Journal of Applied Physics*, vol. 59, no. 10, p. 3318, 1986.

[125] E. H. Synge, "XXXVIII . A suggested method for extending microscopic resolution into the ultra-microscopic region," *Philosophical Magazine*, vol. 6, no. June 2012, pp. 356–362, 1928.

[126] E. Synge, "XXIII. An application of piezo-electricity to microscopy," *The London, Edinburgh, and Dublin Philosophical Magazine and Journal of Science*, vol. 13, no. 83, pp. 297–300, 1932.

[127] J. A. O'Keefe, "Resolving Power of Visible Light," *Journal of the Optical Society of America*, vol. 46, no. 5, p. 359, 1956.

[128] A. Lewis, M. Isaacson, A. Harootunian, and A. Muray, "Development of 500 angstrom spatial resolution light microscope," 1984.

[129] D. W. Pohl, W. Denk, and M. Lanz, "Optical stethoscopy Image recording with resolution $\lambda/20$," *Applied Physics Letters*, vol. 44, no. 7, p. 651, 1984.

[130] U. C. Fischer and D. W. Pohl, "Observation of Single-Particle Plasmons by Near-Field Optical Microscopy," *Physical Review Letters*, vol. 62, no. 4, pp. 458–461, 1989.

[131] A. Otto, "Excitation of nonradiative surface plasma waves in silver by the method of frustrated total reflection," *Zeitschrift ffir Physik*, vol. 216, pp. 298–410, 1968.

[132] E. Kretschmann and H. Raether, "Radiative decay of nonradiative plasmons excited by light," *Z. Naturforsch. A*, vol. 23, no. November 1968, pp. 2135–2136, 1968.

[133] H. F. Hess, E. Betzig, T. D. Harris, L. N. Pfeiffer, and K. W. West, "Near-Field Spectroscopy of the Quantum Constituents of a Luminescent System," *Science*, vol. 264, pp. 1740–1745, 1994.

[134] J. K. Trautman, J. J. Macklin, L. Brus, and E. Betzig, "Near-field spectroscopy of single molecules at room temperature," *Nature*, vol. 369, p. 40, 1994.

[135] N. Ocelic, A. Huber, and R. Hillenbrand, "Pseudoheterodyne detection for background-free near-field spectroscopy," *Applied Physics Letters*, vol. 89, no. 10, pp. 1–4, 2006.

[136] W. L. Barnes, A. Dereux, and T. W. Ebbesen, "Surface plasmon subwavelength optics," *Nature*, vol. 424, no. August, pp. 824–830, 2003.

[137] T. Klar, M. Perner, S. Grosse, G. V. Plessen, W. Spirkl, and J. Feldmann, "Surface-Plasmon Resonances in Single Metallic Nanoparticles," *Physical Review Letters*, vol. 80, no. 19, pp. 4249–4252, 1998.

[138] B. Lamprecht, J. P. Goudonnet, J. C. Weeber, Y. Lacroute, A. Dereux, and J. R. Krenn, "Near-field observation of surface plasmon polariton propagation on thin metal stripes," *Physical Review B - Condensed Matter and Materials Physics*, vol. 64, no. 4, pp. 1–9, 2001.

[139] J. R. Krenn, A. Dereux, J. C. Weeber, E. Bourillot, Y. Lacroute, J. P. Goudonnet, G. Schider, W. Gotschy, A. Leitner, F. R. Aussenegg, and C. Girard, "Squeezing the Optical Near-Field Zone by Plasmon Coupling of Metallic Nanoparticles," *Physical Review Letters*, vol. 82, no. 12, pp. 2590–2593, 1999.

[140] A. Woessner, M. B. Lundeberg, Y. Gao, A. Principi, P. Alonso-González, M. Carrega, K. Watanabe, T. Taniguchi, G. Vignale, M. Polini, J. Hone, R. Hillenbrand, and F. H. Koppens, "Highly confined low-loss plasmons in graphene-boron nitride heterostructures," *Nature Materials*, vol. 14, no. 4, pp. 421–425, 2015.

[141] M. B. Lundeberg, Y. Gao, A. Woessner, C. Tan, P. Alonso-González, K. Watanabe, T. Taniguchi, J. Hone, R. Hillenbrand, and F. H. Koppens, "Thermoelectric detection and imaging of propagating graphene plasmons," *Nature Materials*, vol. 16, no. 2, pp. 204–207, 2017.

[142] Z. Fei, G. O. Andreev, W. Bao, L. M. Zhang, A. S. McLeod, C. Wang, M. K. Stewart, Z. Zhao, G. Dominguez, M. Thiemens, M. M. Fogler, M. J. Tauber, A. H.

Castro-Neto, C. N. Lau, F. Keilmann, and D. N. Basov, "Infrared nanoscopy of dirac plasmons at the graphene-SiO2interface," *Nano Letters*, vol. 11, no. 11, pp. 4701–4705, 2011.

[143] Z. Fei, A. S. Rodin, G. O. Andreev, W. Bao, A. S. McLeod, M. Wagner, L. M. Zhang, Z. Zhao, M. Thiemens, G. Dominguez, M. M. Fogler, A. H. Castro Neto, C. N. Lau, F. Keilmann, and D. N. Basov, "Gate-tuning of graphene plasmons revealed by infrared nano-imaging," *Nature*, vol. 486, no. 7405, pp. 82–85, 2012.

[144] Z. Fei, M. D. Goldflam, J. S. Wu, S. Dai, M. Wagner, A. S. McLeod, M. K. Liu, K. W. Post, S. Zhu, G. C. Janssen, M. M. Fogler, and D. N. Basov, "Edge and Surface Plasmons in Graphene Nanoribbons," *Nano Letters*, vol. 15, no. 12, pp. 8271–8276, 2015.

[145] F. Hu, Y. Luan, Z. Fei, I. Z. Palubski, M. D. Goldflam, S. Dai, J. S. Wu, K. W. Post, G. C. Janssen, M. M. Fogler, and D. N. Basov, "Imaging the Localized Plasmon Resonance Modes in Graphene Nanoribbons," *Nano Letters*, vol. 17, no. 9, pp. 5423–5428, 2017.

[146] Q. Guo, C. Li, B. Deng, S. Yuan, F. Guinea, and F. Xia, "Infrared Nanophotonics Based on Graphene Plasmonics," *ACS Photonics*, vol. 4, no. 12, pp. 2989–2999, 2017.

[147] J. F. Li, Y. F. Huang, Y. Ding, Z. L. Yang, S. B. Li, X. S. Zhou, F. R. Fan, W. Zhang, Z. Y. Zhou, D. Y. Wu, B. Ren, Z. L. Wang, and Z. Q. Tian, "Shell-isolated nanoparticle-enhanced Raman spectroscopy," *Nature*, vol. 464, no. 7287, pp. 392–395, 2010.

[148] S. Nie and S. R. Emory, "Probing Single Molecules and Single Nanoparticles by SERS," *Science*, vol. 266, no. 5193, pp. 1102–1106, 1994.

[149] K. Kneipp, Y. Wang, H. Kneipp, L. T. Perelman, I. Itzkan, R. R. Dasari, and M. S.

Feld, “Single Molecule Detection Using Surface-Enhanced Raman Scattering (SERS) Katrin,” *Physical Review Letters*, vol. 78, no. 9, p. 1667, 1997.

[150] P. L. Stiles, J. A. Dieringer, N. C. Shah, and R. P. Van Duyne, “Surface-enhanced Raman spectroscopy,” *Annual Review of Analytical Chemistry*, vol. 1, p. 601, 2008.

[151] R. Hillenbrand and F. Keilmann, “Complex optical constants on a subwavelength scale,” *Physical Review Letters*, vol. 85, no. 14, pp. 3029–3032, 2000.

[152] F. Keilmann and R. Hillenbrand, “Near-field microscopy by elastic light scattering from a tip,” *Phil. Trans. R. Soc. Lond.*, vol. 362, no. 1817, pp. 787–805, 2004.

[153] B. Knoll and F. Keilmann, “Near-field probing of vibrational absorption for chemical microscopy,” *Nature*, vol. 399, no. May, pp. 7–10, 1999.

[154] O. Mitrofanov, I. Brener, M. C. Wanke, R. R. Ruel, J. D. Wynn, A. J. Bruce, and J. Federici, “Near-field microscope probe for far infrared time domain measurements,” *Applied Physics Letters*, vol. 77, no. 4, p. 591, 2000.

[155] M. C. G. Giordano, S. T. Mastel, C. Liewald, L. Columbo, M. Brambilla, L. Viti, A. Politano, K. Zhang, L. Lianhe, A. G. Davies, E. H. Linfield, R. A. Hillenbrand, F. Keilmann, G. Scamarcio, and M. S. Vitiello, “Phase-resolved terahertz self-detection near-field Microscopy,” *Optics Express*, vol. 26, no. 14, pp. 3430–3438, 2018.

[156] T. H. Maiman, “Stimulated Optical Radiation in Ruby,” *Nature*, vol. 187, pp. 493–494, 1960.

[157] A. L. Schawlow and C. H. Townes, “Infrared and Optical Masers,” *Physical Review*, vol. 112, no. 6, pp. 1941–1949, 1958.

[158] A. P. Alivisatos, “Semiconductor Clusters, Nanocrystals, and Quantum Dots,” *Science*, vol. 271, pp. 933–937, 1996.

[159] J. Van der Ziel, R. Dingle, R. C. Miller, W. Wiegmann, and W. A. Nordland Jr., "Laser oscillation from quantum states in very thin $GaAsAl_{0.2}Ga_{0.8}As$ multilayer structures," *Applied Physics Letters*, vol. 26, no. 8, pp. 463–465, 1975.

[160] M. S. Vitiello, G. Scalari, B. Williams, and P. De Natale, "Quantum cascade lasers: 20 years of challenges," *Optics Express*, vol. 23, no. 4, p. 5167, 2015.

[161] Y. Arakawa and A. Yariv, "Quantum Well Lasers-Gain, Spectra, Dynamics," *IEEE Journal of Quantum Electronics*, vol. 22, no. 9, pp. 1887–1899, 1986.

[162] L. Bosco, M. Franckie, G. Scalari, M. Beck, A. Wacker, and J. Faist, "Thermoelectrically cooled THz quantum cascade laser operating up to 210 K," *Applied Physics Letters*, vol. 115, no. 010601, 2019.

[163] J. Faist, M. Beck, T. Aellen, E. Gini, and E. Gini, "Quantum-cascade lasers based on a bound-to-continuum transition," *Applied Physics Letters*, vol. 78, no. 2, pp. 147–149, 2001.

[164] R. Köhler, A. Tredicucci, C. Mauro, F. Beltram, H. E. Beere, E. H. Linfield, A. G. Davies, and D. A. Ritchie, "Terahertz quantum-cascade lasers based on an interlaced photon-phonon cascade," *Applied Physics Letters*, vol. 84, no. 8, pp. 1266–1268, 2004.

[165] G. Scalari, L. Ajili, J. Faist, H. E. Beere, and E. H. Linfield, "Far-infrared (λ 87μm) bound-to-continuum quantum-cascade lasers operating up to 90 K," *Applied Physics Letters*, vol. 82, no. 19, p. 3165, 2003.

[166] B. S. Williams, H. Callebaut, S. Kumar, Q. Hu, and J. L. Reno, "3.4-THz quantum cascade laser based on longitudinal-optical-phonon scattering for depopulation," *Applied Physics Letters*, vol. 82, no. 7, pp. 1015–1017, 2003.

[167] Amanti, Maria I., G. Scalari, R. Terazzi, M. Fischer, M. Beck, J. Faist, A. Rudra, P. Gallo, and E. Kapon, "Bound-to-continuum terahertz quantum cascade laser with a single-quantum-well phonon extraction/injection stage," *New Journal of Physics*, vol. 11, 2009.

[168] S. Kohen, B. S. Williams, and Q. Hu, "Electromagnetic modeling of terahertz quantum cascade laser waveguides and resonators," *Journal of Applied Physics*, vol. 97, no. 5, 2005.

[169] R. Chhantyal-Pun, A. Valavanis, J. Keeley, P. Rubino, I. Kundu, Y. Han, P. Dean, L. Li, A. Giles Davies, and E. Linfield, "Gas spectroscopy with integrated frequency monitoring through self-mixing in a terahertz quantum-cascade laser," *Optics Letters*, vol. 43, no. 10, 2018.

[170] Y. L. Lim, T. Taimre, K. Bertling, P. Dean, D. Indjin, A. Valavanis, S. P. Khanna, M. Lachab, H. Schaider, T. W. Prow, H. Peter Soyer, S. J. Wilson, E. H. Linfield, A. Giles Davies, and A. D. Rakić, "High-contrast coherent terahertz imaging of porcine tissue via swept-frequency feedback interferometry," *Biomedical Optics Express*, vol. 5, no. 11, p. 3981, 2014.

[171] M. Wienold, L. Schrottke, M. Giehler, R. Hey, W. Anders, and H. T. Grahn, "Low-voltage terahertz quantum-cascade lasers based on LO-phonon-assisted interminiband transitions," *Electronics Letters*, vol. 45, no. 20, pp. 9–11, 2009.

[172] I. Kundu, *Frequency tunable terahertz quantum cascade lasers.* PhD thesis, The University of Leeds, 2014.

[173] A. Fathimulla, "Single-step lift-off process using chlorobenzene soak on AZ4000 resists," *J. Vac. Sci. Technol*, vol. 3, pp. 25–27, 1985.

[174] A. Callegari, E. T. Pan, and M. Murakami, "Uniform and thermally stable AuGeNi ohmic contacts to GaAs," *Applied Physics Letters*, vol. 46, no. 12, pp. 1141–1143, 1985.

[175] S. Donati, *Electro-Optical Instrumentation: Sensing and Measuring with Lasers.* Upper Saddle River, NJ, USA: Prentice Hall PTR, 2004.

[176] J. R. Tucker, *A Self-Mixing Imaging System Based on an Array of Vertical-Cavity*

Surface-Emitting Lasers (VCSELs). PhD thesis, The University of Queensland, 2007.

[177] K. Petermann, *Laser Diode Modulation and Noise*. Advances in Opto-Electronics, Springer Netherlands, 1988.

[178] J. Y. Law and G. P. Agrawal, "Effects of optical feedback on static and dynamic characteristics of vertical-cavity surface-emitting lasers," *IEEE Journal on Selected Topics in Quantum Electronics*, vol. 3, no. 2, pp. 353–358, 1997.

[179] Y. Yu, H. Ye, and J. Yao, "Analysis for the self-mixing interference effects in a laser diode at high optical feedback levels," *Journal of Optics A: Pure and Applied Optics*, vol. 5, no. 2, pp. 117–122, 2003.

[180] K. I. Kallimani and M. J. O'Mahony, "Relative intensity noise for laser diodes with arbitrary amounts of optical feedback," *IEEE Journal of Quantum Electronics*, vol. 34, no. 8, pp. 1438–1446, 1998.

[181] F. P. Mezzapesa, L. L. Columbo, M. Brambilla, M. Dabbicco, S. Borri, M. S. Vitiello, H. E. Beere, D. A. Ritchie, and G. Scamarcio, "Intrinsic stability of quantum cascade lasers against optical feedback," *Optics Express*, vol. 21, no. 11, p. 13748, 2013.

[182] T. Taimre, K. Bertling, Y. L. Lim, P. Dean, D. Indjin, and A. D. Rakić, "Methodology for materials analysis using swept-frequency feedback interferometry with terahertz frequency quantum cascade lasers.," *Optics express*, vol. 22, no. 15, pp. 18633–47, 2014.

[183] G. Giuliani, M. Norgia, S. Donati, and T. Bosch, "Laser diode self-mixing technique for sensing applications," *Journal of Optics A: Pure and Applied Optics*, vol. 4, no. 6, 2002.

[184] R. P. Green, J. H. Xu, L. Mahler, A. Tredicucci, F. Beltram, G. Giuliani, H. E. Beere, and D. A. Ritchie, "Linewidth enhancement factor of terahertz quantum cascade lasers," *Applied Physics Letters*, vol. 92, no. 7, pp. 2006–2009, 2008.

[185] P. Dean, O. Mitrofanov, J. Keeley, I. Kundu, L. H. Li, E. H. Linfield, A. G. Davies, and A. Giles Davies, "Apertureless near-field terahertz imaging using the self-mixing effect in a quantum cascade laser," *Applied Physics Letters*, vol. 091113, no. 9, 2016.

[186] T. Hagelschuer, M. Wienold, H. Richter, L. Schrottke, H. T. Grahn, and H.-W. Hübers, "Real-time gas sensing based on optical feedback in a terahertz quantum-cascade laser," *Optics Express*, vol. 25, no. 24, p. 30203, 2017.

[187] G. P. Agrawal and N. K. Dutta, *Semiconductor lasers*. New York : Van Nostrand Reinhold, 2nd ed ed., 1993. First ed. published 1986 under title: Long-wavelength semiconductor lasers.

[188] A. D. Rakić, K. Bertling, Y. L. Lim, S. J. Wilson, M. Nikolić, T. Taimre, D. Indjin, A. Valavanis, E. H. Linfield, A. G. Davies, G. Walker, B. Ferguson, T. W. Prow, H. Schaider, and H. P. Soyer, "Biomedical applications of terahertz self-mixing interferometry," *SPIE Newsroom*, pp. 4–6, oct 2014.

[189] M. A. Brun, F. Formanek, A. Yasuda, M. Sekine, N. Ando, and Y. Eishii, "Terahertz imaging applied to cancer diagnosis," *Physics in Medicine and Biology*, 2010.

[190] R. M. Woodward, B. E. Cole, V. P. Wallace, R. J. Pye, D. D. Arnone, E. H. Linfield, and M. Pepper, "Terahertz pulse imaging in reflection geometry of human skin cancer and skin tissue," *Physics in Medicine and Biology*, vol. 47, no. 21, pp. 3853–3863, 2002.

[191] K. J. Siebert, T. Löffler, H. Quast, M. Thomson, T. Bauer, R. Leonhardt, S. Czasch, and H. G. Roskos, "All-optoelectronic continuous wave THz imaging for biomedical applications.," *Phys. Med. Biol.*, vol. 47, pp. 3743–3748, nov 2002.

[192] M. Nazarov, A. Shkurinov, V. Tuchin, and X. Zhang, "Terahertz Tissue Spectroscopy and Imaging," *Handbook ofPhotonics for Biomedical Science*, no. May, pp. 519–617, 2010.

[193] E. Pickwell, A. J. Fitzgerald, P. F. Taday, B. E. Cole, R. J. Pye, T. Ha, M. Pepper, and V. P. Wallace, "Terahertz imaging and spectroscopy of skin cancer," *Conference Digest of the 2004 Joint 29th International Conference on Infrared and Millimeter Waves and 12th International Conference on Terahertz Electronics*, pp. 821–822, 2004.

[194] H. Hoshina, S. Nakajima, M. Yamashita, C. Otani, and N. Miyoshi, "Terahertz imaging diagnostics of the cancer tissues with chemometrics technique," *IRMMW-THz 2006 - 31st International Conference on Infrared and Millimeter Waves and 14th International Conference on Terahertz Electronics*, vol. 041102, no. 2007, p. 195, 2006.

[195] M. He, A. K. Azad, S. Ye, and W. Zhang, "Far-infrared signature of animal tissues characterized by terahertz time-domain spectroscopy," *Optics Communications*, vol. 259, no. 1, pp. 389–392, 2006.

[196] Y. Sun and E. Pickwell-MacPherson, "The effects of formalin fixing on terahertz properties of biological samples," *33rd International Conference on Infrared and Millimeter Waves and the 16th International Conference on Terahertz Electronics, 2008, IRMMW-THz 2008*, vol. 14, no. December 2009, pp. 1–7, 2008.

[197] A. Rahman, A. K. Rahman, and B. Rao, "Early detection of skin cancer via terahertz spectral profiling and 3D imaging," *Biosensors and Bioelectronics*, vol. 82, pp. 64–70, 2016.

[198] D. Markl, M. Ruggiero, and J. Zeitler, "Pharmaceutical applications of terahertz spectroscopy and imaging," *European Pharmaceutical Review*, vol. 21, no. 4, 2016.

[199] V. P. Wallace, E. MacPherson, J. A. Zeitler, and C. Reid, "Three-dimensional imaging of optically opaque materials using nonionizing terahertz radiation," *Journal of the Optical Society of America A*, vol. 25, no. 12, p. 3120, 2008.

[200] D. R. Grischkowsky and D. M. Mittleman, *Sensing with Terahertz Radiation*, vol. 85

of *Springer Series in Optical Sciences*. Berlin, Heidelberg: Springer Berlin Heidelberg, 2003.

[201] K. Kawase, Y. Ogawa, Y. Watanabe, and H. Inoue, "Non-destructive terahertz imaging of illicit drugs using spectral fingerprints," *Optics Express*, 2003.

[202] Y. C. Shen, T. Lo, P. F. Taday, B. E. Cole, W. R. Tribe, and M. C. Kemp, "Detection and identification of explosives using terahertz pulsed spectroscopic imaging," *Applied Physics Letters*, 2005.

[203] M. Walther, B. M. Fischer, A. Ortner, A. Bitzer, A. Thoman, and H. Helm, "Chemical sensing and imaging with pulsed terahertz radiation," 2010.

[204] A. D. Rakić, T. Taimre, K. Bertling, Y. L. Lim, P. Dean, D. Indjin, Z. Ikonić, P. Harrison, A. Valavanis, S. P. Khanna, M. Lachab, S. J. Wilson, E. H. Linfield, and A. G. Davies, "Swept-frequency feedback interferometry using terahertz frequency QCLs: a method for imaging and materials analysis," *Optics Express*, vol. 21, no. 19, p. 22194, 2013.

[205] H. S. Lui, T. Taimre, K. Bertling, Y. L. Lim, P. Dean, S. P. Khanna, M. Lachab, A. Valavanis, D. Indjin, E. H. Linfield, a. G. Davies, and a. D. Rakić, "Terahertz inverse synthetic aperture radar imaging using self-mixing interferometry with a quantum cascade laser," *Optics letters*, vol. 39, no. 9, pp. 2629–32, 2014.

[206] A. Valavanis, P. Dean, Y. L. Lim, R. H. S. Alhathlool, M. Nikolić, R. Kliese, S. P. Khanna, D. Indjin, S. J. Wilson, A. D. Rakić, E. H. Linfield, and A. G. Davies, "Self-Mixing Interferometry With Terahertz Quantum Cascade Lasers," *IEEE Sensors Journal*, vol. 13, no. 1, pp. 37–43, 2013.

[207] H. Hübers, S. G. Pavlov, A. D. Semenov, R. Kohler, L. Mahler, A. Tredicucci, and E. H. Linfield, "Terahertz quantum cascade laser as local oscillator in a heterodyne receiver," *Optics Express*, vol. 13, no. 15, pp. 5890–5896, 2005.

[208] M. Salih, P. Dean, A. Valavanis, S. P. Khanna, L. H. Li, M. Salih, P. Dean, A. Valavanis, S. P. Khanna, L. H. Li, J. E. Cunningham, and A. G. Davies, "Terahertz quantum cascade lasers with thin resonant-phonon depopulation active regions and surface-plasmon waveguides," *Journal of Applied Physics*, vol. 113, 2013.

[209] T. L. Jester, "Crystalline silicon manufacturing progress," *Progress in Photovoltaics: Research and Applications*, vol. 10, no. 2, pp. 99–106, 2002.

[210] D. Macdonald, A. Cuevas, A. Kinomura, Y. Nakano, and L. J. Geerligs, "Transition-metal profiles in a multicrystalline silicon ingot," *Journal of Applied Physics*, vol. 97, no. 3, 2005.

[211] O. D. Patterson, S. C. C. Lei, and D. M. Salvador, "E-Beam Inspection for Detection of Sub-Design Rule Physical Defects," *ASMC*, p. 383, 2012.

[212] O. D. Patterson, J. Lee, D. M. Salvador, S. C. C. Lei, and X. Tang, "Detection of sub-design rule physical defects using E-beam inspection," *IEEE Transactions on Semiconductor Manufacturing*, vol. 26, no. 4, pp. 476–481, 2013.

[213] M. Herrmann, M. Tani, K. Sakai, and R. Fukasawa, "Terahertz imaging of silicon wafers," *Journal of Applied Physics*, vol. 91, no. 3, pp. 1247–1250, 2002.

[214] M. Van Exter and D. Grischkowsky, "Optical and electronic properties of doped silicon from 0.1 to 2 THz," *Appl. Phys. Lett.*, Vol. 56, No 17, 23 April 1990.

[215] J. Dai, J. Zhang, W. Zhang, and D. Grischkowsky, "Terahertz time-domain spectroscopy characterization of the far-infrared absorption and index of refraction of high-resistivity, float-zone silicon," *Journal of the Optical Society of America B*, vol. 21, no. 7, p. 1379, 2004.

[216] P. Rostam-Khani, J. Philipsen, E. Jansen, H. Eberhard, and P. Vullings, "Quantitative analysis of surface contaminants on silicon wafers by means of TOF-SIMS," *Applied Surface Science*, vol. 252, no. 19, pp. 7255–7257, 2006.

[217] T. Gluodenis, "Characterization of Surface Metal Contamination on Silicon Wafers Using Surface Metal Extraction Inductively Coupled Plasma Mass Spectrometry (SME-," *Agilent Technologies Inc.*, 2009.

[218] S. Takahashi, T. Miyoshi, Y. Takaya, and K. Saito, "In-process measurement method for detection and discrimination of silicon wafer surface defects by laser scattered defect pattern," *CIRP Annals-Manufacturing*, vol. 47, no. 2, pp. 459–462, 1998.

[219] F. Shimura, H. Tsuya, and T. Kawamura, "Surface- and inner-microdefects in annealed silicon wafer containing oxygen," *Journal of Applied Physics*, vol. 51, no. 1, pp. 269–273, 1980.

[220] Y. C. Chiou, J. Z. Liu, and Y. T. Liang, "Micro crack detection of multi-crystalline silicon solar wafer using machine vision techniques," *Sensor Review*, vol. 31, no. 2, pp. 154–165, 2011.

[221] N. Palina, M. P. Peloso, K. Banas, B. Hoex, and A. G. Aberle, "Study on defects in multicrystalline silicon wafer cells by electroluminescence and synchrotron radiation induced X-ray emission," *27th European Photovoltaic Solar Energy Conference and Exhibition*, no. January 2017, pp. 91–94, 2012.

[222] T. Orellana, E. M. Tejado, C. Funke, W. Fütterer, S. Riepe, H. J. Moller, and J. Y. Pastor, "How do Impurity Inclusions Influence the Mechanical Properties of Multicrystalline Silicon ?," *International Journal of Metallurgical & Materials Engineering*, vol. 1, no. 1, pp. 1–11, 2015.

[223] K. Bertling, S. Han, T. Wu, C. Zhao, Y. L. Lim, P. Dean, S. P. Khanna, D. Indjin, E. H. Linfield, A. G. Davies, S. J. Wilson, T. Taimre, and A. D. Rakic, "Determining Ethanol Content of Liquid Solutions Using Laser Feedback Interferometry with a Terahertz Quantum Cascade Laser," *IEEE Sensors Letters*, vol. 2, no. 3, pp. 2–5, 2018.

[224] F. Buersgens, R. Kersting, and H.-T. Chen, "Terahertz microscopy of charge carriers

in semiconductors," *Applied Physics Letters*, vol. 112115, no. February 2006, pp. 88–91, 2006.

[225] G. Acuna, S. F. Heucke, F. Kuchler, H. Chen, A. J. Taylor, and R. Kersting, "Surface plasmons in terahertz metamaterials," *Optics Express*, vol. 16, no. 23, pp. 18745–18751, 2008.

[226] A. Bitzer, H. Merbold, A. Thoman, T. Feurer, H. Helm, and M. Walther, "Terahertz near-field imaging of electric and magnetic resonances of a planar metamaterial Abstract :," *Optics Express*, vol. 17, no. 5, pp. 1351–1353, 2009.

[227] O. Mitrofanov, Y. Wenlong, R. J. Thompson, J. Yuxuan, I. Brener, P. Wei, C. Berger, W. A. de Heer, and J. Zhigang, "Probing terahertz surface plasmon waves in graphene structures," *Applied Physics Letters*, vol. 103, no. 11, pp. 111105 (4 pp.)–111105 (4 pp.), 2013.

[228] I. Khromova, M. Navarro-Cía, I. Brener, J. L. Reno, A. Ponomarev, and O. Mitrofanov, "Dipolar resonances in conductive carbon micro-fibers probed by near-field terahertz spectroscopy," *Applied Physics Letters*, vol. 107, no. 2, p. 021102, 2015.

[229] K. Nielsen, H. K. Rasmussen, J. L. Adam, C. Paul, M. Planken, O. Bang, and P. U. Jepsen, "Bendable , low-loss Topas fibers for the terahertz frequency range," *Optics Express*, vol. 17, no. 10, pp. 8845–8854, 2009.

[230] O. Mitrofanov, T. Tan, P. R. Mark, B. Bowden, J. A. Harrington, and J. A. Harrington, "Waveguide mode imaging and dispersion analysis with terahertz near-field microscopy microscopy," *Applied Physics Letters*, vol. 171104, no. January 2009, pp. 10–13, 2016.

[231] C.-m. Chiu, H.-w. Chen, Y.-r. Huang, Y.-j. Hwang, W.-j. Lee, H.-y. Huang, and C.-k. Sun, "All-terahertz fiber-scanning near-field microscopy," *Optics Letters*, vol. 34, no. 7, pp. 1084–1086, 2009.

[232] B. Knoll and F. Keilmann, "Enhanced dielectric contrast in scattering-type scanning near-field optical microscopy," *Optics Communications*, vol. 182, no. August, pp. 321–328, 2000.

[233] A. Bitzer and M. Walther, "Terahertz near-field imaging of metallic subwavelength holes and hole arrays," *Applied Physics Letters*, vol. 92, no. 231101, 2008.

[234] R. Lecaque, S. Gr, and C. Boccara, "THz emission Microscopy with sub-wavelength broadband source," *Optics Express*, vol. 16, no. 7, pp. 2388–2390, 2008.

[235] M. A. Seo, A. J. L. Adam, J. H. Kang, J. W. Lee, S. C. Jeoung, Q. H. Park, P. C. M. Planken, and D. S. Kim, "Fourier-transform terahertz near-field imaging of one-dimensional slit arrays : mapping of electric-field-, magnetic-field-, and Poynting vectors," *Optics Express*, vol. 15, no. 19, pp. 11781–11789, 2007.

[236] L. Novotny and B. Hecht, *Principles of Nano-Optics*. Cambridge University Press, 2006.

[237] H. Richter, N. Rothbart, and H. W. Hübers, "Characterizing the beam properties of terahertz quantum-cascade lasers," *Journal of Infrared, Millimeter, and Terahertz Waves*, vol. 35, no. 8, pp. 686–698, 2014.

[238] A. Cvitkovic, N. Ocelic, and R. Hillenbrand, "Analytical model for quantitative prediction of material contrasts in scattering-type near-field optical microscopy," *Optics Express*, vol. 15, no. 14, p. 8550, 2007.

[239] S. Amarie and F. Keilmann, "Broadband-infrared assessment of phonon resonance in scattering-type near-field microscopy," *Physical Review B - Condensed Matter and Materials Physics*, vol. 83, no. 4, pp. 1–9, 2011.

[240] K. S. Novoselov, A. K. Geim, S. V. Morozov, D. Jiang, Y. Zhang, S. V. Dubonos, I. V. Grigorieva, and A. A. Firsov, "Electric Field Effect in Atomically Thin Carbon Films," *Science*, vol. 306, no. 5696, pp. 666–669, 2004.

[241] I. Meric, M. Y. Han, A. F. Young, B. Ozyilmaz, P. Kim, and K. L. Shepard, "Current saturation in zero-bandgap , top- gated graphene field-effect transistors," *Nature Nanotechnology*, vol. 3, no. November, 2008.

[242] M. C. Lemme, T. J. Echtermeyer, M. Baus, and H. Kurz, "A Graphene Field-Effect Device," *IEEE Electron Device Letters*, vol. 28, no. 4, pp. 282–284, 2007.

[243] F. Bonaccorso, Z. Sun, T. Hasan, and A. C. Ferrari, "Graphene photonics and optoelectronics," *Nature Photonics*, vol. 4, no. 9, pp. 611–622, 2010.

[244] M. Liu, X. Yin, E. Ulin-avila, B. Geng, T. Zentgraf, L. Ju, F. Wang, and X. Zhang, "A graphene-based broadband optical modulator," *Nature*, vol. 474, no. 7349, pp. 64–67, 2011.

[245] S. Bae, H. Kim, Y. Lee, X. Xu, J.-s. Park, Y. Zheng, J. Balakrishnan, T. Lei, H. R. Kim, Y. I. Song, Y.-j. Kim, and K. S. Kim, "Roll-to-roll production of 30-inch graphene films for transparent electrodes," *Nature Nanotechnology*, vol. 5, no. August, pp. 1–5, 2010.

[246] A. You, M. A. Y. Be, and I. In, "Organic solar cells with solution-processed graphene transparent electrodes transparent electrodes," *Applied Physics Letters*, vol. 263302, no. March, 2008.

[247] X. Wang, L. Zhi, and K. Mu, "Transparent , Conductive Graphene Electrodes for Dye-Sensitized Solar Cells," *Nano Letters*, vol. 8, no. 1, pp. 323–327, 2008.

[248] R. Degl'Innocenti, L. Xiao, S. J. Kindness, V. S. Kamboj, B. Wei, P. Braeuninger-Weimer, K. Nakanishi, A. I. Aria, S. Hofmann, H. E. Beere, and D. A. Ritchie, "Bolometric detection of terahertz quantum cascade laser radiation with graphene-plasmonic antenna arrays," *Journal of Physics D: Applied Physics*, vol. 50, no. 17, 2017.

[249] T. Low and P. Avouris, "Graphene plasmonics for terahertz to mid-infrared applications," *ACS Nano*, vol. 8, no. 2, pp. 1086–1101, 2014.

[250] F. H. Koppens, T. Mueller, P. Avouris, A. C. Ferrari, M. S. Vitiello, and M. Polini, "Photodetectors based on graphene, other two-dimensional materials and hybrid systems," *Nature Nanotechnology*, vol. 9, no. 10, pp. 780–793, 2014.

[251] A. Tredicucci and M. S. Vitiello, "Device concepts for graphene-based terahertz photonics," *IEEE Journal on Selected Topics in Quantum Electronics*, vol. 20, no. 1, 2014.

[252] L. Vicarelli, M. S. Vitiello, D. Coquillat, A. Lombardo, A. C. Ferrari, W. Knap, M. Polini, V. Pellegrini, and A. Tredicucci, "Graphene field-effect transistors as room-temperature terahertz detectors," *Nature Materials*, vol. 11, no. 10, pp. 865–871, 2012.

[253] F. H. Koppens, D. E. Chang, and F. J. García De Abajo, "Graphene plasmonics: A platform for strong light-matter interactions," *Nano Letters*, vol. 11, no. 8, pp. 3370–3377, 2011.

[254] A. M. Dubrovkin, J. Tao, X. Chao Yu, N. I. Zheludev, and Q. Jie Wang, "The reduction of surface plasmon losses in quasi-suspended graphene," *Scientific Reports*, vol. 5, pp. 1–9, 2015.

[255] A. Y. Nikitin, P. Alonso-GonzÃ¡lez, S. VÃ©lez, S. Mastel, A. Centeno, A. Pesquera, A. Zurutuza, F. Casanova, L. E. Hueso, F. H. Koppens, and R. Hillenbrand, "Real-space mapping of tailored sheet and edge plasmons in graphene nanoresonators," *Nature Photonics*, vol. 10, no. 4, pp. 239–243, 2016.

[256] R. Degl'Innocenti, D. S. Jessop, Y. D. Shah, J. Sibik, J. A. Zeitler, P. R. Kidambi, S. Hofmann, H. E. Beere, and D. A. Ritchie, "Low-bias terahertz amplitude modulator based on split-ring resonators and graphene," *ACS Nano*, vol. 8, no. 3, pp. 2548–2554, 2014.

[257] P. R. Wallace, "The band theory of graphite," *Physical Review*, vol. 71, no. 9, pp. 622–634, 1947.

[258] A. H. Castro Neto, F. Guinea, N. M. R. Peres, K. S. Novoselov, and A. K. Geim, "The electronic properties of graphene," *Rev. Mod. Phys.*, vol. 81, pp. 109–162, Jan 2009.

[259] M. Jablan, M. Soljacic, and H. Buljan, "Plasmons in Graphene: Fundamental Properties and Potential Applications," *Proceedings of the IEEE*, vol. 101, no. 7, pp. 1689–1704, 2013.

[260] S. Reich, J. Maultzsch, C. Thomsen, and P. Ordejón, "Tight-binding description of graphene," *Physical Review B - Condensed Matter and Materials Physics*, vol. 66, no. 3, pp. 354121–354125, 2002.

[261] S. Shin, S. Kim, T. Kim, H. Du, K. S. Kim, S. Cho, and S. Seo, "Graphene transfer with self-doping by amorphous thermoplastic resins," *Carbon*, vol. 111, pp. 215–220, 2017.

[262] J. C. Ren, Z. Ding, R. Q. Zhang, and M. A. Van Hove, "Self-doping and magnetic ordering induced by extended line defects in graphene," *Physical Review B - Condensed Matter and Materials Physics*, vol. 91, no. 4, pp. 1–7, 2015.

[263] D. A. Siegel, S. Y. Zhou, F. El Gabaly, A. V. Fedorov, A. K. Schmid, and A. Lanzara, "Self-doping effects in epitaxially grown graphene," *Applied Physics Letters*, vol. 93, no. 24, pp. 1–4, 2008.

[264] C. Coletti, C. Riedl, D. S. Lee, B. Krauss, L. Patthey, K. Von Klitzing, J. H. Smet, and U. Starke, "Charge neutrality and band-gap tuning of epitaxial graphene on SiC by molecular doping," *Physical Review B - Condensed Matter and Materials Physics*, vol. 81, no. 23, pp. 1–8, 2010.

[265] L. Kong, A. Enders, T. S. Rahman, and P. A. Dowben, "Molecular adsorption on graphene," *Journal of Physics Condensed Matter*, vol. 26, no. 44, 2014.

[266] O. Leenaerts, B. Partoens, and F. M. Peeters, "Adsorption of small molecules on graphene," *Microelectronics Journal*, vol. 40, no. 4-5, pp. 860–862, 2009.

[267] P. Lazar, P. Jurec, and M. Otyepka, "Adsorption of Small Organic Molecules on Graphene," *Journal of the American Chemical Society*, vol. 135, pp. 6372–6377, 2013.

[268] X. Dong, D. Fu, W. Fang, Y. Shi, P. Chen, and L. Li, "Doping Single-Layer Graphene with Aromatic Molecules," *small*, vol. 5, no. 12, pp. 1422–1426, 2009.

[269] P.-h. Ho, Y.-c. Yeh, D.-y. Wang, S.-s. Li, H.-a. Chen, and Y.-h. Chung, "Self-Encapsulated Doping of n-Type Graphene Transistors with Extended Air Stability," *ACS Nano*, pp. 6215–6221, 2012.

[270] R. Phillipson, C. J. Lockhart De La Rosa, J. Teyssandier, P. Walke, D. Waghray, Y. Fujita, J. Adisoejoso, K. S. Mali, I. Asselberghs, C. Huyghebaert, H. Uji-I, S. De Gendt, and S. De Feyter, "Tunable doping of graphene by using physisorbed self-assembled networks," *Nanoscale*, vol. 8, no. 48, pp. 20017–20026, 2016.

[271] H. Wang, T. Taychatanapat, A. Hsu, K. Watanabe, T. Taniguchi, P. Jarillo-herrero, and T. Palacios, "BN / Graphene / BN Transistors for RF Applications," *Nano*, vol. 32, no. 9, pp. 1209–1211, 2011.

[272] R. Degl'innocenti, D. S. Jessop, C. W. Sol, L. Xiao, S. J. Kindness, H. Lin, J. A. Zeitler, P. Braeuninger-Weimer, S. Hofmann, Y. Ren, V. S. Kamboj, J. P. Griffiths, H. E. Beere, and D. A. Ritchie, "Fast Modulation of Terahertz Quantum Cascade Lasers Using Graphene Loaded Plasmonic Antennas," *ACS Photonics*, vol. 3, no. 3, pp. 464–470, 2016.

[273] A. Scidà, S. Haque, E. Treossi, A. Robinson, S. Smerzi, S. Ravesi, S. Borini, and V. Palermo, "Application of graphene-based flexible antennas in consumer electronic devices," *Materials Today*, vol. 21, no. 3, pp. 223–230, 2018.

[274] L. A. Falkovsky and A. A. Varlamov, "Space-time dispersion of graphene conductivity," *European Physical Journal B*, vol. 56, no. 4, pp. 281–284, 2007.

[275] L. A. Falkovsky, "Optical properties of graphene," *Journal of Physics*, 2008.

[276] Z. Q. Li, E. A. Henriksen, Z. Jiang, Z. Hao, M. C. Martin, P. Kim, H. L. Stormer, and D. N. Basov, "Dirac charge dynamics in graphene by infrared spectroscopy," *Nature Physics*, vol. 4, no. 7, pp. 532–535, 2008.

[277] N. Ashcroft and N. Mermin, *Solid State Physics*. Philadelphia: Saunders College, 1976.

[278] P. A. Huidobro, A. I. Fernández-Domínguez, J. B. Pendry, L. Martín-Moreno, and F. J. Garcia-Vidal, *Spoof Surface Plasmon Metamaterials*. Elements in Emerging Theories and Technologies in Metamaterials, Cambridge University Press, 2018.

[279] W. H. Backes, F. M. Peeters, F. Brosens, and J. T. Devreese, "Dispersion oflongitudinal plasmons for a quasi-two-dimensional electron gas," *Physical Review B*, vol. 45, no. 15, 1992.

[280] S. A. Mikhailov and K. Ziegler, "New electromagnetic mode in graphene," *Physical Review Letters*, vol. 99, no. 1, pp. 1–4, 2007.

[281] N. D. Mermin, "Lindhard dielectric function in the relaxation-time approximation," *Physical Review B*, vol. 1, no. 5, pp. 2362–2363, 1970.

[282] E. H. Hwang and S. Das Sarma, "Dielectric function, screening, and plasmons in two-dimensional graphene," *Physical Review B - Condensed Matter and Materials Physics*, vol. 75, no. 20, pp. 1–6, 2007.

[283] R. R. Nair, P. Blake, A. N. Grigorenko, K. S. Novoselov, T. J. Booth, T. Stauber, N. M. R. Peres, and A. K. Geim, "Fine Structure Constant Defines Visual Transparency of Graphene," *Science*, vol. 320, p. 1308, 2008.

[284] Z. Fang, Y. Wang, Z. Liu, A. Schlather, and P. M. Ajayan, "Plasmon-Induced Doping of Graphene," *ACS Nano*, no. 11, pp. 10222–10228, 2012.

[285] V. W. Brar, M. S. Jang, M. Sherrott, S. Kim, J. J. Lopez, L. B. Kim, M. Choi, and H. Atwater, "Hybrid Surface-Phonon-Plasmon Polariton Modes

in Graphene/Monolayer h-BN Heterostructures," *Nano Letters*, vol. 14, no. 7, pp. 3876–3880, 2014.

[286] A. Principi, G. Vignale, M. Carrega, and M. Polini, "Impact of disorder on Dirac plasmon losses," *Physical Review B - Condensed Matter and Materials Physics*, vol. 88, no. 12, pp. 6–10, 2013.

[287] J. Wang, F. Ma, W. Liang, and M. Sun, "Electrical properties and applications of graphene, hexagonal boron nitride (h-BN), and graphene/h-BN heterostructures," *Materials Today Physics*, vol. 2, pp. 6–34, 2017.

[288] A. Principi, M. Carrega, M. B. Lundeberg, A. Woessner, F. H. Koppens, G. Vignale, and M. Polini, "Plasmon losses due to electron-phonon scattering: The case of graphene encapsulated in hexagonal boron nitride," *Physical Review B - Condensed Matter and Materials Physics*, vol. 90, no. 16, pp. 1–14, 2014.

[289] M. B. Lundeberg, Y. Gao, R. Asgari, C. Tan, B. V. Duppen, M. Autore, P. Alonso-González, A. Woessner, K. Watanabe, T. Taniguchi, R. Hillenbrand, J. Hone, M. Polini, and F. H. Koppens, "Tuning quantum nonlocal effects in graphene plasmonics," *Science*, vol. 357, no. 6347, pp. 187–191, 2017.

[290] O. Madelung, U. Rössler, and M. Schulz, eds., *Boron nitride (BN) dielectric constants: Datasheet from Landolt-Börnstein - Group III Condensed Matter · Volume 41A1α: "Group IV Elements, IV-IV and III-V Compounds. Part a - Lattice Properties" in SpringerMaterials (https://dx.doi.org/10.1007/10551045_16)*. Springer-Verlag Berlin Heidelberg, 1970-2017.

[291] M. P. Lavin-Lopez, J. L. Valverde, A. Garrido, L. Sanchez-Silva, P. Martinez, and A. Romero-Izquierdo, "Novel etchings to transfer CVD-grown graphene from copper to arbitrary substrates," *Chemical Physics Letters*, vol. 614, pp. 89–94, 2014.

[292] S. Pisana, M. Lazzeri, C. Casiraghi, K. S. Novoselov, A. K. Geim, A. C. Ferrari,

and F. Mauri, "Breakdown of the adiabatic Born-Oppenheimer approximation in graphene," *Nature Materials*, vol. 6, no. 3, pp. 198–201, 2007.

[293] A. C. Ferrari, J. C. Meyer, V. Scardaci, C. Casiraghi, M. Lazzeri, F. Mauri, S. Piscanec, D. Jiang, K. S. Novoselov, S. Roth, and A. K. Geim, "Raman spectrum of graphene and graphene layers," *Physical Review Letters*, vol. 97, no. 18, pp. 1–4, 2006.

[294] A. C. Ferrari, "Raman spectroscopy of graphene and graphite: Disorder, electron-phonon coupling, doping and nonadiabatic effects," *Solid State Communications*, vol. 143, no. 1-2, pp. 47–57, 2007.

[295] M. Lazzeri and F. Mauri, "Nonadiabatic Kohn anomaly in a doped graphene monolayer," *Physical Review Letters*, vol. 97, no. 26, pp. 29–32, 2006.

[296] Y. Yin, Z. Cheng, L. Wang, K. Jin, and W. Wang, "Graphene, a material for high temperature devices - Intrinsic carrier density, carrier drift velocity, and lattice energy," *Scientific Reports*, vol. 4, pp. 1–6, 2014.

[297] S. Russo, M. F. Craciun, M. Yamamoto, S. Tarucha, and A. F. Morpurgo, "Double-gated graphene-based devices," *New Journal of Physics*, vol. 11, 2009.

[298] A. Eckmann, A. Felten, A. Mishchenko, L. Britnell, R. Krupke, K. S. Novoselov, and C. Casiraghi, "Probing the nature of defects in graphene by Raman spectroscopy," *Nano Letters*, vol. 12, no. 8, pp. 3925–3930, 2012.

[299] D. L. Nika and A. A. Balandin, "Two-dimensional phonon transport in graphene," *J. Phys.: Condens. Matter*, vol. 24, 2012.